Modeling of the Human Brain to Predict Spatial and Temporal Temperature Profiles for the Selective Hypothermia Treatment of an Ischemic Stroke

Zur Erlangung des akademischen Grades eines

DOKTOR-INGENIEURS

von der KIT-Fakultät für

Elektrotechnik und Informationstechnik

des Karlsruher Instituts für Technologie (KIT)

genehmigte

DISSERTATION

von

Yannick Lutz, M.Sc.

geb. in Freiburg i. Br.

Tag der mündlichen Prüfung:	16. Juli 2020
Referent:	Prof. Dr. rer. nat. Olaf Dössel
1. Korreferent:	Prof. Dr.-Ing. Giorgio Cattaneo
2. Korreferent:	Dr.-Ing. Axel Loewe

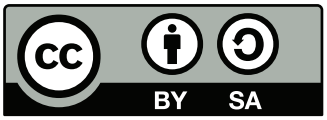

Danksagung

Diese Arbeit entstand während meiner Tätigkeit als wissenschaftlicher Mitarbeiter am Institut für Biomedizinische Technik des Karlsruher Instituts für Technologie zwischen Februar 2017 und April 2020. Hiermit möchte ich all Jenen, die diese Arbeit ermöglicht, mich während dieser Zeit unterstützt und somit zum Erfolg dieser Arbeit beigetragen haben, meinen Dank aussprechen.

An erster Stelle möchte ich mich ganz herzlich bei Herrn Prof. Dr. rer. nat. Olaf Dössel für seine fachliche Betreuung und die Übernahme des Hauptreferats bedanken. Ich danke ihm für die regelmäßigen konstruktiven Diskussionen und für seine Unterstützung bei schwierigeren Projektteilabschnitten. Ein weiterer besonderer Dank geht an Herrn Prof. Dr.-Ing. Giorgio Cattaneo für die Übernahme des ersten Korreferats. Außerdem möchte ich ihm für alle gemeinsamen fachlichen Diskussionen danken, die mir eine große Hilfe während meiner gesamten Arbeit waren. Auch bei Herrn Dr.-Ing. Axel Loewe möchte ich mich für die Übernahme des zweiten Korreferats und für die langjährige, positive Zusammenarbeit besonders bedanken. Durch den produktiven fachlichen Austausch sowie durch sein wertvolles Feedback im Bereich der Modellierung konnte ich während meiner gesamten Zeit am Institut profitieren. Vielen Dank auch an das Bundesministerium für Wirtschaft und Energie für die Förderung dieses Projekts (ZF4363901AK6) und die Ermöglichung dieser Promotion.

Ein herzliches Dankeschön für die gute Zusammenarbeit und die produktiven Diskussionen geht auch an alle Kollegen am Institut. Durch die familiäre Arbeitsatmosphäre und die kollegiale, großartige Unterstützung ließen sich auch schwere Phasen der Promotion erfolgreich meistern. Besonders hervorheben möchte ich die Zusammenarbeit mit Steffen Schuler, der mir immer ein toller Bürokollege war. Die Einblicke in das inverse Problem der Elektrokardiographie waren mir oft eine willkommene, kleine Abwechslung und seine Ratschläge bei widerspenstigen Meshproblemen eine große Hilfe. Zusätzlich konnte ich mit Michael Kircher, Dr.-Ing. Gustavo Lenis, Ady Naber, Nicolas Pilia und Dr.-Ing. Stefan Pollnow immer wieder spannende Fragen und Themen diskutieren.

Für seine medizinische Expertise und die positive Zusammenarbeit während der gesamten Zeit dieser Promotion möchte ich Prof. Dr. med. Stephan Meckel herzlich danken. Seine medizinischen Anmerkungen waren mir stets eine große Hilfe, von der der medizinische Aspekt dieser Dissertation enorm profitierte. Vielen Dank auch für die Ermöglichung des Beiwohnens bei einem Eingriff aus der Tier-Studie.

Des Weiteren möchte ich mich bei Juliane Müller von der Technischen Universität Dresden bedanken. Vielen Dank für die spannenden fachlichen Diskussionen und die Bereitstellung von perioperativen Thermographieaufnahmen.
Ein weiteres großes Dankeschön geht an Samuel Voß von der Otto von Guericke Universität Magdeburg. Die gemeinsamen Überlegungen und seine Realisierung eines vergleichenden Experimentalaufbaus führten zu spannenden und hilfreichen Diskussionen.
Ein weiterer besonderer Dank geht an alle meine betreuten Studenten, die mich bei meiner Arbeit großartig unterstützt haben. Ihr Engagement in den einzelnen Projekten und die fachlichen Diskussionen haben zum Erfolg dieser Arbeit beigetragen. Besonders hervorheben möchte ich in diesem Zusammenhang die Arbeiten von Rosa Daschner, Tobias Meißner und Lorena Krames.
Herrn Manfred Schroll möchte ich für seine technische Unterstützung während meiner gesamten Zeit am Institut danken. Auf seine schnelle und unkomplizierte Hilfe bei jedweden technischen Problemen konnte ich mich immer verlassen. Frau Ramona Modery möchte ich für Ihre organisatorische Unterstützung bei der Beschaffung von Literatur und der Bewältigung sonstiger Probleme danken. Ein großer Dank geht auch an Frau Irene Günter, die bei allen organisatorischen und verwaltungstechnischen Problemen für mich immer eine kompetente Anlaufstelle und Hilfe war.
Ein weiteres herzliches Dankeschön geht an Laura Unger, Dr. med. Judith Lutz-Dold, Nicolas Pilia und Steffen Schuler für die Korrektur ausgewählter Kapitel dieser Dissertation.
Ein ganz besonderer Dank geht an meine Familie und meine Freunde, die mich während meines gesamten Studiums und der anschließenden Promotion zu jeder Zeit unterstützt und an mich geglaubt haben. Vor allem danke ich an dieser Stelle meinen Eltern, ohne die diese Promotion nie möglich gewesen wäre. Zu guter Letzt danke ich meiner Freundin Lara für ihre pausenlose, liebevolle Unterstützung.

Contents

Abbreviations and Symbols

Abbreviations

ACA	anterior cerebral artery
ACoA	anterior communicating artery
AIS	acute ischemic stroke
ATP	adenosine triphosphate
BA	basilar artery
CBF	cerebral blood flow
CCA	common carotid artery
CCT	cranial computed tomography
CI	confidence interval
CmA	callosomarginal artery
CMR	cerebral metabolic rate
CO	cardiac output
CoW	circle of Willis
CSF	cerebrospinal fluid
CSI	cold saline infusion
CT	connective tissue
DC	direct current
DPL	dual-phase-lag
DSA	digital subtraction angiography
ECA	external carotid artery
EMS	emergency medical services
FEM	finite element method
FIV	final infarct volume
GM	gray matter
ICA	internal carotid artery
LVO	large vessel occlusion
MAP	mean arterial pressure
MCA	middle cerebral artery
MR	magnetic resonance
MRA	magnetic resonance angiography
MRI	magnetic resonance imaging

MT	mechanical thrombectomy
mTICI	modified treatment in cerebral infarction
NDF	numerical differentiation formulas
ODE	ordinary differential equation
PCA	posterior cerebral artery
PCoA	posterior communicating artery
PHM	"*Population Head Model*"
ROSC	return of spontaneous circulation
rtPA	recombinant tissue plasminogen activator
SBH	selective brain hypothermia
SLC	secondary leptomeningeal collateral
SPL	single-phase-lag
TH	therapeutic hypothermia
TPR	total peripheral resistance
TTM	targeted temperature management
VA	vertebral artery
WM	white matter

Symbols

Po	Poisson number
Nu	Nußelt number
Gr	Grashof number
Pr	Prantl number
Ra	Rayleigh number
Re	Reynolds number
De	Dean number

Chapter 1

Introduction

1.1 Motivation

Stroke is the third–most common cause of death in Western countries. With a one-year mortality rate of 25% and a prevalence rate (2013–2016) of 2.5% in the US, stroke is one of the most common serious diseases [1]. What darkens the picture even further is that stroke survivors have a 33–55% probability of retaining a permanent disability.
Therapeutic hypothermia (TH) could potentially decrease cerebral damage in case of acute ischemic stroke (AIS) and lower these numbers. Randomized clinical studies show that mild TH (33 °C-35 °C) improves clinical neurological outcome in patients with cardiac arrest after return of spontaneous circulation (ROSC) [2–4]. However, cerebral ischemia due to AIS represents a considerably different pathophysiological scenario than cardiac arrest. This is because it emerges focally while the other organs are still physiologically perfused. So far, only in animal models TH has shown a clear neuroprotective effect [5, 6]: In a meta-analysis of animal stroke models with both temporary and permanent cerebral ischemia, hypothermia was correlated to an overall reduction in infarct core size of 44% at temperatures of 35 °C or below [7].
For the clinical use in AIS patients, TH is safe and feasible [8], whereas the therapeutic outcome and efficacy remains uncertain [9–11]. By analyzing previous studies and their results, Jackson et al. [12] proposed a speculative synthesis that the success of TH in AIS therapy is dependent on several factors:

- Depth (32-36 °C),
- Duration (24, 48, 72, 96 h),
- Technology (cold saline infusion (CSI), endovascular heat exchange, esophageal or surface cooling,...),
- Timing (emergency medical services (EMS), within 6 h, ...),
- Risks (infection, arrhythmia, coagulopathy, hemodilution, ionic imbalances, ...),
- Cold-stress pathways (activation of cold-stress molecules in biological systems [12]),

in addition an adequate targeted temperature management (TTM) by means of selective brain hypothermia (SBH) is essential. For example, in 2018 a clinical study with 113 patients demonstrated that endovascular mechanical thrombectomy (MT), combined with a time-limited, intra-arterial selective cold saline infusion, led to a significant reduction of the final infarct volume in case of large vessel occlusion (LVO), followed by recanalization [13].
In this thesis, the cooling capacity of a novel intracarotid blood cooling sheath [14] is evaluated, enabling the combination with the MT procedure. This possibly allows inducing an early prereperfusion cooling effect especially in the penumbra by using the cold blood stream via ipsilateral secondary leptomeningeal collateral (SLC). In the critical phase of reperfusion, inflammatory pathways can be activated which lead to a possible reperfusion injury [15–17]. The rapid decrease in the ischemic parenchyma might enable a cold reperfusion ($\approx 2\,°C$ temperature decrease, 10 min after cooling), which could mitigate reperfusion injury and is an advantage compared to other cooling strategies. Furthermore, carotid blood cooling helps to avoid possible disadvantages of systemic cooling methods (slow and limited cooling, adverse effects) and does not lead to hemodilution induced by CSI [18].
However, the positive effect of the new catheter device and of SBH in general depends, on the one hand, on the time required for brain cooling and the temperature range that can be achieved. On the other hand, the control of the brain temperature still requires invasive or complex magnetic resonance (MR)-based measurements. A numerical computational model could predict the achievable spatio-temporal decrease in brain temperature. It could be used to evaluate the effectiveness of the novel catheter device and to identify possible influences that need to be taken into account.

1.2 Aim of the Thesis

Generally, under physiological conditions, the brain temperature is controlled in a narrow range [19, 20] and is mainly influenced by blood perfusion and metabolic heat production [21]. In case of an acute ischemic stroke due to a LVO, the early brain hypothermia can be only induced by penumbral perfusion via the collateral vasculature. Thus, the cooling capacity of the catheter and the resulting spatial temperature distributions are highly dependent on the patient's cerebral circulation. However, the cerebral arterial anatomy varies distinctly from patient to patient and affects the local ischemic perfusion rates.
At the Institute of Biomedical Engineering (IBT) of the Karlsruhe Institute of Technology (KIT), the main objective of this research project was the development of a general brain temperature model containing the most important blood vessels and blood-perfused brain tissue. The model contains the specific thermal tissue properties (specific heat capacity, heat conduction, and metabolic heat production) and takes the arterial circulation anatomy into account to calculate specific spatio-temporal temperatures for SBH therapy using endovascular blood cooling. Therefore, the following two tasks need to be fulfilled:

- **Generation of a computational cerebral blood flow model:** The hemodynamics model needs to calculate the blood flow rates and blood volumes from the main cere-

bral arteries to the arterioles in as much detail as needed for the calculation of bioheat transfer. The hemodynamics model relies on an electrical analogy (approach of Avolio [22]) and is comprised of many resistances (corresponding to the flow resistance), capacitors (mirroring the vessel's elasticity and ability to buffer volume), and inductivities (mirroring the mass inertia of blood). The brain parenchyma is modeled as a variable terminating resistance. The hemodynamics model allows for consideration of collateral blood flow, vasomotion by means of autoregulation mechanisms, and vessel stenosis/occlusion. Furthermore, a realistic pulsatile cardiac output (CO) is considered.

- **Generation of a 3D cerebral heat transfer model:** Using Pennes' equation [23], heat transfer is calculated in a realistic 3D finite element method (FEM) model. For this purpose, the brain is discretized into about one million volumetric elements. Each element mirrors the adequate thermal properties depending on its corresponding tissue type. The volumetric perfusion rates are calculated by means of the above-mentioned hemodynamics model. If the temporal course of blood cooling is specified, the model calculates the temporal course of cerebral temperature for each volumetric element.

- **Application of the model:** The finished model predicts the resulting cerebral spatio-temporal temperature for various anatomical and occlusion scenarios such as variations in anatomy of the circle of Willis (CoW). In this context, the influence of different cerebral blood flow conditions on the remaining perfusion and the catheter's cooling capacity is analyzed. Furthermore, the predicted model results are compared with available, comparable measurements and simulated data from the literature.

1.3 Structure of the Thesis

This thesis is structured into three (I–III) major parts. The first part includes the fundamentals: medical and mathematical fundamentals. The medical fundamentals give an overview of all physiological processes and anatomical structures involved and necessary to consider for a detailed cerebral temperature model. The mathematical fundamentals contain major fluid mechanical and thermodynamic basics, which form the fundamentals of the methods used in the modeling process.
The second major part contains the modeling and is split in two chapters: modeling of the cerebral hemodynamics and modeling of cerebral temperature. The chapter 'Modeling of the Hemodynamics' explains, among other things, the transmission line approach, which was used as a basis for the cerebral blood flow model. It also describes the anatomy of the cerebral arterial circulation and the variations of the anatomy considered to model interindividual differences. The chapter ends with the presentation of the blood flow rates that were used for the temperature calculation.
The chapter 'Modeling Cerebral Temperature' describes the temperature calculation with the

realistic 3D brain model. It describes Pennes' equation and discusses the assumptions made. Furthermore, it describes the geometry generation and its division into terminal perfusion regions to account for individual changes in spatial ischemic perfusion. It also contains the description of the assumed boundary conditions for the temperature simulation, i.e. how the blood flow rates from the hemodynamics model were coupled to the geometry, which resulting blood temperatures were considered, how the systemic body was coupled, and which external conditions for heat release were assumed. Subsequent to the description of the modeling, the resulting cerebral spatio-temporal temperatures for different anatomical variations of arterial blood supply are presented, and the results are discussed and compared with other models from the literature or comparable measured data. However, since a direct comparison is only possible to a limited extent due to the consideration of the new catheter, for which no measured variables are available yet, an adaptation of the model to cooling with CSI is presented and the results are compared with models of other groups. In the last part of the chapter the detailed 3D brain model is compared with a simplified energetic model. With the energetic model, a fast estimation of the mean cooling in the penumbra could be established, without the need for a complex simulation with the FEM model.
The last part of the thesis provides a short conclusion of this work and gives an outlook for future work.

PART I

FUNDAMENTALS

Chapter 2

Medical Anatomical and Physiological Fundamentals

This chapter is intended to briefly explain the most important anatomical and physiological conditions of the body, which are relevant for creating a model of spatially and temporally variable brain temperature. The presented topics cover only a small part of the complete human physiology, but should nevertheless give an insight into the relevant processes which are necessary for a modeling as realistic and accurate as possible.
The chapter is divided into six thematic blocks (cf. Sec. 2.1-2.6). The first block gives an overview of the structure, function, and regulation of the human circulation. In the second section, regulation mechanisms are more precisely described, especially focused on brain perfusion. The brain with its anatomy and the cerebral blood supply are the subject of the third part of the chapter. It deals mainly with the arterial supply of the brain and the course of the three main cerebral arteries. This part of the chapter also deals in more detail with the collateral circulation, which is important for stroke and cooling. The fourth part of the chapter contains basic information about the disease stroke and its therapy. One therapeutic option is inducing hypothermia, which is further explained in the fifth block. Here, the use of the catheter system, which was considered in this work, is explained in more detail. The discussion of hypothermia leads to the sixth and last part of the chapter. In this part the temperature balance of the body and its regulation mechanisms are presented.

2.1 The Circulatory System

The function of the circulatory system is to maintain optimal survival and function of the cells. To do this, the needs of the body tissue must be satisfied: transport of nutrients into the cells, removal of waste products, transmission of hormones through the body, and so on. To maintain the proper supply, the heart and blood vessels are monitored to provide the necessary cardiac output and arterial pressure to ensure the required tissue flow.

2.1.1 Structure of the Circulation

The circulation can be divided into the systemic circulation and the pulmonary circulation (Fig. 2.1). The systemic circulation is also called the greater circulation or peripheral circulation, since it supplies blood flow to all the tissues of the body [24].

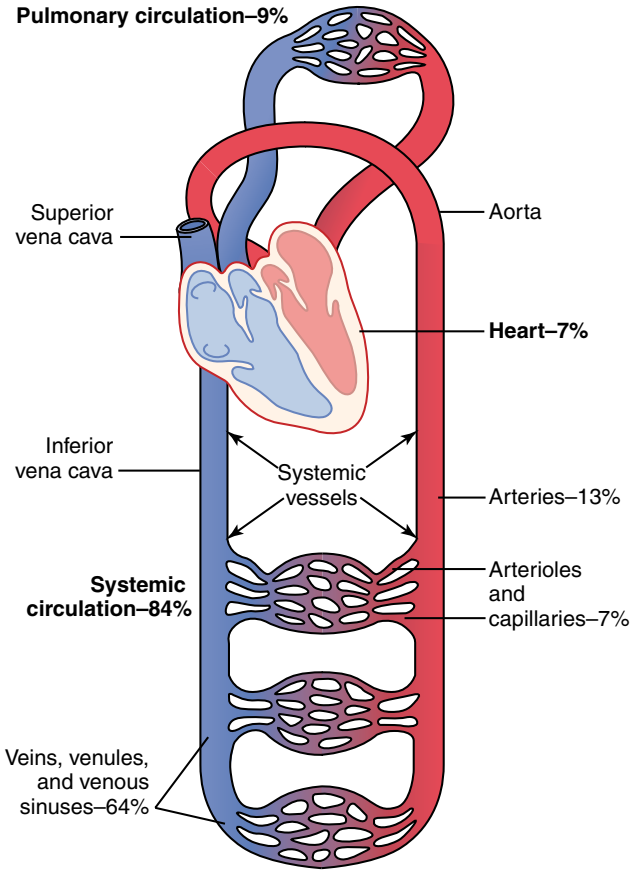

Figure 2.1: Distribution of blood (in percentage of total blood amount) in the different parts of the body's circulatory system. Figure taken from [24].

In general, arteries transport the blood (the cardiac output (CO)) away from the heart. The arteries near the heart are called the elastic type because they are exposed to large pressure fluctuations (25 mm Hg [24]) and have a particularly large number of elastic fibers. They adapt to the pulsatile pressure curves, which leads to a smoothing of the pulsatile pressure and flow curves (known as the windkessel effect). In arteries further away from the heart there is a more even flow and pressure (Fig. 2.2). These arteries are of the muscular type and have less elasticity. [19, 20]

The large arteries branch out more and more to smaller vessels up to the arterioles and finally the capillaries. The wall of the capillaries consists of only one cell layer, through

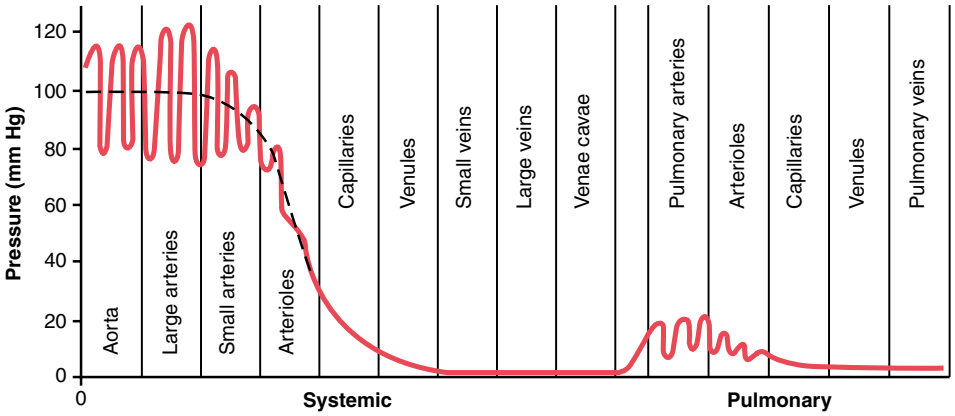

Figure 2.2: Normal blood pressures in the different portions of the circulatory system (person is lying horizontally). Figure taken from [24].

which the exchange of substances between blood and the surrounding tissue or interstitial space takes place [19].

The diameter of the individual arteries decreases in the course of branching from approx. 2.7 cm (ascending aorta) to approx. 9 μm (capillaries) [20]. At the same time, due to the extremely high number of capillaries (approx. 5 billion), the total cross-sectional area increases with the degree of branching and amounts to approx. 3500 cm^2 at the level of the capillaries [20]. Despite the large cross-sectional area of the arterioles and capillaries, the flow resistance increases proportionally according to the Hagen-Poiseuille law ($R \sim \frac{1}{r^4}$ (cf. Sec. 3.1)). Due to their high resistance, they have a significant influence on the total peripheral resistance (TPR) [19, 24].

The TPR is defined as the quotient of mean arterial pressure (MAP)[1] and the CO:

$$\mathrm{CO} = \frac{\mathrm{MAP}}{\mathrm{TPR}}. \tag{2.1}$$

As the blood flows through the systemic circulation, the mean blood pressure gradually drops to about 0 mm Hg until it reaches the end of the venae cavae, where they open into the right atrium of the heart (Fig. 2.1). The average "functional" pressure in most vascular beds is about 17 mm Hg, a pressure so low that little plasma escapes through the tiny pores of the capillary walls, although nutrients can easily diffuse through the same pores to the outer tissue cells [24].

In the subsequent pulmonary circuit, the pressure is also pulsatile but distinctly lower compared to the aorta (mean pulmonary arterial pressure of 16 mm Hg). The mean pulmonary capillary pressure averages only 7 mm Hg (Fig. 2.2). Yet, the total blood flow through the lungs per minute is the same as through the complete systemic circulation [20, 24].

[1] For the systemic circulation, the MAP is defined as the difference of the mean pressure in the aorta $\bar{P}_{\mathrm{Aorta}}$ and the mean pressure in the vena cava $\bar{P}_{\mathrm{v.cava}}$

2.1.2 Circulatory Function and Regulation

Three basic principles sum up all basic functions of the system [24]:

- **Depending on the tissue requirements, the supply of each individual body tissue is almost always precisely controlled:** The micro-vessels of each tissue continuously monitor the demand (availability of oxygen and other nutrients, accumulation of carbon dioxide and other waste products), which in turn directly affects the local blood vessels and dilates or constricts them. In addition, the tissue flow is controlled by the central nervous system and hormone-balanced.
- **CO is controlled mainly by the sum of all the local tissue flows:** After blood has flown through a tissue, it returns instantly to the heart via the veins and is immediately pumped back into the arteries. The heart thus functions as an automatic machine that responds to the demands of the body (Frank–Starling law [25]). The heart is supported by special nerve signals to pump the required amounts of blood.
- **Arterial pressure regulation is generally independent of local blood flow control or control of CO:** Arterial blood pressure is regulated by several processes. If the pressure drops significantly below the normal value of about 100 mm Hg, a flood of nerve reflexes triggers a series of circulatory changes within seconds. Nervous signals (a) particularly increase the pumping capacity of the heart, (b) cause a contraction of the large venous blood reservoirs and (c) cause a general constriction of most arterioles in the body.

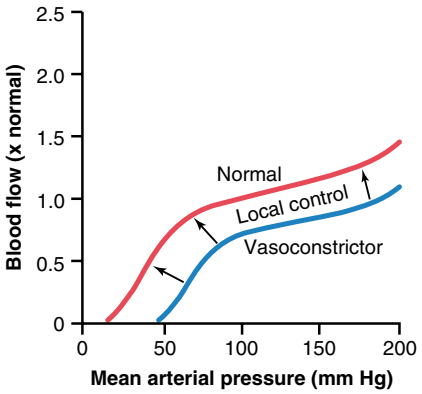

Figure 2.3: Effect of changes in arterial pressure (over a period of several minutes) in a tissue such as skeletal muscle. Blood flow between 70-175 mm Hg is "autoregulated" [20, 24]. The blue curve shows the effect of sympathetic nerve stimulation (vasoconstriction) by hormones (nor-epinephrine, angiotensin II, vasopressin, or endothelin) [24]. Figure taken from [24].

Effects of Pressure on Tissue Blood Flow

The impact of variations of arterial pressure on blood flow in many tissues is usually non-linear and smaller than one would expect. An increase in mean arterial pressure initiates a compensatory increase in vascular resistance within a few seconds through activation of the local control mechanisms (cf. Sec. 2.2). Conversely, a reduction in mean arterial pressure leads to a prompt reduction of vascular resistance in most tissues.
This ability to adjust local vascular resistance and to maintain normal local blood flow in a wide range of mean arterial pressure (Fig. 2.2) is called blood flow autoregulation (cf. Sec. 2.2).
In addition, changes in blood flow in tissues rarely last longer than a few hours, even when mean arterial blood pressure rises or elevated levels of vasoconstrictors are present. The local autoregulatory mechanisms of each tissue cancel out most of the effects of vasoconstrictors to ensure blood flow that meets the needs of the tissue [19, 24].

2.2 Local Control of Blood Flow

Since every organ has individual requirements, almost every type of tissue has the ability to control its own local blood flow in proportion to its metabolic needs. In this work, the blood supply to the brain is the focus of interest, so this section will concentrate on the processes in the brain. A detailed description of all known processes can be found in [19, 24, 26].

Mechanisms of Control

The control of local blood flow can be divided temporally (Fig. 2.4): On the one hand, there are acute control mechanisms, which enable rapid vasomotion in the arterioles, metarterioles, and precapillary sphincters. This happens within seconds to minutes and leads to very rapid maintenance of appropriate local tissue blood flow [24]. On the other hand, there are long-term control mechanisms, which lead to controlled changes in flow over days, weeks, or months. These changes are caused by an increase or decrease in the physical size and number of actual blood vessels.
Since for the evaluation of changed blood flow conditions due to large vessel occlusion (LVO) in case of acute ischemic stroke (AIS) mainly the acute control mechanisms are of importance, these shall be explained in more detail:

Acute Control Mechanisms

In every tissue of the body, a rapid increase in arterial pressure leads to an immediate increase in blood flow. But within less than a minute, blood flow in most tissues returns almost to its original normal level, although arterial pressure remains elevated. This phenomenon is called

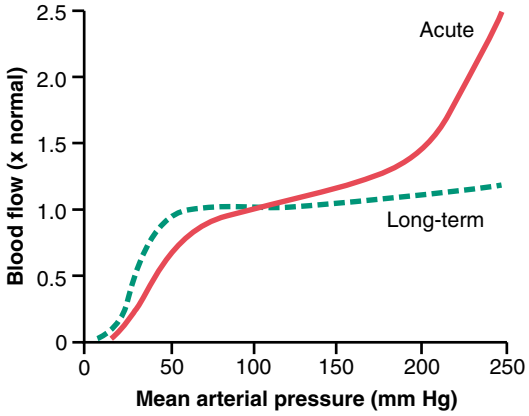

Figure 2.4: Impact of raised arterial pressure on blood flow through a muscle. The solid red curve results if pressure is raised over minutes. The dashed green curve results if pressure is raised slowly over many weeks. [24]. Figure taken from [24].

"autoregulation" of blood flow. In the range of arterial pressures from about 70 mm Hg to 175 mm Hg, blood flow increases by only about 20-30% (solid red curve in Fig. 2.4). There are two theories to explain this acute autoregulation mechanism. They are known as metabolic and myogenic theory.

The metabolic theory says that if the arterial pressure becomes too great, the increase in flow will supply the tissue with too much oxygen and too many other nutrients. This "washes out" the vasodilators released by the tissue. The reduced tissue concentration of the vasodilators then causes the blood vessels to constrict and the flow to return to almost normal values despite the increased pressure [24].

The myogenic theory, which is also known as Bayliss-effect [27], is based on the observation that sudden stretch of small blood vessels causes the smooth muscle of the vessel wall to contract[2]. This led to the hypothesis that high arterial pressure stretching the vessel causes reactive vascular constriction that reduces blood flow nearly back to normal. On the other hand, at low pressures, the vessel is less streched, so that the smooth muscle relaxes, reducing vascular resistance and leading to a normal flow. The myogenic vessel response is inherent to vascular smooth muscle and is independent of neural or hormonal influences. It is most pronounced in arterioles but can also be observed in arteries, venules, veins, and even lymphatic vessels [24, 27]. However, the myogenic pressure-sensing mechanism cannot directly detect changes in tissue blood flow. Therefore, the role in regulation of local blood flow remains unclear. Metabolic mechanisms appear to override the myogenic mechanism if the metabolic demands of the tissues are significantly increased [24, 28].

Effect of Tissue Metabolism and Oxygen Saturation

An increase (e.g., in the skeletal muscles) in metabolism (cf. Fig. 2.5 a) or a decrease in oxygen saturation (cf. Fig. 2.5 b) leads to an increase in local tissue blood flow due to va-

[2]The contraction is initiated by stretch-induced vascular depolarization. The depolarization rapidly increases calcium ion influx from the extracellular fluid into the cells, causing vessel contraction.

sodilatation [20, 24]. An increase in metabolism up to eight times normal increases the blood flow acutely about fourfold [24]. A decrease in arterial oxygen saturation to about 25% of normal increases the blood flow through an isolated dog leg about three-fold (almost complete compensation) [24].

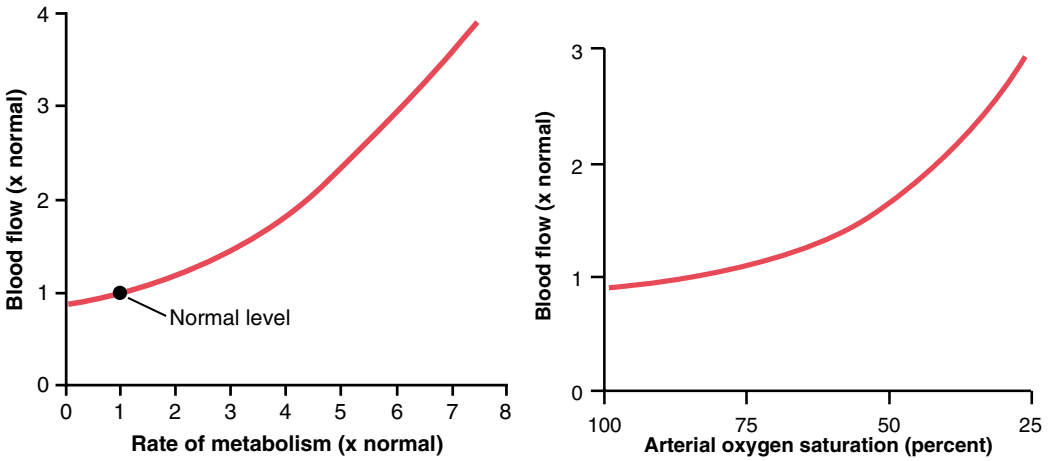

(a) Effect of increasing metabolism

(b) Effect of decreasing arterial oxygen saturation (through an isolated dog leg).

Figure 2.5: Different factors influencing local tissue blood flow. Figures taken from [24].

Effect of Carbon Dioxide and Hydrogen

Since the excitability of the brain depends to a large extent on the precise control of carbon dioxide concentration as well as hydrogen ion concentration, the concentrations of carbon dioxide and hydrogen ions in the brain are monitored in addition to the control of oxygen concentration. An increase expands the brain's vessels and allows the excessive carbon dioxide or hydrogen ions to be quickly washed out of the brain tissue. [24]

The mechanisms for local blood flow control described above are also called "metabolic mechanisms". They act in response to the metabolic needs of the tissues. Two other particular examples of metabolic control of local blood flow are "reactive hyperemia" and "active hyperemia" [24]:

Reactive Hyperemia

If the tissue blood supply was blocked for a few seconds up to an hour or more and then the blockage dissolves, blood flow normally increases immediately to four to seven times normal. This very high flow will continue for a few seconds if the blockage lasted only a few seconds. Reactive hyperemia occurs when the blood supply is insufficient for one or more hours. This means that the excessive flow is maintained for a longer period of time. Reactive hyperaemia is one of the "metabolic" blood flow regulation mechanisms, since the lack of blood flow activates all those factors that cause vasodilatation. The phase of excessive flow lasts long

enough to compensate almost exactly for the oxygen deficiency created during the occlusion phase [24, 29].

Active Hyperemia

When a tissue becomes highly active, e.g., brain during rapid mental activity, the blood flow through the tissue increases. The increase in local metabolism causes the cells to rapidly consume the nutrients in the tissue fluid and also to release large amounts of vasodilating substances. The result is the dilation of local blood vessels and thus an increase in local blood flow. In this way, the active tissue receives the additional nutrients it needs to maintain its increased function. [19, 20, 24]

2.3 Brain Anatomy and Physiology

The brain is the center of the nervous system and lies within the cranial cavity of the skull. It can be divided into three major parts: the cerebrum (forebrain), the mesencephalon (midbrain) and the rhombencephalon (hindbrain, consisting of the medulla oblongata, the pons and the cerebellum) (cf. Fig. 2.6 a). The brain volume can differ slightly between individuals ($\approx$1350 cm^3 for men and $\approx$1200 cm^3 for women) and decreases after reaching adulthood [30].

2.3.1 Basic Brain Anatomy

The whole brain consists of two different tissue types: gray matter (GM) and white matter (WM). WM is made from myelinated axons which are the reason for the whitish color. Grey matter processes signals, while white matter transmits the bioelectrical signals to other brain areas. The different tasks explain also the different required blood perfusion rates. The perfusion rate of GM is about three times higher as it has a higher need for oxygen and nutritions [20]. GM is mostly present in the outer layer of the brain (cortex) but also exists subcortically as nuclei (basal ganglia, brainstem nuclei) near the diencephalon. White matter is mostly present in the deep parts of the brain and at the superficial parts of the spinal cord [31] .

Cerebrum

The cerebrum is the largest part of the brain and is responsible for motor, sensory and cognitive functions. It can be divided into a right and a left hemisphere. The two hemispheres share the control of some body functions, whereby certain tasks can generally be assigned to one hemisphere of the brain. The right hemisphere is generally responsible for spatial perception, creative, artistic tasks, and creative thinking. The left hemisphere is the control center for language and rational tasks such as calculating and writing [20]. Sensory and motory tasks are controlled by both hemispheres: The left hemisphere controls the right body

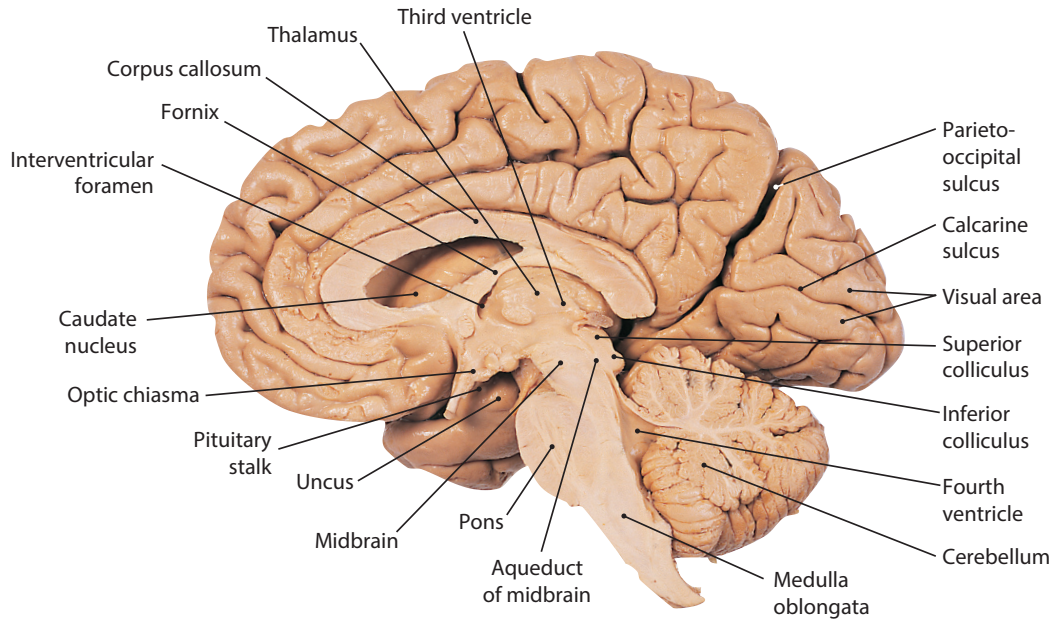

(a) Median sagittal section of the brain

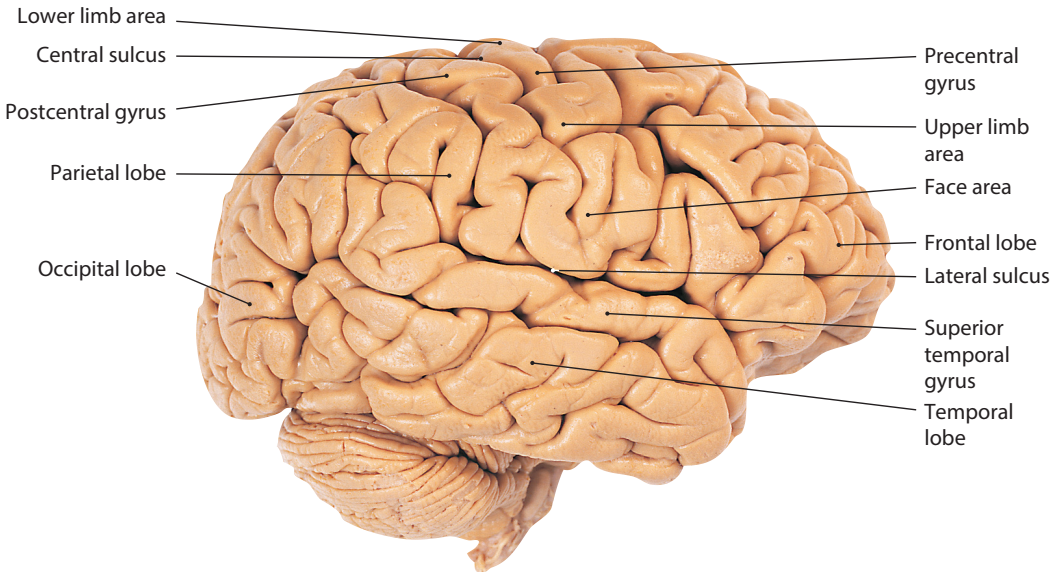

(b) Lateral view on the cerebral cortex

Figure 2.6: Right side of the brain, after removal of the arachnoid mater and surface vessels. Figures taken from [32].

side and the right hemisphere controls the left body side. Therefore, deficits in coping with the respective tasks during a stroke already indicate the position or the affected hemisphere. Each hemisphere of the cerebrum can be distinguished in a frontal, occipital, parietal, and a temporal lobe (cf. Fig. 2.6 b). Sometimes, an additional subcortical insular lobe[3] is mentioned

[3]underneath the temporal frontal and parietal lobe behind the Sylvian fissure

as fifth lobe [33]. The left and right hemisphere are separated by the longitudinal fissure and connected via the corpus callosum (cf. Fig. 2.6 a). The corpus callosum forms the floor of the longitudinal fissure and the roof of the lateral ventricles [34]. With a length of about ten centimeters it is the largest white matter structure in the human brain and consists of 200-300 million axonal projections [35]. The lateral ventricles are part of four cavities in the brain that contain cerebrospinal fluid (CSF), which is produced by the lining of the ventricles. The two lateral ventricles (one in each hemisphere) form the largest cavities and are connected to the third ventricle, which lies deeper in the brain. The fourth ventricle runs along the brain stem and lies underneath the third ventricle. All four ventricles are connected to each other, and also to the central canal of the spinal cord and to the subarachnoid space (space between two of the linings that separate the brain from the skull). The CSF circulates throughout the ventricular system and deals as a shock absorber against head traumata and provides nutrients supporting a chemical brain balance. [36]
In the course of human evolution, the surface of the cerebral cortex has continued to increase, leading to the development of a sinuous surface with grooves and furrows. The grooves and furrows are also known as sulci and gyri (cf. Fig. 2.6 b).

Brainstem and Cerebellum

The brainstem (midbrain, pons and medulla oblongata) and the cerebellum have an evolutionary older origin and are the control center for basic vital functions. The cerebellum lies dorsal underneath the cerebrum and has with finely spaced parallel grooves a unique structure. It plays an important role in precise motor control but might be also involved in cognitive functions (attention, language as well as regulating fear and pleasure responses) [37]. The brainstem works as information gateway between the central and peripheral nervous system. It is home to vital functions like breathing, control of the heartrate and reflexes. [20]

2.3.2 Cerebral Arterial Circulation

Although the brain accounts for only about 3% of the body weight, the $\approx$ 90 billion neurons in the brain are responsible for about one fifth of the body's total oxygen consumption [38]. As a result, 15-20% of the cardiac output is delivered to the brain [39].
Arterial blood is brought to the brain by the internal carotid artery (ICA) and the vertebral arteries (cf. Fig. 2.7 and Fig. 2.8) [32].

The two vertebral arteries branch from the subclavian arteries and run cranially up through the foramina in the transverse processes of the upper six cervical vertebrae. They enter the skull through the foramen magnum and unite to form the single midline basilar artery (BA), which lies on the ventral (anterior) surface of the pons (cf. Fig. 2.8).
The BA divides into the two posterior cerebral arteries (PCAs). The PCAs are each joined by the respective posterior communicating artery (PCoA) to the ICA. [32]
After the branching the ICA terminates as it divides into its two main branches: the middle

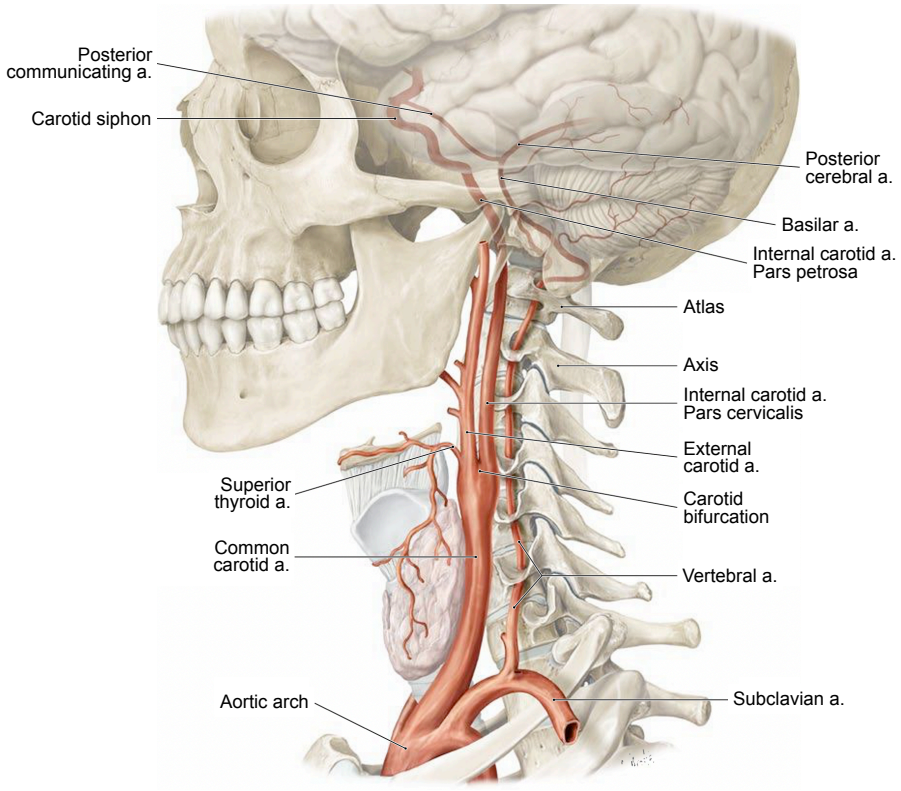

Figure 2.7: Arterial blood supply of the brain. Figure obtained from [40].

cerebral artery (MCA) and the anterior cerebral artery (ACA). The MCA runs laterally in the lateral sulcus to emerge on the lateral surface of the cerebral cortex and the ACA unites to its fellow by the very short anterior communicating artery (ACoA) and runs on to the medial surface of the cerebral hemisphere (cf. Fig. 2.8). [32]

The brain differs in its blood supply from other organs such as the liver or kidney as it does not have a specific enema for supplying vessels. All major arteries run along the cortex or inside the gyri before branching out into smaller arteries and finally perfusing the brain tissue from the outside to the inside (Fig 2.10 b) [41].

The three main cerebral arteries (ACA, MCA and PCA) are mainly responsible[4] for the arterial blood supply of the cerebrum (cf. Fig. 2.10 a). Their anatomy is described in more detail in the following sections. The cerebellum and the brainstem are mainly supplied by arteries (pontine arteries, superior and inferior cerebellar arteries) originating from the basilar and vertebral arteries (cf. Fig. 2.8 cf. Fig. 2.9).

After supplying the brain parenchyma with oxygen and nutrition, the venous blood accumulates in the dural venous sinuses and reenters the systemic circulation mostly via the internal jugular vein [41, 42].

[4]supply of the GM and WM in the brain center is also partly provided via the anterior choroidal artery

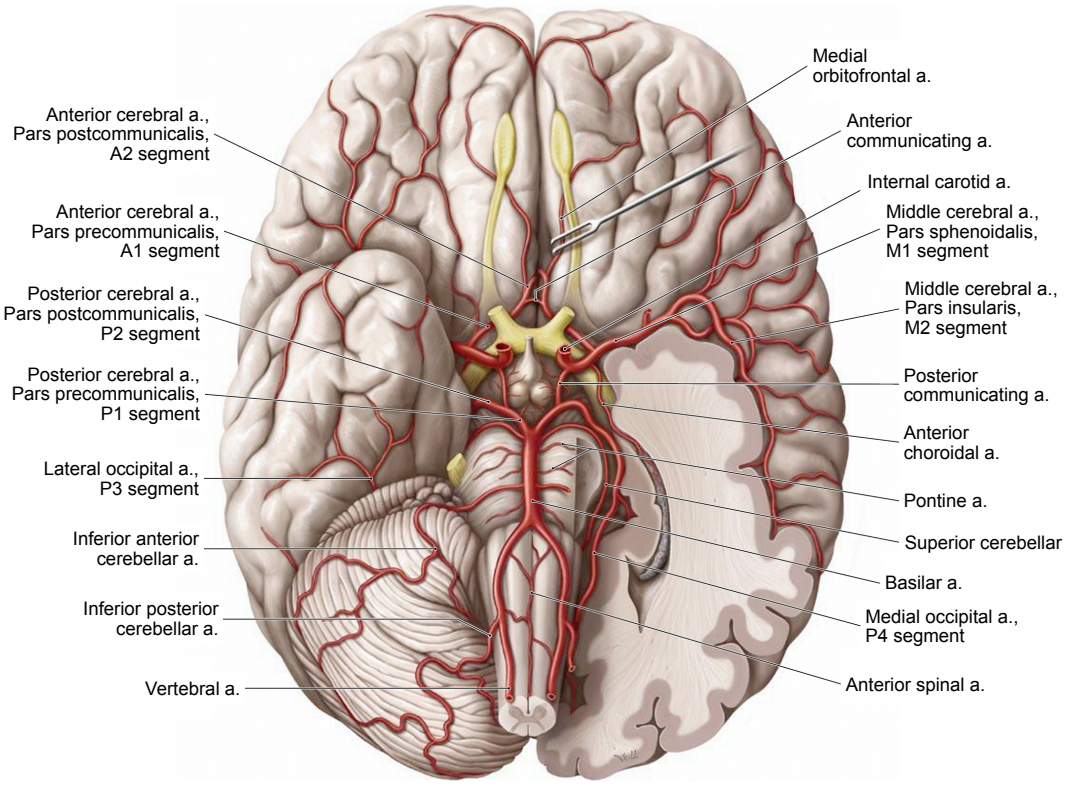

Figure 2.8: Arteries at the base of the brain. Figure obtained from [40].

The Circle of Willis

The circle of Willis (also known as cerebral arterial circle) is an arterial ring structure that supplies blood to the brain and lays in the interpeduncular fossa at the base of the brain. It is named after the British physician Thomas Willis, who was the first to describe the ring structure in 1664. The CoW connects the posterior and the anterior cerebral circulation via the PCoAs [44]. The posterior circulation is formed by the PCAs, while the ACA and MCA form the anterior part of the cerebral circulation. Furthermore, the CoW also connects the circulations in the left and right hemisphere via the ACoA. The ring structure of the CoW can be seen in Fig. 2.8 and schematically in Fig. 2.11.
The CoW is a circulatory anastomosis. Its communicating arteries (PCoAs and ACoA) are also referred to as primary collaterals [45]. The CoW leads to a redundancy within the arteries in the cerebral circulation. If one part of the circle becomes occluded or stenosed or one of the arteries supplying the circle is blocked or narrowed, blood flow via the communicating arteries of the CoW can often sustain cerebral perfusion to avoid ischemia [46].

Although the CoW can have major importance for remaining perfusion in case of large vessel occlusion, the CoW is “one of the most variable parts of the human vascular system” [47]. Various anomalies and variations of the CoW are known to exist [48]. Not even

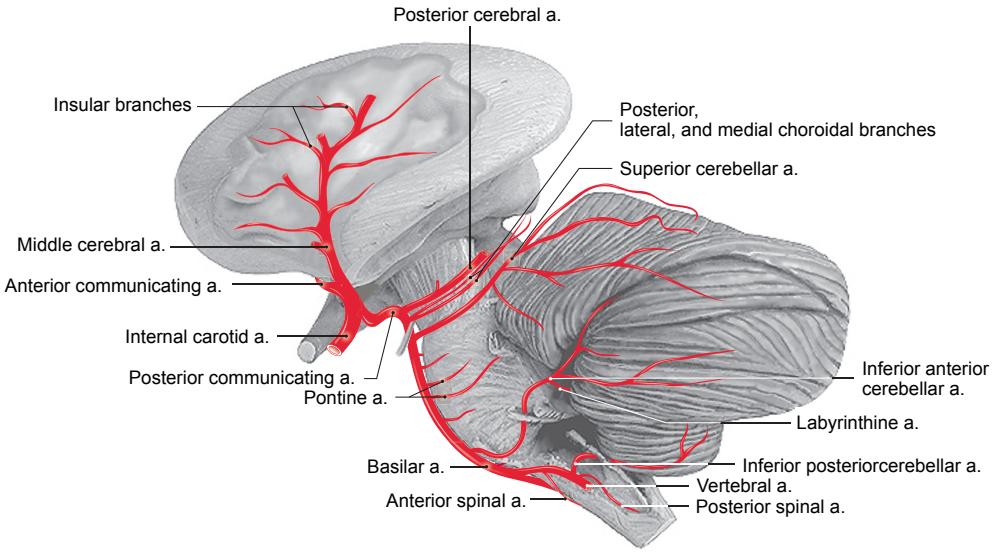

Figure 2.9: The brainstem and the cerebellum are supplied mainly by arteries branching from the BA or the VAs. Figure taken from [43].

Willis's original illustration conforms to the usual textbook description [49]. Arteries forming the CoW can be not present at all, can be present multiple times or can have such a small diameter (hypoplastic), that almost no blood flow is possible [50].
For the occurrence of different variations, different information can be found in the literature: Lippert & Papst [51] state an occurrence rate of the complete structure of 49%. This is in good accordance to Hafez et al. [50], who examined 120 brains of healthy patients (60 male, 60 female) and ten cadavers' brains. In their study a complete CoW was present in 45% of the cases. An even lower occurrence rate was stated by Bergman et al. In a composite review of 1413 brains [49] the classic anatomy of the circle was present in 34.5% of cases.
As most common variations Lippert & Papst list a missing (or hypoplastic) PCoA (9%), both missing PCoAs (9%), a missing PCA-P1 segment (9%) or the combination of missing PCoA and missing contralateral PCA-P1 segment (9%) [51]. In an other common variation, the PCA-P1 is narrowed and its ipsilateral PCoA is large, so the ICA supplies the posterior cerebral circulation.

Anterior Cerebral Artery

The ACA is compared to the MCA the smaller sub-branch of the bifurcating ICA. Its branches supply the frontal lobe and the cortex areas near the longitudinal fissure (cf. Fig. 2.10). The ACA supplies ≈ 30% of each hemisphere with arterial blood [52].
The ACA runs within the longitudinal fissure above the corpus callosum. Its branches rise to the cortex of the frontal and parietal lobe and then run along the cortex surface (Fig. 2.12). The ACA can be divided into five segments (A1-A5): The A1 segment branches from the ICA and extends to the branching of the ACoA. The A2 segment extends from the branching

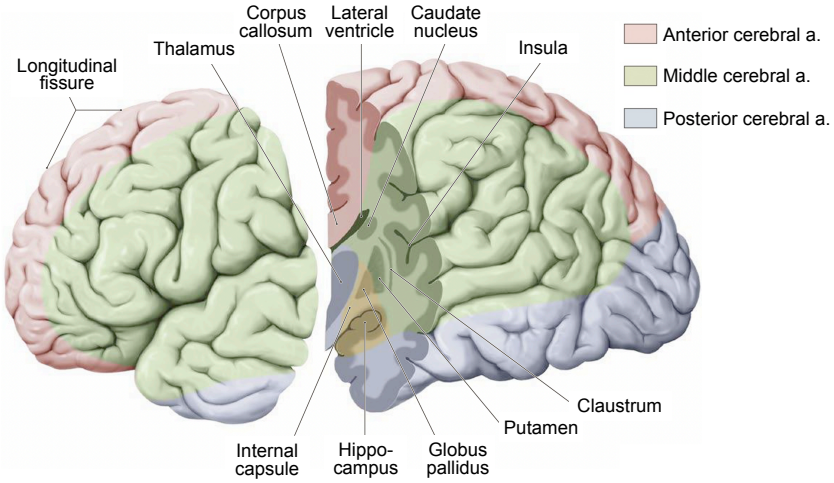

(a) Lateral view on the left hemisphere: Most of the lateral surface is supplied by the MCA (green areas). The branches of the MCA rise from the depth of the insula to the cortex. The branches of the ACA supply the frontal lobe and the cortex areas near the longitudinal fissure (red areas). The PCA supplies the occipital lobe and the lower parts of the temporal lobe (blue areas). The blood supply of the GM and WM in the center (yellow area) is more complex (partly via the anterior choroidal artery). Figure obtained from [40].

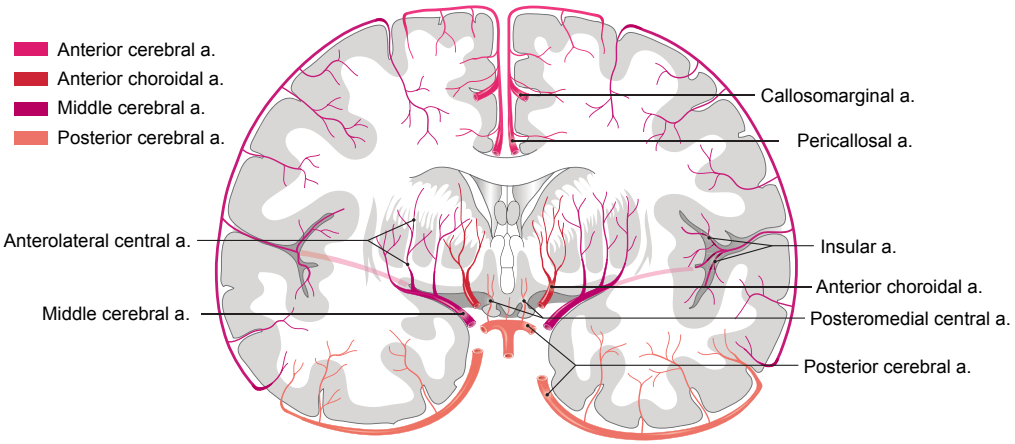

(b) Frontal section of the brain in the region of the corpus striatum (a nucleus (a cluster of neurons) in the subcortical basal ganglia of the forebrain) showing the arterial blood supply of the cortex, basal ganglia and the internal capsule. Figure obtained from [43].

Figure 2.10: Arterial blood supply of the brain.

of the ACoA to the bifurcation of the pericallosal artery and the callosomarginal artery (CmA) [5] (cf. Fig. 2.12). The A2 segment forms the origin of the orbitofrontal and frontopolar arteries. The A3 segment is also termed as the pericallosal artery. It is one[5] of the (or the only) main terminal branches of the ACA. It extends in the pericallosal sulcus to form the internal parietal arteries and the precuneal branches. The callosal arteries are considered as the A4 and A5 segments of the ACA. The CmA is a typically present[5] terminal branch of the ACA. It branches from the pericallosal artery. Branches of the CmA are the medial

[5] a typical course of the callosomarginal artery is assumed

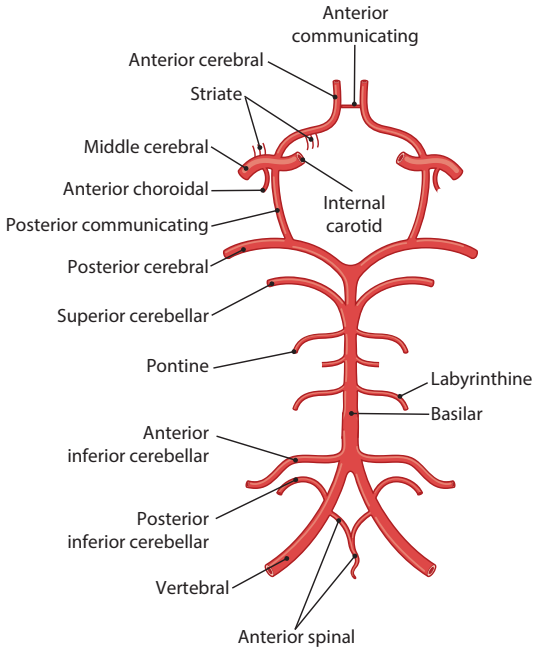

Figure 2.11: Arterial circle (circle of Willis) at the base of the brain. Figure obtained from [32].

frontal arteries and the paracentral artery. However, depending on anatomical ACA variation, the CmA can also have an atypical shape (absent or only small pronounced with almost no cortical branches). In this case, the branches mentioned will originate from the pericallosal artery. In a postmortem anatomical study of 76 hemispheres, the artery was present in only 60% of the cases [53], while other angiography studies predict an occurrence rate of 67% [54] or 50% [55].
For the ACA, some names of cortical branches differ in literature and the nomenclature in English, German or Latin is not always consistent [32, 33, 40, 43, 53, 54, 56].

Middle Cerebral Artery

The MCA is the biggest main cerebral artery as it receives 60-80% [57] of the blood leaving the ICA and supplies $\approx$ 50% of the cerebrum's hemisphere [52]. The MCA runs laterally to the CoW and has a characteristic double bending within the Sylvia fissure before its cortical branches split. The branches of the MCA rise from the depth of the insula to the cortex (cf. Fig. 2.13 a).
The MCA main trunk can be divided into four segments (M1-M4): The M1 segment is called sphenoidal segment due to its origin and loose lateral tracking of the sphenoid bone (but it is also known as the horizontal segment). The M1 segment splits into smaller branches before these reach the cortical surface. In an anatomical study with 70 unfixed brain hemispheres from 35 cadavers, Umansky et al. [58] found in 64% of the hemispheres a bifurcating MCA-M1 segment into a superior and inferior M2 segment. In 29% of the cases, the M1 segment

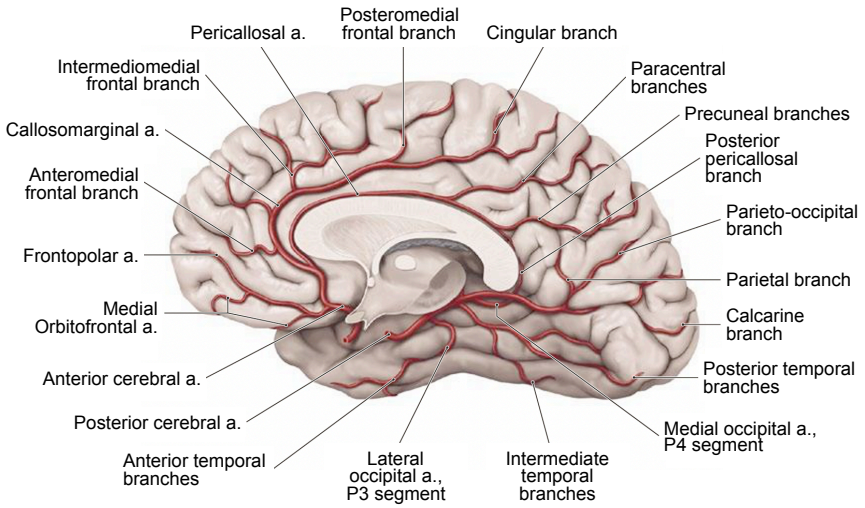

Figure 2.12: Branchings of the anterior cerebral artery and the posterior cerebral artery at the medial surface of the cerebrum. Figure obtained from [40].

trifurcated into an additional medial M2 trunk. A monofurcation or tetrafurcation of the M1 segment is also possible but exists in fewer cases [58, 59]. The M2 segments are known as the insular segments as they extend anteriorly on the insula. The M3 or opercular segments extend laterally exteriorly from the insula towards the cortex. The M2 and M3 segments are sometimes grouped as Sylvian segment. The M4 segments are the finer terminal or cortical segments beginning at the external of the Sylvian fissure. They extend distally and supply the cortex of the brain (cf. Fig. 2.13 b). [59]
The cortical branches of the MCA are named and described by the areas that they irrigate (cf. Fig. 2.13 b):

- **Frontal lobe:** Lateral frontobasal artery (also know as the orbitofrontal artery), prefrontal arteries, pre-rolandic (also known as precentral) artery and the rolandic (or central) arteries
- **Parietal lobe:** Anterior & posterior parietal arteries, angular artery and temporooccipital artery.
- **Temporal lobe:** Temporopolar artery and anterior, middle and posterior temporal arteries.

Posterior Cerebral Artery

The PCA is the smallest of main cerebral arteries[6]. It branches from the BA and supplies the occipital lobe and the lower parts of the temporal lobe (cf. Fig. 2.10) [40]. Its supply region accounts for $\approx 20\%$ of each hemisphere [52].
Analogous to the ACA and the MCA, the PCA's main trunk can be divided into four segments

[6]due to its smaller size, only few microsurgical studies about the PCA can be found in literature

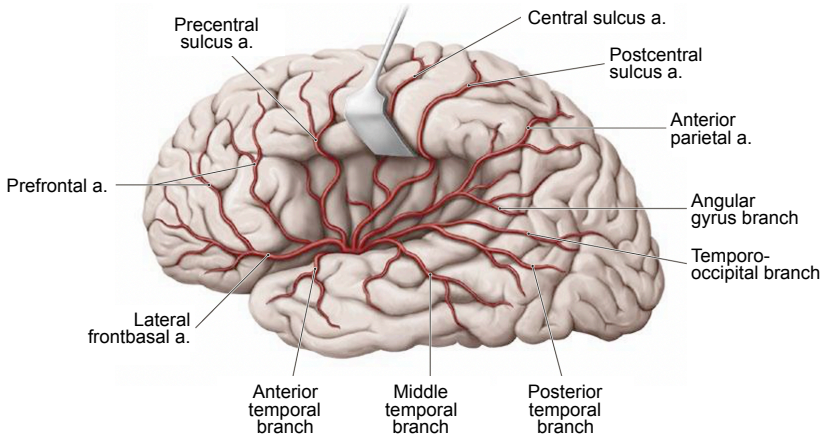

(a) Course of the MCA in the depth of the lateral sulcus.

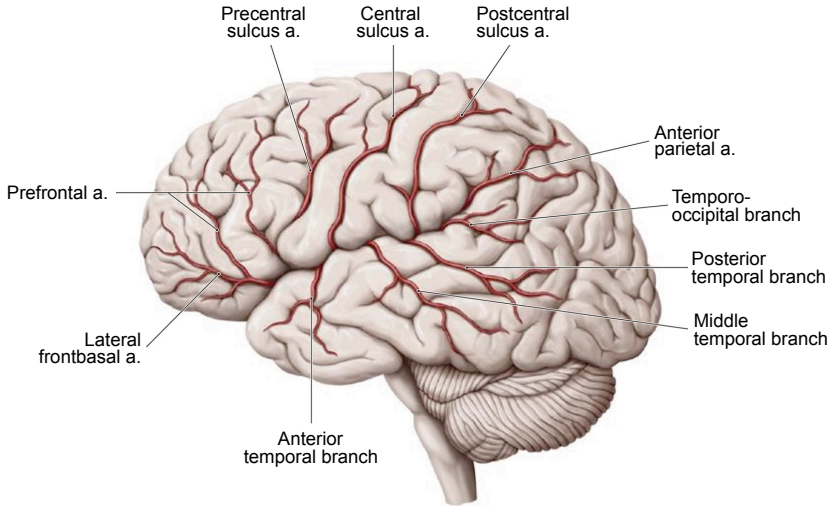

(b) Cortical branches of MCA at the lateral cerebral hemisphere

Figure 2.13: Branchings of the middle cerebral artery. Figures obtained from [32].

(P1 to P4). The P1 segment is the part between branching from the BA and branching of the PCoA. For the P2 to P4 segments the PCA has turned completely posterior. The course of the PCA and most of its terminal cortical branches can be seen in Fig. 2.12. Major variations or abnormalities are not known for the PCA. [60]

2.3.3 Cerebral Collateral Circulation

Generally, cerebral collaterals are defined as redundancies in the vascular tree, which can partially sustain blood flow to ischemic areas when primary conduits are blocked [61]. They allow bilateral blood flow depending on pressure gradient. For physiological conditions, the difference in pressure is almost zero and therefore no collateral blood flow occurs [62]. Cerebral collateral circulation includes extracranial sources (cf. Fig. 2.14 a) of cerebral blood

flow and intracranial routes (cf. Fig. 2.14 b) of ancillary perfusion. The intracranial collaterals are commonly divided into primary or secondary collateral pathways. Primary collaterals include the arterial segments of the CoW, whereas the ophthalmic artery and leptomeningeal vessels constitute secondary collaterals [45]. The secondary leptomeningeal collaterals (SLCs) connect the distal segments of the MCA with distal branches of the ACA and PCA. They are also known as pial collaterals. After a LVO, they allow for partially maintained blood flow in the ischemic penumbra and delay or prevent cell death (cf. Fig. 2.15) [61]. However, collateral circulation varies dramatically between individuals, and collateral extent is a significant predictor of stroke severity and recanalization rate [61]. A qualitative statement about the collateralization was proposed by Liebeskind et al., who classify the degree of collateralization in "poor","partial" or "strong / good" (cf. Fig. 2.15) [45].
A more detailed description about collateral blood flow in AIS and their therapeutic potential can be found in [63] and [64].

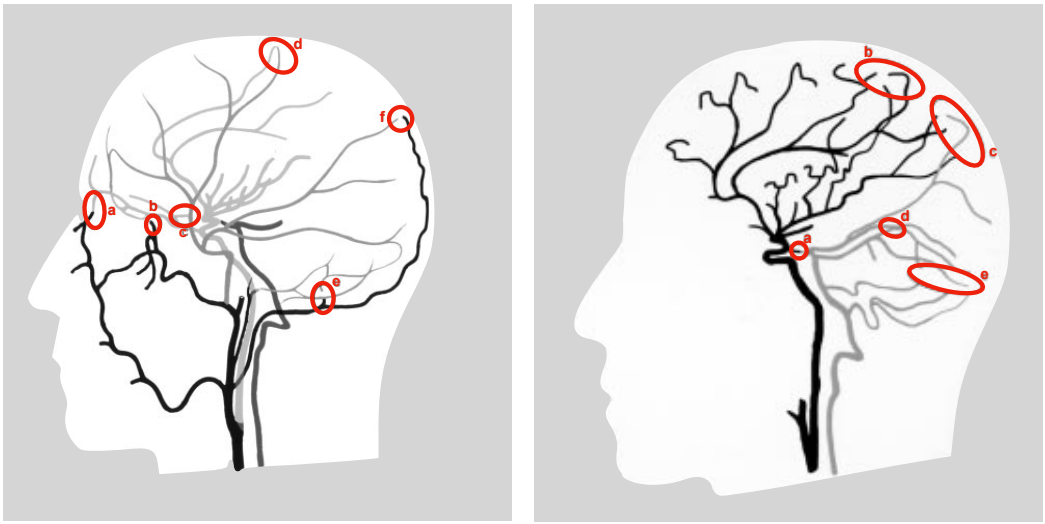

(a) Extracranial collaterals: Anastomoses from the ophthalmic artery to the facial artery (a), the maxillary artery (b), and to the middle meningeal arteries (c); and dural arteriolar anastomoses from the middle meningeal artery (d) and occipital artery through the mastoid foramen (e) and parietal foramen (f) [45].

(b) Intracranial collaterals: PCoA (a); leptomeningeal anastomoses between ACA and MCA (b) and between PCA and MCA (c); tectal plexus between posterior cerebral and superior cerebellar arteries (d); anastomoses of distal cerebellar arteries (e) [45].

Figure 2.14: Extra- and intracranial collaterals. Figures obtained from [45].

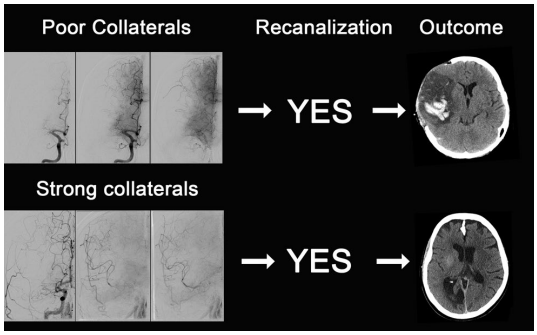

Figure 2.15: A strong association between collateral status (determined with DSA) at baseline and outcome in CCT can be seen: (Top) Baseline frontal digital subtraction angiography projection in arterial, parenchymal and early venous phase shows poor filling of the macrovascular pial arterial tree in right M1 occlusion. Despite successful recanalization (TICI: 2b) an unfavorable outcome with complete MCA infarction and hemorrhagic transformation was seen in CCT and ensued necessitating decompression hemicraniectomy. (Bottom) A strong filling of the pial collaterals at baseline in in right M1 occlusion led to a favorable outcome with only limited striatal infarction conspicuous after successful recanalization (TICI: 2b). [64]. Figure obtained from [64].

2.4 Stroke

A cerebrovascular accident or stroke is a brain injury that lasts for more than 24 hours. It can be localized and is caused by a vascular episode. A transient ischemic attack (TIA) is a focal ischemic episode that lasts less than 24 hours. [65]

2.4.1 Classification

Strokes can be divided into two main types [32]:

- **Hemorrhagic:** A hemorrhagic stroke is caused by a rupture of a blood vessel or an abnormal vessel structure that ruptures (intracerebral hemorrhage or subarachnoid hemorrhage). The rupture causes intracranial bleeding, which affects usually a larger brain region [65].
- **Ischemic:** The ischemic stroke has a much higher probability of occurrence (87%) than the hemorrhagic stroke. It is caused by an interruption in the blood supply to the brain, which can be caused by four pathologies: 1. thrombosis (a locally forming blood clot is occluding a blood vessel (cf. Fig. 2.16 a)), 2. embolism (a blood clot formed elsewhere in the body is occluding a blood vessel (cf. Fig. 2.16 b)), 3. hypoxia (a general, systemic decrease in blood supply (cf. Fig. 2.16 c) and 4. cerebral venous sinus thrombosis (a blood clot in the dural venous sinuses drains blood from the brain). Besides these four pathologies, a stroke can also be present without an obvious explanation, which is called cryptogenic (of unknown origin) and constitutes for 30-40% of all ischemic strokes [66, 67]. An ischemic stroke can also develop bleeding within ischemic areas, which is called "hemorrhagic transformation". [68]

As in this thesis ischemic stroke is of main interest, only the ischemic stroke shall be explained in more detail in the following.

In literature, there exists multiple classifications for AIS. The “Oxford Community Stroke Project” (OCSP), which is also known as the “Bamford” or “Oxford” classification, is one of the most used. It is based primarily on the initial symptoms: Depending on the extent of the symptoms, the stroke event is classified as total anterior circulation infarct (TACI), partial anterior circulation infarct (PACI), lacunar infarct (LACI) or posterior circulation infarct (POCI). This classification gives information about severity, the cause, the affected brain area and the prognosis.

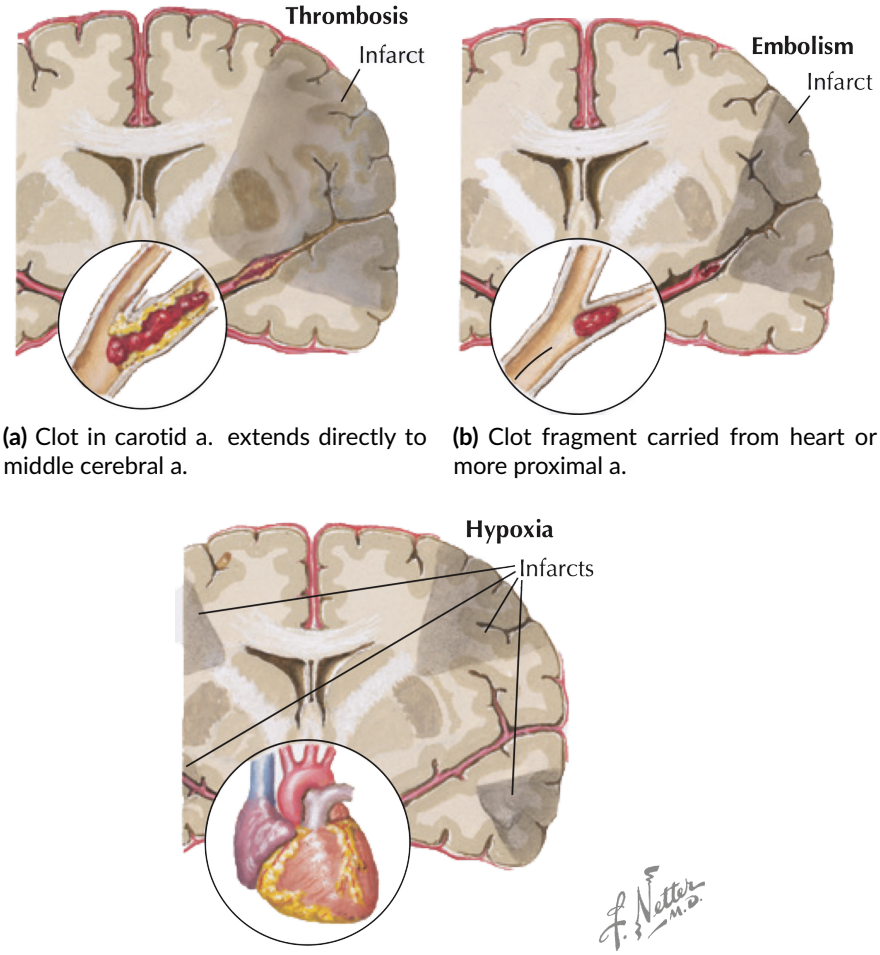

(a) Clot in carotid a. extends directly to middle cerebral a.

(b) Clot fragment carried from heart or more proximal a.

(c) Hypotension and poor cerebral perfusion: border zone infarcts, no vascular occlusion

Figure 2.16: Ischemic Stroke. Figures taken from [65].

2.4.2 Epidemiology

Stroke is the third leading cause of death and physical disability in the USA. With a prevalence rate (2013-2016) of 2.5% in the population older than 20 years, stroke is one of the most common serious diseases. Especially, as the prevalence rate increases with age. On the basis of pooled data from several large studies (1995-2011), the probability of death within one year or five years after a stroke was highest in individuals older than 75 years (one-year probability of death after first stroke: white males 33%, white females 36%, black males 25% and black females 27%). [1, 69]
In Germany, prevalence rates are similar to the USA and the one-year mortality rate is between 20 to 30% [70].
The probability for men to suffer stroke is 25% higher than for women [71]. Yet women have a higher mortality rate (60% of deaths from stroke occur in women [72]) since women live longer. Therefore, on average women are older when they suffer stroke and thus more often killed [71].

2.4.3 Treatment for Acute Ischemic Stroke

The importance of rapid stroke intervention has been known for some time. In the early 1990s, it was summarized with the slogan “Time is Brain!” [73]. However, it was not until years later that the positive effect of a rapid restoration of cerebral blood flow (fewer brain cells die in this way) was proven and quantified [74, 75].
The immediate therapy in the first few hours aims to remove the blockage. Therefore, two general possibilities exist: 1. Dissolving the occluding clot via a thrombolysis with recombinant tissue plasminogen activator (rtPA) or 2. Removal of the blood clot by mechanical thrombectomy (MT). Whereas, a combination of both therapies has shown overwhelming efficacy over alteplase (rtPA) alone [76, 77].
If large parts of the brain are affected in a stroke, there can be considerable brain swelling with secondary brain injury in the surrounding tissue. This phenomenon is also known as "malignant cerebral infarction" because it has an even more dismal prognosis. Drug treatment can reduce the excessive intracranial pressure, but some circumstances require a hemicraniectomy (temporary surgical removal of the skull on one side of the head). [78]

Classification of the Response of Therapy

In 2003, Higashida et al. [79] introduced the “thrombolysis in cerebral infarction” (TICI) grading system as a tool for determining the response of thrombolytic therapy for ischemic stroke. In neurointerventional radiology it is commonly used to describe patient’s post endovascular revascularization and to predict a prognosis [80].
However, three collaborative groups [81] recommended in 2013 to modify the scale and to

change its name to "modified treatment in cerebral infarction" (mTICI). The change shall better reflect the increased use of endovascular therapies:

- **Grade 0:** No perfusion
- **Grade 1:** Penetration with minimal perfusion
- **Grade 2:** Partial perfusion
- **Grade 2A:** Only partial filling (less than two-thirds) of the entire vascular territory is visualized
- **Grade 2B:** Complete filling of all of the expected vascular territory is visualized but the filling is slower than normal
- **Grade 3:** Complete perfusion

2.5 Therapeutic Hypothermia

Hypothermia generally describes the condition of a reduced core body temperature (physiological value of $\approx$ 37 °C). However, hypothermia is often used to describe the falling of any body temperature below 35 °C [82]. A distinction is made between mild, moderate severe and profound hypothermia, whereby the classification (Table 2.1) according to body core temperature values[7] [82] and symptoms (Swiss staging system [84]) is common.

Table 2.1: Hypothermia classification

By temperature [82]		By symptoms [84]	
Mild	35–32 °C	Stage 1	Shivering and awake
Moderate	32–28 °C	Stage 2	Not shivering and drowsy
Severe	28–20 °C	Stage 3	Not shivering and unconscious
Profound	< 20 °C	Stage 4	No vital signs

Therapeutic hypothermia (TH) (now known as targeted temperature management (TTM)) refers to an active lowering of a certain body temperature for a certain period of time to improve recovery after a period of interruption of blood flow to the brain. Although Hippocrates mentioned the use of snow and ice to reduce bleeding 400 BC [18], TH first appeared in literature in the 1940-50s, when it was mentioned for use in cardiac arrest patients [85]. Today, it is well known that TTM improves neurological recovery after global ischemia and thus reduces mortality. It is mainly used in patients with cardiac arrest [2–4] and in infants with moderate or severe hypoxic ischemic encephalopathy [86].

[7] Classification not uniform in the literature [82, 83]

2.5.1 Therapeutic Physiology

The neuroprotective effect of TTM has been attributed to a reduced cerebral metabolic rate (CMR), which is expressed by a reduction in oxygen consumption and adenosine triphosphate (ATP) demand [87]. The amount of ATP that neurons require to survive is proportional to the CMR. Ischemic cell death is caused by an imbalance in ATP supply (i.e., hypoxia-mediated loss of oxidative phosphorylation) versus demand (high oxygen consumption ($CMRO_2$) of brain tissue) [12]. For temperatures between 37–27 °C, each 1 °C drop in brain temperature decreases the $CMRO_2$ by $\approx 6-7\%$ [88, 89]. Therefore, TTM can lower the development of ischemia during reduced cerebral blood flow (CBF) by decreasing the ATP utilization and oxygen tension thresholds required to sustain tissue viability [87].
Especially in the ischemic core, the area of maximum and irreversible damage in case of AIS, ATP levels are completely depleted and neurons are necrotically killed [90]. In contrast, neurons in the penumbra, which is surrounding the ischemic core, are functionally impaired but may be saved: Here the ATP level is reduced but not completely depleted which makes the neurons in this region susceptible to apoptosis [91]. TTM reduces the need for ATP and could extend the neurotherapeutic time window in the penumbra. Fig. 2.17 shows the approximate time line of the major molecular pathway onsets following ischemic stroke.
Additionally, TTM is associated to reduce early gene expression of c-fos and disperse of excitatory neurotransmitters which plays a central role in the prevention of neuronal cell death [92]. Furthermore, TTM decreases the permeability of the the blood brain barrier to inflammatory cytokines and substances such as free radicals and thrombin, which are potentially harmful and can increase cerebral edema [93, 94].
There are other factors which are improved and/or impacted by TTM, but their role in mediating hypothermic protection is much more complex, less compelling, and less well understood [12].

2.5.2 Adverse Effects

During patient treatment with TTM, multiple side effects can occur: one of the most prominent side effect is pneumonia (reported in 50% of patients) and shivering [95]. Other possible complications are: infection, bleeding, arrhythmia and high blood sugar [96]. Furthermore, hypothermia induces a “cold diuresis” possible leading to electrolyte abnormalities (hypokalemia, hypomagnesaemia, and hypophosphatemia) and hypovolemia [97].

2.5.3 Cooling Methods

Before TTM is induced, pharmacological drugs must be administered to control shivering, which is a typical side effect of hypothermia (occurs typically when the body core temperature drops below 36 °C) [98]. To prevent and treat shivering typically acetaminophen, buspirone, opioids including pethidine (meperidine), dexmedetomidine, fentanyl, and/or propofol is

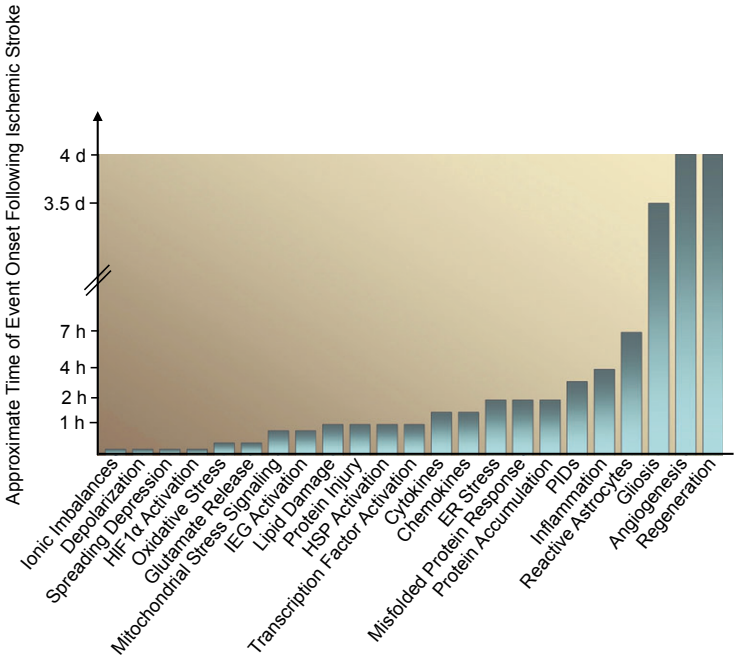

Figure 2.17: Approximate time line of molecular pathway onsets following ischemic stroke. Figure taken from [15].

administered [99]. During cooling the systemic core body temperature is measured (e.g., via the esophagus, rectum, bladder or within the pulmonary artery) to guide cooling [96].
Today, two methods are used in general to induce TTM: Endovasular cooling and surface cooling. Surface cooling has been used for years to treat fever and includes methods such as ice packing, convective air blankets, alcohol bathing, water mattresses and cooling jackets. Surface cooling has the advantage that it does not require a central venous catheter. Therefore, no specialist knowledge of catheter placement is required and the associated risks and increased effort involved in the placement of a central venous catheter are avoided. However, external cooling is slower than endovascular cooling. Another disadvantage is the necessary use of sedatives and paralytics to avoid discomfort and shivering at target temperatures below 35 °C [100]. Selective cooling of the head could bypass some limitations of systemic cooling [101]. Recent studies with cooling helmets show promising results but the helmets needed several hours to reach the target temperatures [102].
Endovascular cooling is induced using cooling catheters, which are placed into a femoral vein. The catheters can use cooled saline solution, which circulates through either a metal coated tube or a balloon in the catheter. The cold saline solution cools the blood, which in turn cools the entire body. Cooling rates between 1.5-2 °C per hour are common [103].
Endovascular blood cooling is faster than surface cooling and was proven to be safe and effective [104]. However, it is also more prone for side effects, such as bleeding, infection, vascular puncture, and deep vein thrombosis [8].

2.5.4 Role in Stroke Therapy

The therapeutic effect of TH in AIS therapy remains equivocal, as currently there exists no clear evidence supporting the use of targeted temperature management and clinical trials have not been completed [9, 10]. So far, only in animal models a temperature reduction to 35°C or below was associated with a distinct reduction of the final infarct volume (FIV) (-44%) [7].

Selective Brain Hypothermia

Despite the so far unproven clear neuroprotective effect of TH in AIS therapy, selective brain hypothermia (SBH) remains promising as it enables quick and effective brain cooling [9] and potentially avoids or at least limits the disadvantages of systemic cooling methods (slow, limited cooling and side effects such as pneumonia, cardiac arrhythmia) [105]. To induce SBH, helmets and intranasal sprays can be used but cooling the blood stream in the large brain-supplying arteries (e.g., the ICA) has the advantage to use the blood flow as a strong energy vector flowing directly into the brain parenchyma [16]. Furthermore, intracarotid cooling can be combined with MT in the scope of one endovascular procedure, using the same access and navigation instruments. This approach is particularly promising as cooling could be applied before or during the critical phase of reperfusion (first 15 min after reperfusion, cf. Fig. 2.18) [15, 16]. A reperfusion can potentially activate inflammatory pathways (cf. Fig. 2.18) resulting in a so-called “reperfusion injury” [15, 17].
In 2018, a recent cohort study with 113 patients, demonstrated that endovascular mechanical thrombectomy combined with a time-limited, intraarterial cold saline infusion (CSI) (50 ml of 4 °C cold 0.9% saline infused into the ischemic territory at 10 $\frac{\text{ml}}{\text{min}}$ before recanalization plus further CSI into the ischemic brain directly after MT at 30 $\frac{\text{ml}}{\text{min}}$ for 10 min) led to a significant reduction of FIV (19.1 ml; 95% confidence interval (CI) 3.2 to 25.2; P= 0.038) in case of large-vessel occlusion followed by recanalization [13].
For intracarotid blood cooling three different methods have been suggested, which potentially allow combined catheter-based MT intervention: 1. extracorporeal blood cooling, 2. CSI, and 3. intracarotid closed-loop cooling.
In this work, the cooling performance of a recently developed intracarotid closed-loop cooling catheter [14] is evaluated. On the one hand, intracarotid closed-loop cooling could be not as effective as CSI or extracorporeal cooling, but on the other hand it does not lead to hemodilution induced by CSI [18] and might be more feasible than extracorporeal cooling. The catheter system was developed by Acandis GmbH, Germany and is schematically shown in Fig. 2.19 a. The catheter has an outer diameter of approximately 3.3 mm (8 Fr sheath) and consists of a central shaft with three cavities. Four balloons are placed in series at the distal end of the catheter, each with an outer lumen of 4 mm. The three cavities of the shaft include two smaller shafts for the coolant in- and outlets and one large central 6 Fr lumen for delivery of dedicated catheters for MT procedure (a microcatheter for transport of a stent retriever, a distal access catheter for direct clot aspiration or a coaxial system for

stent retriever plus distal aspiration MT). The coolant flows through the inlet and outlet of the main lumen into the four balloons. The coolant first flows to the distal catheter tip and then backwards through the balloons to an extracorporeal cooling unit, thus enabling a countercurrent heat exchange with the surrounding blood flow within the carotid artery. [16]

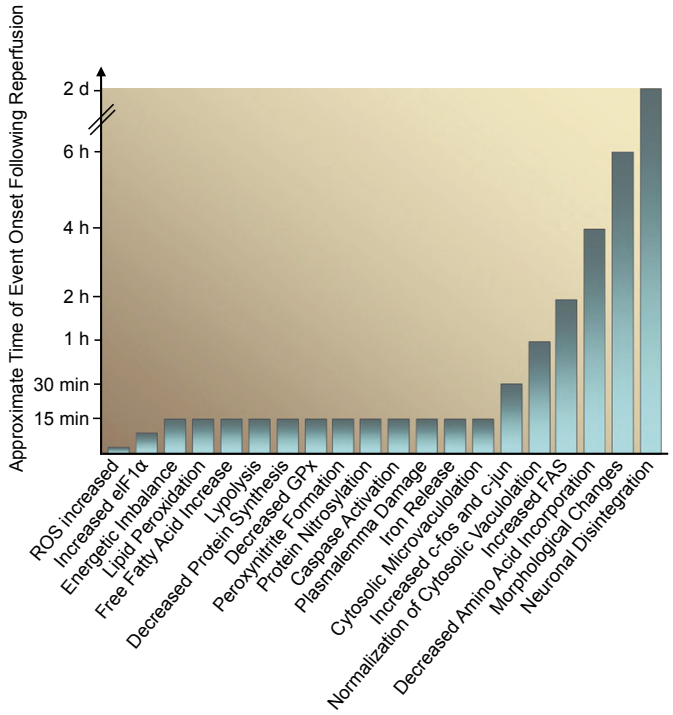

Figure 2.18: Approximate time line of molecular pathway onsets following reperfusion. Figure taken from [15].

The cooling procedure can be divided into in three different phases:

1. **Prereperfusion cooling:** As soon as the catheter is placed in the common carotid artery (CCA), coolant flow is activated. However, since arteries distal to the occlusion can not be perfused directly with cooled blood, the cooling effect is limited to hypoperfused penumbral brain tissue which can be perfused by cold blood coming from collateral arteries (e.g., leptomeningeal anastomoses). Nevertheless, a neuroprotective effect can possibly already be provided during and before vessel recanalization, potentially providing a very early neuroprotection and thus extending the therapeutic time window for MT [16].
2. **Intrareperfusion cooling:** Directly subsequently to recanalization, cold blood can enter the recanalized vessel and the ischemic core tissue possibly providing a “cold reperfusion”. In this cooling phase the clot is pressed at the vessel wall and engaged

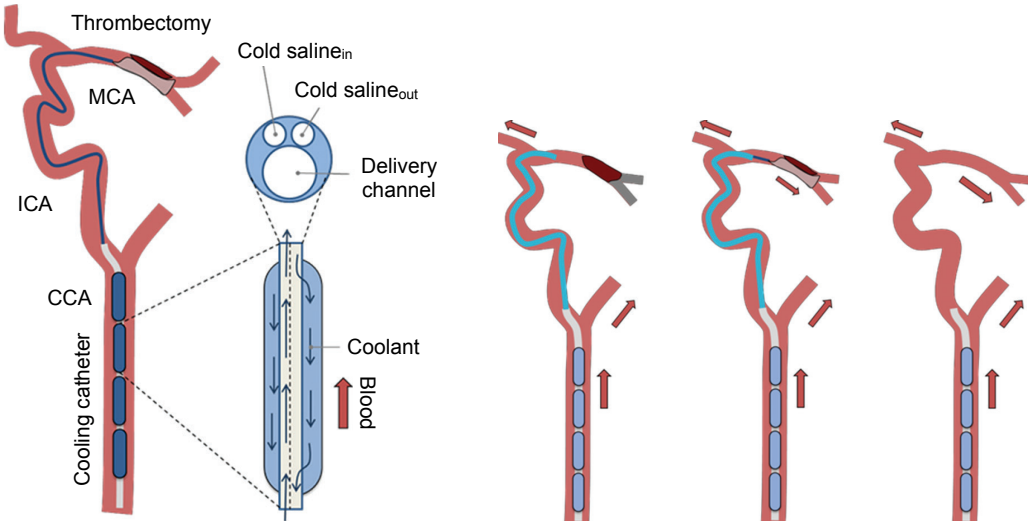

(a) Schematic depiction of the catheter construction.

(b) Pre-, intra- and postreperfusion cooling phases with the recently developed intracarotid blood-cooling catheter.

Figure 2.19: Intracarotid blood cooling with a heat exchange catheter. Pictures obtained from[16]

by a stent-like device [16]. Furthermore, distal angiography and additional, potentially needed recanalization procedures can be performed [16].

3. **Postreperfusion cooling:** After successful MT procedure, the cooling catheter can potentially be kept inside the carotid artery for several minutes and early neuroprotection is prolonged by the cooled blood that supplies the reperfused brain territory [16].

So far, the new catheter device is not in clinical use and only limited in-vitro and in-vivo test measurement data exist. In vitro experiments with catheter prototypes and artificial blood revealed that temperature reduction is less pronounced for higher blood substitute flow rates: For a flow rate of 250 $\frac{\text{ml}}{\text{min}}$, a mean temperature drop between the catheter inlet and outlet of $-2.17 \pm 0.07\,°\text{C}$ was measured and for a coolant flow rate of 400 $\frac{\text{ml}}{\text{min}}$, a mean temperature drop of $-1.55 \pm 0.06\,°\text{C}$ was measured [14].
In a first in vivo study with 9 sheep, the cooling catheters were placed in the carotid arteries and the catheter's balloons were flushed with cold saline for three hours. During cooling, the brain temperature was measured by intraparenchymal probes (frontal & temporal) and by a probe in the vena cava. Experiment results showed a significantly stronger brain temperature decrease in the ipsilateral hemisphere compared to the contralateral hemisphere and to systemic temperature. A 2 °C temperature drop for the ipsilateral side was observed after approx. 30 min of cooling, compared to approx. 1 °C in the contralateral side [106].

2.6 Body Heat Balance

The human being is a homeothermic creature. He can keep his body core temperature constant ($\approx 37\,°C$) despite changing environmental conditions. The body shell (skin and extremities) on the other hand are poikilothermic [20].
In order to keep the core body temperature constant, the body's own heat production plus heat absorption must be in balance with the heat output. The heat production of the body depends on its energy turnover. At rest, 56% of the heat is generated by the internal organs, 18% by the skin and muscles, 16% by the brain and 8% by other parts of the body. During physical work, the heat output of the body increases significantly and the proportion of heat produced by the muscles (cf. Sec. 2.2) can be up to 90%. [20]
To keep the body warm, it may be necessary to generate additional heat through body movements and muscle shivering. In addition, heat can be generated without shivering (especially in babies) in the brown fat tissue. [20, 42]
The heat generated by the body is absorbed by the bloodstream and transported to the body surface. However, this internal heat flow is only possible if the skin temperature is lower than the temperature of the body core. In addition, the heat transport is strongly influenced by the blood circulation of the skin.
The heat transfer of the skin to the environment is determined by three mechanisms: radiation, convection and evaporation (cf. Sec. 3.2.2). The composition of the heat release depends on the ambient temperature. For high ambient temperatures above 36 °C the body can only release heat to the environment by evaporation, since heat emission by radiation and convection is no longer sufficient. The body can lose 2428 kJ of energy per liter of evaporated liquid. Since the heat dissipation by evaporation depends on the difference in vapor pressures (cf. Sec. 3.2.2) at the skin surface and in the environment, a person cannot tolerate temperatures above 33 °C at very high humidity. [20]

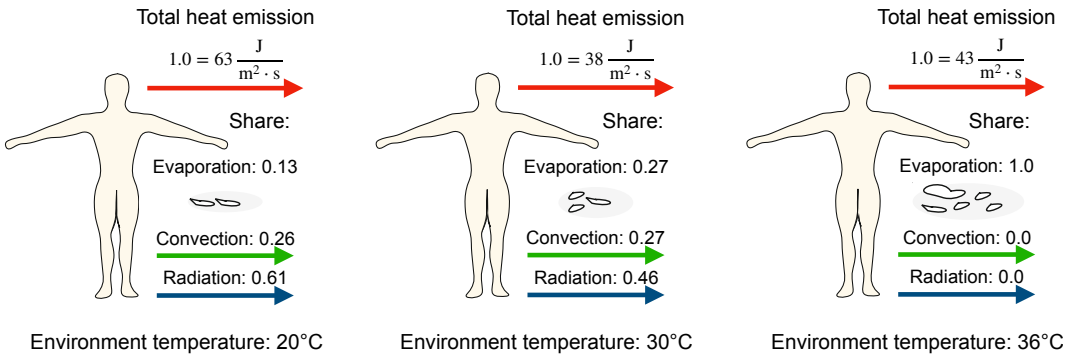

Figure 2.20: Proportion of the various heat emission processes to the environment of the unclothed, resting body for different ambient temperatures. Modified with permission from [107].

Temperature Management

The task of thermoregulation is to keep a mean core body temperature constant despite fluctuations in the absorption, production and release of heat. The mean target value is $\approx 37\,°C$ with daily variations of about $0.6\,°C$ being normal [20, 108].
The control center of temperature regulation is the hypothalamus. It contains thermal sensors which register the core temperature. In addition, the temperature of the spinal cord and skin is controlled. If the temperature deviates from the mean target and actual value, the temperature is regulated [108]. An overview of the body's heat balance management and the nervous influence is shown in Fig. 2.21. If the core temperature exceeds the mean target temperature, the internal heat flow is increased by a dilatation of the vessels in the skin, a redirection of the refluxing blood flow into veins near the surface and an increase in sweat production [20]. If the core temperature falls below the mean target temperature, the heat emission is reduced by vasoconstriction in the body shell and heat production is increased by arbitrary muscle movement and shivering [20].
The so-called thermoneutral zone lies between the temperatures that lead to a temperature influence through sweating or shivering. When a person is at rest and almost unclothed, this zone covers an ambient temperature range of $\approx$ 27-32 °C. The thermal neutral zone in which no vasomotion is activated, is considerably smaller and has a range of $\approx 0.5\,°C$ [109]. Generally, the thresholds vary daily in both sexes (circadian rhythm) and monthly in women (up to 0.5 °C) [110].
Anesthesia affects thermoregulatory control and leads to perioperative hypothermia [111]. Anesthesia is known to extend the thermoneutral zone by $\approx$ 2-3 °C for vasoconstriction and shivering [110]. In a clinical study with patients who were put into hypothermia during a neurosurgical intervention, it was shown that in about half of the patients a constriction of the skin vessels occurs, in the others there was no vasomotor reaction [112]. When using hypothermia by means of surface cooling, the spread of the thermoneutral zone due to anesthesia can have a particularly influence on the cooling capacity.

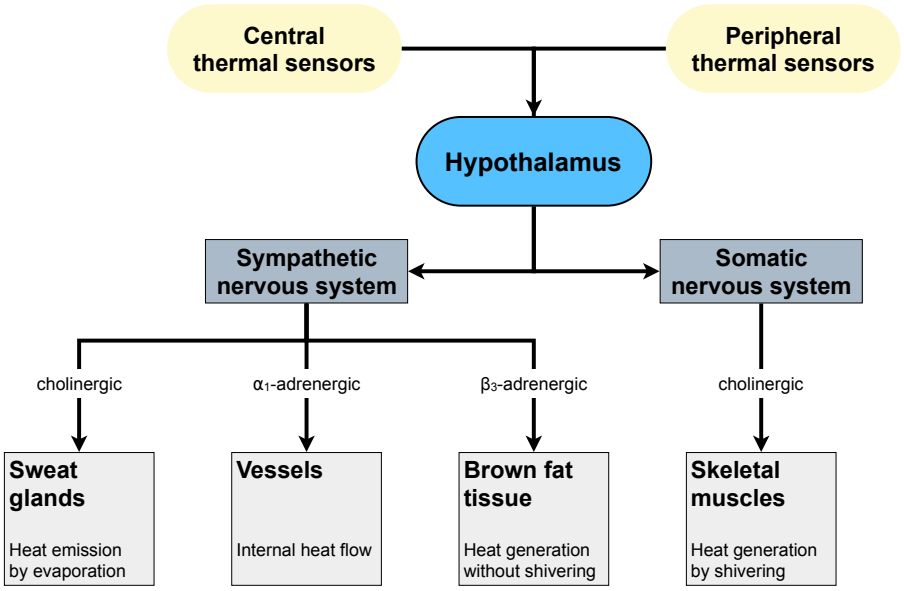

Figure 2.21: Nervous influence on the body's own heat balance. Figure inspired from [20].

Chapter 3

Mathematical Fundamentals

3.1 Fluid Mechanical Basics

The description of cerebral blood flow conditions leads to the fundamental problem of calculating fluid flow through an elastic tube. Therefore, equations for the description of pressure and flow in such a tube model are derived in the following according to [113].

Fluid Flow through an Elastic Tube

Generally, the Navier-Stokes equation can be interpreted as the momentum theorem, which is the application of Newton's axioms to a continuity. A standard form used for compressible fluids is:

$$\rho\dot{\vec{v}} = \rho \cdot \left(\frac{\partial \vec{v}}{\partial t} + (\vec{v} \cdot \nabla)\vec{v} \right) = -\nabla p + \mu \Delta \vec{v} + (\eta + \mu)\nabla(\nabla \cdot \vec{v}) + \vec{f}, \tag{3.1}$$

with ρ being the fluid's density, $\vec{v}$ being the flow velocity and p being the (static) pressure. The parameters μ and η are known as Lamé constants, where μ is the kinematic viscosity of the flowing fluid and η is the Lamé-modul. The vector $\vec{f}$ is a volume force density like gravity or the Coriolis force.
If blood is assumed to be an incompressible Newtonian fluid[1], the following continuity (3.2) and simplified Navier-Stokes (3.3) equation are valid:

$$\frac{\partial \rho}{\partial t} + \nabla \cdot (\rho \cdot v) = 0, \tag{3.2}$$

$$\rho \cdot \left(\frac{\partial v}{\partial t} + (v \cdot \nabla)v \right) = -\nabla p + \mu \cdot \nabla^2 \vec{v} + \vec{f}. \tag{3.3}$$

For flow in a horizontal, elastic tube with a circular cross section the continuity equation in cylindrical coordinates (r, φ, z) is:

$$\frac{\partial \rho}{\partial t} + \frac{1}{r} \cdot \frac{\partial}{\partial r}(\rho r v_r) + \frac{1}{r} \cdot \frac{\partial}{\partial \varphi}(\rho v_\varphi) + \frac{\partial}{\partial z}(\rho v_z) = 0, \tag{3.4}$$

[1] density ρ and viscosity μ are assumed to be constant

and the Navier-Stokes equation is:

$$\rho \cdot \left[\frac{\partial v_r}{\partial t} + v_r \cdot \frac{\partial v_r}{\partial r} + \frac{v_\varphi}{r} \cdot \frac{\partial v_r}{\partial \varphi} - \frac{v_\varphi^2}{r} + v_z \cdot \frac{\partial v_r}{\partial z} \right] = \tag{3.5a}$$

$$F_r - \frac{\partial p}{\partial r} + \mu \cdot \left[\frac{\partial}{\partial r} \left(\frac{1}{r} \cdot \frac{\partial}{\partial r} (r v_r) \right) + \frac{1}{r^2} \frac{\partial^2 v_r}{\partial \varphi^2} - \frac{2}{r^2} \frac{\partial v_\varphi}{\partial \varphi} + \frac{\partial^2 v_r}{\partial z^2} \right],$$

$$\rho \cdot \left[\frac{\partial v_\varphi}{\partial t} + v_r \cdot \frac{\partial v_\varphi}{\partial r} + \frac{v_\varphi}{r} \cdot \frac{\partial v_\varphi}{\partial \varphi} + \frac{v_\varphi \cdot v_r}{r} + v_z \cdot \frac{\partial v_\varphi}{\partial z} \right] = \tag{3.5b}$$

$$F_\varphi - \frac{1}{r} \cdot \frac{\partial p}{\partial \varphi} + \mu \cdot \left[\frac{\partial}{\partial r} \left(\frac{1}{r} \cdot \frac{\partial}{\partial r} (r v_\varphi) \right) + \frac{1}{r^2} \frac{\partial^2 v_\varphi}{\partial \varphi^2} + \frac{2}{r^2} \frac{\partial v_r}{\partial \varphi} + \frac{\partial^2 v_\varphi}{\partial z^2} \right],$$

$$\rho \cdot \left[\frac{\partial v_z}{\partial t} + v_r \cdot \frac{\partial v_z}{\partial r} + \frac{v_\varphi}{r} \cdot \frac{\partial v_z}{\partial \varphi} + v_z \cdot \frac{\partial v_z}{\partial z} \right] = \tag{3.5c}$$

$$F_z - \frac{\partial p}{\partial z} + \mu \cdot \left[\frac{1}{r} \cdot \frac{\partial}{\partial r} \left(r \cdot \frac{\partial v_z}{\partial r} \right) + \frac{1}{r^2} \frac{\partial^2 v_z}{\partial \varphi^2} + \frac{\partial^2 v_z}{\partial z^2} \right].$$

For this rotationally symmetric system, we consider the components of the velocity in direction φ as well as all derivatives with respect to φ to be zero ($v_\varphi = 0$ and $\frac{\partial}{\partial \varphi} = 0$). Additionally, we do not account for gravity. Since there are no other forces on the vessels, $\vec{f} = 0$ is valid. With these assumptions the Navier-Stokes equations (3.5) can be simplified:

$$\rho \cdot \left[\frac{\partial v_r}{\partial t} + v_r \cdot \frac{\partial v_r}{\partial r} + v_z \cdot \frac{\partial v_r}{\partial z} \right] = \tag{3.6a}$$

$$- \frac{\partial p}{\partial r} + \mu \cdot \left[\frac{\partial^2 v_r}{\partial r^2} + \frac{1}{r} \cdot \frac{\partial v_r}{\partial r} - \frac{v_r}{r^2} + \frac{\partial^2 v_r}{\partial z^2} \right],$$

$$\rho \cdot \left[\frac{\partial v_z}{\partial t} + v_r \cdot \frac{\partial v_z}{\partial r} + v_z \cdot \frac{\partial v_z}{\partial z} \right] = \tag{3.6b}$$

$$- \frac{\partial p}{\partial z} + \mu \cdot \left[\frac{\partial^2 v_z}{\partial r^2} + \frac{1}{r} \cdot \frac{\partial v_z}{\partial r} + \frac{\partial^2 v_z}{\partial z^2} \right].$$

If we consider two more assumptions:

- The maximal, and thus the mean velocity, in axial direction z is small compared to the speed of wave propagation ($\frac{\partial}{\partial z} = 0$ and $\frac{\partial^2}{\partial z^2} = 0$).
- The mean radial velocity v_r is negligible compared to the axial velocity v_z ($v_r \ll v_z$).

the continuity equation and the Navier-Stokes equation can be processed to the following basic equations:

$$\boxed{\frac{v_r}{r} + \frac{\partial v_r}{\partial r} + \frac{\partial v_z}{\partial z} = 0} \tag{3.7}$$

$$\frac{\partial^2 v_r}{\partial r^2} + \frac{1}{r} \cdot \frac{\partial v_r}{\partial r} - \frac{v_r}{r^2} - \frac{\rho}{\mu} \cdot \frac{\partial v_r}{\partial t} = \frac{1}{\mu} \cdot \frac{\partial p}{\partial r} \approx 0 \tag{3.8a}$$

$$\frac{\partial^2 v_z}{\partial r^2} + \frac{1}{r} \cdot \frac{\partial v_z}{\partial r} - \frac{\rho}{\mu} \cdot \frac{\partial v_z}{\partial t} = \frac{1}{\mu} \cdot \frac{\partial p}{\partial z} \tag{3.8b}$$

Since the pressure can be regarded as almost independent of r, only equation (3.8b) will be considered in the following.
Defining the flow q as:

$$q = \int_0^{r_0} 2\pi r v_z \, \mathrm{d}r, \tag{3.9}$$

with r_0 being the vessel's radius, leads together with Eq. 3.8b to:

$$\begin{aligned} \frac{\rho}{\pi}\frac{\partial q}{\partial t} &= 2\mu \int_0^{r_0} \left(r \cdot \frac{\partial^2 v_z}{\partial r^2} + \frac{\partial v_z}{\partial r} - \frac{r}{\mu}\frac{\partial p}{\partial z} \right) \mathrm{d}r, \\ \Rightarrow \frac{\rho}{\pi}\frac{\partial q}{\partial t} &= 2\mu \int_0^{r_0} \left(r \cdot \frac{\partial^2 v_z}{\partial r^2} + \frac{\partial v_z}{\partial r} \right) \mathrm{d}r - \frac{\partial p}{\partial z} \cdot r_0^2. \end{aligned}$$

By further transformation we obtain:

$$\frac{\rho}{\pi \cdot r_0^2} \cdot \frac{\partial q}{\partial t} = -\frac{\partial p}{\partial z} + \frac{2\mu}{r_0} \cdot \frac{\partial v_z}{\partial r}\Big|_{r=r_0}. \tag{3.10}$$

For the stationary case the following applies:

$$\frac{\partial p}{\partial z} = \frac{2\mu}{r_0} \cdot \frac{\partial v_z}{\partial r}\Big|_{r=r_0}. \tag{3.11}$$

After integration over r, the Hagen-Poiseuille equation follows [114]:

$$v_z(r) = -\frac{r_0^2}{4 \cdot \mu} \cdot \frac{\partial p}{\partial z} \cdot \left(1 - \frac{r^2}{r_0^2} \right). \tag{3.12}$$

The maximal velocity $v_{z,\max}$ is:

$$v_{z,\max} = -\frac{r_0^2}{4 \cdot \mu} \cdot \frac{\partial p}{\partial z}. \tag{3.13}$$

For the flow q it applies:

$$q = \int_0^{r_0} 2\pi r \cdot v_z(r) \, \mathrm{d}r = \frac{v_{z,\max}}{2} \pi r_0^2 = -\frac{r_0^4 \pi}{8 \cdot \mu} \cdot \frac{\partial p}{\partial z}, \tag{3.14}$$

and a further condition for the pressure change in direction z follows:

$$\frac{\partial p}{\partial z} = -\frac{8\mu}{\pi r_0^4} \cdot q. \tag{3.15}$$

By combining Eq. 3.11 and Eq. 3.15 for stationary conditions it follows:

$$\frac{2\mu}{r_0} \cdot \frac{\partial v_z}{\partial r}\Big|_{r=r_0} = -\frac{8\mu}{\pi r_0^4} \cdot q. \tag{3.16}$$

If a laminar flow profile is assumed for the segments, the solution for the stationary case (Eq. 3.16) can be inserted in the general solution (Eq. 3.10) and the following differential equation can be obtained:

$$\boxed{-\frac{\partial p}{\partial z} = \frac{\rho}{\pi r_0^2} \cdot \frac{\partial q}{\partial t} + \frac{8\mu}{\pi r_0^4} \cdot q} \tag{3.17}$$

To obtain an equation for the determination of the flow, the continuity equation in the simplified form (Eq. 3.7) is used:

$$\begin{aligned} &\frac{v_r}{r} + \frac{\partial v_r}{\partial r} + \frac{\partial v_z}{\partial z} = 0, \\ \Rightarrow &\frac{\partial v_z}{\partial z} = -\left(\frac{v_r}{r} + \frac{\partial v_r}{\partial r}\right) \\ \Rightarrow &\frac{\partial v_z}{\partial z} = -\frac{\partial (v_r \cdot r)}{\partial r \cdot r}. \end{aligned}$$

Considering the determination of flow, it results in:

$$\begin{aligned} &\frac{\partial q}{\partial z} = \int_0^{r_0} 2\pi \cdot r \frac{\partial v_z}{\partial z} \, \mathrm{d}r, \\ \Rightarrow &\frac{\partial q}{\partial z} = -2\pi \int_0^{r_0} \frac{v_r \cdot \partial r}{\partial r} \, \mathrm{d}r \\ \Rightarrow &\frac{\partial q}{\partial z} = -2\pi \int_0^{r_0} v_r \, \mathrm{d}r \\ \Rightarrow &v_r\Big|_{r=r_0} = -\frac{1}{2\pi r_0} \cdot \frac{\partial q}{\partial z}. \end{aligned} \tag{3.18}$$

The Barlow's formula for thin-walled tubes (with the wall thickness d) under internal pressure is used for determining the expression $v_r\Big|_{r=r_0}$ [115]. The parameter x_r represents the radial shift of a point. Furthermore we assume the following:

- Validity of Hook's law: $\sigma = E \cdot \epsilon$, where E is Young's modulus, σ is the uniaxial stress and ε is the strain
- Only small displacements in radial direction
- A small wall thickness compared to the vessel's diameter

$$\begin{aligned} &\partial p = \frac{\sigma \cdot d}{r}, \\ &\sigma = \frac{E}{1 - Po^2} \cdot \left(\frac{x_r}{r} + Po \cdot \frac{\partial x_r}{\partial r}\right), \\ \Rightarrow &\sigma = \frac{E}{1 - Po^2} \cdot \frac{x_r}{r} \\ \Rightarrow &\partial p = \frac{E}{1 - Po^2} \cdot \frac{x_r}{r} \cdot \frac{d}{r} \\ \Rightarrow &\frac{\partial p}{\partial t} = \frac{E}{1 - Po^2} \cdot \frac{v_r \cdot d}{r^2} \\ \Rightarrow &\frac{\partial p}{\partial t} = \frac{E \cdot d}{(1 - Po^2) \cdot r_0^2} \cdot v_r\Big|_{r=r_0}, \end{aligned} \tag{3.19}$$

where Po is the Poisson number.
If we assume a not compressible vessel wall, $Po = \frac{1}{2}$ is valid and we obtain:

$$\frac{\partial p}{\partial t} = \frac{4 \cdot E \cdot d}{3 \cdot r_0^2} \cdot v_r\Big|_{r=r_0}. \tag{3.20}$$

Together with Eq. 3.18 a differential equation to determine the flow can be formed:

$$\boxed{-\frac{\partial q}{\partial z} = \frac{3\pi r_0^3}{2Ed} \cdot \frac{\partial p}{\partial t}} \tag{3.21}$$

The results can be summarized in the following differential equations for pressure and flow:

$$\boxed{\begin{aligned} -\frac{\partial q}{\partial z} &= \frac{3\pi r_0^3}{2Ed} \cdot \frac{\partial p}{\partial t} && \text{(3.22a)} \\ -\frac{\partial p}{\partial z} &= \frac{\rho}{\pi r_0^2} \cdot \frac{\partial q}{\partial t} + \frac{8\mu}{\pi r_0^4} \cdot q && \text{(3.22b)} \end{aligned}}$$

A more detailed derivation of the differential equations for pressure and flow is described in [113].

3.2 Basics of Thermodynamics

3.2.1 First Law of Thermodynamics

The first law of thermodynamics is also known as the principle of conservation of energy:

Theorem 3.1 (First Law of Thermodynamics) *The internal energy U of a closed system[2], changes exclusively by the transport of heat Q via the system boundaries or by work dissipated W within the system:*

$$\mathrm{d}U = \mathrm{d}Q + \mathrm{d}W.$$

Considering a finite volume V with its edge ∂V, we obtain:

$$\iiint_V \rho \cdot c \cdot \frac{\partial T}{\partial t}\,\mathrm{d}V = -\oiint_{\partial V} \dot{\vec{q}}\,\mathrm{d}\vec{A} + \iiint_V \dot{w}\,\mathrm{d}V,$$

for energy conservation with the material dependent density ρ and specific heat capacity c , the heat flux density $\dot{\vec{q}}$ and the power density $\dot{w}$.
With the Gaussian integral theorem, the surface integral can be transformed into a volume integral. For a differential notation a punctual view follows:

$$\boxed{\rho \cdot c \cdot \frac{\partial T}{\partial t} = -\nabla \dot{\vec{q}} + \dot{w}} \tag{3.23}$$

3.2.2 Forms of Heat Transfer

Heat transfer is the transport of thermal energy. A distinction is made between different forms of transfer, which are explained below.

Conduction

Conduction is molecular heat transport in solid, non-moving liquid or gaseous media due to a temperature gradient [21]. The heat is transmitted by vibration excitation of neighbouring molecules. The process can be described by Fourier's law:

Theorem 3.2 (Fourier's Law) *The heat flux density caused by conduction is proportional to the temperature gradient:*

$$\dot{\vec{q}} = -\lambda \cdot \nabla T, \tag{3.24}$$

with λ being a material specific constant known as heat conductivity.

[2] no mass transport across the system boundaries

By inserting Fourier's law in Eq. 3.23, the heat diffusion equation follows for a heat conducting body[3]:

$$\boxed{\rho \cdot c \cdot \frac{\partial T}{\partial t} = \nabla(\lambda \nabla T) + \dot{w}.} \tag{3.25}$$

Radiation

Radiation is the exchange of heat through thermal radiation. A black body has the emission coefficient $\epsilon = 1$. Its radiant intensity can be described by the Stefan-Boltzmann law:

Theorem 3.3 (Stefan-Boltzmann Law) *The heat flux density of a black body caused by heat radiation is proportional to the fourth power of temperature:*

$$\dot{q} = \sigma \cdot T^4,$$

with σ being the Stefan-Boltzmann constant having the value $\approx 5.6704 \cdot 10^{-8} \frac{\mathrm{W}}{\mathrm{m^2 K^4}}$.

For a gray body, the emission coefficient is $\epsilon < 1$. Thus, the heat flux density of thermal radiation is:

$$\dot{q} = \sigma \cdot \epsilon \cdot T^4.$$

The simplest case of heat exchange is the exchange between two infinitely extended flat black bodies with the temperatures T_1 and T_2. Here, the heat flux density from body 1 to body 2 corresponds to the difference in the emitted heat flux densities:

$$\dot{q}_{1-2} = \sigma \cdot (T_1^4 - T_2^4).$$

According to Kirchhoff's radiation law, the absorption coefficient α is equal to the emission coefficient ϵ.
If two infinitely extended flat gray bodies exchange heat, the heat radiated by body 1 is only partially absorbed by body 2. The remaining thermal energy is reflected and meets body 1 again, which in turn reflects part of it. If body 2 is assumed to be not radiating, the effective heat flux density of body 1 is:

$$\dot{q}_1 = \sigma \cdot \epsilon_1 \cdot \sum_{n=0}^{\infty} (1-\epsilon_2)^n (1-\epsilon_1)^n \cdot T_1^4.$$

Since $|\epsilon| < 1$, the following applies for the geometric series:

$$\dot{q}_1 = \sigma \cdot \epsilon_1 \cdot \frac{1}{1-(1-\epsilon_1)(1-\epsilon_2)} \cdot T_1^4.$$

If the same applies for body 2, the heat flux density from body 1 to body 2 is again the difference of the both heat flux densities:

$$\dot{q}_{1-2} = \sigma \cdot \frac{1}{\frac{1}{\epsilon_1} + \frac{1}{\epsilon_2} - 1} \cdot (T_1^4 - T_2^4) = \sigma \cdot E \cdot (T_1^4 - T_2^4),$$

[3] in which there is no convection

with E being the so-called “degree of radiation heat exchange”.
For more complex arrangements (several bodies of finite expansion), so-called shape factors are introduced for the calculation of the heat exchange [116].

Convection

Within a fluid or when a fluid moves around a solid, heat exchange can occur through convection. Convection is always associated with the transport of particles that carry their energy with them. Consequently, convection is not possible in non-permeable solids or in vacuum. In gases or liquids, however, convection can hardly be avoided.
A distinction is made between free and forced convection. In free convection, temperature gradients create a density gradient and thus a heat flux. In forced convection, the flow acts on the system from outside. [117].
The convective heat transfer between a solid body and a fluid is not only dependent on the material, but also on the flow dependent temperature boundary layer. This boundary layer forms on the surface of the solid body. Within the boundary layer a linear temperature course can be assumed (cf. Fig. 3.1) and the temperatures outside the boundary layer remain unaffected. At the surface of the solid, the flow velocity is zero and the temperature corresponds to the surface temperature T_{Surface}. At the other end of the boundary layer the temperature has the constant value of the fluid T_{Fluid}. The heat conduction can thus be specified depending on the boundary layer thickness δ_d and can be ascribed to heat conduction:

$$\dot{q} = \frac{\lambda}{\delta_d} \cdot (T_{\text{Fluid}} - T_{\text{Surface}}),$$

Since the boundary thickness can not be defined easily and is dependent on multiple factors, a heat transfer coefficient α is introduced:

$$\dot{q} = \frac{\lambda}{\delta_d} \cdot (T_{\text{Fluid}} - T_{\text{Surface}}) = \alpha \cdot \Delta T. \tag{3.26}$$

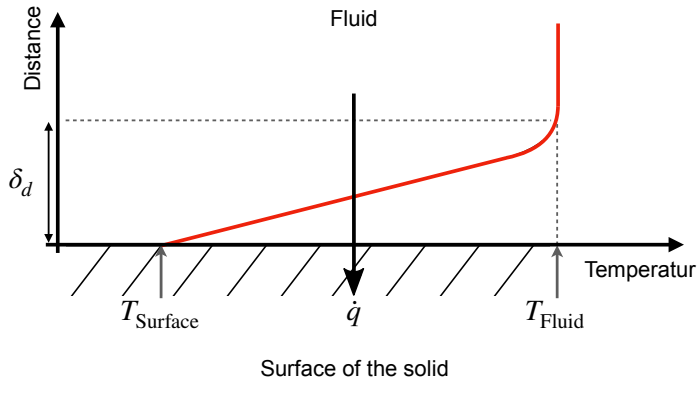

Figure 3.1: Convection: Course of temperature within a boundary layer. Figure inspired by [117].

Evaporation

Heat transfer by evaporation occurs between two media with different vapor pressure p_{H_2O}. The heat flux density is proportional to the difference of the vapor pressures Δp_{H_2O} [118]:

$$\dot{q} = h_{evap} \cdot \Delta p_{H_2O},$$

where h_{evap} is a heat exchange coefficient.

PART II

MODELING

Chapter 4

Modeling of the Hemodynamics

The brain is well thermally insulated by hair, scalp, skull bone and underlying layers. Therefore, the brain temperature is mainly influenced by the heat production of metabolism and blood perfusion. Under physiological conditions, the perfusion of the brain with arterial blood is controlled in a narrow range by the cerebral autoregulation (see Sec. 2.2). The corresponding global physiological perfusion rates for gray matter (GM) and white matter (WM) are known from literature [119]. In the case of large vessel occlusion (LVO), primary collaterals in the circle of Willis (CoW) and secondary leptomeningeal collaterals (SLCs) redistribute the blood flow and partially compensate the primary, impaired supply routes (cf. Sec. 2.3.3). In this case, the remaining perfusion rates depend on the collateral circulation. However, the extent of the secondary collateralization and the anatomical structure of the CoW vary from patient to patient (cf. Sec. 2.3.2). Differences in cerebral arterial anatomy can lead to spatially different perfusion rates and thus to different ischemic conditions. In order to represent the resulting perfusion rates in an ischemic stroke spatially as accurately as possible, the structure of the cerebral vascular system must be considered in detail. The modeling of the hemodynamics as basis for cerebral temperature calculation will be explained in this chapter.

To determine spatially different perfusion rates without enormous computational costs, mean flow rates were calculated with a one-dimensional 'transmission line' blood flow model. This approach is explained in the first part of this chapter (cf. Sec. 4.1). Furthermore, the Avolio model [22] (a hemodynamics model of the whole human arterial tree) is introduced, which was extended by Schwarz et al. [120] with segments forming the CoW. This model built the basis for the development of the hemodynamics model used in this thesis.

However, for the determination of spatially variable perfusion rates during an occlusion, the model considers too few branching of the main cerebral arteries. Therefore, the model was further extended. The extension of the model with a detailed circulation of the main cerebral arteries and the inclusion of the SLCs is explained in the second part of this chapter (cf. Sec. 4.2). To take interindividual differences in the cerebral circulation into account, the underlying anatomy of the developed model can be varied. These variations and their modeling is content of the third part of this chapter (cf. Sec. 4.3).

As mentioned in Sec. 2.1.1, the fine network of capillaries determines primarily the total

peripheral resistance (TPR) and blood flow conditions. Therefore, the modeling has a major influence on the corresponding cerebral perfusion rates and the temporal temperature course of brain tissue. The modeling of the corresponding terminating segments in the hemodynamics model is explained and discussed in detail in the fourth part of this chapter (cf. Sec. 4.4). In this part, the consideration of the autoregulation is also addressed.
The fifth part of this chapter deals with the evaluation of the simulated blood flow rates (cf. Sec. 4.5). It is split in two parts: In the first part, the resulting flow rates are presented and discussed by a comparison with measured in-vivo blood flow rates for physiological blood flow conditions. The second part presents the blood flow results for a LVO in the right middle cerebral artery (MCA)-M1 segment.

4.1 Basis of the Hemodynamics Model

Models of human hemodynamics are a topic, that has been studied for several decades. Depending on the intended use, different approaches have been developed for the modeling of blood flow: For the representation of the entire body circulation, mostly one-dimensional flow simulations are used, since they require less computational effort compared to more complex 3D simulations. This allows a possibly necessary real-time capability of the models [121]. If a detailed finite element method (FEM) flow simulation is required, e.g., to model changed flow conditions caused by aneurysms [122] or to analyze the detailed blood flow in the CoW [123, 124], the geometry of the vessels is reproduced exactly in a 2- or 3D model.

4.1.1 Transmission Line Model

Transmission line models belong to the group of 1D flow models. They are based on the electromechanical analogy between electrical conduction and flow in an elastic tube. For known mechanical properties and dimensions of a vessel, pulsatile flow- and pressure curves can be simulated. In 1980, Avolio [22] used the transmission line approach in 128 segments to model the whole arterial tree of a human on a digital calculator. Even today, the model is still used for different applications [121, 125, 126] and forms the basis for the hemodynamics model in this thesis.
In the following sections, the basic equations of the transmission line approach will be derived. Different possibilities of discretization of the transmission line are considered, which were developed by Schwarz et al. and are needed for the simulation of a complex topology. Finally, the Avolio model and its extension by Schwarz et al. with the CoW [120] is briefly introduced.

Electrical Analogue

In Sec. 3.1, differential equations for the pressure and the flow in an elastic tube with circular cross section have been derived, which build the basis for the transmission line models:

$$-\frac{\partial q}{\partial z} = \frac{3\pi r_0^3}{2Ed} \cdot \frac{\partial p}{\partial t}, \tag{4.1a}$$

$$-\frac{\partial p}{\partial z} = \frac{\rho}{\pi r_0^2} \cdot \frac{\partial q}{\partial t} + \frac{8\mu}{\pi r_0^4} \cdot q. \tag{4.1b}$$

If the coefficients are summarized in the differential equations (Eq. 4.1), the analogy of the transmission behavior of an elastic tube (under the given circumstances) to the electrical conduction equation becomes obvious:

$$-\frac{\partial p}{\partial z} = L' \cdot \frac{\mathrm{d}q}{\mathrm{d}t} + R' \cdot q \tag{4.2}$$

$$-\frac{\partial q}{\partial z} = C' \cdot \frac{\mathrm{d}p}{\mathrm{d}t}., \tag{4.3}$$

where the pressure p is the electric voltage, the flow q the electric current, and

$$L' = \frac{\rho}{\pi r_0^2}, \quad R' = \frac{8\mu}{\pi r_0^4}, \quad C' = \frac{3\pi r_0^3}{2Ed}.$$

The summarized coefficients can be interpreted as electrical analogies, where R' corresponds to the flow resistance per unit length according to the Hagen-Poiseuille equation and L' results from the mass inertia of the fluid. C' represents the compliance per unit length, which is a measure of elasticity and reflects the vessel's ability to buffer volume.
For excitation with the harmonic frequency ω in an elastic tube of the length Δz, the relation between the complex amplitude of the input pressure $\hat{p}^{\mathrm{in}}$ and the output pressure $\hat{p}^{\mathrm{out}}$ is:

$$\hat{p}^{\mathrm{in}} = \hat{p}^{\mathrm{out}} \cosh(\gamma \Delta z) + \hat{q}^{\mathrm{out}} \cdot Z_0 \cdot \sinh(\gamma \Delta z), \tag{4.4}$$

and the relation between the input flow $\hat{q}^{\mathrm{in}}$ and output flow $\hat{q}^{\mathrm{out}}$ is:

$$\hat{q}^{\mathrm{in}} = \hat{q}^{\mathrm{out}} \cosh(\gamma \Delta z) + \frac{\hat{p}^{\mathrm{out}}}{Z_0} \sinh(\gamma \Delta z), \tag{4.5}$$

with

$$Z_0 = \sqrt{\frac{R' + j\omega L'}{j\omega C'}} \quad \text{and} \quad \gamma = \sqrt{R' + j\omega L' \cdot j\omega C'}.$$

Discussion & Limitations of the Electrical Analogue

Due to the assumption of a pulsating flow and the numerous bifurcations in the hemodynamics model presented later, the flow profile in the arteries deviates from a parabolic shape, which is assumed in the Hagen-Poiseuille law. This leads to a higher flow resistance. In addition, the fact that the elastic vessels expand depending on the pressure, which changes the vessel's radius, is neglected (for L' and R'). Furthermore, the rheological properties of blood only approximately correspond to those of a Newtonian fluid. Nevertheless, the Hagen-Poiseuille law is assumed to be an acceptable estimation of the flow resistance [26].

4.1.2 Discretization Schemes

Standard Quadripol

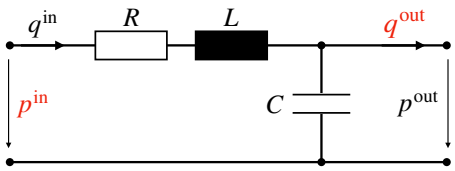

Figure 4.1: Standard discretization of the transmission line approach: Standard-quadripole. The input variables are marked with red color.

One possibility to discretize the partial differential equations for flow and pressure (cf. Eq. 4.2 and Eq. 4.3) is to replace the differential with respect to the flow direction z by a difference quotient:

$$\frac{p^{\text{in}} - p^{\text{out}}}{\Delta z} = L' \cdot \frac{\mathrm{d}q}{\mathrm{d}t} + R' \cdot q, \tag{4.6}$$

$$\frac{q^{\text{in}} - q^{\text{out}}}{\Delta z} = C' \cdot \frac{\mathrm{d}p}{\partial t}, \tag{4.7}$$

where p^{in} and p^{out} are the input respectively output pressure and q^{in} and q^{out} are the input respectively output flow of a short elastic tube with the length Δz. In the following, this short elastic tube (with the length Δz) will be referred to as "segment".
A segment meets the condition of an electrically short line if its length Δz is sufficiently small in relation to the smallest occurring wavelength λ_{min}. Since the flow resistance of larger vessels are very low [127] and a loss-free line is assumed, it is neglected for estimating the speed of wave propagation c. The following condition for the length Δz follows:

$$\Delta z \ll \lambda_{\text{min}} = \frac{1}{f_{\text{max}}\sqrt{L'C'}}, \tag{4.8}$$

with the general relation

$$\lambda = \frac{1}{f\sqrt{L'C'}}.$$

For physiological conditions, a maximal frequency f_{max} of up to 15 Hz is assumed [22].
Defining $R := R'\Delta z$, $L := L'\Delta z$ and $C := C'\Delta z$, the following state space representation of Eq. 4.6 and Eq. 4.7 is valid:

$$\frac{\mathrm{d}p^{\text{out}}}{\mathrm{d}t} = \frac{1}{C} \cdot \left(q^{\text{in}} - q^{\text{out}}\right) \tag{4.9}$$

$$\frac{\mathrm{d}q^{\text{in}}}{\mathrm{d}t} = -\frac{R}{L} \cdot q^{\text{in}} + \frac{1}{L} \cdot \left(p^{\text{in}} - p^{\text{out}}\right), \tag{4.10}$$

and

$$\Delta z^2 \ll \frac{1}{15\,\mathrm{Hz}\sqrt{LC}}, \tag{4.11}$$

should be respected.

The equivalent circuit of the system is shown in Fig. 4.1 and is called standard-quadripole in the following. According to Eq. 4.9 and Eq. 4.10, the input pressure p^{in} and output flow q^{out} build the boundary conditions for this state space representation.

If a vessel is too long compared to the required short length Δz (cf. 4.11), it can be represented by a series of standard-quadripoles (cf. Fig. 4.2 a). In addition, branching vessels can be modeled using Kirchhoff's laws. An example of a simple bifurcation is shown in Fig. 4.2 b. For this bifurcation, the following applies:

- $p_1^{\mathrm{out}} = p_2^{\mathrm{in}} = p_3^{\mathrm{in}}$
- $q_1^{\mathrm{out}} = q_2^{\mathrm{in}} + q_3^{\mathrm{in}}$

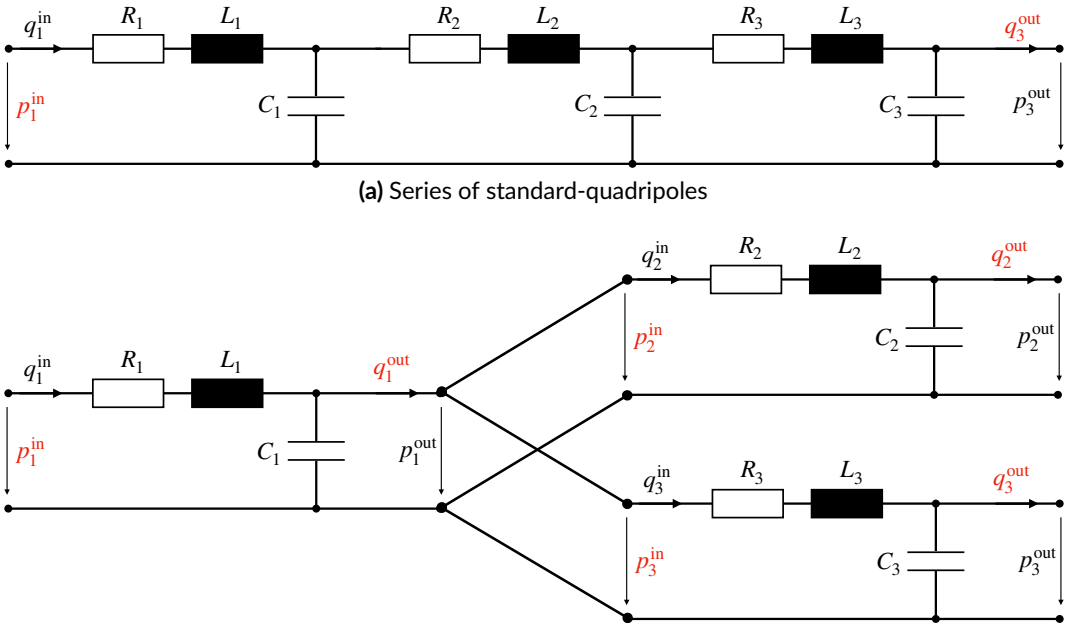

(a) Series of standard-quadripoles

(b) Bifurcating vessels

Figure 4.2: A too long segment (cf. 4.11) can be represented by a series of standard-quadripoles (a) and branching vessels can be modeled using Kirchhoff's laws (b).

Alternative Discretization

In the Avolio model [22], the arterial anatomy has a tree structure. The macroscopic whole body arterial system can be considered as an acyclic graph and the use of standard-quadripoles is sufficient to model arterial blood flow. However, the modeling of a more complex arterial anatomy includes the consideration of ring structures, where the boundary conditions for the input variables of the standard-quadripoles are not met. Extending the Avolio model with the CoW, Schwarz et al. solved this problem with the use of different variations in the standard-quadripole aiming at a closed representation of the entire system in the state space [120]: Schwarz et al. considered three more quadripoles with respective boundary conditions for flow and pressure and proofed that all variations are a discretization of the same transmission line model [121].

Inverse-Quadripole

For the inverse-quadripole, the input flow q^{in} and the output pressure p^{out} are the boundary conditions. The equivalent circuit is depicted in Fig. 4.3 a and the corresponding differential equations are:

$$\begin{aligned} \frac{\mathrm{d}p^{\text{in}}}{\mathrm{d}t} &= \frac{1}{C} \cdot \left(q^{\text{in}} - q^{\text{out}}\right), \\ \frac{\mathrm{d}q^{\text{out}}}{\mathrm{d}t} &= -\frac{R}{L} \cdot q^{\text{out}} + \frac{1}{L} \cdot \left(p^{\text{in}} - p^{\text{out}}\right). \end{aligned}$$

π-Quadripole

The equivalent circuit of the π-quadripole is depicted in Fig. 4.3 b. It is described by a third order system. Solving the respective differential equations needs the knowledge about the boundary conditions for the input flow q^{in} and the output flow q^{out}:

$$\begin{aligned} \frac{\mathrm{d}p^{\text{in}}}{\mathrm{d}t} &= \frac{2}{C} \cdot \left(q^{\text{in}} - q^{\text{RL}}\right), \\ \frac{\mathrm{d}p^{\text{out}}}{\mathrm{d}t} &= \frac{2}{C} \cdot \left(q^{\text{RL}} - q^{\text{out}}\right), \\ \frac{\mathrm{d}q^{\text{RL}}}{\mathrm{d}t} &= -\frac{R}{L} \cdot q^{\text{RL}} + \frac{1}{L} \cdot \left(p^{\text{in}} - p^{\text{out}}\right), \end{aligned}$$

where q^{RL} is the current flowing into the resistance and inductance. Due to its boundary conditions, the π-quadripole is suitable as a root segment. It was used as the first segment of the hemodynamics model where the heart is feeding blood into the system.

T-Quadripole

The equivalent circuit of the T-quadripole is depicted in Fig. 4.3 c. It is also described by a third order system. The input pressure p^{in} and the output pressure p^{out} are the respective boundary conditions:

$$\begin{aligned}
\frac{\mathrm{d}p^{\mathrm{C}}}{\mathrm{d}t} &= \frac{1}{C} \cdot \left(q^{\text{in}} - q^{\text{out}}\right), \\
\frac{\mathrm{d}q^{\text{in}}}{\mathrm{d}t} &= -\frac{R}{L} \cdot q^{\text{in}} + \frac{2}{L} \cdot \left(p^{\text{in}} - p^{\mathrm{C}}\right), \\
\frac{\mathrm{d}q^{\text{out}}}{\mathrm{d}t} &= -\frac{R}{L} \cdot q^{\text{out}} + \frac{2}{L} \cdot \left(p^{\mathrm{C}} - p^{\text{out}}\right),
\end{aligned}$$

where p^{C} is the pressure loss due to the capacity. Using the T-quadripole, the input and output pressure must be given. Therefore, the T-quadripole was used to model the SLCs (cf. Sec. 4.2.5).

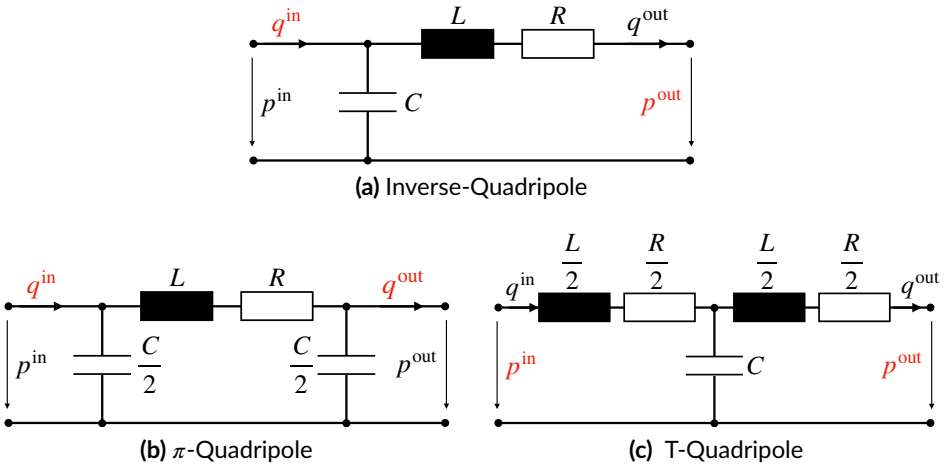

Figure 4.3: Different possibilities for the discretization of the transmission line. The corresponding input boundary conditions are marked with red color.

Summarizing, the different variants of the quadripoles cover all possible constellations of boundary conditions.

4.1.3 Avolio Model

In 1980, Avolio published a transmission line model including the general arterial anatomy of the human body [22]. The model is based on studies by Noordergraaf at al. [128] and contains 128 segments. The topology of the model is shown in Fig. 4.4 and the parameters of the segments are listed in Tab. A.1 in the Appendix (cf. Sec. A.1).
The root of the Avolio model is the ascending aorta (segment 1). From the initial segment, Avolio's model spreads into a tree structure down to the smallest considered vessels (diameter

$\approx 1\,\text{mm}$). These smallest segments have no successor segments and are referred to as terminal segments in the following. The terminal segments are followed by the resistance network of arterioles, the capillaries, and the venous system. The modeling of the terminal segments is explained in more detail in Sec. 4.4.

Due to the acyclic tree structure of the Avolio model, the entire system can be built with standard-quadripoles. However, since an input flow curve is used as boundary condition for the initial segment, the first segment was replaced by a π-quadripole (cf. Fig. 4.3 b). As input flow curve, a digitized and slightly modified flow curve [121] from Brandes et al. [26] was used, which was normalized to a cardiac output (CO) of 85 ml/s (cf. Sec. 4.4). The distribution of the CO to the terminal segments in the Avolio model is shown in Fig. 4.4 in red color.

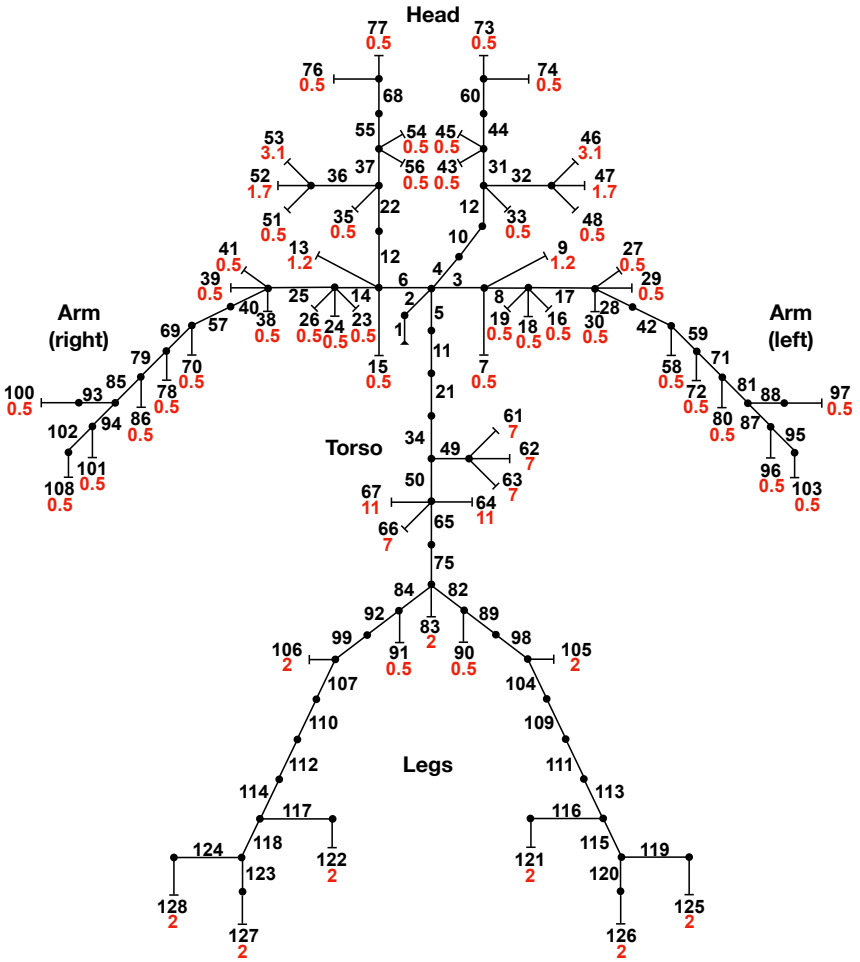

Figure 4.4: Topology of the Avolio Model [22]. The numbering of the segments is written in black and was taken from [121]. The red numbers indicate the relative percentage share of the CO and were taken from [129].

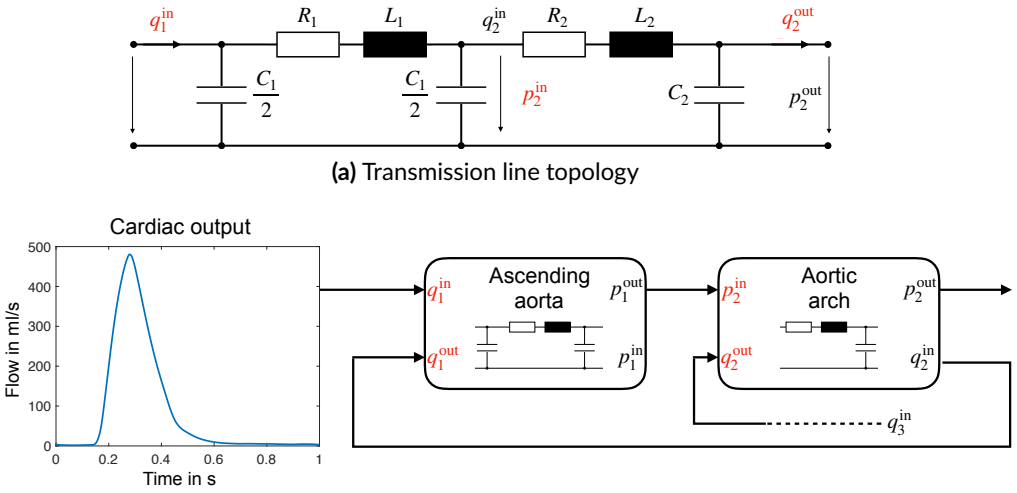

(a) Transmission line topology

(b) Modeling in *Simulink* with the used CO flow curve

Figure 4.5: First segments in the hemodynamics model.

4.1.4 Circle of Willis

In 2008, Schwarz [121] used the Avolio model to analyze resulting hypothermic conditions induced by the heart-lung machine in operations. For this purpose, Schwarz integrated the CoW in the Avolio model and evaluated different branching configurations. Fig. 4.6 shows the topology of Schwarz's extension for a complete CoW. For the integration, Schwarz added ten segments (129-138, parameters are listed in Tab. A.2) and changed the position of the vertebral arteries (segment 9 & 13). In the Avolio model, the vertebral arteries are defined as terminal segments, while Schwarz changed them to a more realistic branching, considering a merging into the basilar artery (BA) (segment 129). A detailed description of the model extension is given in [121].

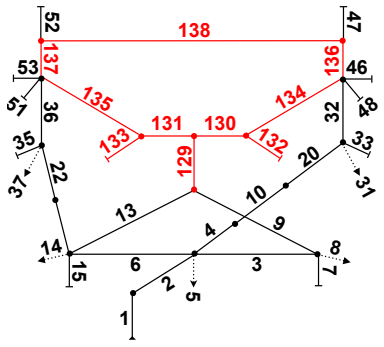

Figure 4.6: Topology of the added circle of Willis (red segments). The dotted black arrows indicate the branching of further arteries.

4.1.5 Discussion of Sec. 4.1

The transmission line approach was considered as an established way to simulate complex hemodynamics systems with reasonable computational effort. However, the simplicity of the model relies on a number of assumptions. Neglecting the influence of the branching angle in the vascular system seems particularly relevant. In this context, Schwarz discussed and analyzed this potentially problematic assumption in detail in his work [121]. He carried out 3D flow simulations in a bifurcation with variable branching angles in cooperation with the Institute for Fluid Mechanics of the University Karlsruhe. His investigations show that the geometry of the branches has no significant influence on the distribution of the flow. The division is mainly determined by the subsequent flow resistances [121].
However, for his conclusion, Schwarz gave two decisive limitations: Firstly, that the vessels before and after branching must be sufficiently long in relation to their diameter (expression of a laminar flow). Additionally, the segments must not have any drastic bends, otherwise the flow profile will shift and secondary flows will form.
These restrictions should be fulfilled at most points of the hemodynamics model, especially since the flow resistances of the modeled vessels are still significantly smaller than the peripheral terminal resistances [130–132]. Critical, however, is the anterior communicating artery (ACoA), since it is only very short but a central branch. For the modeling of very short vessels, Ciéslicki & Ciésla [130] proposed a flow resistance[1], which corresponds to the Hagen-Poiseuille resistance for low flow velocities but increases with the Reynolds number (Re), so that a nonlinear dependence on the flow velocity results. In the case of strongly curved segments, Ciéslicki & Ciésla gave a flow resistance, which additionally depends on the Dean number (De) [130]. In addition to Re, the ratio of the pipe diameter and the radius of curvature is included in De. Through their adjustments of the flow resistance, Ciéslicki & Ciésla achieved significant improvements in comparison with experimental results, especially in pathological cases with an occlusion of afferent cerebral vessels. However, their model is a static direct current (DC) model and the results cannot be transferred directly to a dynamic model. By comparing 1D and 3D flow simulations in the CoW, Moore et al. [123, 133] observed that the flow resistance in the ACoA is significantly greater than the Hagen-Poiseuille resistance and proposed a nine-fold increase. Since Moore et al. investigated pulsatile flow in contrast to Ciéslicki & Ciésla, their approach was adopted in Schwarz's modeling and also in this work for the ACoA.

4.2 Extension of the Cerebral Circulation

Despite the inclusion of the CoW, the extended model of Schwarz [121] considers only one terminal segment for each of the three main cerebral arteries (ACA, MCA, PCA) per hemisphere. This means that only one global perfusion rate could be calculated for each main

[1] derived from theoretical and experimental studies

cerebral artery. However, in the case of an acute ischemic stroke (AIS) induced by LVO, local spatial perfusion rates in the supply areas of the main cerebral arteries can differ due to the SLCs (cf. Sec. 2.3.3). Further branching of the main cerebral arteries must be taken into account for the modeling of spatially different perfusion rates within the major vascular territory of a main cerebral artery.
As with the vessels of the CoW, the anatomy of the main cerebral arteries varies greatly between individuals (cf. Sec. 4.2). An extensive literature research was carried out by Krames, Daschner, and Meißner during their respective work at the supervised student theses [134–136] to determine the structure of the main cerebral arteries, which are the most commonly described in [53, 58–60, 137].

4.2.1 Anterior Cerebral Artery

The structure of the ACA's main trunk depends on the shape of the callosomarginal artery (CmA) (cf. Sec. 2.3.2) [138]. Perlmutter et al. [56] identified two general ACA types: The typical and most common case is a branching of the A1 segments into the CmA and pericollosal arteries, which is referred to as a "typical ACA" in the following. The second ("atypical") case includes no CmA or only a small one with almost no cortical branches [56]. Following the classification of Perlmutter et al., these two variations of the ACA were implemented (typical & atypical). The topology of the segments is shown in Fig. 4.7 a and Fig. 4.7 b. In literature, various data about segment lengths for the main trunk of the ACA can be found [53, 56, 138]. To model the ACA segments, data were taken from the most recent and the most homogeneous studies: For the outer artery diameters, values proposed by Cilliers [59] were used. For the distances between the branching of the cortical branches, results by Stefani et al. [53] were used. Due to lack of literature data, no distinction between right and left hemisphere was made. The parameters of the segments can be found in Tab. A.3 and Table. A.6.

4.2.2 Middle Cerebral Artery

The MCA is the largest of the three main cerebral arteries and therefore also the most precisely described in literature. In 70 unfixed brain hemispheres from 35 brains, Umansky et al. [58] studied the lengths of the proximal MCA segments (M1 and M2 segments), their outer diameters, and the distance between the branching of the cortical branches. In addition, they identified the two most typical MCA shapes: The most common shape with a probability of occurrence of $\approx 64\%$ was a bifurcation of the M1 segment into superior and inferior M2 segments. The second most common shape found by Umansky et al. was a trifurcation into superior, middle and inferior M2 segments (cf. Sec. 2.3.2). Following Umansky's classification, a distinction was made between bifurcation and trifurcation for the MCA. Additionally, differences in the left and right hemisphere were considered. The resulting topology of the

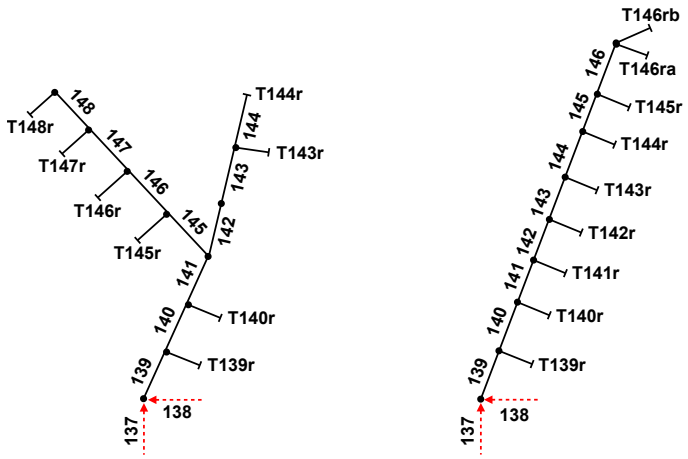

(a) Typical CmA **(b)** Absent CmA

Figure 4.7: Topology of the ACA: The figure shows the topologies for the right ACA as no differentiation between left and right hemisphere was made. If the AC has a typical CmA, it was defined as 'typical'. If the ACA has an absent CmA, it was defined as 'atypical'.

four different MCA shapes can be seen in Fig. 4.8. The parameters of the segments can be found in the Tables A.4, A.7.

4.2.3 Posterior Cerebral Artery

The PCA is the smallest main cerebral artery and therefore also the least described in literature. In 1978, Zeal & Rhoton [60] examined the PCA in 50 brain hemispheres. Independent of the hemisphere, Zeal & Rhoton identified one most common shape of the PCA, which was present in $\approx 44\%$ of the analyzed hemispheres. Furthermore, they measured the lengths and radii of the segments in the main trunk and the distance between the branching of the cortical segments. Their work was used to implement a model of the PCA. The topology was used in both hemispheres and is depicted in Fig. 4.9. The parameters of the segments can be found in the Tab. A.5 and Tab. A.8.

4.2.4 Cortical Branches

For the terminal cortical segments of the main cerebral arteries, no reliable measured values for the length and the radii could be found in literature. Therefore, the "*Brain Vascular Database*" [139] was used, which contains 61 digitally reconstructed artery trees from 3 T MR images. The database was founded by Wright et al. [139], who traced vessels in images of magnetic resonance angiography (MRA). The vessels are approximated as a series of interconnected tapered cylinders, quantified by their position, diameter and link to the previous node. In the database, the ACoA is not reconstructed and each segment is adjacent to a

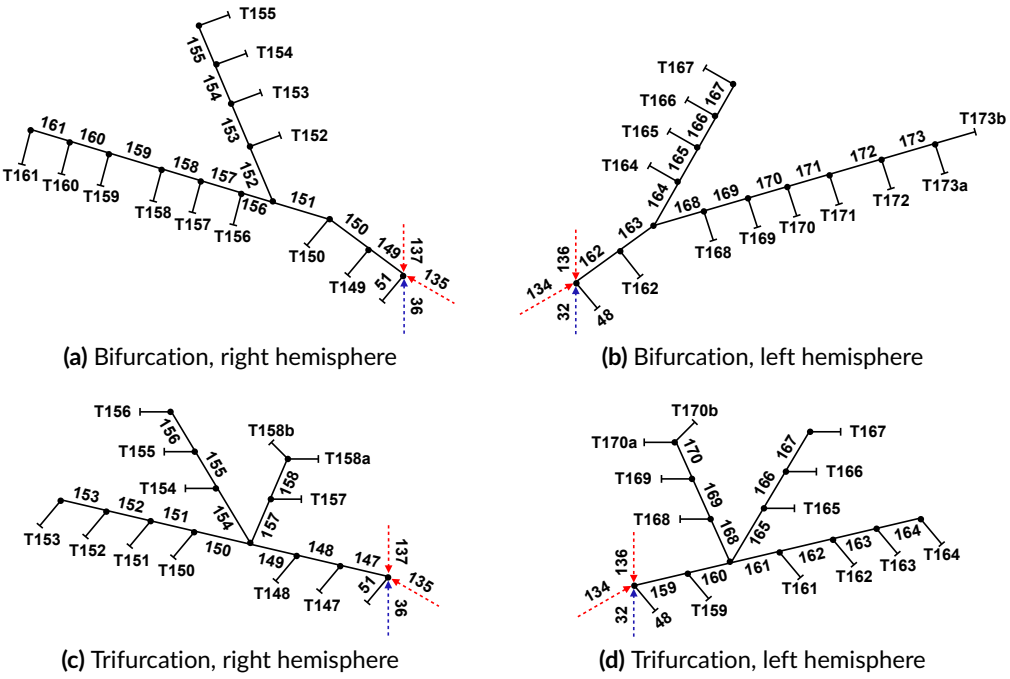

(a) Bifurcation, right hemisphere

(b) Bifurcation, left hemisphere

(c) Trifurcation, right hemisphere

(d) Trifurcation, left hemisphere

Figure 4.8: Different considered topologies of the MCA.

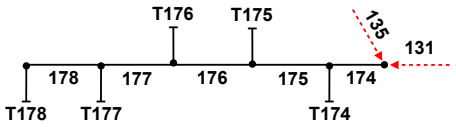

Figure 4.9: Topology of the PCA. No distinction was made between left and right hemisphere.

maximum of two succeeding segments [139]. As a consequence, every tree in the data base can be interpreted as a directed acyclic and binary graph, which is stored in an ASCII file in the swc-format [140]. The trees in the database are labeled using seven different classes: one class comprising arteries belonging to the CoW (left & right internal carotid artery (ICA), BA and left & right posterior communicating artery (PCoA)), the other classes represent the left and right main cerebral arteries ACA, MCA and PCA.

One tree of the 61 trees in the database was not considered for the parameter extraction due to misalignment compared to the other 60 trees. The other trees were converted into *VTK* files [141] by approximating the cylindrical segments with polygons of degree 20.

For the extraction of the radii and lengths of the cortical branches, the artery trees were processed in three steps, which are explained in more detail in the following paragraphs. Fig. 4.11 shows an overview of the extraction process.

The basic idea was to segment all trees in the database in order to identify the cortical branches that were considered in the anatomies modeled in the hemodynamics model (cf. Sec. 4.2). For this purpose, the trees were first aligned with the coordinate system of the "*Colin 27*"

geometry [142] (cf. Sec. 5.2). In a second step, the trees were classified for each hemisphere individually according to the above described anatomies (typical / atypical ACA, bi- / trifurcating MCA). Subsequently, surface maps showing the distribution of the perfusion regions of the main cerebral arteries on the brain's cortex were used to assign the respective cortical branches in the trees.

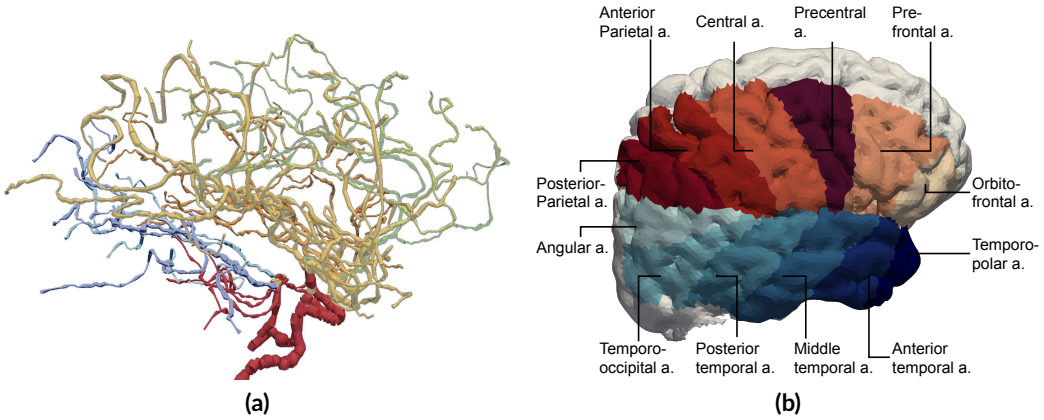

Figure 4.10: (a) Exemplary cerebral arterial tree from the Brain Vasculature Database [139]. The colors represent the CoW and the main cerebral arteries. (b) Surface map of the most common distribution of terminal perfusion regions of the MCA on the cortex. Classification according to [137]. The colors in (a) and (b) are unrelated.

Coordinate transformation

Before the actual segmentation was applied, a transformation of the arterial trees to the coordinate system of the *Colin27* geometry (cf. Sec. 5.2.1) was necessary as the later on used surface maps were mapped onto the brain's surface of this geometry. The following transformation was performed:

$$\vec{t} = \begin{bmatrix} 0 \\ 147 \\ -209 \end{bmatrix}, \qquad \vec{r} = \begin{bmatrix} 90 \\ -2 \\ 0 \end{bmatrix},$$

where $\vec{t}$ denotes translation (in mm) and $\vec{r}$ the rotation (in °) performed for Cartesian coordinates (x, y and z).

Classification

Since the hemodynamics model does not consider variation in the anatomy of the PCA, only the ACA and the MCA of the arterial trees in the database were classified.

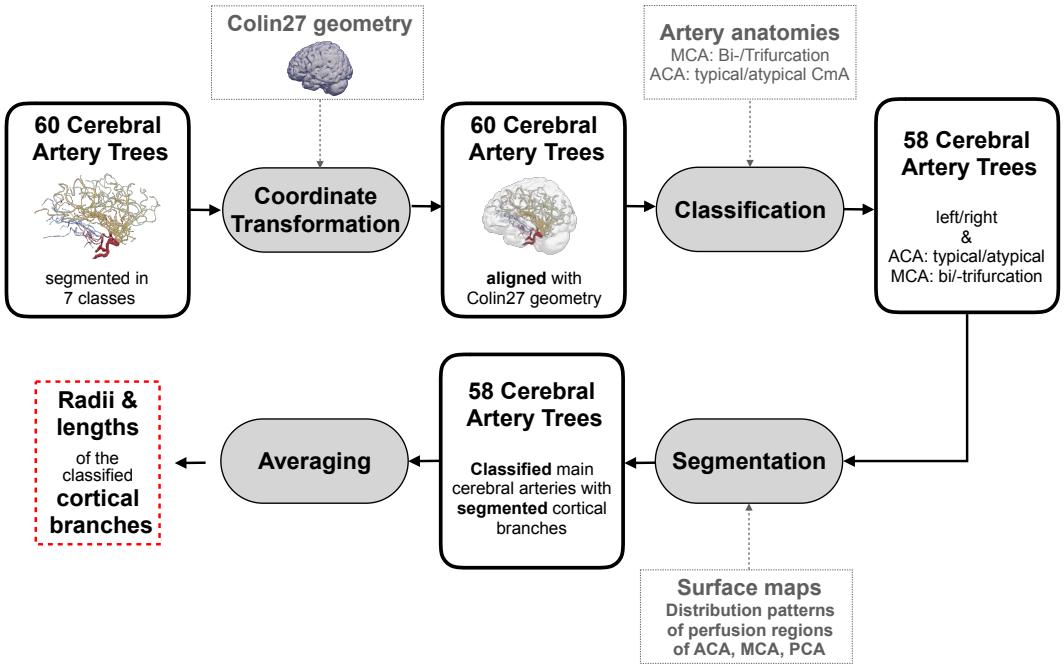

Figure 4.11: Procedure for segmentation of the cerebral artery trees.

The segmentation of the ACA was done manually due to the characteristic shape of the CmA. If an ACA in the database showed a branching of the CmA with more than two cortical branches, the ACA was classified as “typical”. If the ACA showed no branching of a CmA, or only a small CmA with a maximum of two cortical branches existed, the CmA was classified as “atypical”. Following this approach, two arterial trees of the database were left out in the following due to a bihemispheric or an exceptional shape of the ACA. The result of the classification of all 120 analyzed ACAs is listed in Tab. A.10.

Before the classification of the MCAs in the database was performed, early branches of the MCA were identified, since they have no influence on the classification. Early branches are small, short arteries emanating from the M1 segments before the MCA splits into inferior, middle or superior M2 trunks. Fig. 4.12 a shows exemplary the branching of early branches. The temporopolar (92%) and the anterior temporal (51%) artery [58] have the highest probability to be an early branch has. For the identification of the early branches, every branching point within the first 50 mm of the MCA was analyzed: If a branching artery has no more than three leaves, it was considered to be an early branch. If a branch has more than three leaves, it was handled as a potential main trunk (M2 segment) of the MCA. To evaluate a possible mono-, bi-, tri- or tetrafurcation, an automatic classification was implemented by interpreting the MCA as an acyclic, directed and binary graph: The first branching of the main trunk was considered to be the branching point of two sub trees (A & B). For both resulting sub trees, the next branching point was searched and the resulting four sub-sub trees (I-IV) were analyzed (cf. Fig. 4.12 b) regarding two criteria: Firstly, the number of leaves per sub-sub tree (n_I-n_{IV}) and second the distance between the origin node of the sub-sub tree and the

node of the first main branching (d_1 & d_2) were evaluated. Analyzing these two parameters of the four sub-sub trees (cf. Fig. 4.13), threshold values for the parameters were determined. If a sub-sub tree had three or more terminal leaves and the distance between its origin and the first main division was smaller than 6 mm, it was considered a valid "furcation". These values were chosen aiming at a proportion of around 2/3 bifurcations, which is in accordance with literature values [58, 59].
The results of the classification for the MCAs are listed in Tab. A.10 while the respective schematic examples for a mono-, bi-, tri- or tetrafurcation are depicted in Fig. 4.13.

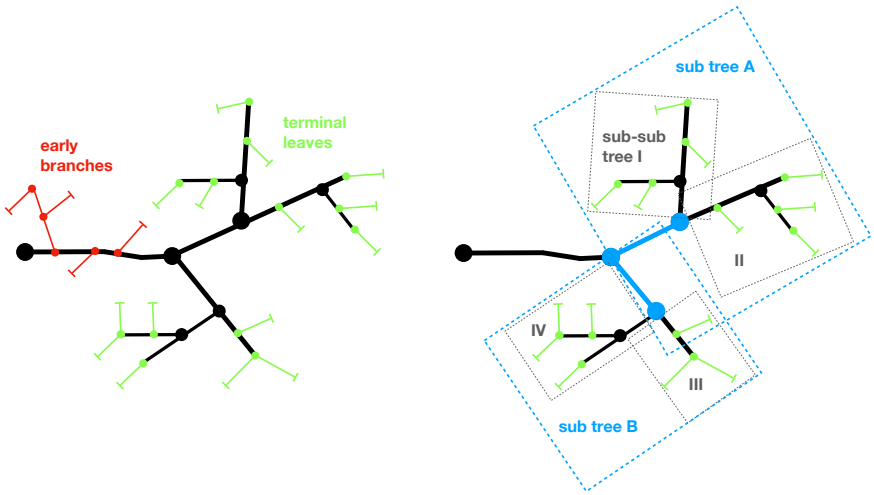

(a) Early MCA branches

(b) The MCA was split into two sub trees (blue dashed boxes A & B) and four sub-sub trees (gray dashed boxes I-IV)

Figure 4.12: Classification of the MCA into mono-bi-tri- or tetrafurcation.

Labeling

For the segmentation of the cortical branches, reference surface maps from literature were used showing the distribution of the terminal perfusion regions of the main cerebral arteries on the brain's cortex. Surface maps of Gibo et al. [137] were used for the MCA, maps of Perlmutter et al. [56] for the ACA, and maps of Zeal et al. [60] for the PCA. The surface maps are different for the left and right hemisphere and Perlmutter et al. additionally considered the variation for the ACA considering an absent CmA or a present CmA with cortical branches. These color maps from literature were mapped manually onto the surface of the "*Colin27*" geometry using the software *Blender* (version 2.79) [143]. The transferred color map of the right MCA is depicted exemplary in Fig. 4.10 b.

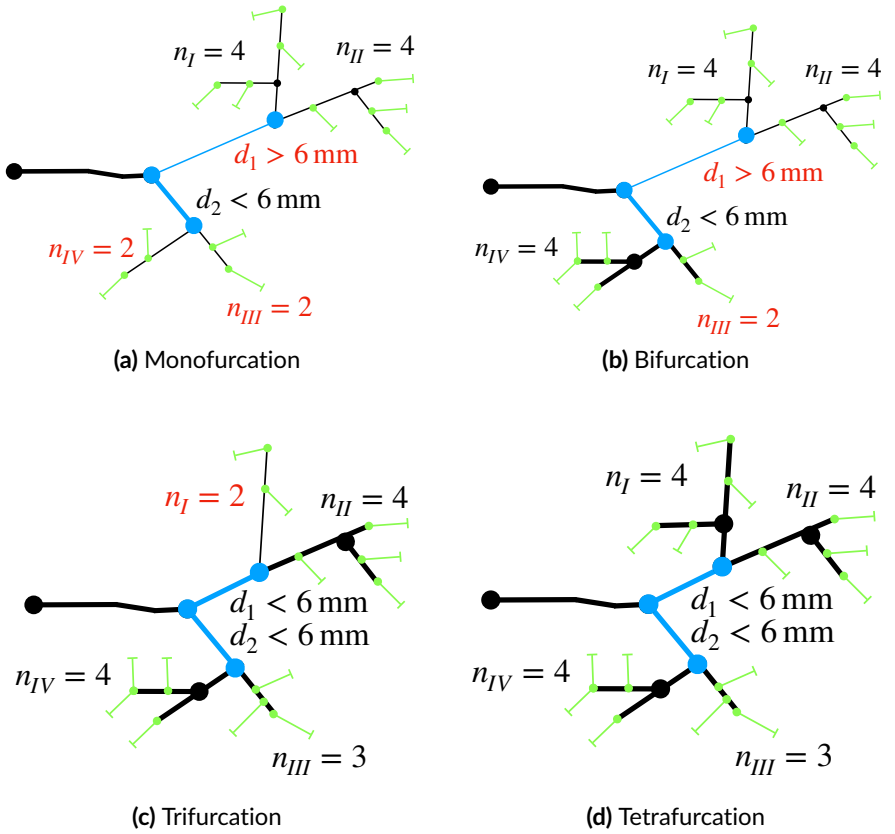

(a) Monofurcation **(b)** Bifurcation

(c) Trifurcation **(d)** Tetrafurcation

Figure 4.13: Possible classifications for the MCA.

Different sizes of the arterial trees were equalized by scaling all artery trees linearly to the bounding box of the brain before the cortical branches in the arterial trees were finally labeled. For the labeling, nearest neighbor mapping was used to find the closest cortical point on the map for each end point of an artery in an arterial tree of the database. Subsequently, the last part of all branches (from their leaves to the next branching) were labeled according to the closest surface region found.

Discussion & Limitations of Sec. 4.2.4

The surface maps used for the labeling of the cortical branches reflect only the most common distributions of the supply regions of the cortical branches on the cortex surface. Perlmutter et al. [56] gave no quantification of the occurrence likelihood for the ACA, while Gibo et al. [137] state an occurrence likelihood of around 28% for the MCA. Zeal et al. [60] gave 44% for the PCA. However, the cerebral arterial anatomies vary between individuals, which would also result in patient individual surface maps. For the generalized model in this thesis, the cortical branches considered do not define terminal regions, but the other

way around. This means an artery ending in the MCA's temporo-occipital terminal region is considered to be a temporo-occipital artery. Therefore, differences in the surface maps could result in different resulting spatial brain temperatures. Furthermore, exceptional shapes of the main cerebral arteries, such as a bihemispheric course (cf. Sec. 4.2.4), were not considered at all. Nevertheless, the mean spatial temperature decrease would stay unaffected for the major anatomical variants.

4.2.5 Secondary Leptomeningeal Collaterals

As already explained in Sec. 2.3.3, the shape and extent of the SLCs mainly influence the remaining spatial perfusion rates in case of AIS and potentially also affect the clinical outcome [45, 62, 63, 144, 145]. In literature, most authors analyze collaterals with respect to the final infarct volume (FIV) or remaining perfusion in case of LVO. In this context, the degree of collateralization is often divided into "strong", "partial" or "poor" [144]. Due to this medical focus on leptomeningeal collateralization, only few and no recent data of collateral origin, lengths or radii was found in literature. Vander Eecken & Adams [146, 147] gave information about the origin and the end of leptomeningeal anastomoses in 1953 and 1960. Their work was used to include seven SLCs per hemisphere (one between the ACA and the PCA, three between the ACA and the MCA and three between the PCA and the MCA). Due to lack of data, the inner radii of the SLCs were calculated as the mean value of the radii of the connected cortical segments and the lengths were calculated as the sum of the lengths of the connected cortical segments. In Tab. 4.1 and in Sec. A.3.2, Tab. A.9, the parameters of the added ipsilateral SLCs and the connected segments are listed.

Table 4.1: Added ipsilateral SLCs for Anatomy I (cf. Sec. 4.3.2) in the hemodynamics model.

Segment	Description	Connected Segments	Length (cm)	Radius (cm)	Source
179	PCA–MCA (right)	T150-T175r	27.11	0.04	[139, 146]
180	PCA–MCA (r)	T157-T176r	38.62	0.04	[139, 146]
181	PCA–MCA (r)	T160-T176r	45.45	0.04	[139, 146]
182	ACA–MCA (r)	T147r-T153	34.00	0.04	[139, 146]
183	ACA–MCA (r)	T148r-T155	41.39	0.04	[139, 146]
184	ACA–MCA (r)	T144r-T158	37.62	0.04	[139, 146]
185	PCA–ACA (r)	T144r-T176r	32.80	0.04	[139, 146]
186	PCA–MCA (left)	T168-T175l	28.36	0.04	[139, 146]
187	PCA–MCA (l)	T172-T176l	43.82	0.04	[139, 146]
188	PCA–MCA (l)	T173a-T176l	42.71	0.04	[139, 146]
189	ACA–MCA (l)	T147l-T166	39.26	0.04	[139, 146]
190	ACA–MCA (l)	T148l-T167	39.09	0.04	[139, 146]
191	ACA–MCA (l)	T144l-T171	30.91	0.04	[139, 146]
192	PCA–ACA (l)	T144l-T176l	25.10	0.04	[139, 146]

Discussion & Limitations of Sec. 4.2.5

Due to the high degree of interindividual variability in collateral circulation, precise and general information about dimensions and anatomy of the SLCs is lacking (cf. Sec. 2.3.3). Therefore, only collaterals for which reliable data could be found in literature were included in the hemodynamics model. This led to the consideration of seven ipsilateral SLCs between the main cerebral arteries per hemisphere.
Nevertheless, collateral circulation in reality is far more complex and a much finer network of secondary collateralization exists [144, 145]. This fact mainly affects resulting spatial perfusion rates, as in reality, reduced perfusion due to a LVO could result in more focal ischemic conditions (cf. Sec. 5.4.5). This fact would result in an underestimation of the resulting cooling effect in brain regions, which in reality do not suffer from ischemic conditions.

Integration into the Hemodynamics Model

The consideration of anastomoses leads to a cyclic graph for the whole cerebral hemodynamics topology. Therefore, an implementation using only standard-quadripoles was not possible for the structure of the main cerebral arteries. The flow through the SLCs is determined by the blood pressure difference between the connected main cerebral arteries. The input and output pressure was considered as boundary conditions and the collaterals were implemented using T-quadripoles (cf. Sec. 4.1.1). In Fig. 4.14, the resulting equivalent circuit of an exemplary collateral (segment 180) is shown. However, the implementation in *Simulink* (cf. Fig. 4.15) led to the problem of a fixed definition of the blood flow direction. For all SLCs implemented, the flow direction was determined in the direction to the MCA. To allow for both flow directions, a *Simulink* block was created, which sets the output collateral flow to negative values in case of a positive output flow. Thus, the integration of the SLCs was possible without changing the other standard-quadripole segments in the rest of the model.

4.2.6 Discussion & Limitations of Section 4.2

The anatomies described above for the main cerebral arteries and the SLCs cover only the most common shapes described and observed in literature. They were used to further extend the hemodynamics model and to establish a general model of the main cerebral arteries. However, since most previous studies about the main cerebral arteries have a medical focus, it was not possible to find all required parameters for blood flow modeling using the transmission line approach. Some parameters needed to be estimated, averaged or calculated:

Wall thickness: All wall thicknesses d of the main cerebral arteries' segments were calculated using their respective radii r:

$$d = \eta \cdot r. \tag{4.12}$$

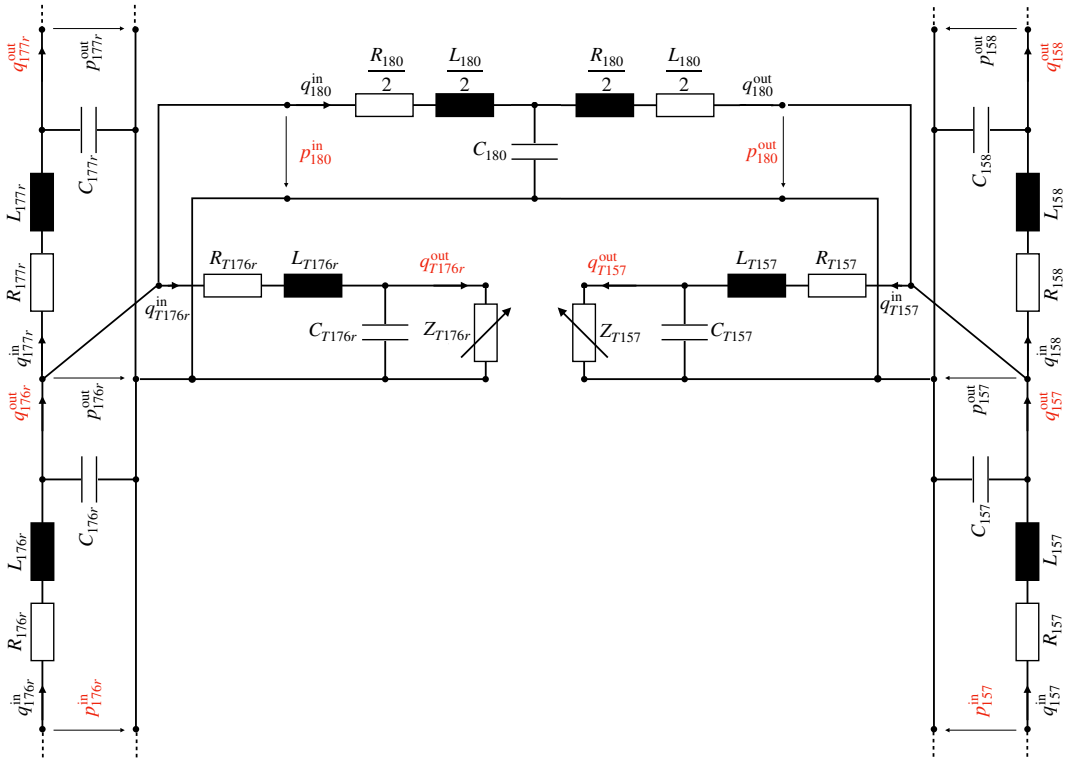

Figure 4.14: Equivalent circuit of one exemplary SLC (segment 180) connecting the MCA and the PCA.

The factor η was set to 0.25. It reflects the mean value of the relation between the radius and wall thickness for all segments in the Avolio model [22].

Young's modulus: For all main cerebral arterial segments, a value of $E = 1.6 \cdot 10^6$ Pa was chosen by analyzing the main cerebral arteries in Schwarz's model [121].

Nevertheless, a patient-specific anatomy could also be different to the anatomies considered in this thesis. However, the considered variations in the anatomy of the main cerebral arteries (Anatomy I vs. Anatomy II), the variations in the CoW, and the variations in the secondary leptomeningeal collateralization degree (cf. 4.3) cover the major anatomical variants and the corresponding results can be used to quantify the range of uncertainty coming along with the assumptions made in modeling the cerebral hemodynamics.

4.3 Variations in Cerebral Arterial Anatomy

As described in Sec. 2.3 and Sec. 4.2, the anatomy of the cerebral circulation is highly patient-specific and variable. To evaluate possible changes in case of a LVO due to varying circulation, the anatomy of the main cerebral arteries, missing segments in the CoW, and the degree of collateralization can be varied in the hemodynamics model.

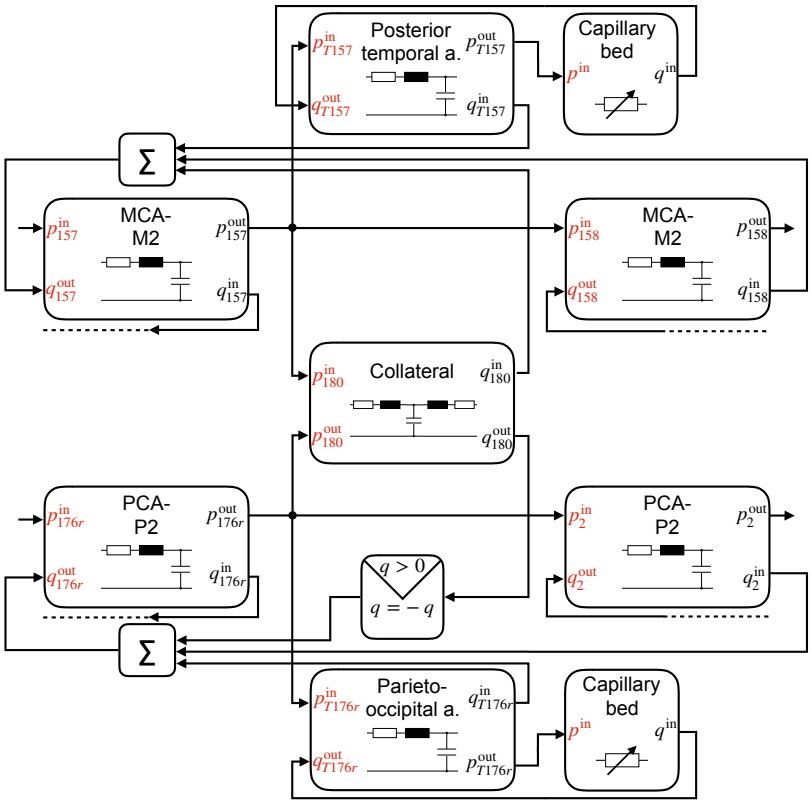

Figure 4.15: Schematic *Simulink* implementation of the SLC segment 180.

4.3.1 Variations in the Circle of Willis

As mentioned in Sec. 2.3.2, the arteries forming the CoW show great inter-individual differences and it is assumed that in about 50% of the population, one segment in the CoW is hypoplastic (very small or incompletely developed) or missing [48, 51]. An incomplete CoW could affect blood flow compensation in case of a LVO [124]. To model the effects of an incomplete CoW, the approach of Alastruey et al. was adopted, which was also used by Schwarz [121] and considers ten different variations in the CoW (hypoplastic segments are considered to be absent). The missing segments for each variation are listed in Tab. 4.2 and the respective topology of the CoW is depicted in the Appendix in Sec. A.5, Fig. A.2.

4.3.2 Shape of the Main Cerebral Arteries

Taking into account all possible combinations of the identified shapes of the main cerebral arteries, a total of eight anatomies for cerebral blood flow would result. For the cerebral temperature calculation, each anatomy would have to be coupled with an adapted brain geometry (cf. Sec. 5.2) whereas the range of possible differences in model output due to anatomical variations can be covered by considering only two different anatomies. Since

Table 4.2: Considered variations in the CoW. The respective topology of the CoW is depicted in Fig. A.2

Variation	Missing artery	Missing segment
a	ACoA	138
b	PCoA (left)	134
c	PCoA (right)	135
d	PCoAs	134 & 135
e	ACA-A1 (l)	136
f	ACA-A1 (r)	137
g	PCA-P1 (l)	130
h	PCA-P1 (r)	131
i	PCoA (l) & PCA-P1 (r)	134 & 131
j	PCoA (r) & PCA-P1 (l)	135 &130

the goal of this work is to estimate the achievable range of temperature decrease with the newly developed cooling catheter, the hemodynamics calculations were limited to these two anatomies. The first anatomy ("Anatomy I") is intended to represent the most probable branching of the main cerebral arteries and considers a bilateral MCA bifurcation and an ACA with typical branching of the CmA in both hemispheres. The second considered anatomy ("Anatomy II") is intended to contain the greatest possible difference in the anatomy compared to Anatomy I. It includes a bilateral MCA trifurcation and an ACA without a CmA in both hemispheres. The entire topology of the cerebral arterial structure is shown for Anatomy I in Fig. 4.16 and in the Appendix (cf. Sec. A.3) in Fig. A.1 for Anatomy II. In Tab. 4.3, an overview on the composition of the two anatomies is given. The table also lists the number of terminal segments for each main cerebral artery. The modeling of the hemodynamics is part of [148] and preliminary versions of the hemodynamics model were presented in [149–152].

Table 4.3: Considered shape of the main cerebral arteries (Anatomy I vs. II)

	Anatomy I		Anatomy II	
	Shape	**Number of terminal segments**	**Shape**	**Number of terminal segments**
ACA	typical	8	atypical	9
MCA (left)	bifurcating	12	trifurcating	12
MCA (right)	bifurcating	12	trifurcating	12
PCA	no variation	5	no variation	5
		$\sum = 50$		$\sum = 52$

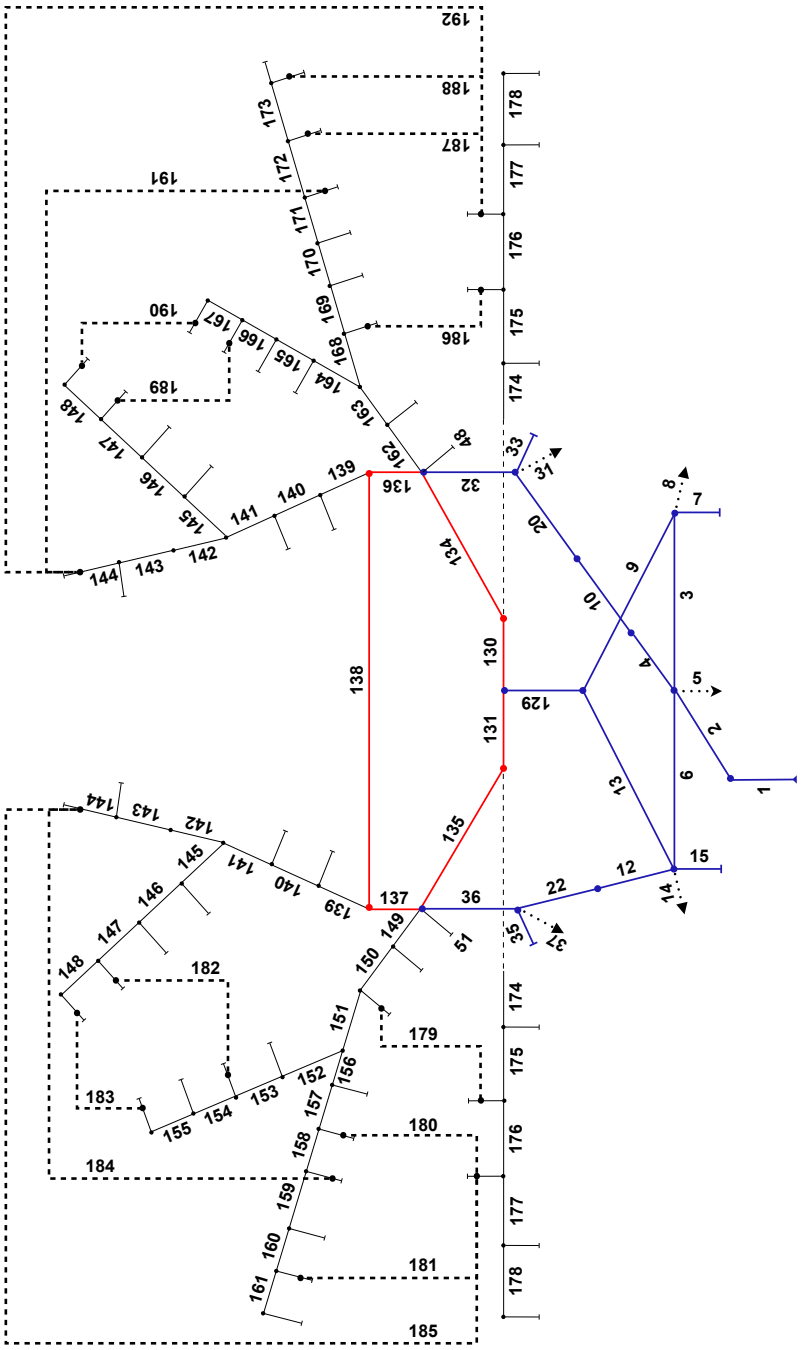

Figure 4.16: Cerebral hemodynamics model with Anatomy I (bifurcating MCA into superior and inferior M2 trunks and an ACA consisting of a typical CmA. ACA segments: 139–146, MCA segments: 147–170, PCA segments: 171–175, SLCs: 176–189. The blue segments were taken from the work of Avolio [22]. The red segments represent the CoW, which was added to Avolio's model by Schwarz et al. [120]. For the terminal segments of the cortical branches, the numbers have been omitted for a clearer presentation but can be found in the respective Tables (A.3–A.5).

4.3.3 Collateralization Degree

As mentioned in Sec. 2.3.3 and Sec. 4.2.5, secondary leptomeningeal collateralization varies between individuals and in literature the degree of collateralization is often divided into "good / strong", "partial" or "poor" [45, 144]. Since only limited data about the SLCs was found in the literature, a consideration of a more complex collateral network was not possible. To account for inter-individual differences and to represent different collateralization degrees, three variations of the original collateral radii $\tilde{r}_{\mathrm{Col},i}$ (cf. Tab. 4.1 and Tab. A.9) were implemented:

$$r_{\mathrm{Col},i} = f_{\mathrm{Col}} \cdot \tilde{r}_{\mathrm{Col},i}, \text{ with } f_{\mathrm{Col}} \in [0.85, 1, 1.15].$$

Discussion & Limitations of the Modeled Secondary Collateralization

To account for inter-individual differences in the collateral degree, the radii of the SLCs were altered uniformly for all 14 SLCs in the model. However, this approach also leads to a spatially uniform increase or decrease in collateral blood flow. In reality, however, a more pronounced spatial variance in the expression of the collaterals and thus in the resulting flow would be possible. This fact could result in more focal ischemic conditions (cf. Sec. 5.4.5), which could represent an under- or overestimation of the resulting cooling effect in affected brain regions.

4.4 Terminal Resistances

The terminal segments represent the smallest considered arteries in the hemodynamics model. Subsequent to these small arteries, a fine network of arterioles and capillaries exists (cf. Sec. 2.1.1). This capillary bed has a major influence on the TPR but cannot be modeled with single segments. Therefore, it is summarized into terminating impedances Z_i. Since the post-capillary pressure in the venules is very low (cf. Fig. 2.2), the residual venous pressure is also considered by these terminal impedances in many transmission line models [22, 113, 129]. An example of terminal segments with their terminating impedances Z_{T176} & Z_{T157} is shown in Fig. 4.14 (segments T157, T176).
On the one hand, the terminal impedances significantly determine the arterial blood pressure and the resulting mean flow into the terminal branches of the hemodynamics model. On the other hand, they influence the wave reflection behavior at the end of a transmission line. For the description of the terminal impedances, two different approaches can be found in the literature: alternating current (AC) and direct current (DC) models.

4.4.1 AC Models

AC models focus on the simulation of realistic wave reflection properties (the realistic simulation of pulse shapes) by an appropriate choice of the terminating impedance Z. For this purpose, mean-free pressure and flow signals are used. The Avolio model [22] for example is an "AC model".
For these models, the line equations form a wave equation (cf. Eq. 4.4 and Eq. 4.5). If the complex amplitudes of pressure or flow ($\hat{p}^{\text{out}}$ or $\hat{q}^{\text{out}}$) at the end of the line ($z = 0$ at the start of the line, $z = \Delta z$ at the end of the line) are known, the solution of the line equations for a harmonic excitation is:

$$\hat{p}(z) = \hat{p}^{\text{out}} \cosh(\gamma(z - \Delta z)) + \hat{q}^{\text{out}} \cdot Z_0 \cdot \sinh(\gamma(z - \Delta z)),$$
$$\hat{q}(z) = \hat{q}^{\text{out}} \cosh(\gamma(z - \Delta z)) + \frac{\hat{p}^{\text{out}}}{Z_0} \sinh(\gamma(z - \Delta z)).$$

This solution is a superposition of incoming and reflected waves:

$$\hat{p}(z) = \underbrace{\frac{1}{2}(\hat{p}^{\text{out}} + \hat{q}^{\text{out}} \cdot Z_0) \cdot e^{-\gamma(z-\Delta z)}}_{:=\hat{p}_{\text{in}}(z)\,\text{(incoming pressure)}} + \underbrace{\frac{1}{2}(\hat{p}^{\text{out}} - \hat{q}^{\text{out}} \cdot Z_0) \cdot e^{\gamma(z-\Delta z)}}_{:=\hat{p}_{\text{re}}(z)\,\text{(reflected pressure)}}$$
$$\hat{q}(z) = \underbrace{\frac{1}{2}(\hat{q}^{\text{out}} + \hat{p}^{\text{out}} \cdot Z_0) \cdot e^{-\gamma(z-\Delta z)}}_{:=\hat{q}_{\text{in}}(z)\,\text{(incoming flow)}} + \underbrace{\frac{1}{2}(\hat{q}^{\text{out}} - \hat{p}^{\text{out}} \cdot Z_0) \cdot e^{\gamma(z-\Delta z)}}_{:=\hat{q}_{\text{re}}(z)\,\text{(reflected flow)}}.$$

Thus a reflection factor $\Theta(z)$ can be calculated, which is defined as the quotient of the complex amplitudes of the reflected and incoming wave:

$$\Theta(z) = \frac{\hat{p}_{\text{re}}(z)}{\hat{p}_{\text{in}}(z)} = \frac{\hat{q}_{\text{re}}(z)}{\hat{q}_{\text{in}}(z)} = \frac{\hat{p}^{\text{out}} - \hat{q}^{\text{out}} \cdot Z_o}{\hat{p}^{\text{out}} + \hat{q}^{\text{out}} \cdot Z_o} e^{2 \cdot \gamma(z-\Delta z)}.$$

Together with the terminating impedance $Z = Z^{\text{term}}$ at the end of the transmission line, Θ^{term} is:

$$\Theta^{\text{term}} = \frac{Z^{\text{term}} - Z_0}{Z^{\text{term}} + Z_0}.$$

In literature, different values for Θ can be found (0.1-0.8) [22, 26, 153]. Typically, two types of terminating impedances are used: A real terminating resistance R^{term} with a constant reflection factor or a three element Windkessel (R-L-C-segment) with a frequency-dependent reflection factor. In [121], more information about AC models and how to chose Z^{term} is provided.

4.4.2 DC Models

In contrast to AC models, a realistic mean flow rate and not the shape of the flow or pressure curves is the main focus of DC models. Since in this work, the hemodynamics model is used to determine mean blood perfusion rates of brain tissue, an accurate mean flow calculation is essential. Therefore, a DC approach is used for the hemodynamics model in this thesis.
In DC models, the terminating impedance is a resistance whose value determines the share of CO for each terminal segment as well as a realistic TPR. If the TPR, the CO, and the share of CO for each terminal segment are given, the corresponding terminating resistances R^{term} can be calculated.

Discussion & Limitations of DC Models

Choosing a DC model leads to a mismatch between the characteristic impedance and the terminal resistance and thus to unphysiological reflections at the end of the terminal segments resulting in excessive oscillations [125]. For an unfiltered input flow curve [26], Schwarz et al. noticed an exaggeration of the higher frequency harmonics due to the strong reflections at the end of the terminal segments in a spectral analysis of the pulsatile pressure and flow curves of their pure DC model [129]. A low-pass filtering of the input flow curve using a first order Butterworth filter with five times the heart rate as the cut-off frequency (5 Hz) resulted in suitable flow and pressure curves [121]. This filtered and slightly modified (for steady continuation) input flow curve of the CO (cf. Fig. 4.5 b) was also used in this thesis.
Normally, this reference flow curve shows a reflux at the end of systole, which continues until the aortic valve is closed. However, this characteristic feature is lost due to the low pass filtering.

4.4.3 Calculation of Terminating Resistances

As mentioned above, if the TPR and the share of CO for each terminal segment are given, the corresponding value of the terminating resistances can be calculated. Therefore, mean flow rates are specified and the model is considered to be a resistance network. For hemodynamics models with a tree structure, a simple approach based on the application of Ohm's law along the individual branches of the arterial tree can be used. Each branching point is considered as a node for which the voltage drop can be calculated by knowing the TPR, the CO and the corresponding segments' resistances. Fig. 4.17 shows an exemplary calculation of the terminating resistances for a tree with three leaves: For a known CO $:= q_0$ and a known TPR, the mean arterial pressure (MAP) p_0 can be calculated using Ohm's law (Eq. 2.1). Subsequently, the pressure drop for each node can be calculated recursively:

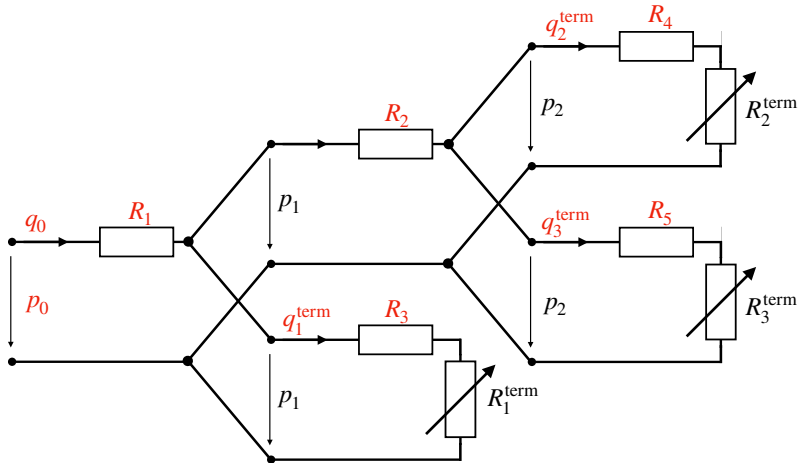

Figure 4.17: Example of an acyclic tree for the calculation of the terminating resistances R_i^{term}. The red parameters have to be defined boundary conditions.

$$p_1 = p_0 - q_0 \cdot R_1,$$
$$\rightarrow p_2 = p_1 - q_1 \cdot R_2,$$

where q_1 is the sum of the terminal currents for the leaves connected to the respective node. By the definition of the percentage share of the CO for each terminal segment (cf. Fig. 4.4), the terminating resistances can be calculated respectively:

$$q_1^{\text{term}} = \frac{p_1}{R_3 + R_1^{\text{term}}},$$
$$\vdots$$
$$\rightarrow R_1^{\text{term}} = \frac{p_1}{q_1^{\text{term}}} - R_3,$$
$$\rightarrow R_2^{\text{term}} = \frac{p_2}{q_2^{\text{term}}} - R_4,$$
$$\rightarrow R_3^{\text{term}} = \frac{p_2}{q_3^{\text{term}}} - R_5.$$

Following the tree structure of the resistance network, any terminating resistance $R_{\text{i}}^{\text{term}}$ can be calculated as follows:

$$R_{\text{i}}^{\text{term}} = \frac{p_{\text{i}}}{q_{\text{i}}^{\text{term}}} - R_{\text{i}}, \tag{4.13}$$

where p_{i} is the pressure in front of the terminal segment i and R_{i} is the respective resistance of the terminal segment.

Schwarz [121] used this basic approach to calculate terminal resistances with a graph-based method for the whole resistance network in his extended Avolio model. However, since the

underlying calculation is designed for acyclic systems, Schwarz had to transform the resistor network into a tree structure by combining resistors and applying the star-delta transformation due to his cyclic model extension with the CoW [121].
However, by considering 14 SLCs, the cerebral hemodynamics model used for this work shows significantly more ring structures than the extended model of Schwarz. Therefore, a transfer into a tree structure is not possible and thus also not the calculation of all terminating resistances using the scheme described above. In this work, the terminating resistances for the cerebral arterial model were calculated using a nodal potential method.

Nodal Potential Method

This method is based on the introduction of potentials p_i for each node i. Fig. 4.18 shows a simple electric circuit for which the method is explained exemplary. Subsequently, a general matrix-based formulation is introduced.
The first step is to introduce a reference potential p_0, which is set to 0 (cf. Fig. 4.18).

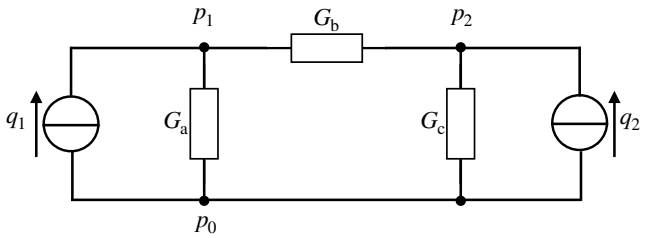

Figure 4.18: Exemplary electric circuit for the nodal potential method.

In the second step, node equations are introduced using conductances $G = \frac{1}{R}$:

$$\begin{aligned} p_1: \quad & 0 = q_1 - (p_1 - p_0) \cdot G_a - (p_1 - p_2) \cdot G_b, \\ p_2: \quad & 0 = q_2 - (p_2 - p_0) \cdot G_a + (p_1 - p_2) \cdot G_b. \end{aligned}$$

These equations can be used to determine a system of equations:

$$\begin{aligned} q_1 &= (G_a + G_b) \cdot p_1 - G_b \cdot p_2 \\ q_2 &= (G_b + G_c) \cdot p_2 - G_b \cdot p_1 \end{aligned}$$

For the given system, the solution follows:

$$p_1 = \frac{(G_b + G_c) \cdot q_1 + G_b \cdot q_2}{G_a G_b + G_b G_c + G_a G_c},$$

$$p_2 = \frac{(G_a + G_b) \cdot q_2 + G_b \cdot q_1}{G_a G_b + G_b G_c + G_a G_c}.$$

With the system of equations, a general matrix equation can be formulated for the system:

$$\begin{bmatrix} (G_\mathrm{a}+G_\mathrm{b}) & -G_\mathrm{b} \\ -G_\mathrm{b} & (G_\mathrm{b}+G_\mathrm{c}) \end{bmatrix} \cdot \begin{bmatrix} p_1 \\ p_2 \end{bmatrix} = \begin{bmatrix} q_1 \\ q_2 \end{bmatrix}. \tag{4.14}$$

The following observations can be made:

1. The diagonal elements are the sum of all coupling coefficients belonging to a node.
2. The other matrix elements are the sum of the conductance between the respective nodes with reversed sign.
3. The term on the right side is the sum of all source currents flowing into the respective node (influx has a positive sign, outflux a negative sign).

Thus, any given circuit can be translated into a matrix equation:

$$\begin{bmatrix} G_{11} & -G_{12} & \dots & G_{1\mathrm{n}} \\ G_{21} & \ddots & & \vdots \\ \vdots & & \ddots & \vdots \\ G_{\mathrm{n}1} & \dots & \dots & G_{\mathrm{nn}} \end{bmatrix} \cdot \begin{bmatrix} p_1 \\ \vdots \\ \vdots \\ p_\mathrm{n} \end{bmatrix} = \begin{bmatrix} \sum\limits_{\text{node 1}} q_i \\ \vdots \\ \vdots \\ \sum\limits_{\text{node n}} q_i \end{bmatrix}, \tag{4.15}$$

with G_{ii} being the sum of all conductances connected to the node i, G_{ij} being the sum of conductances between the node i and j with negative sign and $\sum\limits_{\text{node i}} q_i$being the sum of all source currents (considering the correct sign) flowing into the node i.
The vector with the node potentials $\vec{p}$ can be calculated using the inversion of the conductance matrix $\mathbf{G}$:

$$\vec{p} = \vec{q} \cdot \mathbf{G}^{-1}.$$

Following this approach, the potentials for the nodes in front of a terminal segment were calculated. For the calculation, a conductance matrix $\mathbf{G}$ of size 68×68 was established for Anatomy I and of size 65×65 for Anatomy II, respectively. The value of the
TPR$= 1.2 \frac{\mathrm{mm\,Hg}}{ml/s}$ was adopted from Schulz [129], which resulted in a realistic mean atrial pressure of $\approx 100\,\mathrm{mm\,Hg}$. As the vector with the node potentials $\vec{p}$ contains the needed potentials in front of the terminating resistances, the terminating resistances of the cortical branches were calculated subsequently with Eq. 4.13.
For the terminal segments of the systemic body, the required values of the percentage share of the CO were adopted from the work of Schulz [129] (cf. Fig. 4.4). The required values for the terminal segments of the cortical branches, were calculated using the volumes of the terminal perfusion regions in the brain geometry (cf. Sec. 5.2.3). The exact procedure is explained in the following section.

4.4.4 Terminal Flow Rates for the Cerebral Cortical Segments

To ensure spatially variable blood perfusion, the "*Colin 27*" geometry, which was used for temperature calculation, was divided into "terminal perfusion regions" (cf. Sec. 5.2.3). These regions correspond to the supply regions of the terminal cortical segments in the hemodynamics models.
The volumes of GM and WM ($V_{\mathrm{GM},i}, V_{\mathrm{WM},i}$) building a terminal perfusion region i and physiological reference perfusion rates $\nu_{\mathrm{GM}}, \nu_{\mathrm{WM}}$ [119] (cf. Tab. B.1 first column) were used to calculate individual physiological reference mean flow rates $\underset{\mathrm{Ref}}{\bar{q}}_{\mathrm{Bl},i}$ into the terminal cortical branches of the main cerebral arteries:

$$\boxed{\underset{\mathrm{Ref}}{\bar{q}}_{\mathrm{Bl},i} = \sum_{j=1}^{n} \nu_{\mathrm{GM}} \cdot V_{\mathrm{GM},i,j} + \sum_{k=1}^{m} \nu_{\mathrm{WM}} \cdot V_{\mathrm{WM},i,k},} \tag{4.16}$$

where n is the number of GM parts and m the number of WM parts belonging to the terminal perfusion region i.

Discussion & Limitations of Sec. 4.4.4

Age affects the the cerebral perfusion rate. Parkes et al. [154] investigated the effect of age on cerebral perfusion rate using magnetic resonance imaging (MRI) and arterial spin labeling. The results of Parkes et al. are listed in Tab. 4.4 and Tab. 4.5 and were used to establish the following formula for age dependent perfusion rate of GM and WM for a man:

$$\upsilon_{\mathrm{GM}}(t) = 58 \frac{\mathrm{ml}}{\mathrm{min} \cdot 100\mathrm{ml}} \cdot (1 - 0.0045)^{|t - 44\,\mathrm{y}|},$$
$$\upsilon_{\mathrm{WM}}(t) = 23 \frac{\mathrm{ml}}{\mathrm{min} \cdot 100\mathrm{ml}} \cdot (1 - 0.0034)^{|t - 44\,\mathrm{y}|},$$

where t is the age of the man in years.
For a 60-years old man, the following can be derived:

$$\upsilon_{\mathrm{GM}}(60\,\mathrm{y}) \approx 53.96 \frac{\mathrm{ml}}{\mathrm{min} \cdot 100\mathrm{ml}} \approx 8.99 \cdot 10^{-3} \frac{1}{\mathrm{s}},$$
$$\upsilon_{\mathrm{WM}}(60\,\mathrm{y}) \approx 24.28 \frac{\mathrm{ml}}{\mathrm{min} \cdot 100\mathrm{ml}} \approx 4.05 \cdot 10^{-3} \frac{1}{\mathrm{s}}.$$

However, since no age-dependent values have been specified by Parkes et al. for other tissue and the calculated values are in good accordance with the perfusion rates in the collection of the IT'IS foundation [119], the values of the IT'IS foundation were used for the calculation to consider a uniform collection of thermal properties used for temperature calculation.

Table 4.4: Measured mean perfusion rates (in $\frac{\text{ml}}{\text{min}\cdot 100\text{ml}}$) [154].

Tissue	**Man** (mean age: 44)	**Woman** (mean age: 39)
GM	58 ± 13	68 ± 10
WM	23 ± 3	25 ± 5
Total brain	53 ± 10	62 ± 7

Table 4.5: Annual mean change in perfusion rate (in %) [154].

Tissue	**Man** (mean age: 44)	**Woman** (mean age: 39)
GM	-0.45	13
WM	0.34	8.8
Total brain	-0.37	13

4.4.5 Autoregulation

According to Sec. 2.2, local cerebral flow is regulated by the metabolic autoregulation and the Bayliss effect. Since this work is intended to investigate the effects of LVO on cerebral blood flow conditions, the Bayliss effect on cerebral vessels is of primary importance. Following Schwarz's approach [121, 155], the autoregulation was modeled for the cerebral arteries using a separate controller for each terminating resistance. The controller regulates the mean terminal flow rate considering a specified reference flow rate (Eq. 4.16) by varying the size of the terminating resistance (cf. Fig. 4.19) within a physiological range.

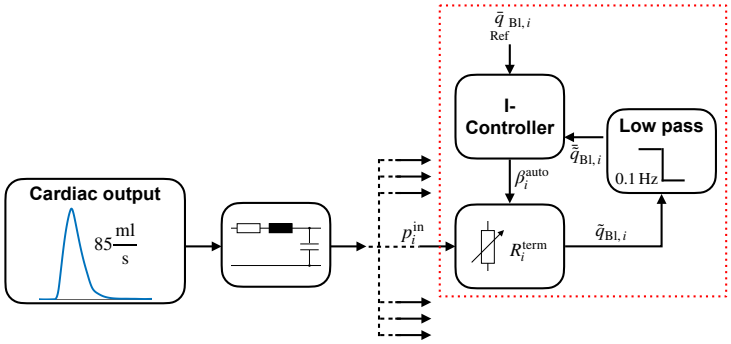

Figure 4.19: Schematic for the cerebral autoregulation (red dashed box) of the terminating resistance R_i^{term}.

The terminal flow into a terminating resistance i is:

$$\tilde{q}_{\text{Bl},i} = \beta_i^{\text{auto}} \frac{p_i^{\text{in}}}{R_i^{\text{term}}},$$

which is controlled by an I-Controller:

$$\frac{\mathrm{d}\beta_i^{\mathrm{auto}}}{\mathrm{d}t} = -K \cdot \left(\bar{\tilde{q}}_{\mathrm{Bl},i} - \underset{\mathrm{Ref}}{\bar{q}}_{\mathrm{Bl},i} \right),$$

where, $\bar{\tilde{q}}_{\mathrm{Bl},i}$ is the mean terminal flow into a terminating resistance i and K is the amplification factor. The amplification factor was set to $0.1\ \frac{1}{\mathrm{ml}}$ by Schwarz et al. [121], which resulted in a realistic time constant for its response behavior. For the determination of the amplification factor, so-called "Newell-curves" were used. In a clinical study by Newell et al. [156], a sudden drop in arterial pressure (from ≈ 100 mm Hg to ≈ 80 mm Hg) was initiated and the time course of the flow in the MCA (representing the autoregulation response) was measured (cf. Fig. 4.20 a).

In addition to the dynamic response, a realistic dependence between the arterial pressure and the flow in the range of the physiological vasomotion was determined: On the one hand side, the limit of vessel dilatation is reached for too low arterial pressure and a further decrease in pressure cannot be compensated. This leads to a reduction in flow (cf. Fig. 4.20 b). On the other hand, the maximum constriction of the vessels is reached for too high arterial pressure and the flow increases above its physiological range.

For the determination of an adequate range of β^{auto}, Schwarz used a static reference curve of Guyton et al. [24] (cf. Fig. 4.20 b). According to Guyton et al., the static curve describes the autoregulation of skeletal muscles but applies approximately to many tissue types. Therefore, it was used by Moorhead et al. [157] and Schwarz [121] for the cerebral autoregulation. The regulated pressure range extends from 75 to 175 mm Hg (cf. Fig. 4.20 b), which is equivalent to limiting $\beta^{\mathrm{auto}} \in [0.53, 1.54]$.

The resulting static regulation behavior was in good accordance with the reference curve of the cerebral autoregulation from Silbernagl et al. [20]. A more detailed description of the implemented autoregulation can be found in [121].

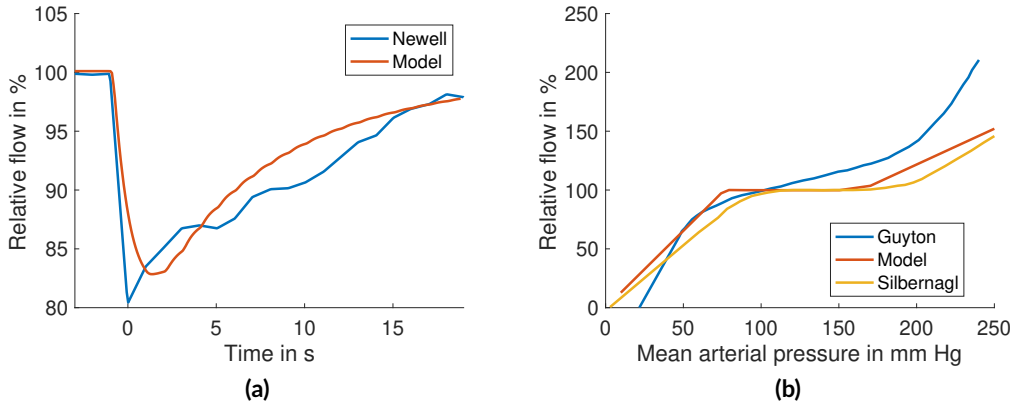

Figure 4.20: Parametrization of cerebral autoregulation: (a) dynamic Response to a sudden drop in arterial pressure (from 100 to ≈ 80 mm Hg), (b) the static behavior and the limits of vasomotion.

4.5 Simulation of Blood Flow

The developed hemodynamics model was used to calculate mean flow rates, which build the basis for the determination of cerebral perfusion rates needed for temperature calculation. The blood flow calculations were performed in *Simulink*, *MATLAB* version 2019b [158]. For a simulation time of 45 s, the ordinary differential equations (ODEs) were solved with a variable time step size[2]. After solving, the flow rates were linearly, equidistantly interpolated, and the last 5 s of simulation were extracted (autoregulation mechanisms should have been equilibrated (cf. Fig. 4.20 a)). Using the last 5 s, the mean flow rates were determined by the arithmetic mean.

4.5.1 Physiological Conditions

For both anatomies considered (Anatomy I & II), the hemodynamics model resulted in cortical blood flow rates, which were in good accordance with the target values defined using Eq. 4.16. The highest relative deviation (+2.63%) was present in the left calcarine branch of the PCA if Anatomy I was used. Fig. 4.21 shows that Anatomy II resulted generally in slightly higher relative deviations compared to the defined target values than Anatomy I (Anatomy I $\approx 0.70\%$, Anatomy II ≈ 1.15). With the exception of the flow rates in the right PCA of Anatomy I (cf. Fig. 4.21c), the flow rates were slightly higher than the target values for both anatomies. Tab. 4.6 lists the resulting summed mean flow rates into the cortical branches of the main cerebral arteries and the mean flow rates in the common carotid artery (CCA) and BA. Additionally, The table provides a comparison to measured literature values [57, 159], which is discussed in more detail below.
Due to the autoregulation, neither CoW variations (cf. Fig. 4.22 a), differences in the anatomical course of the ACA and the MCA (Anatomy I vs Anatomy II) (cf. Fig. 4.21), nor the degree of the secondary collateralization (cf. Fig. 4.22 b) had a marked effect on blood flow into the terminal cortical branches for physiological blood flow conditions without the occurrence of a LVO.

Discussion & Limitations of Sec. 4.5.1

Although the hemodynamics model results are in good accordance with the defined target values, the simulated summed flow rates in the cortical branches of the main cerebral arteries were higher ($\approx 15.4\dot{\%}$) than measured mean values in 111 subjects including healthy young (20 to 30 years) and healthy elderly (64 to 80 years) individuals using phase-contrast MRI [57]. This deviation can be explained by the structure of the hemodynamics model. Especially the inner center of the brain and the brainstem are supplied by smaller vessels (pontine arteries, anterior choroidal arteries, striate arteries (cf. Fig. 2.8 and Fig. 2.11)) in reality, which are not

[2] a variable-step (maximal step size 0.001 s) and a variable-order solver (ode15s) based on the numerical differentiation formulas (NDF) of orders 1 to 5 was used

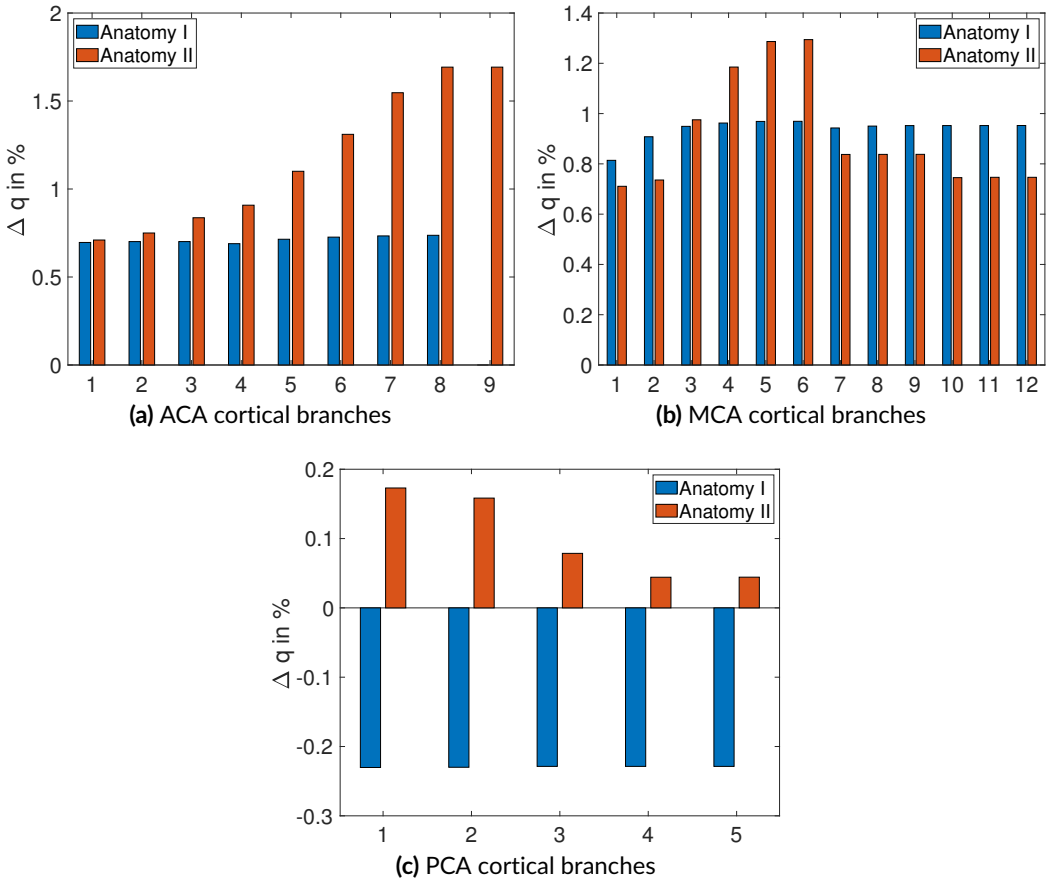

Figure 4.21: Relative deviation of the flow rates q into the cortical branches of the main cerebral arteries in the right hemisphere compared to the target values (complete CoW, no occlusion, "partial" collateralization). Note: Anatomy I only contains eight cortical branches (missing ninth blue bar in subfigure (a)).

considered in the hemodynamics model. These smaller arteries normally supply the brain tissue, which is perfused by the main cerebral arteries in the model. Therefore, the blood flow in the main cerebral arteries is higher in the model compared to the measured values. However, the accordance with the calculated target flow rates (cf. Eq. 4.16) led to realistic physiological perfusion rates (cf. Sec. 5.3.6).

Furthermore, the simulated blood flow rates in the bigger afferent arteries (CCA and BA) are in good accordance with measured values [57] (cf. 4.6). Fahrig et al. [160] state that the afferent cerebral arteries (the vertebral arteries (VAs) and the ICAs behind the branching of the ophthalmic arteries) have a total flow rate of about 11.8 ml/s in an average adult. This measurement is consistent with the value of ≈ 12.3 ml/s predicted by the hemodynamics model.

In addition to the flow in the bigger afferent cerebral vessels, the flow in the collaterals can be compared with data from literature. For physiological conditions without LVO,

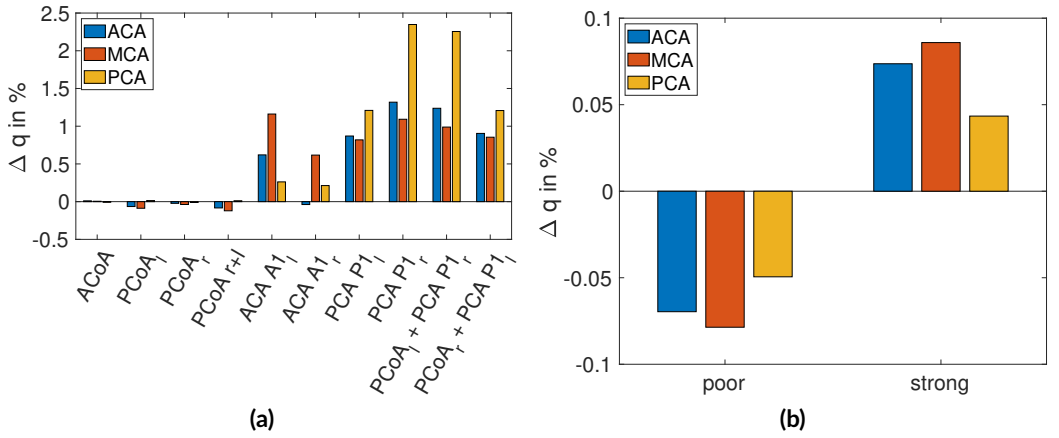

Figure 4.22: Relative deviation of flow rates q into the cortical branches of the right main cerebral arteries compared to (a) a complete CoW or (b) varying collateralization degree. ((a) Anatomy I, "partial" collateralization; (b) Anatomy I, complete CoW).

Table 4.6: Overview on simulated mean cerebral blood flow rates compared to defined target values and measured values from literature (no differentiation between left and right hemisphere was considered). All values are in ml/s.

Artery	Simulation Anatomy I / II	Target value Anatomy I / II	Literature value	Source
ACA (left)	1.7 / 1.7	1.7 / 1.7	1.43 ± 0.25	[57]
ACA (right)	1.6 / 1.6	1.6 / 1.6		
BA	2.6 / 2.7	-	2.4 ± 0.5	[57]
CCA (l)	6.8 / 6.5	-	6.0 ± 2.2	[159]
CCA (r)	7.0 / 6.7	-		
MCA (l)	3.0 / 3.0	3.0 / 3.0	2.5 ± 0.4	[57]
MCA (r)	3.2 / 3.2	3.1 / 3.1		
PCA (l)	1.2 / 1.2	1.2 / 1.2	1.0 ± 0.2	[57]
PCA (r)	1.0 / 1.0	1.0 / 1.0		

Tariq et al. [62] describe the SLCs as dormant. This is in accordance with the results of the hemodynamics model, which predicted a mean total flow close to zero ($|\bar{q}| < 0.01$ ml/s) for the SLCs and the ACoA.

4.5.2 MCA-M1 Large Vessel Occlusion

The main aim of this work was the prediction of resulting cerebral spatio-temporal temperature profiles in case of local hypothermia therapy for an AIS. To analyze the cerebral blood flow conditions in case of an AIS, an occlusion of the right, first MCA-M1 segment was considered (segment 149 in Anatomy I, respectively segment 147 in Anatomy II) as it represents the most common cause for an AIS [161].

For the implementation, the occluded segment was split into three parts [121]. Except for an adapted length, the first (proximal), and the third (distal) part were kept unchanged compared to the physiological artery parameters. Fig. 4.23 shows an exemplary occlusion of the MCA-M1 segment. The vessel occlusion was placed in the middle as a single resistor [121, 149, 162] and represents an almost complete vessel occlusion (degree $D = 0.999$) with the Hagen-Poiseuille resistance $R_{\text{occlusion}}$:

$$R_{\text{occlusion}} = \frac{8 \cdot \mu \cdot l_{\text{occlusion}}}{\pi r^4_{\text{occlusion}}} = \frac{8\mu \cdot l_{\text{occlusion}}}{\pi r_0^4 (1-D)^4}.$$

The length of the occlusion $l_{\text{occlusion}}$ was set arbitrarily to 0.7 cm. For the length of the proximal and distal segment $\Delta\tilde{z}$, the following applies:

$$\Delta\tilde{z} = \frac{l_0 - l_{\text{occlusion}}}{2},$$

where l_0 is the length of the original segment (cf. Tables in Sec. A.1-A.3).
Thus, the parameters of distal and proximal segments in the transmission line follow:

$$\tilde{L} = \frac{\rho \cdot \Delta\tilde{z}}{\pi r_0^2}, \qquad \tilde{R} = \frac{8 \cdot \mu \cdot \Delta\tilde{z}}{\pi r_0^4}, \qquad \tilde{C} = \frac{3\pi \cdot r_0^3 \cdot \Delta\tilde{z}}{2Ed}$$

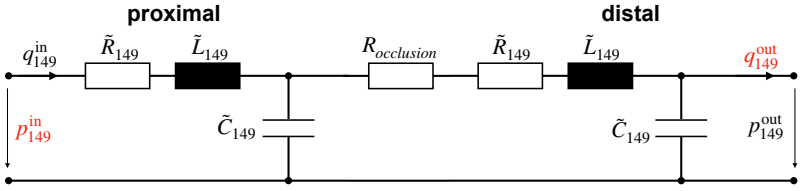

Figure 4.23: Equivalent circuit of an occlusion in the right MCA-M1 segment.

Discussion & Limitations of the Occlusion Modeling

Deposits on the vessel wall (vessel stenosis) can lead to turbulences and non-laminar flow conditions. Therefore, the use of the Hagen-Poiseuille equation to describe the flow resistance is – especially for high degrees of occlusion – only an approximation. However, this approach is used by many authors, as it is stated that the resulting deviations are tolerably small ([121, 162, 163]). Furthermore, a complete vessel occlusion, as considered in this work, changes the problem to the modeling of a terminal segment. The modeling of terminal segments is explained in more detail in Sec. 4.4.

Evaluation

The LVO in the right MCA-M1 segment resulted in a distinct change in the blood flow conditions: Due to the occlusion, the remaining flow into the cortical branches of the right MCA was reduced by ≈ 73% (cf. Fig. 4.24 a & c). It could only be provided by flow through SLCs. Therefore, the flow to the MCA through SLCs increased drastically and the flow through the SLCs from the ACA to the MCA changed its direction to the MCA (cf. Fig. 4.24 e). Although the remaining flow to vascular MCA territory was significantly lower than physiological values, it was still evenly distributed among the twelve terminal segments of the MCA (cf. Fig. 4.24c).
Furthermore, due to the occluded inflow into the MCA-M1 segment, contralateral flow through the ACoA changed its direction and was also significantly increased (cf. Fig. 4.24 f). Despite the increased contralateral ACoA flow, the mean terminal flow rates in the left hemisphere were almost unchanged (cf. Fig. 4.24 b & d). The flow through the right PCoA was decreased (≈ 74.5%), while the flow in the left PCoA was not altered distinctly (< 6.5%) (cf. Fig. 4.24 f).
An overview on the resulting blood flow for a complete CoW and "partial" collateralization is listed in Tab. 4.7.

Table 4.7: Overview on simulated mean cerebral blood flow rates for physiological conditions and a right MCA-M1 occlusion. Comparison between Anatomy I and Anatomy II (complete CoW, "partial" collateralization). All values are in ml/s.

Artery	Scenario			
	physiological Anatomy I	M1 occlusion Anatomy I	physiological Anatomy II	M1 occlusion Anatomy II
ACA (right): $\sum \bar{q}_i$	1.57	1.59	1.57	1.51
MCA (r): $\sum \bar{q}_i$	3.17	0.91	3.17	0.80
PCA (r): $\sum \bar{q}_i$	1.01	1.02	1.01	1.02
ACA (left): $\sum \bar{q}_i$	1.66	1.69	1.71	1.74
MCA (l): $\sum \bar{q}_i$	2.98	3.02	2.99	3.03
PCA (l): $\sum \bar{q}_i$	1.21	1.22	1.19	1.20
SLCs (r): $\sum q_{ACA-MCA}$	-0.04	0.43	-0.18	0.27
SLCs (r): $\sum q_{PCA-MCA}$	0.03	0.48	0.03	0.53
SLCs (r): $\sum q_{PCA-ACA}$	0.02	0.03	0.09	0.12
ACoA	0.00	-0.12	0.01	-0.12
PCoA (r)	0.15	0.05	0.14	0.03
PCoA (l)	0.15	0.14	0.13	0.12
ICA (r)	4.87	2.50	4.55	2.19
ICA (l)	4.76	4.72	4.38	4.34

Influence of the Anatomy of the Main Cerebral Arteries

Variation of the main cerebral arterial anatomy resulted in partly changed blood flow conditions: For Anatomy I, the remaining summed flow into the cortical branches of the right MCA was higher by 11.35% (0.91 ml/s vs 0.80 ml/s) compared to Anatomy II (cf. Fig. 4.24).

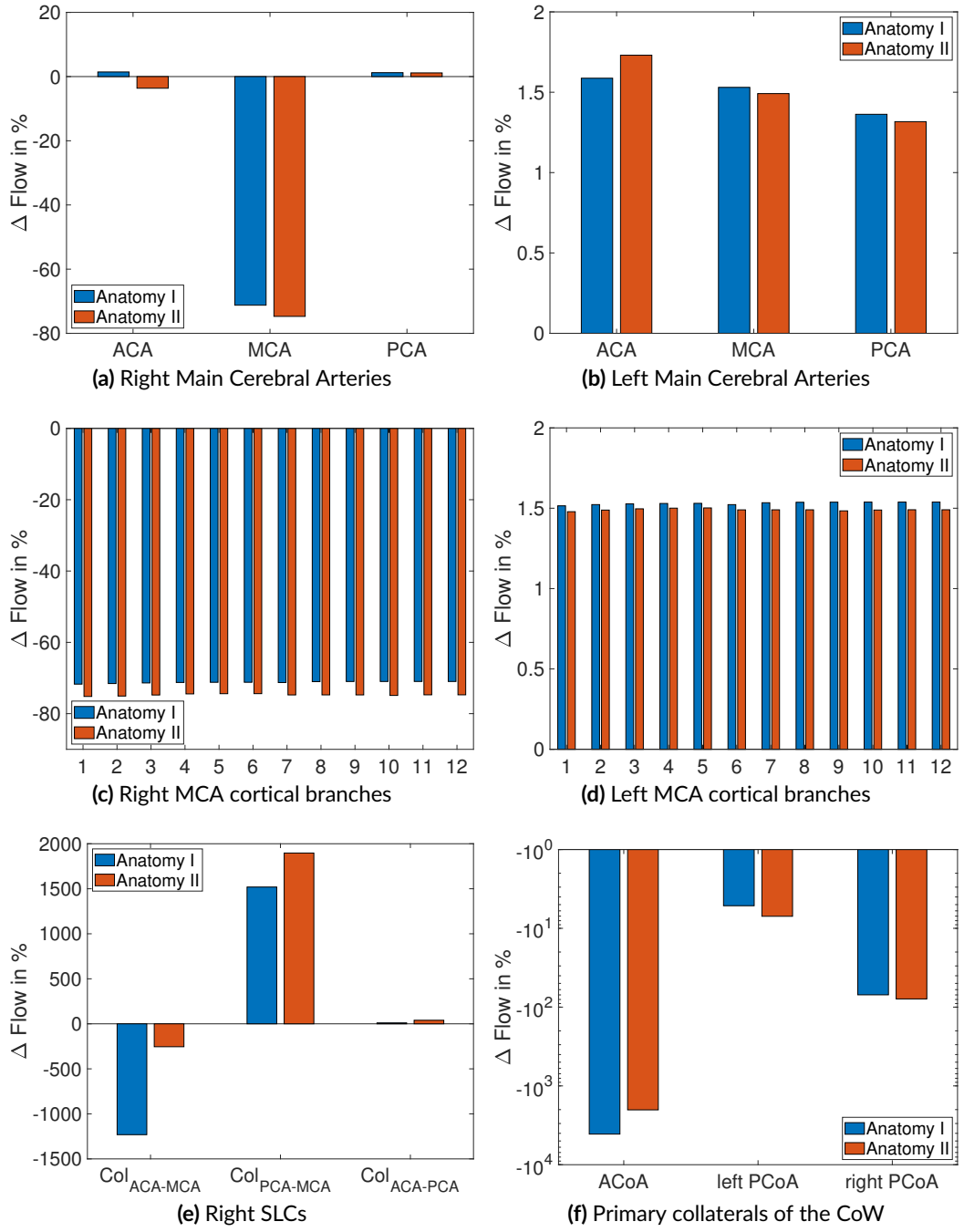

Figure 4.24: Relative deviation of cerebral flow rates in case of a right MCA-M1 occlusion compared to physiological conditions (complete CoW, "partial" collateralization).

Higher differences were prominent for flow through the SLCs to the MCA and for the ACoA: For Anatomy I, the summed right SLC flow from the ACA to the MCA was almost twice as high compared to Anatomy II (0.43 ml/s vs 0.27 ml/s), while for the summed right SLCs flow

from the PCA to the MCA, Anatomy II resulted in higher values (0.48 ml/s vs 0.54 ml/s). The contralateral flow into the ACoA increased distinctly more for Anatomy I compared to physiological conditions (cf. Fig. 4.24 f) but resulted in approximately the same total value (0.12 ml/s) as Anatomy II.

Since other variations (secondary collateral degree and the CoW variations) were performed in the same manner for Anatomy I and II, the model resulted in the same relative blood flow change. Therefore, only the results for Anatomy I are presented and discussed in the following, as Anatomy I represents the more common course of the ACA and the MCA in anatomical studies (cf. Sec. 2.3.2).

Influence of CoW Variations

Compared to a complete CoW, a missing right ACA-A1 (-17.6%) and a missing right PCA-P1 (-15.2%) segment led to the highest relative deviations of the total mean flow into the MCA vascular territory (cf. Fig. 4.25 a (left)). For all other considered CoW variations, the change in the total mean flow into the MCA vascular territory was negligible ($< 2.5\%$).
For a missing right ACA-A1 segment, the total mean flow into the ACA vascular territory was additionally slightly decreased (-6.3%) compared to a complete CoW, since the inflow into the right ACA could only be provided via the ACoA. Therefore, the flow through the ACoA changed its direction[3] and was significantly increased (cf. Fig. 4.25 b (left)) compared to a complete CoW. Additionally, the total mean flow from the right ACA to the right MCA via the SLCs was reduced by 41.6% compared to a complete CoW (cf. Fig. 4.25 c (left)).
For a missing right PCA-P1 segment, the inflow into the right PCA could only be provided via the right PCoA. Therefore, the flow through the right PCoA changed its direction[4] and was significantly increased (cf. Fig. 4.25 b (left)) compared to a complete CoW. Additionally, the summed SLC flow from the right PCA to the right MCA was reduced by 34.3% compared to a complete CoW (cf. Fig. 4.25 c (left)).
An overview on the resulting blood flow in case of a right MCA-M1 occlusion for a missing right ACA-A1 and a missing right PCA-P1 segment is listed in Tab. 4.8.

Influence of the Secondary Collateralization Degree

The variation of the degree of collateralization in the comparison of "partial","poor" or"strong" showed clear effects in the remaining summed flow into the MCA vascular territory: For a "poor" collateralization degree, the total flow into the MCA vascular territory was decreased by 42.0%, while for "strong" collateralization, the total flow was increased by 51.4% (cf. Fig. 4.25 a (right)) compared to a "partial" collateralization. The total flow into the ACA and the PCA vascular territory was not affected when varying the collateralization degree.
On the one hand, the flow through the SLCs to the MCA was distinctly lower ($\approx 42\%$) for a "poor" collateralization compared to "partial" collateralization (cf. Fig. 4.25 c (right)), since

[3]The direction of blood flow is now again the same as in the physiological case without occlusion (left to right).
[4]For physiological conditions, blood in the PCoA is flowing from the PCA to the ICA.

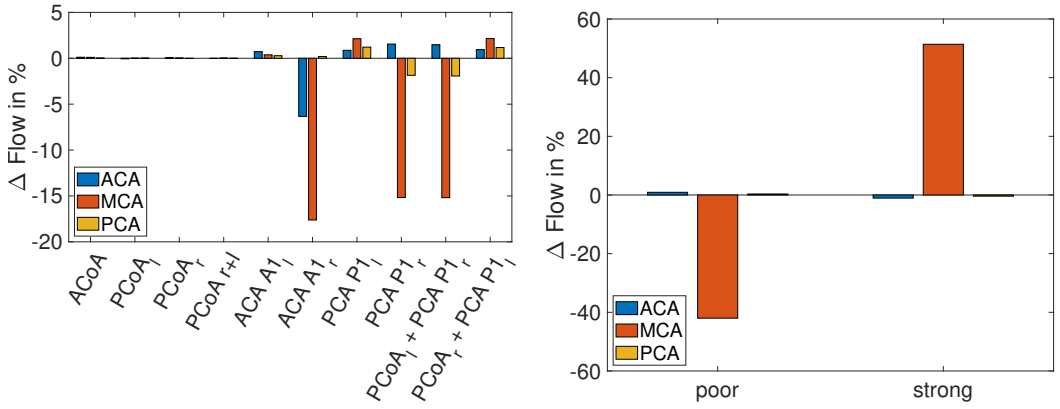

(a) Right main cerebral arteries

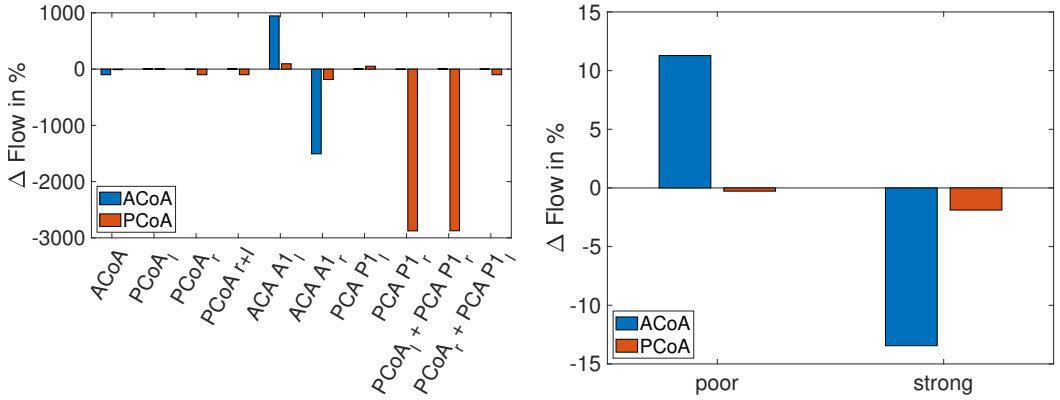

(b) ACoA and right PCoA

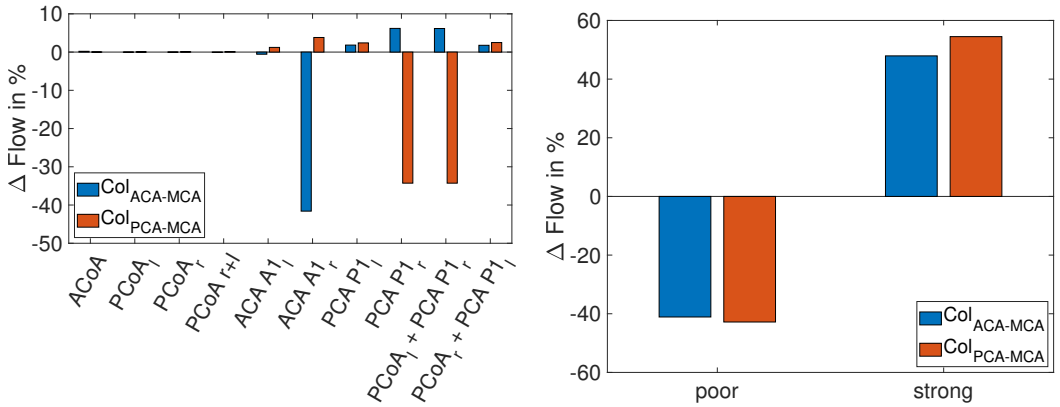

(c) SLCs to the right MCA

Figure 4.25: Relative deviation of flow rates in case of a right MCA-M1 occlusion compared to (left) a complete CoW or (right) a "partial" collateralization degree. (left: Anatomy I, "partial" collateralization; right: Anatomy I, complete CoW).

the flow through the ACoA was higher (cf. Fig. 4.25 b (right)). On the other hand, the flow through the ACoA was decreased (-13.5%) for "strong" collateralization, since the SLCs flow

to the right MCA was increased by ≈ 51.3% compared to "partial" collateralization.
The flow through the PCoAs was almost unaffected by the variation of the collateralization degree (cf. Fig. 4.25 b (right)).
An overview on the resulting blood flow in case of a right MCA-M1 occlusion for "poor" and "strong" collateralization is listed in Tab. 4.8.

Table 4.8: Overview on simulated mean cerebral blood flow rates for a right MCA-M1 occlusion. Comparison between "poor" and "strong" collateralization (complete CoW, Anatomy I) and a missing right ACA-A1 or a missing right PCA-P1 segment ("partial" collateralization, Anatomy I). All values are in ml/s.

Artery	Scenario			
	"poor" collaterals	"strong" collaterals	ACA-A1r missing	PCA-P1r missing
ACA (right): $\sum q_i$	1.61	1.58	1.49	1.62
MCA (r): $\sum q_i$	0.53	1.38	0.75	0.77
PCA (r): $\sum q_i$	1.02	1.02	1.02	1.00
ACA (left): $\sum q_i$	1.69	1.69	1.68	1.71
MCA (l): $\sum q_i$	3.03	3.02	3.02	3.05
PCA (l): $\sum q_i$	1.23	1.22	1.22	1.24
SLCs (r): $\sum q_{ACA-MCA}$	0.25	0.64	0.25	0.46
SLCs (r): $\sum q_{PCA-MCA}$	0.28	0.74	0.50	0.32
SLCs (r): $\sum q_{PCA-ACA}$	0.01	0.05	0.09	-0.04
ACoA	-0.13	-0.10	1.66	-0.11
PCoA (r)	0.05	0.05	-0.04	-1.28
PCoA (l)	0.15	0.13	0.21	0.17
ICA (r)	2.37	2.65	0.47	4.75
ICA (l)	4.78	4.64	6.40	2.59

Discussion & Limitations of the Occlusion Flow Rates

In case of an occlusion of the right MCA-M1 segment, the comparison of the resulting ischemic cerebral blood flows with measured flows is difficult, since there are hardly any measured values for the ACoA and the PCoA in literature for ischemic conditions. In addition, the same limitations for the comparability of the flow rates in the bigger afferent vessels as already described for the physiological conditions (cf. Sec. 4.5.1, Discussion) persist.
Despite these limitations, the simulated ischemic blood flow rates led to realistic ischemic perfusion rates (cf. Sec. 5.4.5). This aspect and the comparability of the perfusion rates are discussed in more detail in Sec. 5.4.5. Furthermore, the occlusion of the MCA-M1 segment and the variation of the cerebral anatomy resulted in reasonable blood flow changes in a realistic range.
Besides the variations in the anatomy of the main cerebral arteries (Anatomy I vs. Anatomy II), the variations in the CoW, and the variations in the secondary leptomeningeal collateralization degree, the effects of variable body height, and different vessel radii in the whole arterial tree were evaluated in a supervised student thesis by Aracri [164]. In his work, Aracri scaled the

segment lengths linearly to consider three different patients heights (± 10 cm) and considered maximal and minimal vessel diameters by analyzing data of the larger cerebral arteries from the literature. Aracri's work showed, that the patient height had almost no influence on the resulting ischemic blood flow conditions. Furthermore, in Aracri's results, it could be observed that for different vessel diameters the range of the predicted ischemic blood flow results is covered by the shown results (cf. Sec. 4.5.2) for the variations in the secondary leptomeningeal collateralization degree.

Chapter 5

Modeling Cerebral Temperature

The cerebral temperature is mainly affected by blood perfusion rates, blood temperature, and metabolic heat production [21, 165]. Under physiological conditions, these parameters are tightly controlled and stay in their physiological ranges. However, in case of acute ischemic stroke (AIS) and endovascular blood cooling, these parameters show spatial variation, which affects the spatio-temporal cerebral temperature. In this chapter, the modeling of cerebral temperature under ischemic conditions and the use of selective brain hypothermia (SBH) is introduced and explained. Therefore, the chapter is divided into five sections. The first section of this chapter explains the heat transfer in living tissue and introduces Pennes' equation for bioheat transfer. Pennes' equation is used as basis for temperature simulation in this thesis. The second section describes the geometry generation. To calculate cerebral temperatures accurately, a realistic brain geometry was processed and divided into individual perfusion regions to account for spatial variations. The third section describes the boundary conditions for the temperature calculation. This involves the coupling with the hemodynamics model and the systemic body, the calculation of resulting arterial blood temperatures after endovascular blood cooling, and heat transfer to the environment.
The fourth section contains the results of the temperature calculation for a large vessel occlusion (LVO) in the right middle cerebral artery (MCA)-M1 segment as well as their discussion and evaluation. Furthermore, the model was adapted to allow for a better comparison with the results of other research groups considering the effect of cold saline infusion (CSI). In the last section of this chapter, a comparison of the detailed 3D temperature model with a simplified energetic model is provided, which can possibly serve as a quicker and surrogate tool to estimate the mean cooling capacity of the catheter.

5.1 Heat Transfer in Living Tissue

Information about spatial temperature distribution in living tissue is of importance in various fields of medical therapy and human physiology (therapeutic hypothermia (TH), cryosurgery, frost bite, ablation lesions for atrial fibrillation patients, skin burns, body thermal regulation ...).

A heat transfer equation for the thermal modeling of blood perfused tissue has to account for three aspects [21]:

- Blood perfusion,
- Vascular architecture,
- Variation in thermal properties and blood flow rate.

Generally, the problem is to describe anisotropic blood flow in the complex system of the arterial and venous circulatory system (cf. Sec. 2.1.1). Furthermore, blood is exchanged between pairs of arteries and veins through capillary bleed-off along vessel walls. This leads to blood draining from the arteries to the veins [166, 167].
Summarizing, thermal energy is exchanged in a blood perfused heterogeneous matrix (mirroring the energy transport between neighboring vessels as well as between vessels and tissue), which is additionally exposed to metabolic heat production [21].
First attempts to model this complex process in equations were already made in the middle of the 20th century and modeling approaches are still subject of current research. In the meanwhile, different equations for bioheat transfer have been developed and proposed [23, 168–179]. In this work, Pennes' equation was used, which was the first model for heat transfer in living tissue, namely in the human forearm. The following sections present the equation as well as the difficulty of determining local cerebral arterial blood temperature.

5.1.1 Variation of the Blood Temperature

Blood enters the circulatory system from the heart into the aorta (cf. Sec. 2.1.1) at the systemic arterial temperature $T_{\mathrm{Sys}} \approx 37\,^{\circ}\mathrm{C}$ (cf. Fig. 5.1). The large primary arteries (aorta and the common carotid artery (CCA)) have a very long thermal equilibration length[1] (5-190 m) since there is almost no heat exchange with the surrounding tissue. Therefore, the blood temperature remains almost unchanged for blood flow through the larger cerebral arteries.
However, the blood temperature T_{Bl} changes in the smaller arteries and matches with the surrounding tissue temperature T_{T} even before reaching the capillaries. Depending on the tissue, the tissue temperature can be above or below the systemic temperature T_{Sys}. Blood flowing back from the capillaries near the surface of the skin has a much lower temperature than blood in deeper tissue layers. This effect is used to regulate the core body temperature by controlling blood flow into the skin vessels. (cf. Sec. 2.6).
The mixing of the blood by the venous confluence of different tissue types brings the blood temperature T_{Bl} back to T_{Sys} during reflux through the vena cava to the heart.

[1] The length of a blood vessel over which the temperature difference between the blood and the solid tissue assimilated themselves [180] (aorta: 190 m, large arteries 4 m, capillaries 2E-7 m) [171].

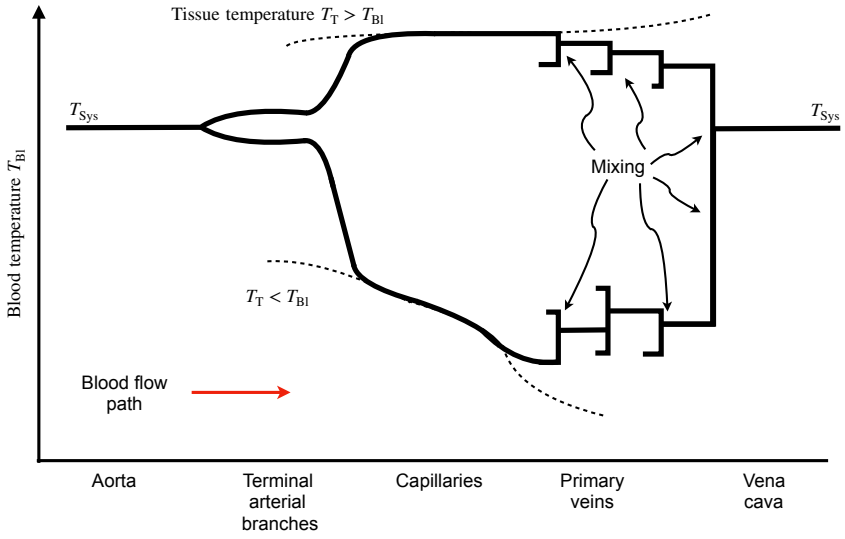

Figure 5.1: Course of blood temperature in the vessels of the circulatory system. Figure inspired from [171].

5.1.2 Pennes' Bioheat Equation

In 1948, Pennes [23] published his bioheat equation, which is still the basis for most models concerning heat transfer in biological tissue. It was used with remarkable success in many applications including the simulation of hypothermia [21, 165].
Four central simplifying assumptions are basis for Pennes' equation [21]:

1. **Equilibration site:** The heat transfer between blood and tissue focuses on the capillary bed. All prearteriole and postvenule heat exchange is neglected.
2. **Blood perfusion:** In the capillary bed, blood flow is assumed to be isotropic and the blood flow direction is neglected.
3. **Vascular architecture:** The local vascular architecture is not taken into account. In the vicinity of the capillary bed, larger blood vessels are neglected.
4. **Blood temperature:** The temperature of the blood T_{Bl}, which perfuses the tissue, is assumed to have systemic temperature T_{Sys}. For the heat transfer, instantaneous energy exchange is considered as well as an equilibrium to the tissue temperature T_T.

With these four assumptions in Pennes' equation, blood perfusion is considered to be an isotropic heat source or sink, which is proportional to the blood flow rate and the difference between tissue temperature T_T and blood temperature T_{Bl}.

Derivation

The tissue element shown in Fig. 5.2 is considered for the derivation of Pennes' equation. It is assumed to be large enough to be saturated with arterioles, capillaries, and venules but small

compared to the characteristic dimension of the considered region [21]. The heat exchange is based on the heat diffusion equation (cf. Eq. 3.25) for this element.
Energy is added to this element by blood perfusion and metabolic heat generation, which can be expressed by power densities (in $\frac{\mathrm{W}}{\mathrm{m}^3}$):

$$\dot{w} = \dot{w}_{\mathrm{Bl}} + \dot{w}_{\mathrm{Met}}.$$

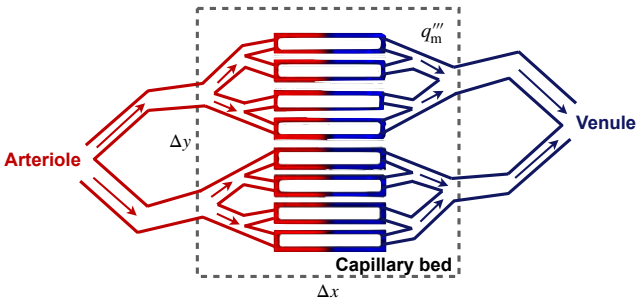

Figure 5.2: Blood perfused tissue element. Figure inspired from [21].

Following Pennes' assumptions, blood perfuses the tissue in the element at systemic temperature T_{Sys} and equilibrates instantaneously to the tissue temperature T_{T}. Thus, $\dot{w}_{\mathrm{Bl}}$ can be expressed as:

$$\dot{w}_{\mathrm{Bl}} = -\rho_{\mathrm{Bl}} \cdot c_{\mathrm{Bl}} \cdot \nu_{\mathrm{Bl}} \cdot \left(T_{\mathrm{T}} - T_{\mathrm{Sys}}\right), \tag{5.1}$$

where ρ_{Bl} is the blood density (in $\frac{kg}{\mathrm{m}^3}$), c_{Bl} the specific heat of blood (in $\frac{\mathrm{J}}{\mathrm{kg \cdot K}}$), and ν_{Bl} the volumetric perfusion rate (in $\frac{1}{\mathrm{s}}$).
Inserting Eq. 5.1 in the heat diffusion equation (Eq. 3.25) results in Pennes' equation:

$$\rho_{\mathrm{T}} \cdot c_{\mathrm{T}} \cdot \frac{\partial T_{\mathrm{T}}}{\partial t} = \nabla\left(\lambda_{\mathrm{T}} \nabla T_{\mathrm{T}}\right) - \rho_{\mathrm{Bl}} \cdot c_{\mathrm{Bl}} \cdot \nu_{\mathrm{Bl}} \cdot (T_{\mathrm{T}} - T_{\mathrm{Sys}}) + \dot{w}_{\mathrm{Met}}, \tag{5.2}$$

where c_{T} is the specific heat of the respective tissue (in $\frac{\mathrm{J}}{\mathrm{kg \cdot K}}$), ρ_{T} the tissue density (in $\frac{\mathrm{kg}}{\mathrm{m}^3}$), and λ_{T} the tissue's thermal conductivity (in $\frac{\mathrm{W}}{\mathrm{m \cdot K}}$).
The first term on the right-hand side in Pennes' equation represents the heat conduction in the three spatial directions. For Cartesian coordinates (x, y, z), $\nabla\left(\lambda_{\mathrm{T}} \nabla T_{\mathrm{T}}\right)$ is defined as:

$$\nabla(\lambda \nabla T) = \frac{\partial}{\partial x}(\lambda \frac{\partial T}{\partial x}) + \frac{\partial}{\partial y}(\lambda \frac{\partial T}{\partial y}) + \frac{\partial}{\partial z}(\lambda \frac{\partial T}{\partial z}).$$

Discussion & Limitations of Sec. 5.1.2

Pennes' equation is the most commonly used model for bioheat transfer and was applied with remarkable success in many applications. Nevertheless, several more detailed models

for bioheat transfer exist, since Pennes' equation comes along with multiple simplifying assumptions, which are not valid for every type of tissue [21].

Equilibration site: Unlike Pennes assumed, the thermal equilibrium of blood and surrounding tissue is reached in the prearterioles and not in the capillary bed (cf. Fig. 5.1).

Blood perfusion: Pennes' equation does not account for directionality of blood flow, which is an important factor in the interchange of energy between vessels and tissue.

Vascular architecture: Since Pennes' equation does not account for vascular architecture, significant features of the circulatory system are not considered (energy exchange with large vessels, countercurrent heat exchange between artery-vein pairs, etc.).

Blood temperature: As illustrated in Fig. 5.1, the arterial blood temperature varies continuously from the aorta to the capillaries. Thus, Pennes' assumption of blood having systemic temperature leads to an overestimation of the effect of blood perfusion.

Fourier's law: Fourier's law of heat conduction is based on an infinite speed of the thermal wave, which is highly unrealistic for heterogeneous biological tissue [181].

More recent models try to compensate the errors resulting from these assumptions by:

- The consideration of a countercurrent factor $(1-\alpha)$ in the perfusion term [165]:

$$\dot{w}_{\mathrm{Bl}} = -(1-\alpha)\cdot\rho_{\mathrm{Bl}}\cdot c_{\mathrm{Bl}}\cdot\nu_{\mathrm{Bl}}\cdot\left(T_{\mathrm{T}}-T_{\mathrm{Sys}}\right).$$

- The adaption of the volumetric perfusion and the blood temperature:

$$\nu_{\mathrm{Bl}} \rightarrow \nu^{*}_{\mathrm{Bl}},$$
$$T_{\mathrm{Sys}} \rightarrow T^{*}_{\mathrm{Bl}}.$$

- The consideration of blood flow directionality [171].
- The modification of Fourier's law (cf. Eq. 3.24) by introducing a phase-lag term [182, 183]:

$$\dot{\vec{q}} = -\lambda\nabla T \rightarrow \dot{\vec{q}} = -\tau_q\frac{\partial\dot{\vec{q}}}{\partial t} - \lambda\nabla T, \tag{5.3}$$

  where the phase-lag time τ_q captures the microscale responses in time due to the heat flux. The replacement of Fourier's law with the adapted heat conduction in Pennes' equation yields the so-called single-phase-lag (SPL) model.
- The modification of the adapted Fourier's law (cf. Eq. 5.3) to capture the microscale response in both time and space by introducing a second phase-lag term [184]:

$$\dot{\vec{q}} = -\tau_q\frac{\partial\dot{\vec{q}}}{\partial t} - \lambda\nabla T \rightarrow \dot{\vec{q}} = -\tau_q\frac{\partial\dot{\vec{q}}}{\partial t} - \lambda\nabla T - \lambda\tau_T\frac{\partial}{\partial t}\nabla T,$$

  where the time delay τ_T can be interpreted as the total time required for the thermal activation in microscale caused by microstructural interactions. The adaptions inserted in Pennes' equation are known as the so-called dual-phase-lag (DPL) model.

There are also completely new approaches, e.g., the three-temperature model of Jiji & Weinbaum [172], the simplified Weinbaum-Jiji bioheat equation [173], and the s-vessel tissue cylinder model [176]. Nevertheless, the original Pennes' equation was used in this work due to its simplicity and

applicability for cerebral temperature calculation: As mentioned in Sec. 2.3.2, the brain blood supply is different from the other organs. All major arteries run along the cortex or inside the gyri before branching out into smaller arteries and finally perfusing the brain tissue from the outside to the inside [41]. The brain perfusion is regulated within a narrow range and respectively high compared to other organs and tissue in rest. Therefore, the net of capillaries is very dense. Furthermore, the brain is thermally well isolated by its outer layers (scalp, scull, meninges, cerebrospinal fluid (CSF)) [185, 186] and cerebral blood flow is not involved in the control of body temperature regulation [20, 24].
These aspects of cerebral blood flow mitigate the limitations of Pennes' assumptions and are the basis for the successful use of Pennes' equation in previous brain temperature simulations by other research groups [185–190].
However, previous studies mainly used Pennes' equation for healthy brain tissue. In a comparative study of different ischemic scenarios, Lillicrap et al. [165] showed that the resulting penumbral and ischemic core temperatures were significantly dependent on cerebral metabolic rate (CMR) and remaining perfusion in the ischemic tissue. This effect is analyzed and discussed in more detail in Sec. 5.4.5 based on the results of the temperature simulations.

5.2 Geometry Generation

For the calculation of spatially detailed cerebral temperatures, a partitioned human brain geometry is essential. The division of the cerebrum into vascular regions of the individual cortical branches of the main cerebral arteries (cf. Sec. 4.2) allows for direct coupling with the cerebral blood flow model. Thus, a spatial perfusion rate can be determined for 100 individual regions[2] in the cerebrum and the influence of SBH can be analyzed. For this purpose, the brain of a detailed 3D head geometry was extracted and further separated in three steps: in the first step, the cerebrum was extracted by means of the extraction of the brainstem and the cerebellum. In the second step, the cerebrum was divided into "major vascular territories" representing the supply territories (cf. Sec. 2.3.2) of the three major cerebral arteries (anterior cerebral artery (ACA), MCA, and posterior cerebral artery (PCA)) per hemisphere. Finally, every major vascular territory was subdivided into "terminal perfusion regions" mirroring the supply regions of the cortical branches in the hemodynamics model (cf. Sec. 4.2.4). This subdivision was part of the work performed by Meißner [136] in his supervised Master's thesis. The division process is explained in more detail in the following subsections and was published in [148].

[2]For Anatomy II, 102 terminal perfusion regions were considered in a separate division process resulting in Geometry II.

5.2.1 Human Brain Atlas "*Colin 27*"

The human brain atlas "*Colin 27*"[3] is the basis of the geometry used in this work. It is widely used as a standard reference in neuroimaging [191–194]. The basic brain atlas was developed at the Montreal Neurological Institute and consists of 27 averaged, aligned magnetic resonance imaging (MRI) scans of Colin Holmes [142, 195]. In 2009, the "*Colin 27*" data set was transformed to a detailed FEM mesh by Fang et al. [196] using the tool *iso2mesh* [197]. Fang's mesh [198, 199] consists of 70,226 nodes and 423,375 tetrahedral elements and distinguishes between four different materials (an outer shell, CSF, gray matter (GM), and white matter (WM)). It was used as basic mesh in this work and is depicted in Fig. 5.3 a.
Fang's mesh consist of tetrahedral elements in good quality but is too coarse (cf. Fig. 5.3 a) for a subdivision in approximately 100 perfusion regions and for spatially accurate temperature calculations. Therefore, Fang's mesh was refined[4] to obtain a finer and uniform tetrahedral mesh (cf. Fig. 5.3 b). Furthermore, the outer shell of Fang's mesh was subdivided into three individual layers (scalp, skull, and connective tissue (CT)) and air-filled sinuses were introduced (cf. Fig. 5.3 b). The thickness of the scalp and the skull were estimated from literature [206–208] to ≈ 5 mm. The separation process ensured that at least two tetrahedrons formed the cladding layers in transmural direction.
The refined head model consists of 755,044 nodes and 4,370,087 tetrahedrons with an average edge length of 1.96 ± 0.67 mm. The refined mesh was the basis for all temperature calculations. The further consideration of the different perfusion regions and their separation was only performed by changing the mesh's cell data material label and not by changing the geometry itself.

Division of the Brain into Hemispheres

Subsequent to the refinement process of Fang's mesh [198], the entire geometry was divided into a left and a right side since SBH is only induced for one hemisphere. The brain and its outer shells were separated individually into a left and a right side.[5] The outer shells were separated by the application of a simple threshold of the x-coordinate. However, due to the asymmetric course of the longitudinal fissure (cf. Sec. 2.3), a simple coordinate threshold was not sufficient for the separation of the brain. For the separation of the cerebrum into the left and the right hemisphere, a Laplace boundary value problem was solved:

$$\nabla^2 \Phi = \Delta \Phi = 0,$$

where Φ is a scalar function, i.e., in this case the electric field potential.
To solve the problem, the cerebrum was put into a bounding box. The lateral walls were

[3] also known as "Average Colin", "MNI 27", or "Average 27"
[4] Remeshing and layer separation were performed using the software tools *Blender* (version 2.79) [143], *Instant Mesh* [200, 201], *GMSH* (version 4.3) [202] and *mmg3D* [203–205].
[5] The CSF was not split into left and right since it is not perfused with blood.

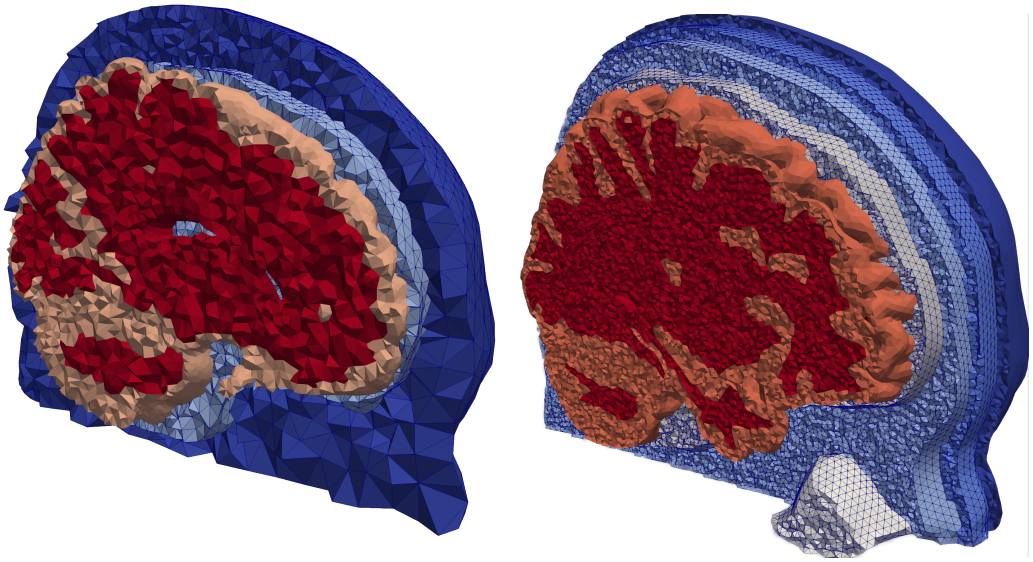

(a) "*Colin 27*" geometry as meshed by Fang et al. [198]

(b) Refined geometry

Figure 5.3: The geometric head model based on the *"Colin 27"* [195] brain atlas. Each color indicates a different material. From outside to inside: (a) outer shell, CSF, GM, and WM; (b) scalp, skull, CT, CSF, GM, and WM, lateral ventricles, sinuses. (Except for the CSF, all other materials were separated in left and right hemisphere for the refined mesh.

assigned with fixed potentials:

$$\Phi(x = -x_0) = 0,$$
$$\Phi(x = +x_0) = 1.$$

The box was meshed around the brain and the box and the whole brain were assigned with different conductivities (κ_{box}, $\kappa_{\text{Brain}} = 100000 \cdot \kappa_{\text{box}}$).
For the final separation, a threshold ($\Phi \gtrsim 0.5$) was applied to the solution (cf. Fig. 5.4) and the cerebrum was split by adjusting the material labels of each tetrahedron in the corresponding hemisphere.

Separation of the Cerebrum

As mentioned in Sec. 2.3.2, the brainstem and the cerebellum are mainly supplied by arteries branching from the basilar artery (BA) and the vertebral artery (VA) (cf. Fig. 2.9) and not by the ACA, MCA, or PCA. Therefore, they needed to be separated from the cerebrum.
Since the refined brain mesh only contained material information concerning the division into GM and WM, the original magnetic resonance (MR) images (cf. Fig. 5.5) of the "*Colin 27*" data set [195] were used to gain spatial information about the boundaries between the cerebrum, brainstem, and cerebellum. In a second step, reference models of the brainstem and

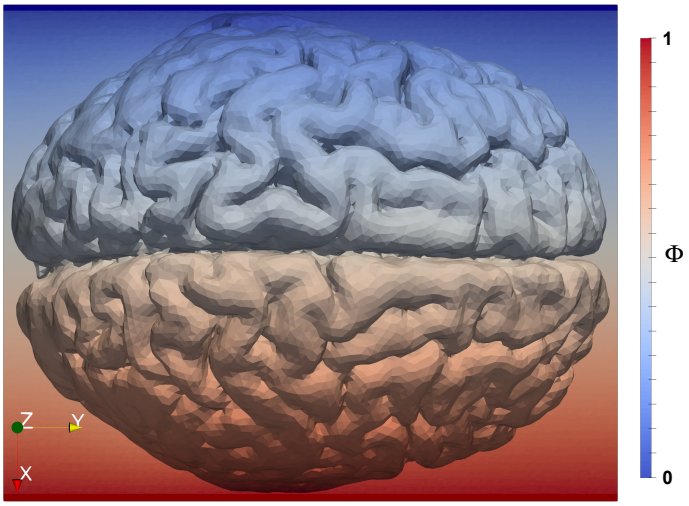

Figure 5.4: For the separation of the cerebrum in the left and right hemisphere, a Laplace boundary value problem was solved.

the cerebellum were created from the MR images. The reference models were used for the final subdivision in the refined mesh.
The brainstem and the cerebellum were segmented in the MR images with the tool *ITK-SNAP* [209, 210]. The resulting surfaces were imported to the software *Blender*[6] [143], where they were smoothed [7]. Subsequently, the smoothed surfaces were meshed[8] to solid tetrahedral reference models.

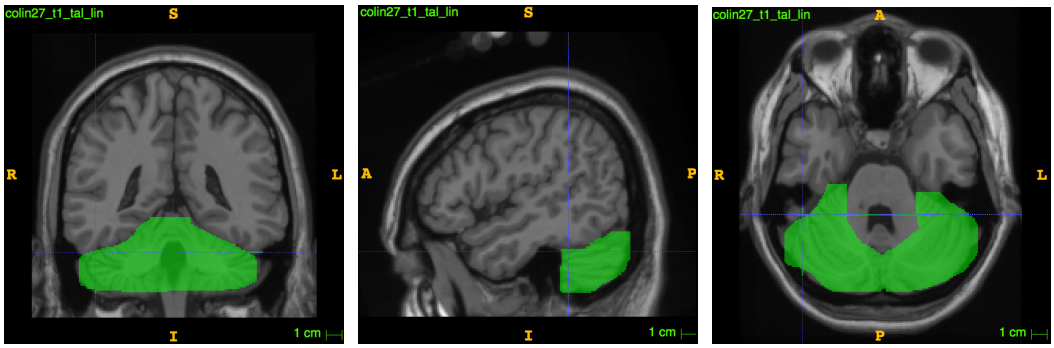

(a) frontal **(b)** sagittal **(c)** transversal

Figure 5.5: Use of *ITK-SNAP* [209, 210] to extract the cerebellum in MR images of the "*Colin 27*" data set [195].

[6]Version 2.79
[7]The reference models were aligned with the refined mesh before the smoothing (cf. Sec. B.3.1)
[8]using the tools *Instant Mesh* [200, 201] and *GMSH* version 4.3 [202]

In the last step, the reference models of the brainstem and the cerebellum were used to find the corresponding cells in the refined brain mesh with a nearest neighbor approach. The affected tetrahedrons material labels were changed to newly introduced material labels for the brainstem and the cerebellum. Fig. 5.6 shows the extracted brainstem and the cerebellum.

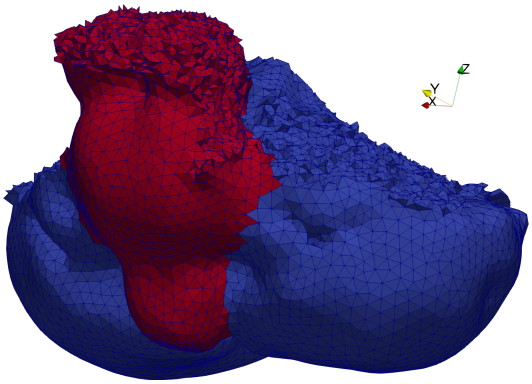

Figure 5.6: Extracted brainstem (red) and cerebellum (blue).

5.2.2 Major Vascular Territories

For the division of the cerebrum into the vascular regions of the main cerebral arteries per hemisphere, two references were used as basis for the division process: First, the 60 digitally reconstructed artery trees from the previously mentioned "*Brain Vascular Database*" [139] were converted into VTK files (cf. Sec. 4.2.4). Second, the work of Mut et al. [52] provided quantitative descriptions of the arborization of the main cerebral arteries in the "*Brain Vascular Database*" and relative volumes of the corresponding vascular territories [52]. The results of Mut et al. as well as a comparison with an anatomical study of 23 human brains by Zwan et al. [47] are listed in Tab. 5.1.

Table 5.1: Relative volumes of the vascular territories of the six main cerebral arteries. Geometry I represents the refined brain mesh divided into terminal perfusion regions supplied by the cortical branches of the hemodynamics model with Anatomy I. Geometry II represents the division into terminal perfusion regions supplied by the cortical branches of the hemodynamics model with Anatomy II.

Major vascular territory	Mut et al. [52]	van der Zwan et al. [47]	Geometry I	Geometry II
ACA right	14%	13%	13.8%	13.7%
ACA left	14.5%	13%	14.5%	14.5%
MCA right	26.5%	26%	26.7%	26.7%
MCA left	25%	26%	25.3%	25.3%
PCA right	9.5%	11%	9.3%	9.3%
PCA left	10.5%	11%	10.5%	10.5%

Fig. 5.7 shows the division process, which can be split in four steps: In the first step, a nearest neighbor approach yielded a corresponding cell in the refined brain mesh (cf. Sec. 5.2.1) for each cell in the 60 extracted and aligned artery trees (cf. Sec. 4.2.4). In the second step, the arterial tree cells, which were already labeled as left / right ACA, MCA, and PCA [139], were used as initial seed cells for an adapted region growing algorithm (explained in detail below) to segment 60 different versions of the six vascular territories in the refined brain mesh. Afterwards, the 60 different segmentations were merged into one final subdivision of vascular territories in the refined brain mesh. For this purpose, a 3D probability map was created from the 60 different, individual segmentations in the third step. The probability of belonging to a certain vascular territory was calculated for each brain cell in the refined mesh across the 60 artery trees.
In the last step, tetrahedrons belonging to one of the six vascular territories with a minimum probability of 75% were assigned with a respective new material label. All remaining cells were marked as unvisited. In a subsequent, second iteration of the modified region growing algorithm, the already assigned cells were used as seeds and all unvisited cells were finally assigned.

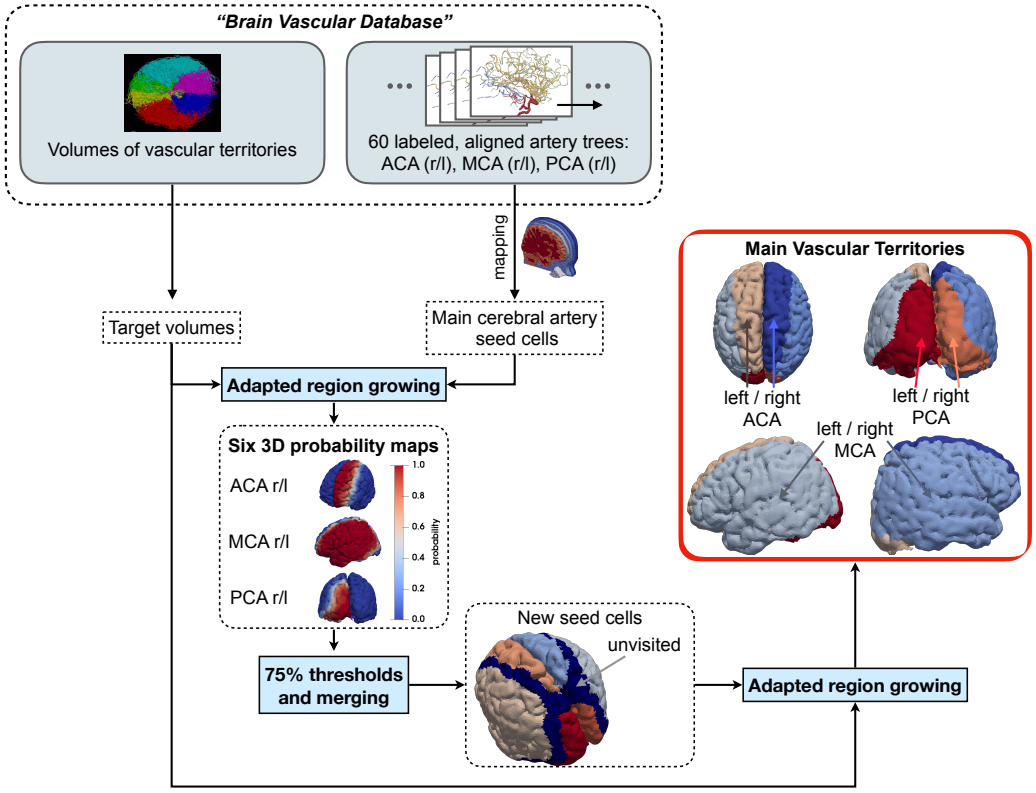

Figure 5.7: Schematic of the division process of the cerebrum into the six major vascular territories.

Region Growing

Region growing algorithms are region-based standard methods in medical image segmentation [107, 211]. Their (semi-)automatic function is based on the choice of seed cells/pixels within a region, which shall be segmented. Firstly, the chosen seeds are marked as visited while all other cells/pixels are marked as unvisited. Subsequently, the region grows iteratively from the chosen seeds by appending adjacent unvisited cells/pixels, which meet a predefined criterion[9]. After a cell/pixel is appended, it is treated like an additional seed cell/pixel. In this way, the region grows until the image boundary or another region is reached. The algorithm terminates when all cells/pixels have been visited or the region does not grow anymore. [107, 211]
Besides the application in medical image segmentation, region growing algorithms are widely used as their functionality is simple and in contrast to other simple segmentation methods they always result in connected regions. Another advantage is the possibility to consider more than one growing region simultaneously by using region labels and defining an order in which the regions grow. [212]

Adapted Region Growing

For the application to separate the six major vascular territories within the refined brain mesh, five modifications were made to the classical region growing algorithm [211] explained above. These adaptions led to the extraction of compact regions, which match the predefined target volumes (cf. Tab. 5.1) of Mut et al. [52]:

- A target volume (relative values from Mut et al. [52]) was defined for each of the six vascular territories. Every region is allowed to grow as long as the target volume has not yet been reached.
- Only one region is allowed to grow per iteration. The region with the maximum deviation from its target volume is selected for growth.
- Each vascular territory region is only allowed to grow within the corresponding hemisphere.
- For the assignment of a neighboring cell to the growing region, no specific criterion needs to be fulfilled. Already visited cells can be assigned to a different region by overwriting the previous assignment.
- The algorithm stops as soon as no more new cells are visited.

A flow chart of the whole adapted region growing process is depicted in Fig. 5.8.

Limitations & Discussion of Sec. 5.2.2

For the classification of the cerebrum into the major vascular regions of the three main cerebral arteries, the relative volume values of Mut et al. [52] were used as target values.

[9] In medical image segmentation, the criterion is mostly a threshold for the pixel's grayscale intensity.

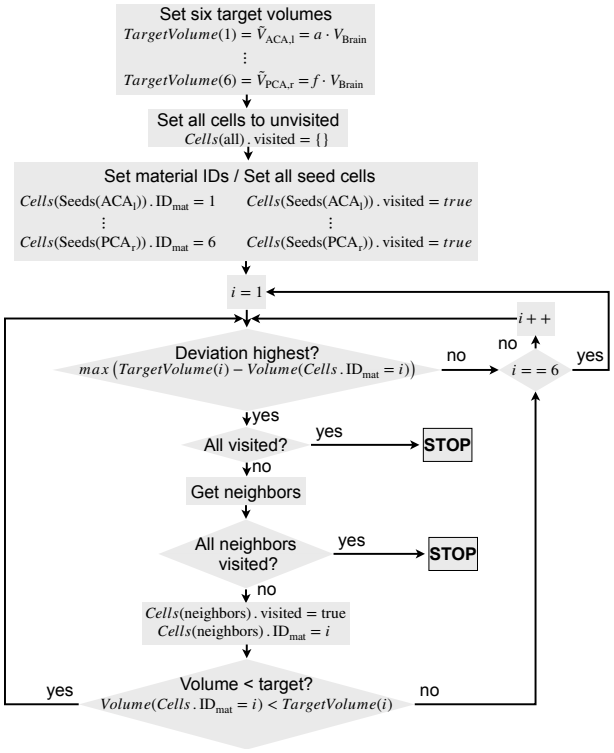

Figure 5.8: Flow chart of the adapted region growing algorithm.

The values are in good agreement with the anatomical study by van der Zwan et al. [47] (cf. Tab. 5.1). The values from Mut et al. were determined on the basis of the "*Brain Vascular Database*", which was also used for the creation of the refined brain mesh in this work. Although Mut et al. provided quantitative descriptions of arterial branches, bifurcation patterns and the shape of the main cerebral arteries in their work, the extracted values are intended to represent mean values representing the major anatomical variants. Since the aim of this work is to create a general but as exact as possible temperature model, the mean values of Mut et al. were adopted and no further subdivision (typical/atypical callosomarginal artery (CmA); bi-/trifurcating MCA) was made for the seed cells of the mapped arteries. However, these known anatomical differences were taken into account in the further refinement of the division into terminal perfusion regions (cf. Sec. 5.2.3).

5.2.3 Terminal Perfusion Regions (Geometry I & II)

The division into terminal perfusion regions allows for the coupling of the brain geometry with the hemodynamics model (cf. Sec. 4.2) and for spatially detailed cerebral temperature calculations. The reference surface maps introduced in Sec. 4.2.4 were used for the division. These maps were manually aligned with the surface of the respective major vascular territories of the refined brain mesh and show the supply region distribution of the main cerebral arteries' cortical branches on the brain's cortex (cf. Sec. 4.2.4). In total, eight different surface

maps were used: Left and right MCA, left and right PCA, left and right ACA (differentiated in having a typical or an atypical CmA). The exemplary color map of the right MCA is depicted in Fig. 4.10 b.
As described in Sec. 4.2.4, the surface maps were used to label the cortical branches in the artery trees of the "*Brain Vascular Database*". The corresponding labeled cells of the cortical branches in the refined brain mesh as well as the mapped surface cells were used as seed cells for a classical region growing, which selects the currently smallest region to grow first. Since all artery trees were subdivided into Anatomy I & II (cf. Sec. 4.2.4) and for the surface maps a distinction between a typical and an atypical course of the CmA was possible, two distinct sets of seed cells were established. These distinct sets of seed cells enabled to consider the different anatomies in the hemodynamics model (Anatomy I & II) also for the division process into terminal perfusion regions (Geometry I & II) . The schematic in Fig. 5.9 visualizes the division process into the terminal perfusion regions.
Similar to the extraction of the major vascular territories (cf. previous subsection), the segmentation results were used to calculate 3D probability maps and a subsequent 75% threshold was applied to merge all segmentation results in two different division versions. A subsequent new region growing procedure with the present divisions as new seed cells resulted in the final divisions of the terminal perfusion regions, namely Geometry I & II, respectively mirroring the hemodynamics models Anatomy I & II (cf. Sec. 4.3.2). In total, the cerebrum of the refined brain mesh was partitioned into 50 (Geometry I) or respectively 52 (Geometry II) terminal perfusion regions.

Discussion & Limitations of Sec. 5.2.3

As already discussed in Sec. 4.2.4, the surface maps from literature reflect only the most common distributions of the supply regions of the cortical branches on the cortex surface and the anatomies can vary between individuals. However, for the purpose of this thesis, to develop a model of spatio-temporal brain temperature covering the major anatomical variants, the most common distributions summarized in these surface maps reflect an adequate resource. Over all, the whole division process resulted in connected regions for every terminal perfusion region and the relative mean volumes for the vascular territories of the three main cerebral arteries resulted in good accordance with the target volumes provided [47, 52] (cf. Tab. 5.1).

5.2.4 Consideration of Gray and White Matter

After the subdivision into the terminal perfusion regions, the latter were divided into GM and WM according to the existing division in the refined brain mesh (cf. Fig. 5.3 b).
However, the highly convoluted cortex led to a fragmentation into many ($\approx$ 200) small sub-areas (cf. Fig. 5.10) and not as desired to exactly two connected parts for each terminal perfusion region. Therefore, a volume threshold of 0.1% of the cerebrum's volume was applied and smaller regions were redistributed by classical region growing. The application of the threshold and subsequent region growing resulted in a final subdivision into GM and

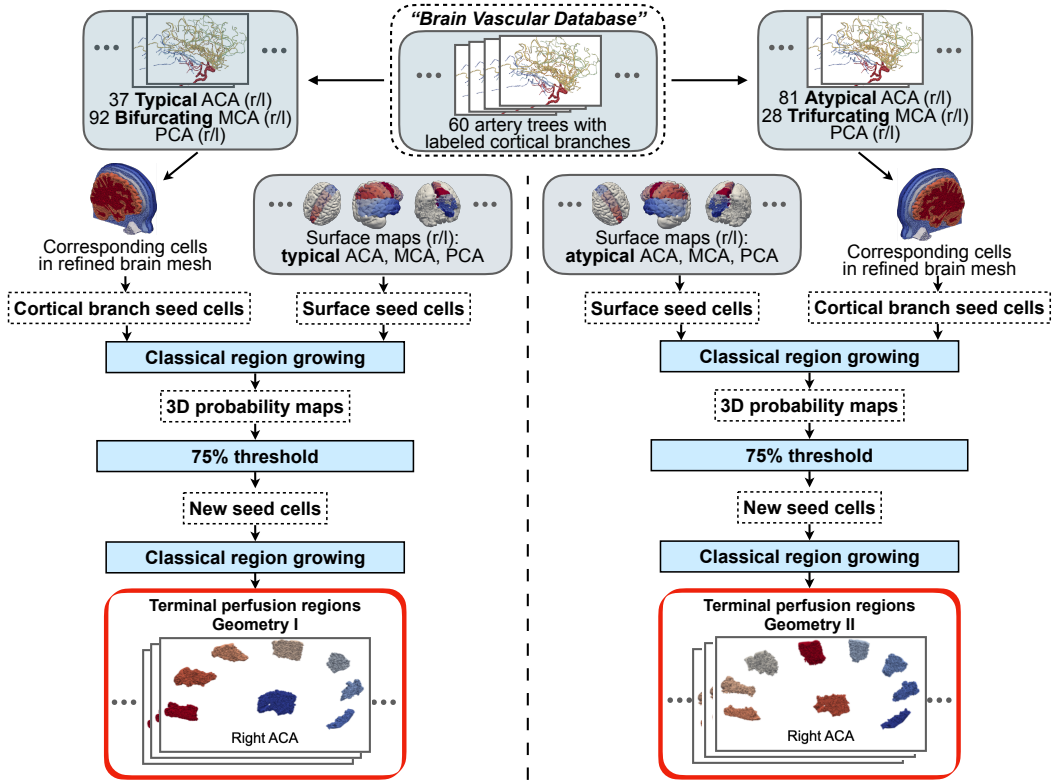

Figure 5.9: Schematic of the division process of the six major vascular territories into terminal perfusion regions. Note: Two ACAs of the 60 artery trees were discarded due to a bihemispheric or an exceptional appearance.

WM with two connected parts for each terminal perfusion region. The exemplary result for the right MCA vascular territory of Geometry I is depicted in Fig. 5.11.

Discussion & Limitations of Sec. 5.2.4

The threshold value for too small GM or WM areas and the reapplication of the classical region growing partly led to local shifts in the original division of GM or WM. However, these shifts were negligibly small due to the small size of the individual reprocessed volumes (cf. Fig. 5.10) and did not lead to changes in the overall composition of the mesh in regard to GM and WM.

5.2.5 Non-Manifolds and Surface Cleaning

Manifolds are an important and widely used mathematical feature in the processing of geometric models [213]: A manifold of the dimension n is a topological space that locally resembles the Euclidean space $\mathbb{R}^n$. The two dimensional case ($n = 2$) reflects that the structure of a surface is locally comparable to a disk in every point. Only at the boundaries, the disk

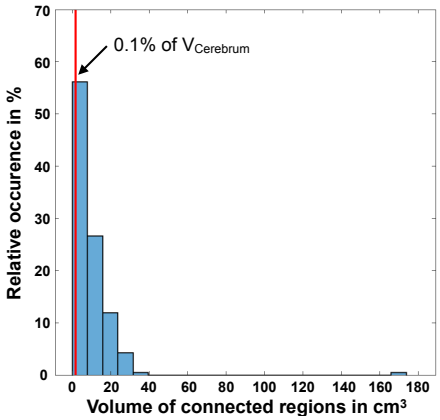

Figure 5.10: Separation of GM and WM led to a fragmentation into many small sub-regions after subdivision into terminal perfusion regions due to the highly convoluted cortex.

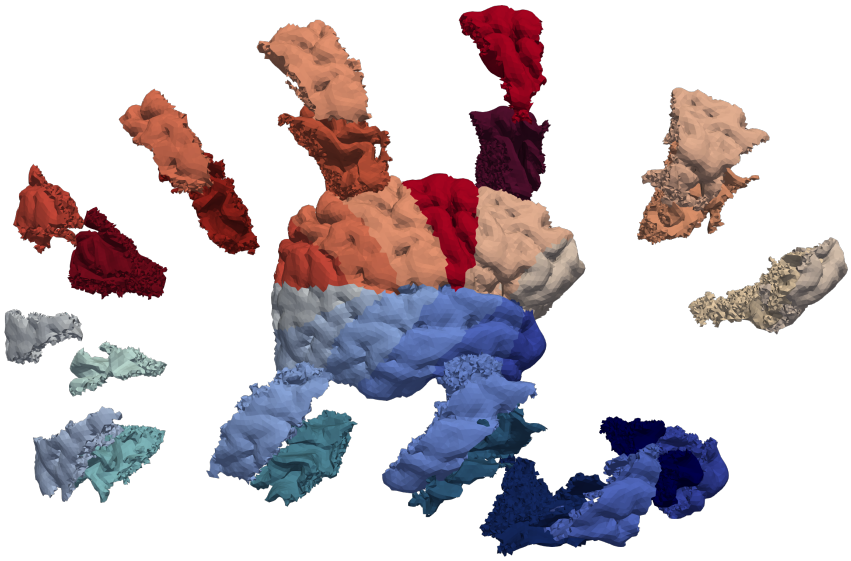

Figure 5.11: Final division into terminal perfusion regions and GM and WM of the right MCA in Geometry I. The "explosion view" gives a better overview on the single terminal perfusion regions with the splitting into GM and WM.

can be truncated [214].

Due to the subdivision of the refined brain mesh (cf. Fig. 5.3 b) into many different perfusion regions by changing the material labels and the application of region growing, the resulting tetrahedral sub-meshes[10] contain geometric errors such as non-manifold edges and/or vertices (cf. Fig. 5.12).

Since faces adjacent to non-manifolds show inconsistencies regarding their orientation, their normal vectors, and their neighborhood [215], the divided mesh could not be used directly for temperature calculation. Instead, the resulting new surfaces between perfusion regions

[10] A sub-mesh reflects an individual perfusion region.

needed to be cleaned first. The surfaces were cleaned iteratively by changing the material of all cells connected to the non-manifold to the most common neighboring material until no more non-manifolds were left.
The non-manifolds edges and vertices were found in different ways: non-manifold edges could be found easily as in a two-manifold mesh without errors, every edge is connected to exactly two faces whereas non-manifold edges are connected to three or more faces.
Non-manifold vertices were found using a graph-based approach: Every face of the mesh's surface was considered to be a node while edges denoted the neighborhood relation between faces. For all vertices of the surface, the adjacent faces were analyzed. For a manifold vertex a path exists from each node to every other node. This results in one single connected graph (cf. Fig. 5.13 a). However, a non-manifold vertex results in two or more separated graphs, which are not connected to each other (cf. Fig. 5.13 b)

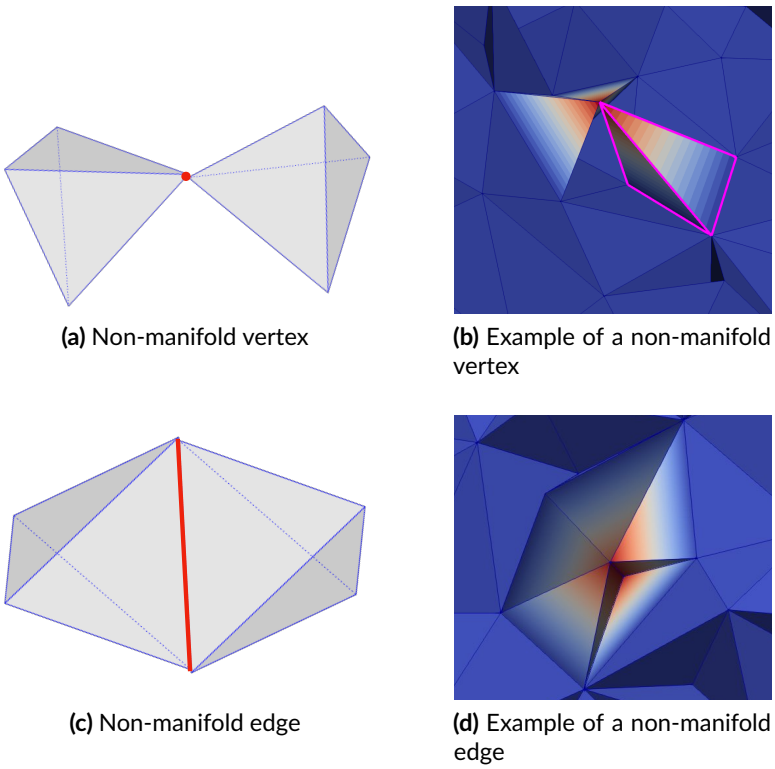

(a) Non-manifold vertex

(b) Example of a non-manifold vertex

(c) Non-manifold edge

(d) Example of a non-manifold edge

Figure 5.12: Possible non-manifolds for a two-manifold [215].

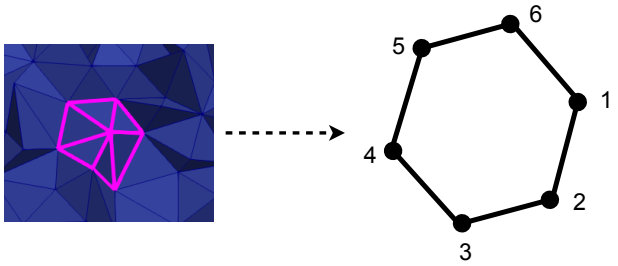

(a) Manifold vertex

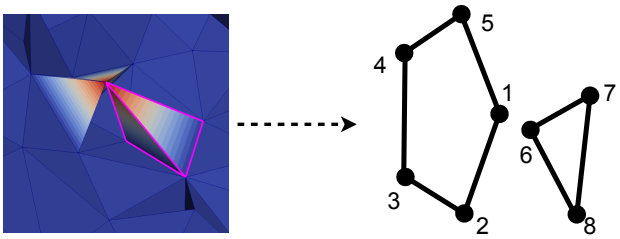

(b) Non-manifold vertex

Figure 5.13: For a manifold vertex, one single connected graph exists. A non-manifold vertex results in two or more separated graphs.

5.2.6 Discussion & Limitations of Sec. 5.2

The human brain atlas "*Colin 27*", which builds the basis for the refined brain mesh, is a standard reference in neuroimaging [191–194]. However, the atlas represents the information of only one individual, namely "Colin Holmes". The extracted cerebrum has a volume of 1456 ml[11]. While literature values vary between mean values of 1100 ml and 1425 ml [30, 216] due to interindividual differences and differences in the measurement technique, the volume of the refined brain mesh is slightly elevated. Furthermore, the lateral ventricles filled with CSF were not excluded in some measurements [30]. Two reasons can explain the elevated volume of the extracted cerebrum: Firstly, the extraction of the brainstem caused deviations. Comparing Fig. 2.9 and Fig. 5.6, one can see that parts of the midbrain could not be distinguished from the cerebrum in the analyzed MR images. Secondly, literature studies show that the "*Colin 27*" brain has a slightly larger volume than the average American male brain (1280 ml) [57, 217].

The brain temperature is mainly influenced by the cerebral blood perfusion and the cerebral metabolic rate. Since these two parameters differ significantly for GM and WM (cf. Tab. B.1), the ratio of GM and WM can have considerable impact on SBH. The "*Colin 27*" brain consists[12] of 44% GM and 56% WM. This composition is not in line with other values from literature, where the share of GM is larger than the share of WM. After an analysis of 52

[11] CSF is not taken into account.
[12] for Geometry I as well as for Geometry II

individuals, Ge et al. stated a share of 59.9% for GM and 40.1% for WM [216], which is in accordance with values proposed by Gur et al. [30] (GM: 55.6%, WM: 44.4%). Both groups used volumetric segmentation of dual echo (proton density and T2-weighted) MRI scans for their analysis. However, both groups also state that the actual percentage share is strongly dependent on the individual's sex and age. The total cerebral blood flow (CBF) resulting from the ratio of GM and WM in the "*Colin 27*" brain sums up to 692 ml/min[13], which is within the range measured by Zaarinkoob et al. [57] (CBF $=717 \pm 123$ ml/min).
Furthermore, in an analysis of all 50 unique head models (reconstructed from MR images) of the "*Population Head Model*" (PHM) Repository [218, 219], the GM to WM ratio showed a wide spread (cf. Fig. 5.14). Additionally, the share of WM exceeds the share of GM for many individuals in the "*PHM Repository*" like in the "*Colin 27*" brain.

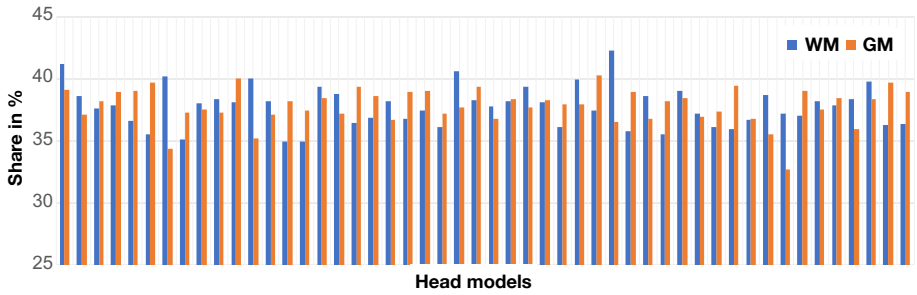

Figure 5.14: GM to WM percentage ratio in all 50 unique head models of the "*PHM Repository*" [218, 219]. The missing percentage share of CSF was omitted for a clearer presentation.

5.3 Boundary Conditions

Pennes' equation was used to model the heat transfer inside the biological tissue of the refined brain mesh. The equation describes the local time-dependent change of tissue temperature depending on three basic terms (cf. Eq. 5.2.) The first term on the right hand-side of the equation accounts for the heat diffusion and is dependent on the heat conductivity of the individual tissue type (cf. Tab. B.1). The second term describes the temperature change due to blood perfusion and is dependent on the blood temperature and the volumetric perfusion rate. Both terms and their modeling are explained in the sections below. The last term represents the produced metabolic heat, which is considered to be temperature dependent.
Besides the dependencies of Pennes' equation, the brain temperature is also affected by heat loss to the environment. The external boundary conditions for tissue with direct contact to the environment are presented in the last part of this section.

[13] considering reference perfusion rates from the IT'IS foundation [119]

5.3.1 Local Perfusion Rates

For the coupling of the hemodynamics model with the brain geometry and for the implementation of spatially different cerebral perfusion rates due to AIS, the refined brain mesh was partitioned into 50 (Geometry I) or respectively 52 (Geometry II) terminal perfusion regions (cf. Sec. 5.2.3). Furthermore, the individual composition of GM and WM for each perfusion region was taken into account. Therefore, the corresponding perfusion rates ($\tilde{\nu}_{\mathrm{GM},i}$, $\tilde{\nu}_{\mathrm{WM},i}$) were calculated individually for each perfusion region i using the corresponding mean terminal flow rate $\tilde{\tilde{q}}_{\mathrm{Bl},i}$ of the cortical branch from the hemodynamics model (cf. Sec. 4.5), the respective volumes of GM and WM ($V_{\mathrm{GM},i}$, $V_{\mathrm{WM},i}$) of the respective terminal perfusion region i (cf. Tab. B.2 and Tab. B.3), and the reference perfusion rates of GM and WM (ν_{GM}, ν_{WM}) from [119] (cf. Tab. B.1):

$$\tilde{\nu}_{\mathrm{GM},i} = \frac{\tilde{\tilde{q}}_{\mathrm{Bl},i}}{V_{\mathrm{GM},i} + \frac{\nu_{\mathrm{WM}}}{\nu_{\mathrm{GM}}} \cdot V_{\mathrm{WM},i}}, \tag{5.4a}$$

$$\tilde{\nu}_{\mathrm{WM},i} = \frac{\tilde{\tilde{q}}_{\mathrm{Bl},i}}{V_{\mathrm{WM},i} + \frac{\nu_{\mathrm{GM}}}{\nu_{\mathrm{WM}}} \cdot V_{\mathrm{GM},i}}. \tag{5.4b}$$

The schematic in Fig. 5.15 visualizes the coupling for Geometry I. Fig. B.1 in the Appendix shows the coupling for Geometry II.

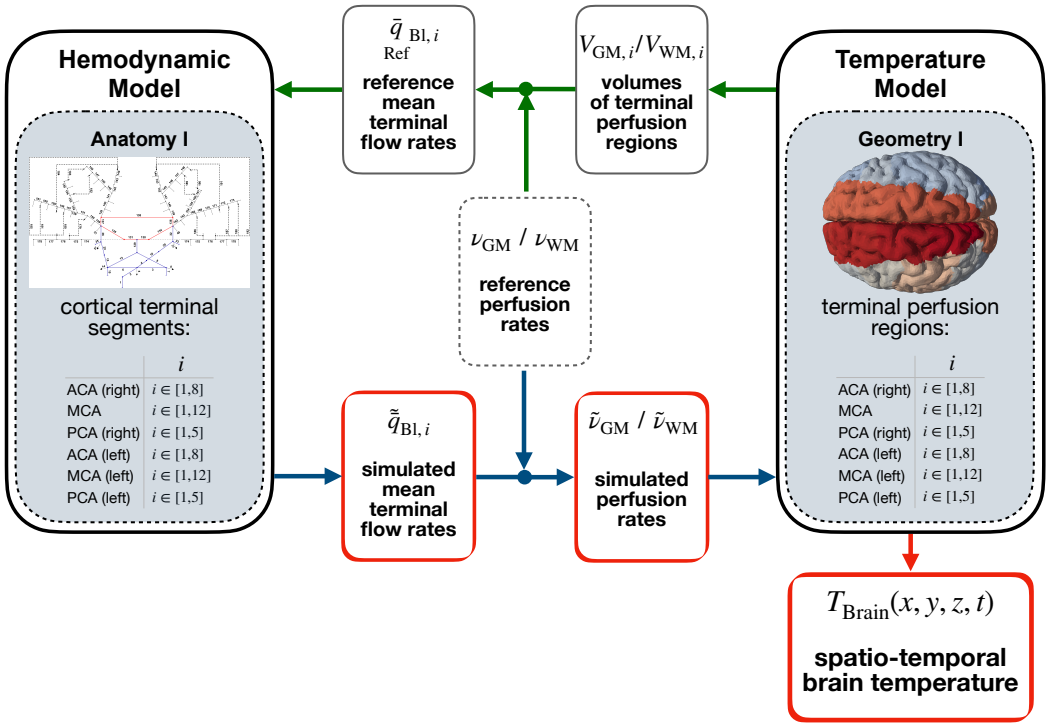

Figure 5.15: Coupling of the hemodynamics and temperature model for Anatomy / Geometry I.

Discussion & Limitations of Sec. 5.3.1

For the determination of the spatial volumetric perfusion rates for each terminal perfusion region, the mean terminal flow rates $\tilde{\tilde{q}}_{\mathrm{Bl},i}$ of the corresponding cortical branches from the hemodynamics model were used. This approach does not require a direct temporal coupling of the hemodynamics model with the temperature model. However, the approach implies the assumption that only the mean perfusion influences the resulting tissue temperature while the actual pulsatile blood flow (cf. Fig. 5.16 a) can be neglected. To verify this assumption, a simplified temperature simulation was performed using a spherical geometry with two layers. The thermal properties of the outer layer were set to those of GM and those of the inner layer to WM. Additionally, the volume of the sphere as well as the ratio of GM to WM corresponded to the refined brain geometry. With two simulations, a temporally constant perfusion was compared to a pulsatile perfusion from the hemodynamics model. In both cases, the tissue was assumed to be perfused with cold blood (30 °C). As demonstrated in Fig. 5.16 b, pulsatile perfusion proved to have no influence on the temporal temperature course.

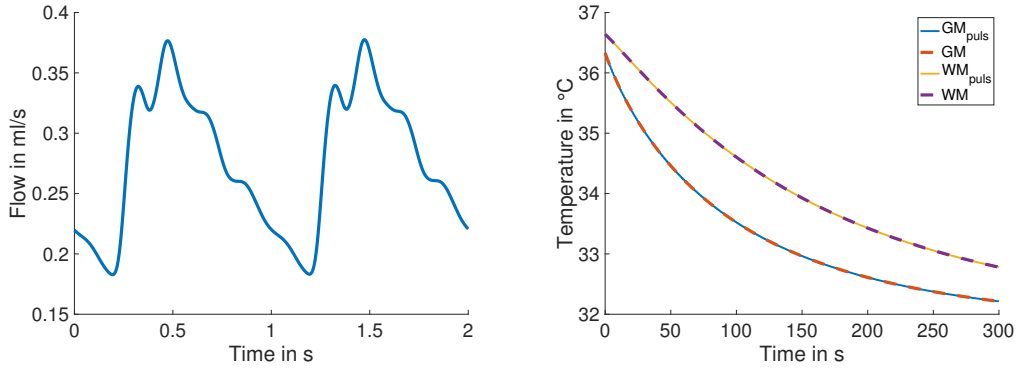

(a) Flow into the right temporopolar MCA branch **(b)** Temperature course for constant and pulsatile perfusion

Figure 5.16: Course of mean temperature in a simplified geometry for GM and WM for a blood temperature of 30 °C. Pulsatile blood flow (a) had no influence on the temporal temperature course (b).

5.3.2 Blood Temperature

Endovascular Blood Cooling

The aim of this work is to predict spatial and temporal cerebral temperature profiles for different SBH scenarios to evaluate the effectiveness and the influences for SBH as therapy

for AIS. As explained in Sec. 2.5.4, this work presumes that the local therapeutic hypothermia is induced by a recently developed endovascular catheter system placed in the right CCA[14, 106], which cools the passing blood by heat exchange.
After analyzing in vitro experiments with artificial blood (cf. Sec. 2.5.4) and consulting the catheter manufacturer, an instantaneous drop in blood temperature of 2 °C from the inlet (systemic temperature T_{Sys}) to the outlet temperature ($T_{\mathrm{CCA,right}}$) at the distal tip of the catheter was assumed:

$$T_{\mathrm{CCA,right}} = T_{\mathrm{Sys}} - 2\,^{\circ}\mathrm{C}.$$

This means that blood flowing through the right CCA behind the cooling catheter is always 2 °C colder than the current systemic temperature.

Discussion & Limitations of Modeling Endovascular Blood Cooling

In reality, the cooling power of the catheter is dependent on various parameters like the blood flow rate, the blood temperature, the vessel architecture, the coolant conditions, which are completely neglected in this work. On the one hand, for higher blood flow rates in the right CCA caused by stress, the cooling rate would decrease [14]. On the other hand, the flow rates would decrease for a LVO due to a changed CBF and the cooling effect would increase. Furthermore, the cooling effect of the catheter is dependent on the difference between the temperature of the coolant and the blood (cf. Sec. 3.2.2). If the blood temperature decreases due to systemic cooling caused by venous blood return (cf. Sec. 5.3.3), the cooling power would decrease as well.
However, there is a lack of clinical studies due to the novelty of the catheter system. Therefore, a constant mean temperature drop of 2 °C caused by the catheter was assumed. This assumption reflects a compromise and disregards the influences mentioned above to evaluate the general cooling effect of the catheter.

Blood Mixing

For the case of endovasular blood cooling, the blood temperature in Pennes' equation (Eq. 5.2) is not at systemic temperature (T_{Sys}) but depends on the blood path on which individual blood mixing with blood coming from other arterial branches (cf. Fig. 4.16 and Fig. A.1) is possible.
Cooled blood (at $T_{\mathrm{CCA,right}}$) flows into the right external carotid artery (ECA) and right ophthalmic artery. Therefore, in the model it was assumed that this cold blood directly perfuses the right side of the outer shells (except for the CSF) of the geometry (cf. Fig. 5.3 b). The cerebrum is supplied by a blood mixture with cold blood from the right internal carotid artery (ICA), and warm blood from the BA and the left CCA. Therefore, at each branching point of the main cerebral arteries, the temperature of the resulting blood mixture was calculated to account for the influence of the primary and secondary collaterals:

$$T_{\text{mix}} = \frac{\sum_{j=1}^{n} T_j \cdot q_j}{\sum_{j=1}^{n} q_j},$$

where T_{mix} is the resulting temperature after mixing of the n influxes q_j with their respective temperatures T_j.

To account for changes in the direction of the fluxes in the hemodynamics model due to vessel occlusion, a universally applicable blood temperature mixing was established by the definition of reference blood flow directions[14] for physiological conditions and adding a "*Heaviside*" step function H to include only inflow with a positive sign:

$$\begin{aligned} T_{\text{mix}} = &\frac{\sum_{j=1}^{n} T_j \cdot |q_{\text{in},j}| \cdot H(q_{\text{in},j})}{\sum_{j=1}^{n} |q_{\text{in},j}| \cdot H(q_{\text{in},j}) + \sum_{k=1}^{m} |q_{\text{out},k}| \cdot H(-q_{\text{out},k})} \\ &+ \frac{\sum_{k=1}^{m} T_k \cdot |q_{\text{out},k}| \cdot H(-q_{\text{out},k})}{\sum_{j=1}^{n} |q_{\text{in},j}| \cdot H(q_{\text{in},j}) + \sum_{k=1}^{m} |q_{\text{out},k}| \cdot H(-q_{\text{out},k}),} \end{aligned} \tag{5.5}$$

with n being the number of defined influxes and m the number of outfluxes per node.

Following this approach, for every branching node, the blood temperature $T_{\text{Bl},i}$ of the arterial blood perfusing a terminal perfusion region i was defined as the resulting mixed temperature T_{mix} of the node connected to the respective terminal segment.

5.3.3 Venous Blood Return

Subsequent to supplying the brain parenchyma with oxygen and nutrients, the venous blood accumulates in the dural venous sinuses and reenters the systemic circulation mostly via the internal jugular vein [41] (cf. Sec. 2.3.2). Due to this venous blood return, the endovascular blood cooling has also an effect on the systemic body as observed in first animal studies with nine sheep [106]. In this work, an energetic model of the systemic body [148–150, 220] was used to evaluate the temporal change in systemic temperature T_{Sys} due to blood cooling. Since the human body can be considered as homoiothermic under physiological conditions, the energetic model focuses on the heat exchange between head and body due to the return of cold venous blood coming from the brain. Heat generation and dissipation as well as temperature regulation in other regions of the body were neglected:

$$\frac{\mathrm{d}T_{\text{Sys}}}{\mathrm{d}t} = -\frac{\rho_{\text{Bl}} c_{\text{Bl}}}{M_{\text{Sys}} c_{\text{Sys}}} \cdot \sum_i q_{\text{Bl},i} \cdot (T_{Sys} - T_{\text{T},i}), \tag{5.6}$$

[14] Physiological blood flow directions: ACoA: left to right, PCoA: PCA to ICA, ACA-MCA secondary leptomeningeal collaterals (SLCs): direction to the MCA, PCA-MCA SLCs: direction to the MCA, ACA-PCA SLCs: direction to the ACA.

where M_{Sys} represents an average systemic mass, c_{Sys} an average heat capacity of the systemic human body[15], $q_{\mathrm{Bl},i}$ the blood flow rate to the terminal perfusion region i and $T_{\mathrm{T},i}$ the tissue temperature of the terminal perfusion region i.

Discussion & Limitations of Sec. 5.3.3

This approach only considers the influence of cold venous blood return on the systemic body temperature. Despite the unphysiological conditions caused by the AIS and despite endovascular blood cooling, the physiologically homoiothermic core body temperature was assumed to be maintained in the thermoneutral zone (cf. Sec. 2.6), such that discrete modeling of thermoregulation is not necessary. This assumption is justifiable especially under conditions of anesthesia, which significantly increases the thermoneutral zone [110, 111] (cf. Sec. 2.6).
Additionally, many simulation studies on SBH by other groups neglect the influence of venous blood return completely [187, 208, 221, 222], stating a desired focus on the impact of the analyzed cooling method.

5.3.4 Temperature Dependencies

If the body is put into hypothermia, the CMR drops below the basal rate (cf. Tab. B.1). This is normally coupled to a decrease in CBF. Konstas et al. [208] analyzed this effect of hypothermia on CBF and cerebral metabolism in a comprehensive literature survey of animal and human data. For mean brain temperature above 25 °C, Konstas et al. derived an exponential decrease for both CBF and metabolism, which was used in this work to account for temperature dependence in each terminal perfusion region i individually:

$$\zeta_i\left(T_{\mathrm{T},i}\right) = \tilde{\zeta}_i \cdot 2.961^{0.08401\cdot(T_{\mathrm{T},i}-37\,°C)}, \tag{5.7}$$

where $\tilde{\zeta}_i$ is either the baseline metabolic power density ($\dot{w}_{\mathrm{Met}}$ in $\frac{W}{m^3}$) at 37 °C (cf. Tab. B.1), or the baseline perfusion rate of GM and WM ($\dot{w}_{\mathrm{i}}$ in $\frac{1}{\mathrm{s}}$) calculated according to Eq. 5.4.

Discussion & Limitations of Sec. 5.3.4

The regulation of CBF and brain temperature is a complex control circuit. The effect of SBH in combination with ischemia on CBF is largely unknown and different hypotheses are discussed and proposed in literature. Some studies even suppose that hypothermia causes an increase in CBF. In an experimental study with isolated vessels of New Zealand white rabbits, Mustafa et al. [223] observed a cooling-induced carotid artery dilatation, which could possibly lead to increased flow rates. Furthermore, Mustafa et al. assumed that this increase might have caused the positive effect observed using selective TH for the treatment of

[15] M_{Sys}=75 kg, c_{Sys}=3470 $\frac{J}{kg\cdot K}$

ischemic stroke in animal studies. This hypothesis is similar to an approach by Zhu et al. and Sukstanskii et al. [224–226], which describes a so-called shielding effect against temperature changes in the brain parenchyma induced by external cooling.
However, these theories and observations describe reactions to external brain or vessel cooling. If endovasular blood cooling is the cause for a decrease in temperature, it remains questionable whether the blood flow would still increase or remain the same. Therefore, the approach by Konstas et al. [208] was chosen in this work since they pooled data from studies investigating the effect of intra-cranial CSI, which is similar to endovascular blood cooling with a heat exchange catheter.

5.3.5 Heat Transfer to the Environment

As mentioned in Sec. 2.6, man is a homoiothermic being with an almost constant mean body core temperature. This means that the heat emission of the body is in balance with the metabolic heat produced by the body itself. The body can exchange heat with its surroundings through the skin. Conduction, convection, radiation, and evaporation are used as forms of heat transfer (cf. Sec. 3.2.2). The following sections explain how the different forms of heat transfer from the skin of the head to the environment were modeled in this work. For all forms, the environment was considered to have the constant temperature $T_{\text{env}} = 20\,^{\circ}\text{C}$.

Convection

In Sec. 3.2.2, a heat transfer coefficient α was introduced to describe the convective heat flux between a surface of a solid and a fluid. Among others, the heat transfer coefficient depends on the following factors:

- the flow velocity and flow type (laminar or turbulent),
- properties and shape of the surface,
- the material properties of the fluid and its aggregate state,
- free or forced convection.

Since an exact estimation of α is hardly possible, the estimation in this work was based on the similarity theory, which is suitable for and often used in applications for standard bodies and fluids with known material properties [117].
Ernst Nußelt, one of the founders of the similarity theory, introduced the Nußelt number Nu for calculations in fluid mechanics [117]. The Nußelt number is dimensionless and can be calculated as follows:

$$Nu = \frac{\alpha \cdot L}{\lambda_{\text{fluid}}}, \tag{5.8}$$

where L is the characteristic length of the fluid dynamical problem considered and λ_{fluid} is the heat conductivity of the streaming around fluid. For the calculation of the convective heat

flux, Eq. 5.8 is rearranged and two more dimensionless numbers are introduced. The Prantl number Pr links the material properties of the fluid:

$$Pr = \frac{\nu \cdot c_p \cdot \rho}{\lambda_{\text{fluid}}},$$

where ν is the kinematic viscosity, c_p the pressure-dependent specific heat capacity, and ρ the density of the fluid.
The Grashof number Gr expresses the properties of the fluid surrounding the problem under consideration of its dynamics:

$$Gr = \frac{L^3 \cdot g \cdot \beta}{\nu^2} \cdot \left(T_{\text{surface}} - T_{\text{fluid}}\right),$$

where g is the acceleration of gravity and β is the coefficient of thermal expansion[16].
The Rayleigh number Ra is the result of multiplying Gr and Pr:

$$Ra = Gr \cdot Pr = \frac{L^3 \cdot g \cdot \beta \cdot c_p \cdot \rho}{\nu \cdot \lambda_{\text{fluid}}} \cdot \left(T_{\text{surface}} - T_{\text{fluid}}\right).$$

For the convective heat flux $\dot{q}_{\text{conv}}$ from the head to the environment, external free convection was assumed and the head to be an ideal sphere.
For a sphere and free convection, the mean Nußelt number $\widetilde{Nu}_{\text{sphere}}$ can be calculated as follows [227]:

$$\widetilde{Nu}_{\text{sphere}} = 2 + \frac{(0.589 \cdot Ra)^{\frac{1}{6}}}{\left(1 + (\frac{0.469}{Pr})^{\frac{9}{16}}\right)^{\frac{4}{9}}}.$$

Using Eq. 3.26 and inserting $\widetilde{Nu}_{\text{sphere}}$ in Eq. 5.8 (with the characteristic length L being set to the sphere's diameter ($d_{\text{sphere}} = 0.2\,\text{m}$)), the convective heat flux was calculated:

$$\dot{q}_{\text{conv}} = \frac{\widetilde{Nu}_{\text{sphere}} \cdot \lambda_{air}}{d_{\text{sphere}}} \cdot \left(T_{\text{env}} - T_{\text{surface}}\right).$$

Radiation

Since Hardy's pioneering experiments [228], the skin is assumed to be an almost ideal black body for the infrared range. This assumption is also supported by more recent experiments in which the difference of two infrared images was calculated: one acquired before projecting a CO_2 laser beam onto the surface of the skin and the other after such projection. The difference image contains the radiation reflected by the skin, which can be used to calculate the emission coefficient [229].
Therefore, the emission coefficient of the scalp was assumed to be $\epsilon_{\text{skin}} = 0.995$.

[16] equal to $\approx \frac{1}{T}$, for ideal gases

Evaporation

In a closed operating room at an ambient temperature of 20 °C, the heat dissipation by evaporation is almost at its temperature-independent baseline value. For the determination of a baseline value for the head, data of Gordon et al. [108] were used:

$$\dot{q}_{\text{evap}} = 7.4 \frac{\text{W}}{\text{m}^2}.$$

Discussion & Limitations of Sec. 5.3.5

In this work, heat transfer from the skin to the environment is considered only for the head. In reality, the patient is lying on an operating table and there is additional heat transfer from the body to the environment as well as heat release via respiration. In a supervised student's Master's thesis [230], the possible effect of varying conditions for the contact to an operating table on the systemic temperature was analyzed on the basis of a simplified body geometry [113, 230, 231]. Furthermore, body core temperature regulation by the adjustment of skin tissue perfusion was integrated. For this purpose, the approach of Fiala et al. [232], which had also been used in the work of Schwarz and his predecessors [113, 121, 233], was adopted. Seim [230] showed in her work that changes in the systemic temperature due to varying environment and coupling conditions also affect cerebral cooling. However, for the procedure of SBH, an additional systemic TH is aimed to be avoided to reduce the risk of possible side effects such as pneumonia. The body temperature is assumed to stay within the thermal neutral zone of temperature regulation. For these reasons and since this work focuses on the modeling of the spatial temperature change by SBH, the consideration of a discrete body model was omitted.

5.3.6 Evaluation of Cerebral Temperatures for Physiological Conditions

For normal environmental conditions and in a physiological state, man is a homoiothermic being. Therefore, the produced heat of the body should be in balance with the dissipated heat to the environment, and a steady state cerebral temperature close to the physiological reference temperature of 37 °C should be reached.
For the assumed boundary conditions[17] (cf. Sec. 5.3), the simulation resulted in a steady state with a mean cerebral temperature of 37.2 °C, a mean temperature for GM of 37.1 °C, and a mean temperature for WM of 37.3 °C (cf. Fig. 5.17 a). The mean surface temperature of the head's skin was 31.9 °C and the mean heat heat flux from the head's surface to the environment was $114.4 \frac{\text{W}}{\text{m}^2}$.

[17] Since no endovascular blood cooling was simulated, the cold venous blood return was not considered.

Fig. 5.17 b shows a transversal section of the resulting physiological perfusion rates. The volumetric mean perfusion rate in GM (0.0136 1/s) and WM (0.0038 1/s) were in good accordance with the reference perfusion rates (cf. Tab. B.1 and Eq. 5.4).

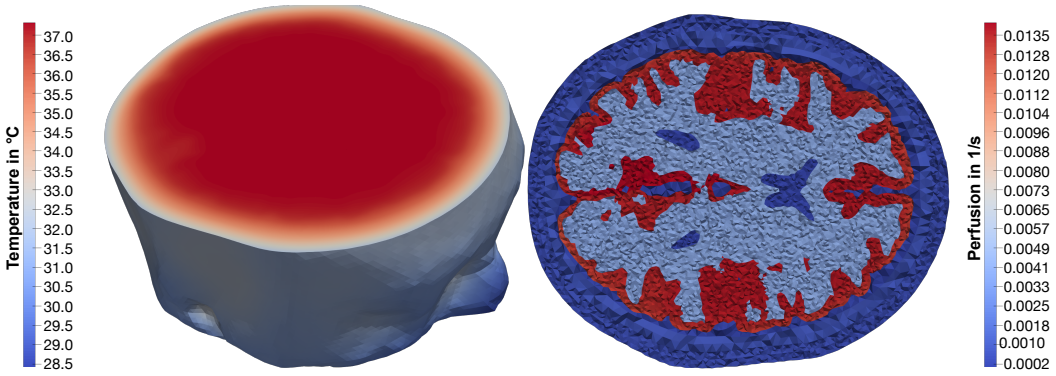

(a) Tissue temperature **(b)** Volumetric perfusion

Figure 5.17: For physiological conditions and the considered boundary conditions the model resulted in a realistic steady state.

5.4 Simulation of Cerebral Temperature for an MCA-M1 Occlusion

The bioheat transfer module of *COMSOL Multiphysics* version 5.4 was used for all temperature calculations. For the calculation of an initial spatial temperature ($T_{\mathrm{T,initial}}$) distribution, a steady-state study was conducted at first. Therefore, all tissue temperatures were set to $T_{\mathrm{T}} = 37\,^{\circ}\mathrm{C}$ and the systemic temperature was fixed to $T_{\mathrm{Sys}} = 37\,^{\circ}\mathrm{C}$. For the subsequent calculations of the time dependent studies ($t \in [0\,\mathrm{s},\ 1800\,\mathrm{s}]$) with endovascular blood cooling, the calculated initial temperature distribution was used as starting temperature ($T_{\mathrm{T}}(t=0) = T_{\mathrm{T,initial}}$) at each point. The venous blood return coupling as well as the blood cooling were activated.

5.4.1 Geometry I vs II

As shown in Fig. 5.18 and Fig. 5.19, the strongest temperature decrease was observed in the right ACA vascular territory ($\approx$ 1.6 °C after 30 min of cooling) for both geometries. Although, the initial temperature before cooling was almost identical for both geometries, a stronger temperature decrease after 30 min of cooling was observed for Geometry I.
Before the start of cooling, the mean temperature in the MCA vascular territory was elevated compared to the physiological reference temperature range (36.8 – 37.2 °C [19, 20]). The

mean temperature of the MCA vascular territory before cooling in Geometry II exceeded the respective temperature in Geometry I ($T_{\mathrm{MCA}}(0\,min) = 37.6\,°\mathrm{C}$) by 0.1 °C (cf. Fig. 5.19, first column). Furthermore, a smaller cooling effect in the MCA vascular territory was observed for Geometry II: after 30 min of cooling, Geometry I resulted in a mean temperature decrease of $\Delta T_{\mathrm{MCA}}(30\,min) = -1\,°\mathrm{C}$ while the mean temperature decrease was $\Delta T_{\mathrm{MCA}}(30\,min) = -0.7\,°\mathrm{C}$ for Geometry II.
Additionally, the spatial temperature distribution showed slight differences (cf. Fig. 5.19): after 30 min of cooling, the remaining highest parenchyma temperature in the MCA vascular territory was lower in Geometry I. The remaining hot spot was more focal in Geometry I since the temperature decrease in regions close to the vascular territories of the ACA and PCA was higher.
Outside the vascular territories of the right ACA and the right MCA, the resulting temperatures did not differ between the geometries. In the left hemisphere, no distinct change in temperature due to endovascular blood cooling was observed, except for a weak cooling of the vascular territory of the left ACA (cf. Fig. 5.18 b).

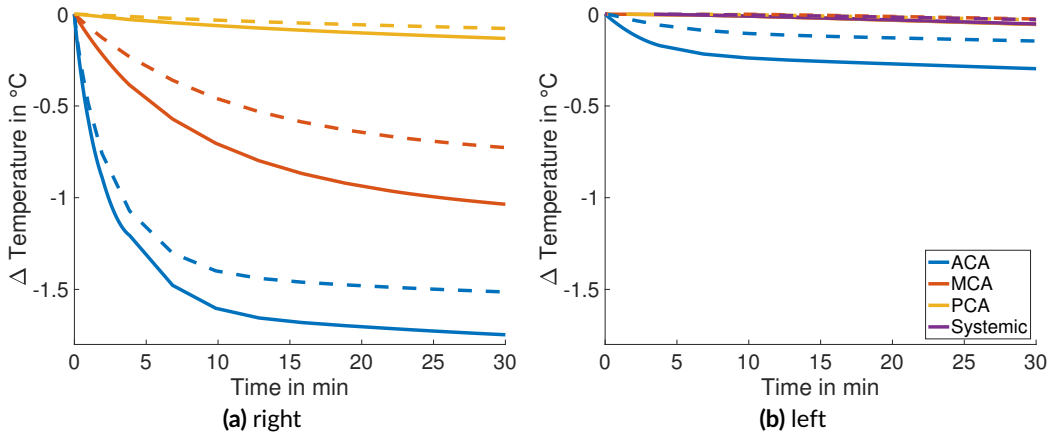

(a) right **(b)** left

Figure 5.18: Temporal course of the mean temperature of the major vascular territories in case of a right MCA-M1 occlusion. The solid lines represent the results for Geometry I and the dashed lines the respective results for Geometry II (complete CoW, "partial" collateralization).

Discussion & Limitations of Sec. 5.4.1

As already described in Sec. 4.5.2, the two anatomies of the main cerebral arteries in the hemodynamics model resulted in different mean blood flow rates to the major vascular territories (11.4% higher total blood flow into the MCA vascular territory in Anatomy I compared to Anatomy II). Generally, the blood perfusion ensures that the heat produced by the metabolism is dissipated. Therefore, the higher remaining perfusion in Geometry I caused the lower initial mean temperature in the MCA vascular territory.

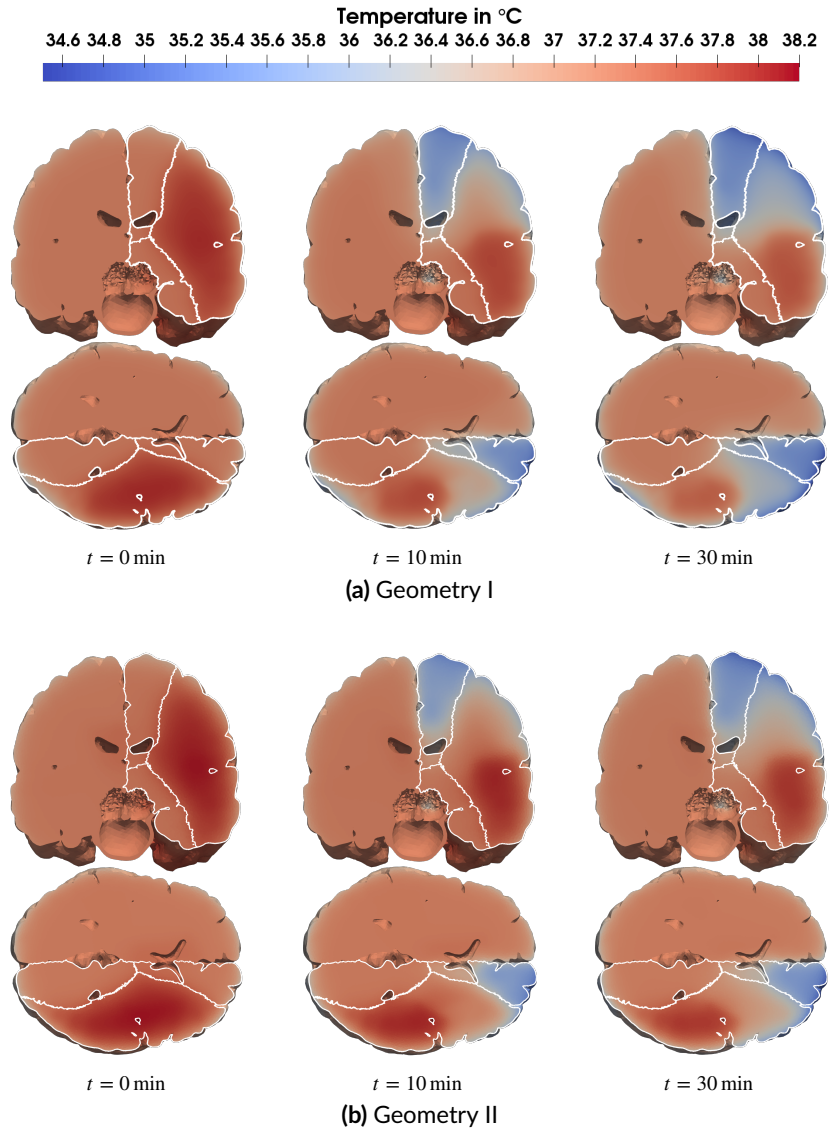

Figure 5.19: Frontal and transversal sections of the cerebrum showing the tissue temperature 0, 10 and 30 min after the start of cooling ('partial" collateralization, complete CoW). The white lines represent the boundaries of the three major vascular territories in the right hemisphere.

The lower temporal cooling effect for Geometry II was partly caused by the lower remaining perfusion. The main reason, however, was the different composition of the SLC flow to the MCA vascular territory: Anatomy II resulted in a smaller remaining SLC flow from the ACA (by 36%) and a higher remaining SLC flow from the PCA (by 10%) compared to Anatomy I (cf. Fig. 4.24e). Since only the SLCs from the ACA bring cold blood to the vascular territory of the MCA in case of the MCA-M1 occlusion, this led to a higher cooling effect.

Since the other anatomical variations considered in this study are identical for Geometry I and II, the relative outcome is identical. Therefore, the results of the other considered anatomy variations are only presented for Geometry I, as it is the more common case in anatomical studies (cf. Sec. 4.2).

5.4.2 Variation of the Secondary Collateralization Degree

To ensure a delimitation of the effects by the individual variation of the cerebral circulation, the resulting temperature courses for different degrees of secondary collateralization are presented only in case of a complete CoW.
Depending on the status of the secondary leptomeningeal collaterals ('poor', 'normal', 'strong'), the perfusion of the right MCA vascular territory decreased by 83.2%, 71.0%, or 56.0% in case of an occlusion in the right MCA-M1 segment compared to no occlusion. This caused different initial mean temperatures in the right MCA vascular territory: For a "strong" collateralization, the mean temperature was 0.2 °C below and for a "poor" collateralization 0.3 °C above the mean temperature for a "partial" collateralization (cf. Fig. 5.20 a, Fig. 5.21).
Despite the differences in the remaining perfusion of the MCA vascular territory, the initial temperature difference remained largely constant during the cooling process (cf. Fig. 5.20 a). The secondary collateralization degree affected the resulting mean temperature after 20 min of cooling only slightly. However, the temperature decrease was noticeably different and resulted in values of 0.78°C, 0.71°C, or 0.6°C for "poor", "partial", or "strong"collateralization after the first 10 min of cooling. After 30 min of cooling, on the contrary, the temperature decrease was $\Delta T_{\mathrm{MCA}}(30\,min) = -1.0\,°\mathrm{C}$, independent of the secondary collateralization degree (cf. Fig. 5.20 a).

Discussion & Limitations of Sec. 5.4.2

The decrease in remaining perfusion had a major impact on the resulting initial temperature and caused a higher mean temperature of the MCA vascular territory for a "poor" degree of collateralization compared to "partial" and "strong" collateralization. Although the remaining secondary collateral flow was highly dependent on the collateralization degree (cf. Sec. 4.5.2), the effect on resulting temperature decrease after 30 min of cooling was the same for the three collateralization degrees. The secondary collateral radii were altered uniformly for all 14 collaterals in the hemodynamics model. Therefore, an in- or decrease in collateral radius led to in- or decreased perfusion with cold blood from the cooled ACA. However, the change in collateral radius led exactly to the same in- or decreased perfusion with blood from the non-cooled PCA.
An individual adaptation of the SLCs by evaluating digital subtraction angiography (DSA) cranial computed tomography (CCT) images could lead to more detailed distributions and could influence the spatial temperature distribution.

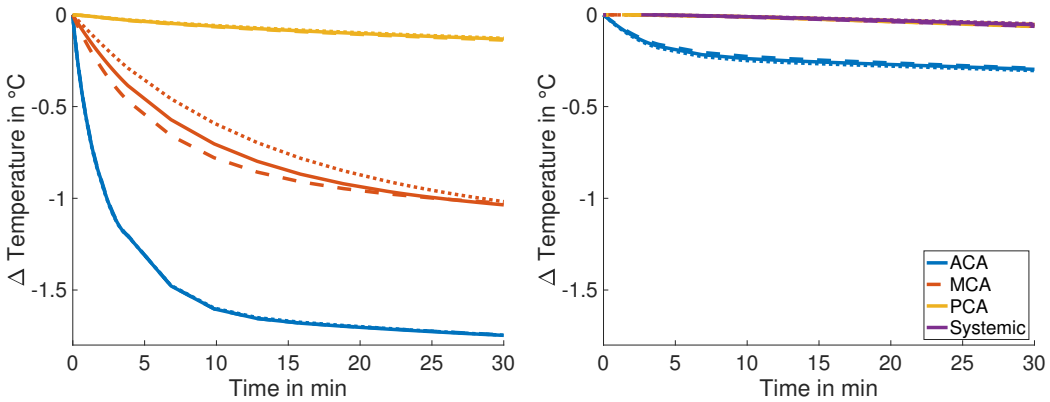

(a) right **(b)** left

Figure 5.20: Temporal course of the mean temperature of the major vascular territories in case of a right MCA-M1 occlusion. The solid lines represent the results for a "partial", the dashed lines for a "strong" and the dotted lines the results for a "poor" collateralization degree (complete CoW, Geometry I). The blue and yellow dashed and dotted lines are covered by the solid lines in (b).

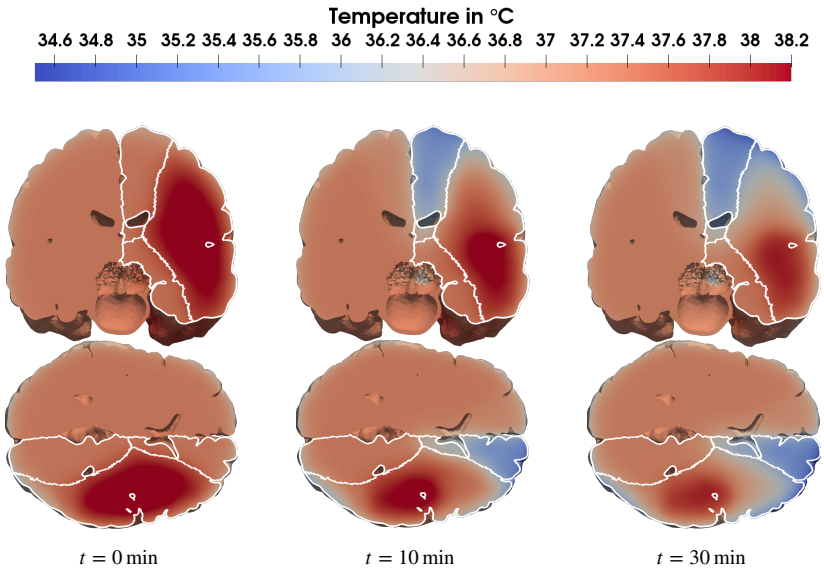

$t = 0\,\text{min}$ $t = 10\,\text{min}$ $t = 30\,\text{min}$

(a) "Poor" collateralization

$t = 0\,\text{min}$ $t = 10\,\text{min}$ $t = 30\,\text{min}$

(b) "partial" collateralization

$t = 0\,\text{min}$ $t = 10\,\text{min}$ $t = 30\,\text{min}$

(c) "Strong" collateralization

Figure 5.21: Frontal and transversal sections of the cerebrum showing the tissue temperature 0, 10 and 30 min after the start of cooling (complete CoW, Geometry I). The white lines represent the boundaries of the three major vascular territories in the right hemisphere.

5.4.3 Variation of the Circle of Willis

As shown in the evaluation of the results of the hemodynamics model (cf. left side of Fig. 4.25), a missing right ACA-A1 segment and a missing right PCA-P1 segment resulted in the highest decrease (-17.6% and -15.2%) in the total mean flow into the vascular territory of the right MCA compared to a complete CoW. The other variations in the CoW did not result in distinctly changed blood flow conditions for an occluded MCA-M1 segment. Therefore, the resulting temperatures are only presented for these two CoW variations in combination with a "partial" collateralization degree.

Compared to a complete CoW, the cooling effect in the right MCA vascular territory was negligibly low for a missing right ACA-A1 segment (< -0.1 °C after 30 min of cooling) (cf. Fig. 5.22 a and Fig. 5.23 b).

On the other hand, a missing right PCA-P1 segment resulted in an increased cooling effect for the right MCA and right PCA vascular territory compared to a complete CoW (cf. Fig. 5.22): A decrease by 1°C in the mean temperature of the right MCA vascular territory was reached after 6.3 min of cooling, while 25 min were needed for a complete CoW. The cooling effect after 30 min was increased by 90% compared to a complete CoW, resulting in a mean temperature decrease of 1.9 °C in the MCA vascular territory.

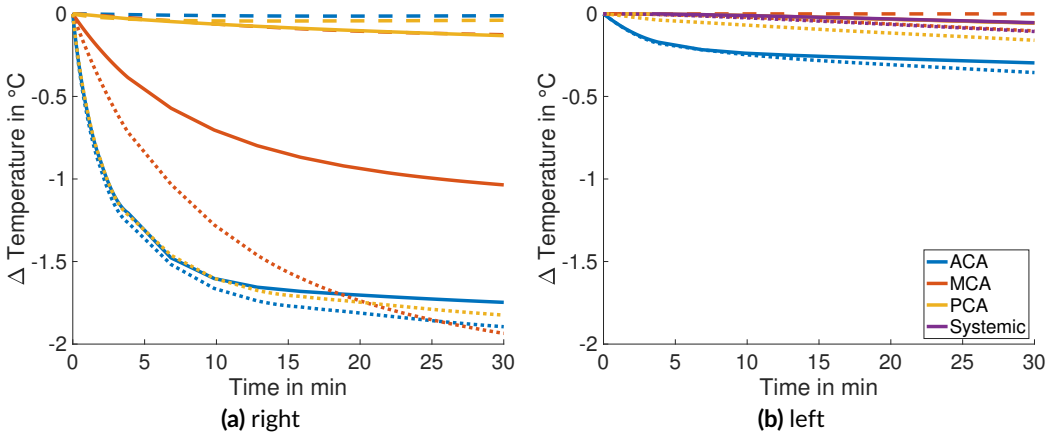

(a) right **(b)** left

Figure 5.22: Temporal course of the mean temperature of the major vascular territories in case of a right MCA-M1 occlusion. The solid lines represent the results for a complete CoW, the dashed lines for a missing right ACA-A1 segment, and the dotted lines the results for a missing right PCA-P1 segment ("partial" collateralization, Geometry I).

Discussion & Limitations of Sec. 5.4.3

The resulting mean temperature decrease in the MCA vascular territory after 30 min of cooling varied markedly between 0.13 °C and 1.94 °C for a missing ACA-A1 or a missing PCA-P1 segment. Due to the blocked inflow into the MCA-M1 segment, the perfusion of the MCA vascular territory was completely provided by blood originating from the secondary collateralization. Therefore, the cooling effect depended mainly on the origin of the collateral blood flow.
The small cooling effect for a missing ACA-A1 segment was caused by the changed blood flow direction in the ACoA. The missing flow through the ACA-A1 segment into the ACA was compensated by the change of flow direction in the ACoA (from -0.12 ml/s to $+1.66$ ml/s, Fig. 4.25 b (left)). As a result, the SLCs between the right ACA and the right MCA were perfused with blood originating from the left brain hemisphere (cf. Fig. A.2) at systemic temperature. The SLCs between the right PCA and the right MCA are also perfused with blood having systemic temperature. Therefore, cooled blood could not reach the parenchyma. For a missing right PCA-P1 segment on the other hand, the cooling effect was increased compared to a complete CoW (by 90% after 30 min of cooling). For a complete CoW, the PCA is perfused with blood originating from the BA at systemic temperature. If the right PCA-P1 segment is missing, blood from the BA cannot enter the right PCA (cf. Fig. A.2). Therefore, the missing PCA-P1 segment is compensated by a changed flow direction in the right PCoA (+0.05 ml/s to -1.28 ml/s) and the SLCs between the right PCA and the right MCA are perfused with cooled blood from the right ICA. In this case, the MCA vascular territory is solely perfused with cooled blood, which leads to a distinctly increased cooling rate.

Tab. 5.2, lists the initial mean temperature and the decrease after 10, 20, and 30 min of cooling for all major vascular territories of the right hemisphere for all considered variations in cerebral anatomy.

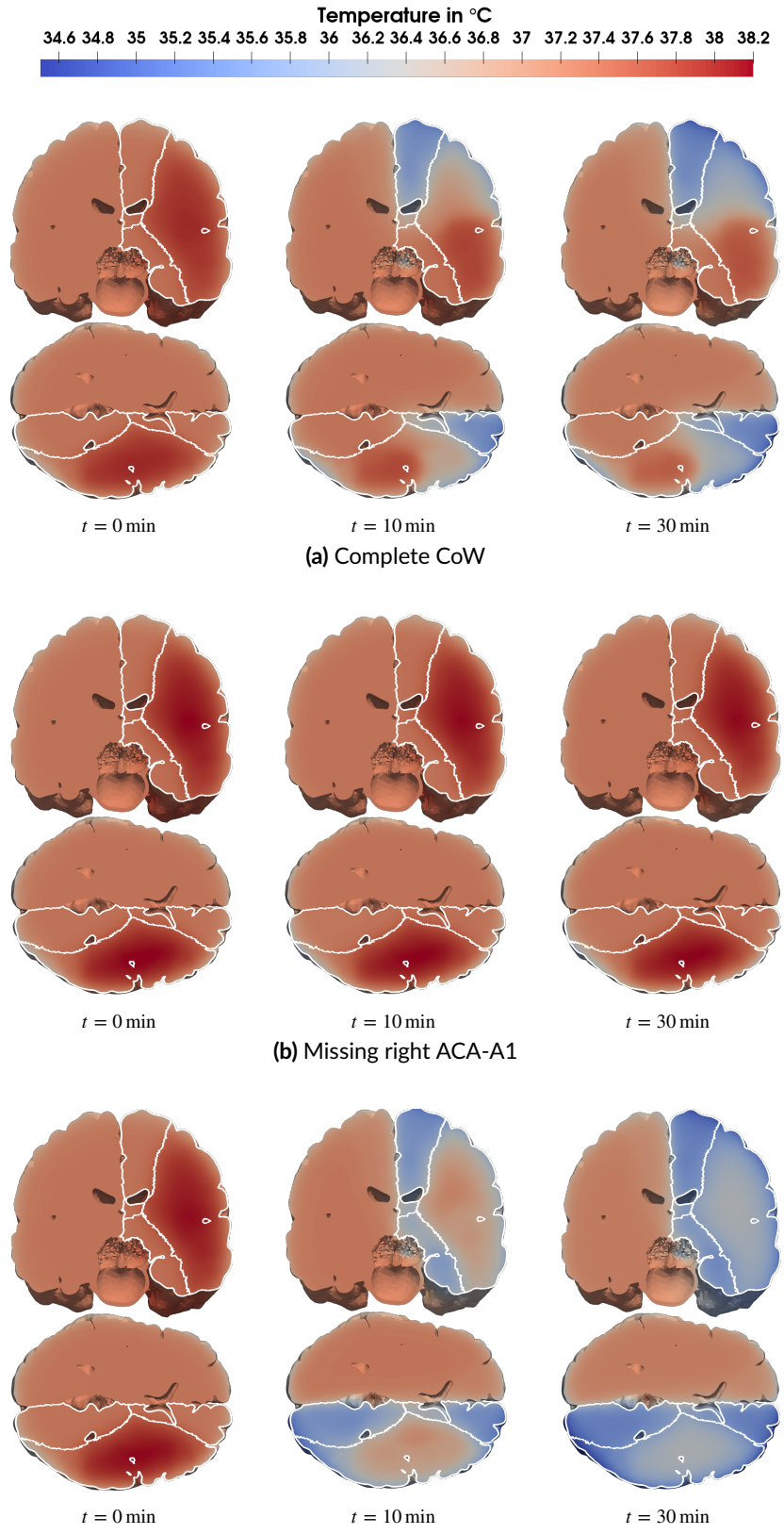

Figure 5.23: Frontal and transversal sections of the cerebrum showing the tissue temperature 0, 10 and 30 min after the start of cooling ("partial" collateralization, Geometry I). The white lines represent the boundaries of the three major vascular territories in the right hemisphere.

Table 5.2: Initial value and change after 10, 20, and 30 min of the mean temperature of the three major vascular territories in the right hemisphere. All values in °C.

Geometry	Occlusion	CoW variation	Degree of SLCs	T_{ACA} T_{MCA} T_{PCA} (0 min)	ΔT_{ACA} ΔT_{MCA} ΔT_{PCA} (10 min)	ΔT_{ACA} ΔT_{MCA} ΔT_{PCA} (20 min)	ΔT_{ACA} ΔT_{MCA} ΔT_{PCA} (30 min)
I	none	complete	partial	37.24 37.22 37.26	-1.63 -1.75 -0.24	-1.76 -1.89 -0.32	-1.83 -1.96 -0.39
I	right MCA-M1	complete	partial	37.27 37.61 37.29	-1.61 -0.71 -0.06	-1.70 -0.94 -0.10	-1.75 -1.04 -0.13
II	none	complete	partial	37.24 37.23 37.26	-1.53 -1.84 -0.25	-1.64 -1.95 -1.67	-1.71 -2.02 -0.40
II	right MCA-M1	complete	partial	37.30 37.71 37.31	-1.40 -0.46 -0.03	-1.48 -0.64 -0.06	-1.51 -0.73 -0.08
I	right MCA-M1	complete	poor	37.29 37.90 37.31	-1.60 -0.60 -0.06	-1.70 -0.87 -0.10	-1.75 -1.02 -0.13
I	right MCA-M1	complete	strong	37.26 37.44 37.28	-1.61 -0.78 -0.07	-1.70 -0.96 -0.11	-1.74 -1.03 -0.14
I	right MCA-M1	missing ACA-A1	partial	37.29 37.71 37.30	-0.01 -0.06 -0.04	-0.01 -0.10 -0.04	-0.01 -0.13 -0.04
I	right MCA-M1	missing PCA-P1	partial	37.27 37.69 37.30	-1.67 -1.29 -1.61	-1.81 -1.74 -1.75	-1.89 -1.94 -1.82

5.4.4 Combination with Mechanical Thrombectomy Procedure

One of the advantages of the analyzed cooling catheter is the possible combination of intracarotid blood cooling with a mechanical thrombectomy (MT) procedure (cf. Sec. 2.5.3). During the prereperfusion phase, the catheter already enables cooling of penumbral brain parenchyma using the SLC flow. This can potentially provide a very early neuroprotection and thus extend the therapeutic time window for MT. In the postreperfusion phase after a successful MT procedure, the cooling catheter can potentially prolong early neuroprotection since the cooled blood can supply the reperfused brain territory to a higher extent [16].

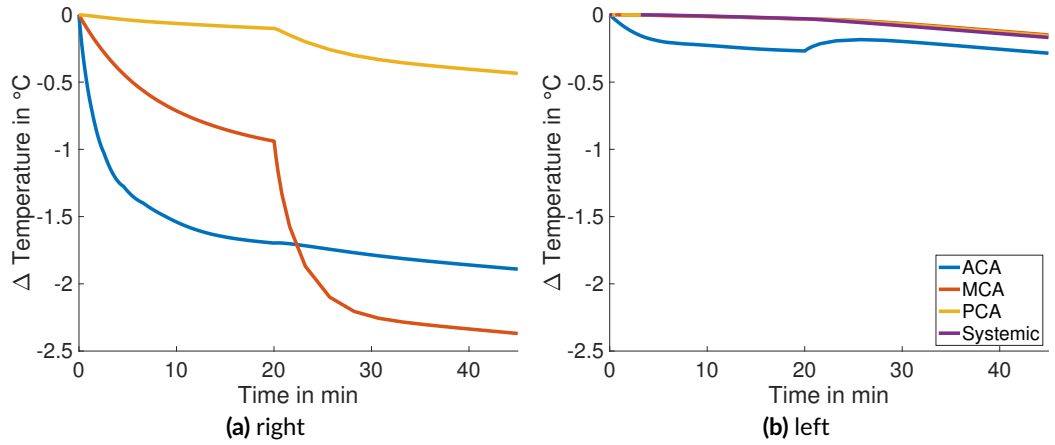

Figure 5.24: Temporal course of the mean temperature of the major vascular territories in case of a successful recanalization (t=20 min) of the right MCA-M1 occlusion ("partial" collateralization degree, Geometry I, complete CoW).

In this work, the possible effect of a successful recanalization on cooling performance was evaluated. Therefore, the recanalization of an MCA-M1 occlusion was imitated by means of a restoration of physiological blood flow rates after 20 min of cooling for a complete CoW and a "partial" collateralization.

The restoration of physiological blood flow rates led to an instantaneous increase of cooling in the right MCA vascular territory (cf. Fig. 5.24 a): In the last 10 min before the reperfusion ($10\,\text{min} < t < 20\,\text{min}$), the mean temperature of the right MCA vascular territory decreased by 0.2 °C. In the first 10 min after recanalization ($20\,\text{min} < t < 30\,\text{min}$), a mean temperature decrease of 1.3 °C resulted for the right MCA vascular territory. A drop of −2 °C in the mean temperature of the right MCA vascular territory was reached after 24.6 min of cooling.

The increased cooling of the MCA vascular territory led to a stronger temperature decrease in the right PCA vascular territory (0.43 °C after 45 min of cooling, cf. Fig. 5.24 a) compared to cooling without reperfusion, whereas the mean temperature in the right ACA vascular territory was barely affected by the thrombectomy.

In the left hemisphere and for the systemic body, the thrombectomy hardly had an influence except for the mean temperature in the ACA vascular territory, which increased slightly by 0.1 °C after the recanalization due to the missing cold flow through the ACoA (cf. Fig. 5.24 b).

Discussion & Limitations of Sec. 5.4.4

In the results described above, one could observe a distinct influence of the anatomy of the cerebral circulation on the cooling effect of the catheter. Nevertheless, the predicted strong temperature decrease in the MCA vascular territory after successful thrombectomy (cf. Fig. 5.24 a) outweighed these dependencies due to the strong cooling effect of the restored MCA inflow. This result suggests that a cold reperfusion ($\Delta T_{\text{MCA}} \approx -2°\text{C}$, 10 min after

recanalization) is possible for all the considered anatomical variations.
The predicted strong temperature decrease in the first 10 min after recanalization is within the target range for a neuroprotective effect in AIS therapy [7, 12, 13, 18] since the molecular pathways of a reperfusion injury are most prominent in the first 15 min after the reperfusion [15] (cf. Sec. 2.5.2).
For the imitation of a successful recanalization, the perfusion rates in the temperature model were restored to physiological values instantaneously at the time of reperfusion. This reflects a best case scenario (modified treatment in cerebral infarction (mTICI) grade 3, cf. Sec. 2.4.3) and reperfusion rates could also be lower or increase slower. Nevertheless, the results of the strong cooling emphasize the marked increase in the cooling effect of the catheter after successful recanalization. Under consideration of the model results for variations in cerebral anatomy, an approximate uncertainty of ± 0.5°C for the cooling effect 45 min after the start of cooling can be stated. For the time needed to reach a 2°C decrease in the temperature of the right MCA vascular territory after the start of cooling, a range between 23-35 min seems feasible, if a recanalization was performed successfully 20 min after the start of cooling.

5.4.5 Discussion & Limitations of Sec. 5.4

The results of temperature calculations in this work cannot be compared directly to clinical data as direct measurement of parenchyma temperature would come along with further harm for the patient. Therefore, a direct parameterization with measured cerebral temperatures and a direct validation of the model is not possible. Nevertheless, some of the model's outputs such as the resulting spatial perfusion rates can be discussed and available measurements of these data can be used for a comparison with the model's output. Furthermore, the predicted cerebral temperature can be compared to first in-vivo measurements within nine sheep.

Resulting Spatial Perfusion

In literature, perfusion rates in the presence of AIS are discussed with a medical focus and are divided into three different types: ischemic core, penumbral parenchyma, and "normally" perfused brain tissue [234]. However, different values can be found in literature for these types. Among others, the deviations are caused by different measurement techniques [234]. In 2001, Baron [234] published an overview of cerebral perfusion rates based on an extensive literature research and the comparison of measurement techniques. Summarizing his results, he proposed a penumbra threshold around 20 $\frac{\text{ml}}{100\,\text{g}\cdot\text{min}}$ and an infarction threshold around 8 $\frac{\text{ml}}{100\,\text{g}\cdot\text{min}}$ (for a stroke duration between 3 and 24 h) [234]. These findings are in accordance with measurements by Konstas et al., who measured an average value of 20.04 $\frac{\text{ml}}{100\,\text{g}\cdot\text{min}}$ for the perfusion in the penumbra using positron emission tomography [208]. A differentiation between GM and WM was not found in the literature for ischemic conditions. For an MCA-M1 occlusion and a "partial" degree of collateralization, the model in this thesis predicted a total mean perfusion of 16 $\frac{\text{ml}}{100\,\text{g}\cdot\text{min}}$, a mean perfusion of 25 $\frac{\text{ml}}{100\,\text{g}\cdot\text{min}}$ for GM, and 8 $\frac{\text{ml}}{100\,\text{g}\cdot\text{min}}$

for WM in the right MCA vascular territory before the start of cooling. For GM as well as for WM, a minimum value of 6 $\frac{\text{ml}}{100\,\text{g}\cdot\text{min}}$ in the right MCA vascular territory was observed. The model's predictions are in a similar range as measured values in literature. However, Fig. 5.25 a shows that the model resulted in a uniform distribution of perfusion for a right MCA-M1 occlusion despite the division of the MCA vascular territory in twelve terminal perfusion regions. A distinction in perfusion regions mirroring ischemic core or penumbra was not possible. The uniform distribution was caused by the resulting uniform terminal blood flow rates into the cortical branches of the right MCA (cf. Fig. 4.24 c). This might be an effect of the relation between vascular resistances of segments within the artery tree and the distinctly higher terminating resistances. In future model versions, this effect could be taken into account by adapting the cerebral vascular resistance ratio under consideration of spatially more detailed perfusion rates.
Nevertheless, the model predicted an ischemic penumbral perfusion for the MCA vascular territory, which is in good accordance with measured perfusion rates for penumbral tissue in literature. The penumbra is of special interest in the evaluation of the cooling catheter's capacity as the penumbra is the major target for the neuroprotective effect of SBH. Consequently, the results of the model can be reliably used to assess the cooling effect on the penumbra.
Additionally, the division of the MCA vascular territory was of great importance for the consideration of spatially different blood temperatures when assessing the cooling effect. As illustrated in Fig. 5.25 b, the division into terminal perfusion regions resulted in marked spatial differences. Such a clear differentiation of the blood temperature in the terminal blood perfusion regions allows for a spatially differentiated temperature calculation. However, the sharp boundaries in arterial blood temperature between the different terminal perfusion regions seem unrealistic[18] and represent a disadvantage of the assumptions in Pennes' equation. To mitigate this effect, a spatial smoothing of the blood temperature could be realized in future model versions, e.g., by means of a 3D Gaussian filter for the arterial blood temperature in the perfusion term of Pennes' equation. In addition, the blood temperature depends on the local blood perfusion conditions. As mentioned above, the model resulted in an overly homogeneous distribution of local blood perfusion in the ischemic case for a right MCA-M1 occlusion.

Flow Dependent Metabolism

As mentioned above in the discussion of Sec. 5.1.2, Lillicrap et al. [165] showed in a simulation study with different ischemia scenarios that the resulting tissue temperature in the penumbra markedly depend on the remaining perfusion and the produced metabolic heat of the ischemic tissue. As described in the section above, the coupling with the hemodynamics model resulted in a mean perfusion rate in accordance with measured values in penumbral tissue. In contrast

[18] In reality, blood vessels cross the boundaries between the terminal perfusion regions, which would lead to a blurring in blood temperture between the hard boundaries of the terminal perfusion regions.

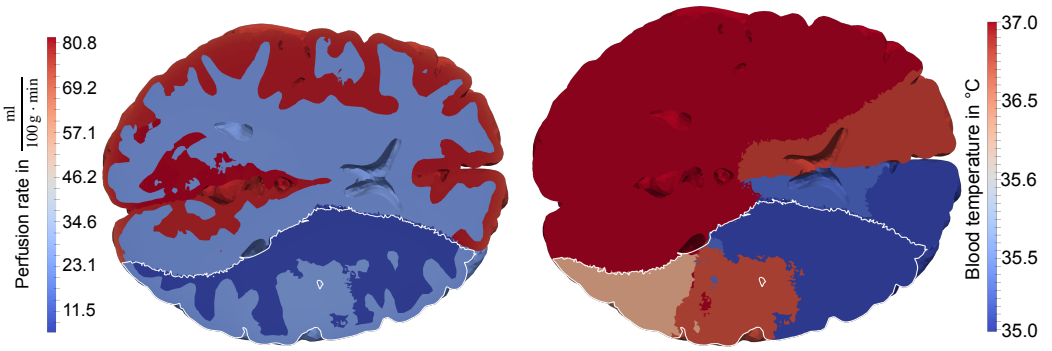

(a) Resulting spatial blood perfusion rate **(b)** Resulting spatial blood temperature

Figure 5.25: Resulting spatial blood temperature and volumetric perfusion rates in case of a right MCA-M1 occlusion 5 s after the start of cooling (Geometry I, complete CoW, "partial" collateralization). The white line represent the boundary of the right MCA vascular territory.

to some other studies [165, 208] considering a reduced metabolism under ischemic conditions, the metabolic reference values [119] for physiological blood flow were used in this work and solely a temperature dependence was integrated. In this way, an increase of heat production due to excitotoxicity [235] and inflammatory reactions [15] was considered in the ischemic tissue[19] [148].

The simulation results showed an initial mean temperature increase of $\approx 0.1 - 0.6\,°C$ in the ischemic regions, which is in agreement with MRI-based measurements [236, 237]. Furthermore, Fig. 5.26 shows that the difference between a perfusion-dependent and a purely temperature-dependent metabolic heat production were almost indistinguishable in terms of the resulting temperature changes in the ischemic MCA region.

As the limitations in the previous chapters showed, the results of the temperature model are based on many assumptions. In addition, the lack of comparable clinical data prevented a direct parameterization with measured cerebral temperatures. In order to keep the uncertainty due to the assumptions and the currently not 100% reliably determinable parameters as small as possible, the focus in this work lay on the temperature decrease and not on the absolute temperature since the influence of many assumptions such as the modeling of metabolism cancels out or minimizes for the temperature differences.

Comparison to an Animal Model

In a recent animal study with 9 sheep, the performance of the novel cooling catheter system was analyzed [106]. Therefore, the cooling catheter was placed in the animal's CCA and the systemic temperature was measured in the inferior vena cava. Furthermore, the animal's brain tissue temperature was measured by probes placed in the frontal and temporal brain

[19] It is assumed that the excitotoxicity and inflammatory reactions approximately compensate the reduction in heat production due to a decreased CMR

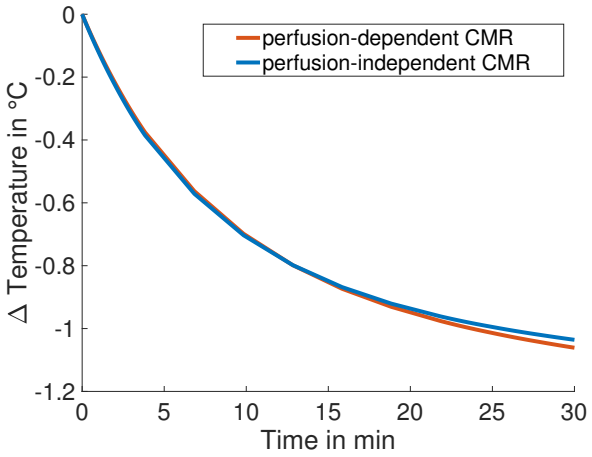

Figure 5.26: Influence of a perfusion dependent or independent metabolic heat production on the course of the mean temperature of the MCA vascular territory for endovascular blood cooling in case of a right MCA-M1 occlusion (Geometry I, complete CoW, "partial" collateralization).

cortices bilaterally by neurosurgical burrhole craniotomies. The detailed setup and study protocol can be found in [106].
As shown in Fig. 5.27, a similar course of parenchyma temperature resulted between the in-vivo results and the simulation of endovascular cooling using physiological blood flow rates of the hemodynamics model.

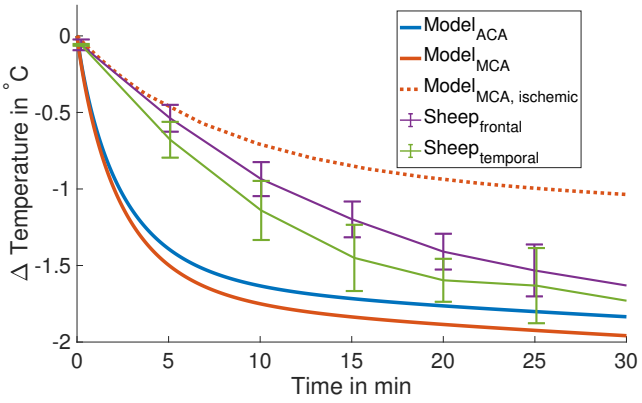

Figure 5.27: Resulting mean temperature in the ACA and MCA vascular territory (Geometry I, complete CoW, "partial" collateralization) for endovascular blood cooling with physiological blood flow rates (dotted line shows result for a right MCA-M1 occlusion) in comparison to an animal study with nine sheep.

The milder decrease of parenchyma temperature measured in sheep in the first 20 min after the start of cooling can be explained by different blood flow velocities between human and sheep in the CCA. In the animal study, a diameter of 6.3 ± 0.6 mm and a blood flow velocity

of 51.9 ± 18.7 cm/s was measured for the medial segment of the CCA with sonography. This would mirror a minimum flow rate of 8.5 ml/s, which is distinctly higher than flow rates in human (cf. Tab. 4.6). Therefore, it is likely that the cooling capacity of the catheter was lower in the sheep. If the measurements in the sheep are compared to the model results for a right MCA-M1 occlusion (cf. Fig. 5.27 dotted line), a better agreement of the cooling capacity in the first 10 min can be observed due to the reduced cooling effect in the ischemic case.
However, a direct comparison of the temperature decreases is hardly possible due to the different arterial and cerebral anatomies in human and sheep [149].

Relation to Previous Work and Simulations

As the assessed endovascular blood-cooling catheter was only recently developed, the presented simulations in this thesis[20] are the first simulations in literature with the new catheter system. Therefore, results can only be compared to models simulating the effects of cold saline infusion, which is the most similar technique to induce SBH. However, there are no other simulations in literature with a realistic brain geometry divided into that many individual perfusion regions, which considers a coupling with a realistic cerebral blood flow model.
Konstas et al. [208] examined the transient and steady-state cerebral temperature response to SBH for different CSI rates into the ICA with a numerical 3D model of a hemisphere. Their model distinguished between GM and WM in healthy brain tissue, penumbral tissue, and ischemic core but did not consider systemic temperature coupling nor the effects of ischemic blood flow conditions on perfusion with cold saline.
After 60 min of CSI (outlet temperature: 1.8-12.1 °C), Konstas' model predicted a mean temperature decrease in the penumbra between 1.2 °C for an infusion rate of 10 ml/min and 8.1 °C for an infusion rate of 50 ml/min [208]. Fig. 5.28 shows that the temperature decrease was the strongest within the first 10 min of infusion independent of the CSI rate. These findings are in accordance with the model in this work, which predicted the most pronounced cooling effect in the first 5-10 min. Despite the similarly strong temperature decrease within the first minutes of cooling, Konstas' model resulted in distinctly higher temperature reduction due to the different cooling technique (CSI allows for higher heat exchange but can also cause hemodilution) and the assumption that all infused cold saline can perfuse the ischemic brain tissue.
In a simple energetic cerebral temperature model, Slotboom et al. [222] simulated the effect of locally induced hypothermia with CSI for the treatment of AIS. They also analyzed different CSI rates of of 7.5, 15, 30, and 45 ml/min assuming a constant outlet coolant temperature of 15 °C. Similar to the assumption of Konstas et al., Slotboom et al. considered coolant flow behind the occluding blood clot, which neglects ischemic blood flow conditions.
Furthermore, they also did not account for temperature dependencies of thermal tissue properties, systemic coupling, or individual spatial perfusion rates. Their model predicts a resulting

[20] and in the publications [148–151, 220] published in this context

mean temperature decrease by 3-9 °C for 300 g of infarcted brain tissue within 6 min of cooling depending on the infusion rate.

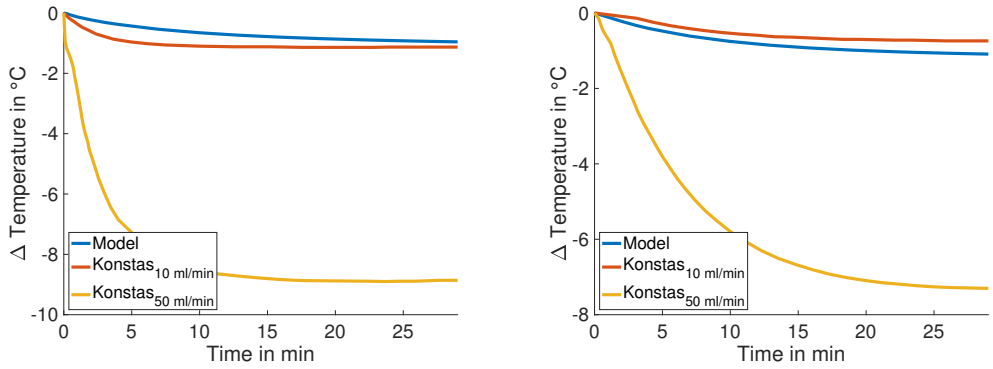

(a) Gray Matter **(b)** White Matter

Figure 5.28: Resulting mean temperature for GM and WM in the vascular territory of the MCA for endovascular blood cooling in case of a right MCA-M1 occlusion (Geometry I, complete CoW, "partial" collateralization) in comparison to penumbral tissue temperature simulated by Konstas et al. [208] for CSI.

5.4.6 Cold Saline Infusion

To enable a more reliable comparison between the model developed in this work and other models in literature, the possibility to model the effects of CSI was added. For this purpose, an additional inflow of $q_{\mathrm{CSI}} = 10\,\mathrm{ml/min}$ or $q_{\mathrm{CSI}} = 50\,\mathrm{ml/min}$ was added for the right ICA in the hemodynamics model, mimicking a constant CSI, and the resulting blood flow rates for a right MCA-M1 occlusion were simulated (cf. Sec. 4.5).
Furthermore, Konstas' [208] measured output temperatures for the cold saline T_{CSI} were adopted, to realize a consistent temperature mixing for the blood temperature in the right CCA:

$$T_{\mathrm{CCA,r}} = \frac{(\tilde{\bar{q}}_{\mathrm{CCA,r}} - q_{\mathrm{CSI}}) \cdot T_{\mathrm{Sys}} + q_{\mathrm{CSI}} \cdot T_{\mathrm{CSI}}}{\tilde{\bar{q}}_{\mathrm{CCA,r}}}.$$

Evaluation

The model predicted a similar course of temperature decrease compared to Konstas' results for the infusion rate of 10 ml/min. The highest difference in temperature was 0.4 °C in the GM and 0.2 °C in the WM between the model and Konstas' results. The model resulted in a difference of <0.1 °C in the GM and <0.2 °C in the WM after 30 min of cooling with the

CSI (cf. Fig. 5.29 a & b).
However, as Fig. 5.29 c & d illustrates, the model predicted a distinctly lower cooling effect compared to the results of Konstas for the higher infusion rate of 50 ml/min. After 30 min of cooling, the model resulted in a difference of 7.6 °C in the GM and 6.4 °C in the WM.

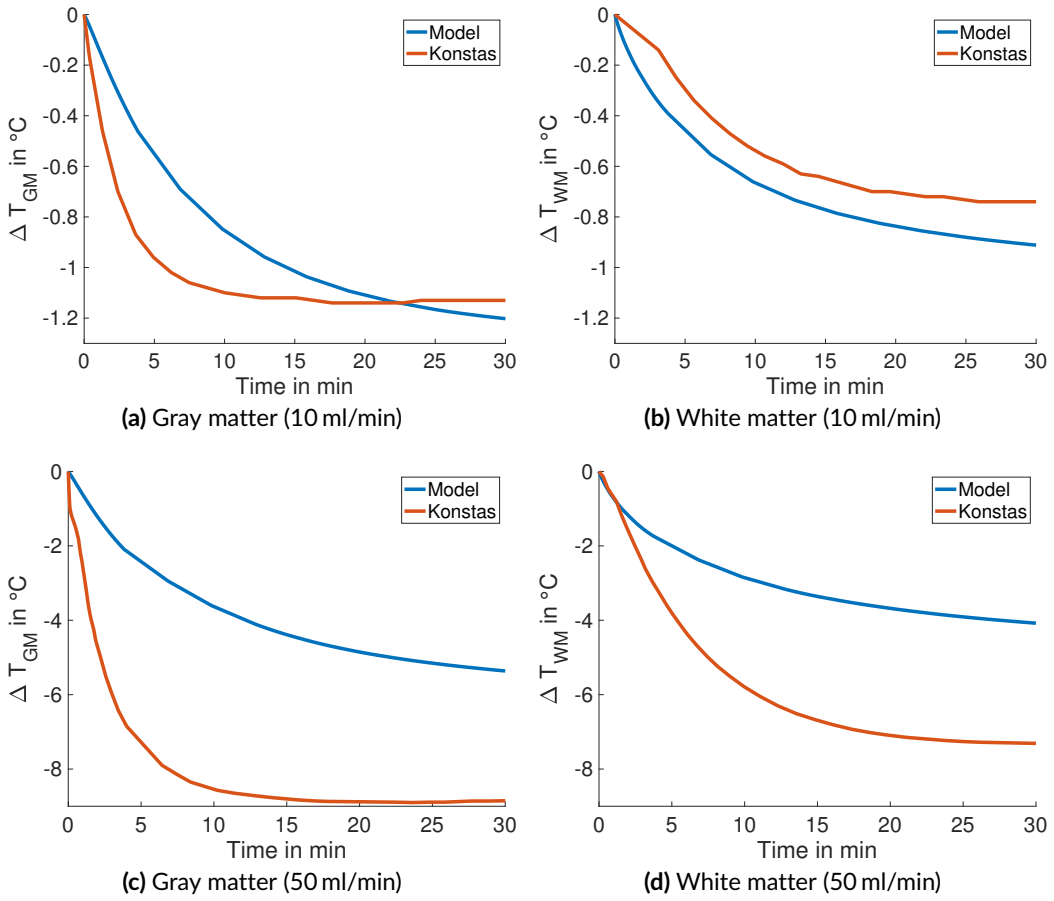

(a) Gray matter (10 ml/min) **(b)** White matter (10 ml/min)

(c) Gray matter (50 ml/min) **(d)** White matter (50 ml/min)

Figure 5.29: Resulting mean temperatures in GM and WM of the vascular territory of the MCA for CSI (10 ml/min and 50 ml/min) in case of a right MCA-M1 occlusion (Geometry I, complete CoW, "partial" collateralization). Comparison to penumbral tissue temperature simulated by Konstas et al. [208].

Discussion & Limitations of Sec. 5.4.6

The CSI led to higher cooling rates compared to endovascular blood cooling with the novel cooling catheter device. Nevertheless, the cooling effect stayed far behind the predicted values of Konstas et al. [208] for an infusion rate of 50 ml/min (cf. Fig. 5.29 c & d). This was mainly caused by the assumption of Konstas et al. that the remaining perfusion rate in the penumbra is completely composed of cold blood originating from the right ICA. This

assumption overestimates the resulting cooling effect since the remaining perfusion in the ischemic penumbra is also partly sustained with warm blood by anastomoses from the PCA, from the ophthalmic artery, from dural arteriolar anastomoses, and from the occipital artery through the mastoid and parietal foramen [45] (cf. Fig. 2.14). The latter fact is considered in the model developed in this thesis in a more realistic way. Here, the warm SLC blood flow from the PCA is considered.
This explanation for a lower cooling effect was underlined by an additional simulation considering a CoW with a missing right PCA-P1 segment. In this case, the remaining blood perfusion originates completely from cold blood originating from the right ICA (cf. Sec. 5.4.3). Fig. 5.30 shows that the course of temperature decrease in the WM, as well as the mean temperature are in good accordance with the results of Konstas for this case. Furthermore it can be seen that the systemic coupling, which is not considered by Konstas et al., leads to an additional cooling effect after the first 15-20 min of cooling.
The remaining differences, i.e., for the GM (cf. Fig. 5.30 a) were caused by differences in perfusion rate (Konstas: $\nu_{\mathrm{GM}}(t=0) = 0.006$ 1/s vs. Model: $\nu_{\mathrm{GM}}(t=0) = 0.004$ 1/s), metabolic heat generation (Konstas: $w_{\mathrm{Met,GM}}(t=0) = 8350\,\mathrm{W/m^3}$ vs. Model: $w_{\mathrm{Met,GM}}(t=0) = 16156\,\mathrm{W/m^3}$), surrounding boundary conditions, and other differently considered thermal properties.

5.5 Comparison to an Energetic Model

Besides elaborate finite element method simulations with 3D geometries, energetic temperature models are often used in literature [220, 222, 238] to describe temperature change in biological tissue. Energetic models focus on the effect of blood perfusion or additional energy release and can be used to quickly calculate the mean temperature change in separate compartments with low computational costs.
To realize a comparison between the detailed 3D-FEM simulation in this thesis and a simplified energetic approach, an energetic temperature model was developed. As Fig. 5.31 illustrates, the model consists of only two compartments. The first compartment represents the right MCA vascular territory and has the same volume and composition of GM and WM as the MCA vascular territory in the 3D geometry. The second compartment represents all other body regions, including the contralateral side of the brain and the rest of the body. It was modeled with an average mass of $M_{\mathrm{Sys}} = 75\,\mathrm{kg}$ and an average specific heat of $c_{\mathrm{Sys}} = 3470\,\frac{\mathrm{J}}{\mathrm{kg\cdot K}}$.
From the systemic compartment, blood is flowing into the right CCA ($q_{\mathrm{CCA,r}}$) at systemic temperature T_{Sys}. As considered in the detailed 3D-FEM model, the blood is cooled instantaneously by 2 °C in the right CCA:

$$T_{\mathrm{Bl,cooled}} = T_{\mathrm{Sys}} - 2\,^{\circ}\mathrm{C}. \tag{5.9}$$

The MCA vascular territory is only perfused by blood coming from the SLCs due to the complete right MCA-M1 occlusion. The MCA compartment is only cooled by the blood

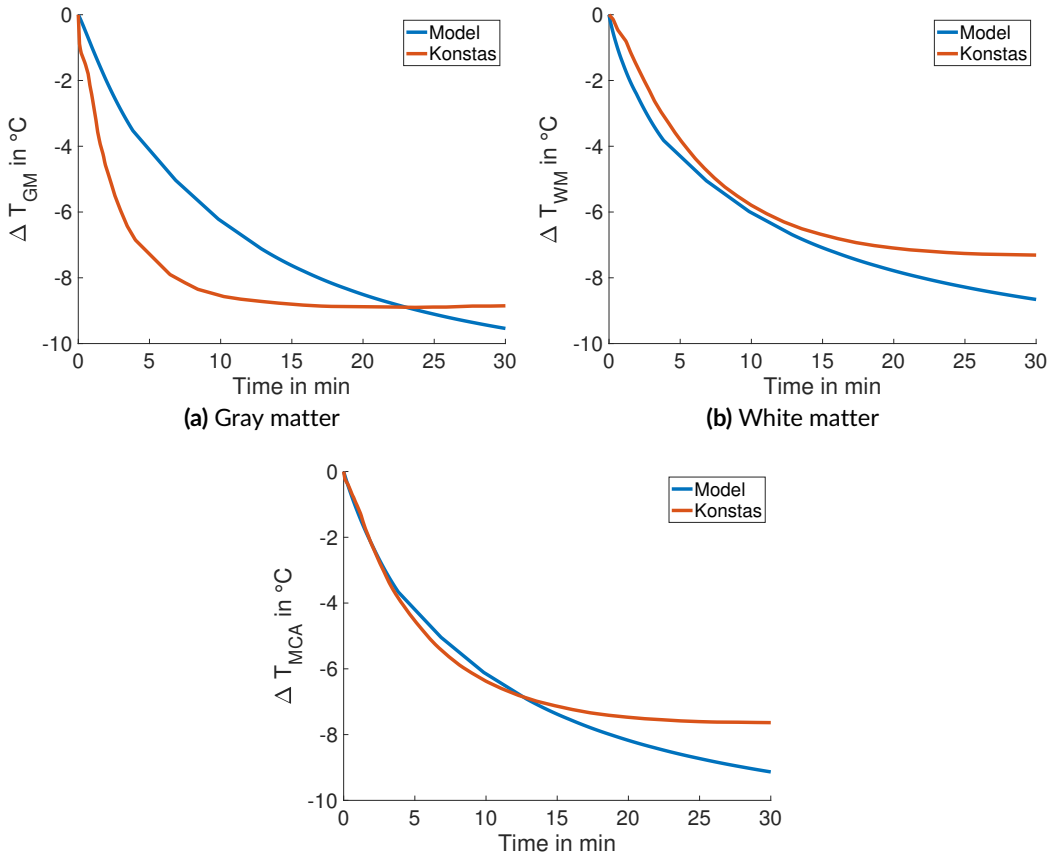

(a) Gray matter **(b)** White matter

(c) MCA vascular territory and penumbra

Figure 5.30: Resulting mean temperatures in the vascular territory of the MCA for CSI of 50 ml/min in case of a right MCA-M1 occlusion and a missing right PCA-P1 segment (Geometry I, "partial" collateralization). Comparison to penumbral tissue temperature simulated by Konstas et al. [208].

originating from the right ACA ($\sum_{i=1}^{3} q_{\mathrm{ACA-MCA,i}}$) for a complete CoW. The SLCs from the right PCA ($\sum_{i=1}^{3} q_{\mathrm{PCA-MCA,i}}$) bring warm blood at systemic temperature to the compartment. Therefore, the mean temperature in the right MCA vascular territory was calculated as follows:

$$\begin{aligned}\frac{\mathrm{d}T_{\mathrm{MCA}}}{\mathrm{d}t} =& -\frac{c_{\mathrm{Bl}}\rho_{\mathrm{Bl}} \cdot \sum_{i=1}^{3} q_{\mathrm{ACA-MCA,i}}}{M_{\mathrm{MCA}} \cdot c_{\mathrm{MCA}}} \cdot (T_{\mathrm{MCA}} - T_{\mathrm{Bl,cool}}) \\ & -\frac{c_{\mathrm{Bl}}\rho_{\mathrm{Bl}} \cdot \sum_{i=1}^{3} q_{\mathrm{PCA-MCA,i}}}{M_{\mathrm{MCA}} \cdot c_{\mathrm{MCA}}} \cdot (T_{\mathrm{MCA}} - T_{\mathrm{Sys}}) \\ =& -c_1 \cdot (T_{\mathrm{MCA}} - T_{\mathrm{Bl,cool}}) - c_2 \cdot (T_{\mathrm{MCA}} - T_{\mathrm{Sys}}).\end{aligned} \tag{5.10}$$

The required summed, mean flow rates through the SLCs were simulated with the hemodynamics model (cf. Sec. 4.5.2). Furthermore, temperature dependency was considered for

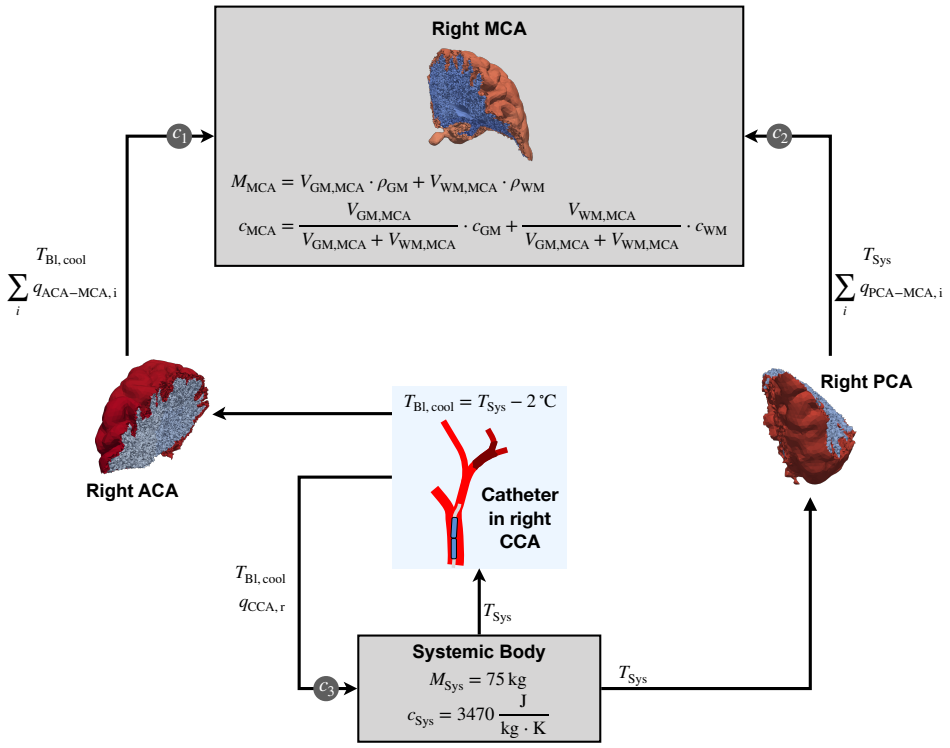

Figure 5.31: Schematic of the energetic temperature model and its two compartments (right MCA vascular territory and systemic body). The coefficients c_1-c_3 were used for the temperature calculation and consist of blood and tissue properties.

the blood flow using Eq. 5.7.

The second compartment (systemic body) was coupled considering the corresponding flow rate in the right CCA (cf. Fig. 5.31) to account for the corresponding cooling effect on the systemic body:

$$\frac{dT_{Sys}}{dt} = -\frac{c_{Bl}\rho_{Bl} \cdot q_{CCA,r}}{M_{Sys} \cdot c_{Sys}} \cdot (T_{Sys} - T_{Bl,cool}) = -c_3 \cdot (T_{Sys} - T_{Bl,cool}) \tag{5.11}$$

5.5.1 Evaluation

For the comparison to the 3D-FEM model, the simulation results with Geometry I were used. Fig. 5.32 shows that for all considered collateralization degrees (“poor”, “partial”, “strong”), the energetic model predicted a temperature course, which was in good accordance with the detailed FEM simulations. The highest deviation in temperature decrease (<0.1 °C) occurred after 30 min of cooling for a “poor” collateralization.

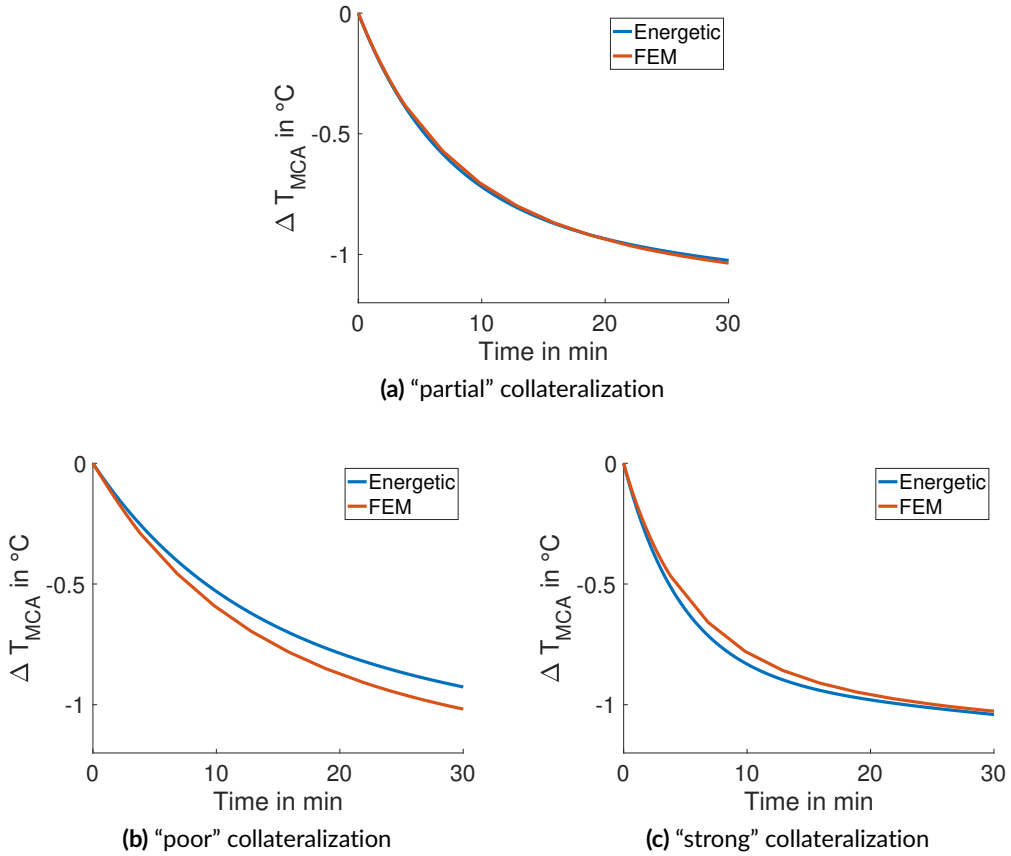

(a) "partial" collateralization

(b) "poor" collateralization

(c) "strong" collateralization

Figure 5.32: Resulting mean temperature in the vascular territory of the MCA for endovascular blood in case of a right MCA-M1 occlusion (Geometry I, complete /acCOW): Comparison between the 3D-FEM Model and a simplified energetic approach [220].

Variations in the CoW

As described in Sec. 4.5.2, the blood temperature in the respective SLCs changes for a missing right ACA-A1 or a missing right PCA-P1 segment. This fact can be considered using Eq. 5.10. Also for the variations in the CoW, the course of temperature decrease was in good accordance ($< 0.15\,°C$) with the FEM simulations. The highest deviations occurred after 30 min of cooling (cf. Fig. 5.33).

5.5.2 Discussion & Limitations of Sec. 5.5

The energetic model resulted in astonishing good accordance with the detailed 3D-FEM simulations. However, the high similarity is caused by four reasons:

- Although the coupling of the hemodynamics model with a realistic 3D brain geometry using approximately 50 terminal perfusion regions was intended to enable spatial differences in perfusion, the FEM model resulted in an overly homogeneous perfusion

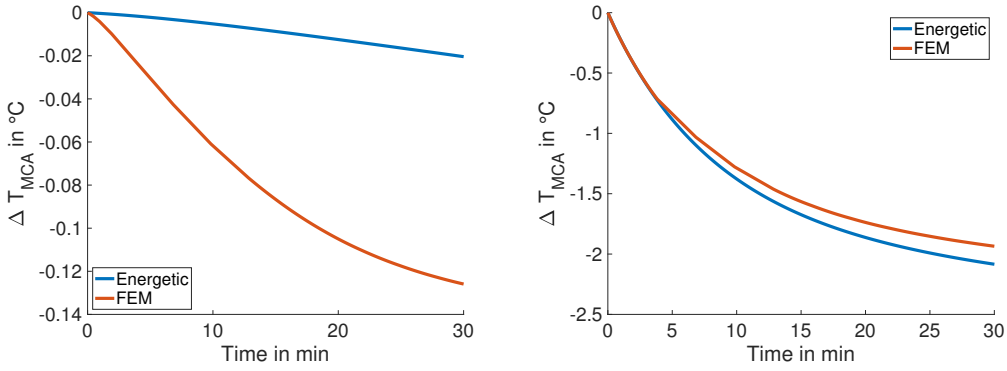

(a) missing right ACA-A1 segment

(b) missing right PCA-P1 segment

Figure 5.33: Resulting mean temperature in the vascular territory of the MCA for endovascular blood in case of a right MCA-M1 occlusion (Geometry I, "partial" collateralization): Comparison between the 3D-FEM Model and a simplified energetic approach [220].

within the whole MCA perfusion region (cf. Sec. 5.4.5 and Fig. 5.25 a). This reulting homogeneous perfusion is similar to the consideration of only one compartment for the MCA.

- The 50 terminal perfusion regions and the individual coupling with blood at different blood temperatures lead to differences in the spatial cooling effect in the 3D-FEM model. Terminal perfusion regions perfused with cold blood from the ACA show a higher temperature decrease compared to regions perfused with blood from the PCA. However, the cold blood flow from the ACA and the warm flow from the PCA are almost balanced (cf. Tab. 4.7). Therefore, the overall effect cancels out for the mean temperature in the MCA vascular territory.
- The influence of heat diffusion in Pennes' equation due to a temperature gradient in the tissue is small compared to the effect of blood perfusion for all the considered scenarios.
- The developed energetic model uses the same flow rates of the detailed hemodynamics model as input values as the 3D-FEM model does. The consideration of individual SLC flow rates at different blood temperatures based on the detailed hemodynamics model leads to a higher grade of complexity as the simplified energetic model pretends. Thus a realistic and detailed hemodynamics model (cf. Sec. A) is essential.

Summarizing these points and the results of the energetic temperature model, the simplified model can be used to predict a mean temperature decrease for ischemic conditions due to AIS in a reliable and faster way compared to the 3D-FEM model.
However, if a spatially more detailed calculations is required for the determination of resulting spatial temperature differences within the MCA vascular territory, a detailed 3D-FEM model is essential and cannot be replaced.

PART III

CONCLUSION

Chapter 6

Outlook

The main objective of the work described in this thesis was to develop a model for the prediction of cerebral spatio-temporal temperature change due to endovascular blood cooling with a novel cooling catheter device. Although the developed model can be already used to reliably describe the mean temperature changes in penumbral tissue, the research carried out so far reflects only the first steps for the development of a cerebral temperature model that is as accurate as required. In this respect, the model can be further improved by the considering the following points, which were already mentioned in the corresponding chapters:

- **Homogeneous perfusion:** As Fig. 5.1 a shows, the model results in a homogeneous spatial perfusion in case of a right middle cerebral artery (MCA) occlusion. A clear distinction of the parenchyma in the ischemic core, penumbra, or "normally" perfused parenchyma is not possible at the moment. This is due to the relative volumetric blood flow rates from the hemodynamics model, which are too homogeneous in case of a right MCA occlusion. To solve this problem, the ratio between the terminating resistances and the flow resistances of the segments building the main cerebral arteries needs to be edited. A consideration of adapted flow resistances, as proposed by Moore et al. [123, 133], or Ciéslicki & Ciésla [130], might result in a more heterogeneous flow distribution for ischemic conditions. In this context, a comparison with cranial computed tomography (CCT) perfusion studies, which are routinely performed for stroke patients, would be apt to result in the most realistic parametrization.
- **Boundaries of perfusion regions:** The use of Pennes' equation and the consideration of various individual spatial perfusion regions lead to sharp boundaries of arterial blood temperatures between regions. A spatial smoothing in the cerebrum of the arterial blood temperature would blur these hard boundaries. However, this would represent an adaptation of Pennes' bioheat transfer model. For this purpose, the underlying physics in *COMSOL Multiphysics* would need to be adapted.

In a second step, or during the implementation of these model modifications, the model's output should be further assessed and compared with already available measurements. Although a direct comparison with cerebral parenchyma temperatures in the endovascular blood cooling process is not possible, other information can be utilized.

To further improve and evaluate the macroscopic heat transfer modeled with Pennes' equation, a corporation project with Voß et al. at the University of Magdeburg can be initiated. In order to gain a better understanding of the interaction between blood perfusion and temperature distribution, an experimental setup was already designed and implemented. In the setup, a homogeneous perfusion medium replaces the brain tissue. Separately sealable tubes represent blood vessels supplying the brain's parenchyma. By measuring the individual volume flow rates, the cross-perfusion can be quantified. At the same time, the temperature is recorded using an optical fiber thermometer and thermography to investigate the perfusion–temperature interaction. With this setup and a corresponding simulation setup using Pennes' equation, possible deviations between the resulting temperature courses can be identified and compensated in the simulation model.
Furthermore, Müller et al. [239] applied thermography for cerebral perfusion imaging during aneurysm surgery. In a second corporation project, more recent thermography images of Müller et al. are used, which show the temperature change in the brain's cortex during open head surgery in acute ischemic stroke (AIS) patients treated with cold saline infusion (CSI). These images can be used for a better model parameterization and validation based on measured values. However, for this purpose, the thermography images need to be evaluated, the model's geometry needs to be adapted, and additional heat transfer from the brain's cortex to the environment has to be analyzed and incorporated in the temperature model.

Chapter 7

Summary

In the present work, a detailed model was developed for the prediction of cerebral spatio-temporal temperature change due to endovascular blood cooling. The model should predict the reachable cooling effect in ischemic brain parenchyma using a novel intracarotid cooling catheter that allows for combination with mechanical thrombectomy (MT) as a therapy for acute ischemic stroke (AIS) patients.
The model is based on a realistic 3D human head model and provides information about the spatial blood perfusion, the arterial blood temperature, and the spatial tissue temperature, which cannot be directly measured in patients. Thus, the model makes a significant contribution to the estimation of the resulting cooling capacity in selective brain hypothermia (SBH) as a therapy for AIS patients. It was used to clarify the following questions, which are important to assess the catheter's efficacy and the clinical outcome:

- Can a potentially neuroprotective temperature decrease of approx. 2 °C be reached within the time window (approx. 30 min of cooling) of MT treatment?
- How does the decrease in temperature depend on the cerebral perfusion rate?
- Which temperature decrease is reachable in penumbral tissue?
- How does selective targeted temperature management (TTM) affect the systemic temperature due to venous blood return?

The coupling of a detailed hemodynamics model of the cerebral arterial tree with a temperature model, under consideration of more than 50 terminal perfusion regions and additional individual consideration of gray matter (GM) and white matter (WM) composition, facilitates the precise assessment of local tissue temperatures during the temporal cooling process. A spatial differentiation of the cerebral blood perfusion to this extent is unique and important for estimating the effect of interindividual differences in cerebral arterial anatomy on cooling. The hemodynamics model is based on the transmission line approach. Here the vascular system is considered as a one-dimensional, linear flow model in which the line equations can be interpreted as electrical analogues. Starting with Avolio's model of the main arterial tree, which was already partly extended by Schwarz et al. with the circle of Willis (CoW), a detailed cerebral hemodynamics model was established that includes the detailed circulation

of the main cerebral arteries and considers secondary leptomeningeal collaterals (SLCs). With respect to an AIS induced by a large vessel occlusion (LVO), local spatial perfusion rates in the supply areas of the main cerebral arteries can differ due to interindividual differences in the cerebral arterial anatomy and the extent of secondary collateralization. An extensive literature research was carried out to determine two structures of the main cerebral arteries (Anatomies I & II), which were found to be the most common in the literature (an atypical or typical callosomarginal artery (CmA), and a bi- or trifurcating middle cerebral artery (MCA)).

Nevertheless, the cerebral anatomy varies greatly from individual to individual, and due to the high degree of individuality, precise and general information about dimensions and arborization of the main cerebral arteries is lacking. Therefore, the "*Brain Vascular Database*" was used, which contains 61 digitally reconstructed artery trees from 3 T magnetic resonance (MR) images. The artery trees in the database were classified and segmented for the extraction of radii and lengths of corresponding cortical branches.

A total of 54 new segments for the main cerebral arteries were added to the model, and additional seven ipsilateral SLCs were considered per hemisphere. To take interindividual differences in the cerebral circulation into account, the underlying anatomy of the developed hemodynamics model can be varied. Ten different variations of the CoW, three collateralization degrees ("poor," "partial," "strong"), two different anatomies of the anterior cerebral artery (ACA), and two different anatomies of the MCA were considered and can be selected independently.

The terminal segments in the hemodynamics model represent the smallest arteries, the capillary bed, and the venous system. They have a major influence on the total peripheral resistance (TPR) and affect mainly the cerebral perfusion rates. The volumes of GM and WM building a terminal perfusion region and physiological reference perfusion rates were used to define individual physiological reference mean flow rates into the terminating resistances. The terminating resistances themselves were calculated with a nodal potential analysis owing to the high complexity of the branching network. Furthermore, the cerebral autoregulation was studied by considering a separate I-controller for each terminating resistance.

The hemodynamics model was used to predict the resulting blood flow conditions and the effect of anatomical variation in case of a right MCA-M1 occlusion, which represents the most common LVO. The hemodynamics model predicted a distinct influence of the collateralization degree on the remaining perfusion for ischemic conditions. Owing to the complete occlusion in the right MCA-M1 segment, the remaining blood flow into the right MCA vascular territory was decreased by 83%, 71%, and 56% for 'poor", "partial", or "strong" collateralization, respectively. Furthermore, the variations in the CoW showed that a missing ACA-A1 and a missing posterior cerebral artery (PCA)-P1 segment had the most distinct influence on the remaining blood flow into the right MCA vascular territory and on the blood flow through the primary collaterals of the CoW. The resulting cerebral blood flow rates were used as the basis for the coupling with a detailed 3D finite element method (FEM) temperature model.

The temperature calculation was based on Pennes' bioheat equation, which is the most commonly used model for bioheat transfer and has been applied with remarkable success in many applications. The equation was solved using the software *COMSOL Multiphysics* and a realistic 3D brain geometry. The geometry was generated based the human brain atlas "*Colin 27*", which is widely used as a standard reference in neuroimaging. A 3D mesh consisting of 4,370,087 tetrahedrons with an average edge length of 1.96 ± 0.67 mm was established for all temperature calculations. The geometry was subdivided into the scalp, the skull, underlying connective tissue (CT), the sinuses, and the brain. Additionally, cerebrospinal fluid (CSF) was considered surrounding the brain and filling the brain's lateral ventricles.
For the simulation of endovascular blood cooling, the novel cooling catheter was assumed to cool the blood in the right common carotid artery (CCA) instantaneously by 2 °C. Therefore, the scalp, the skull, and the underlying CT were split into a left and a right side to consider ipsilateral cooling via the blood flow from the right external carotid artery (ECA) and the tight ophthalmic artery. To consider the cooling effect on the cerebrum, the brain was also subdivided. The brain stem and the cerebellum were extracted since they are not perfused with cold blood from the right CCA. For this purpose, they were segmented in the original MR images of the "*Colin 27*" database. Furthermore, the cerebrum was subdivided into its left and right hemispheres, solving a Laplace boundary problem due to the asymmetric course of the longitudinal fissure.
To realize spatial differentiation in perfusion rates in case of an AIS and to enable the coupling with the detailed cerebral anatomy in the hemodynamics model, the cerebrum was subdivided into terminal perfusion regions that represent the supply regions of the cortical branches in the hemodynamics model. An adapted region growing algorithm was designed for the subdivision process. The algorithm uses the segmented, labeled artery trees of the "*Brain Vascular Database*" and cortical perfusion territory maps from the literature as reference seed cells. To account for the two most common supply distributions, a distinction was made between Anatomy I and Anatomy II from the hemodynamics model.
In total, the tetrahedral mesh was subdivided into about 120 individual perfusion regions. Furthermore, the cooling effect on the systemic body by cold venous blood return, temperature-dependent blood perfusion rates, variable heat transfers to the environment by radiation, natural convection, and evaporation were considered in the temperature calculation.
For physiological conditions without a vessel occlusion, the model is in good accordance with the cerebral target perfusion rates as the deviation in perfusion was $< 4\%$. As indicated above, the remaining perfusion in the right MCA vascular territory was dependent on the considered secondary collateralization degree for a right MCA-M1 occlusion. The model predicted a total mean perfusion of 16 $\frac{\text{ml}}{100\,\text{g}\cdot\text{min}}$, a mean perfusion of 25 $\frac{\text{ml}}{100\,\text{g}\cdot\text{min}}$ for GM, and 8 $\frac{\text{ml}}{100\,\text{g}\cdot\text{min}}$ for WM in the right MCA vascular territory before the start of cooling for a "partial" collateralization. For GM as well as for WM, a minimum value of 6 $\frac{\text{ml}}{100\,\text{g}\cdot\text{min}}$ in the right MCA vascular territory was observed. These results accord with measurements in the literature. Here, a penumbra threshold of 20 $\frac{\text{ml}}{100\,\text{g}\cdot\text{min}}$ and an infarction threshold of 8 $\frac{\text{ml}}{100\,\text{g}\cdot\text{min}}$ are most common. A difference between GM and WM was not found in the literature for ischemic conditions. Contrary to measurements in the literature, the model resulted in a

continuously decreased perfusion within the whole right MCA vascular territory. Anatomical studies show that more focal ischemic conditions and perfusion rates in the affected brain parenchyma can be divided into three different types: ischemic core, penumbral parenchyma, and "normally" perfused brain tissue. However, the predicted ischemic perfusion rate of the model is in good accordance with penumbral tissue, and the cooling effect in the penumbra is of the utmost interest as the possible neuroprotective effect is greatest for the penumbra.
On the one hand, the model predicted a decrease in the mean temperature of the right MCA vascular territory of $\approx 1\,°C$ 30 min after the start of cooling independent of the collateralization degree and the anatomy of the main cerebral arteries. On the other hand, the model resulted in a distinct difference in temperature change for CoW variations. The decrease in the mean temperature of the right MCA vascular territory was negligible for a missing right ACA-A1 segment 30 min after the start of cooling, while for a missing right PCA-P1 segment the decrease in temperature ($\approx 1.9\,°C$ 30 min after the start of cooling) was stronger than in terms of a complete CoW. This difference in cooling capacity was caused by differences in the temperature of the blood perfusing the right MCA vascular territory. In case of a missing right ACA-A1 segment, only warm blood from the basilar artery (BA) and the left hemisphere via the anterior communicating artery (ACoA) perfuses the ischemic right MCA vascular territory. For a missing right PCA-P1 segment, SLCs from the ACA as well as from the PCA bring cold blood to the ischemic right MCA vascular territory.
Since the novel cooling catheter allows for the possible combination of the endovascular blood cooling with an MT procedure, a successful recanalization was imitated by restoring physiological blood flow rates after 20 min of cooling. For this scenario, the model showed an instantaneous increase of cooling in the right MCA vascular territory after recanalization. In the right MCA vascular territory, a mean temperature decrease of 1.3 °C resulted 10 min after the recanalization for a complete CoW and a "partial" collateralization. A drop of $-2\,°C$ in the mean temperature of the right MCA vascular territory was reached 24.6 min after the start of cooling.
This steep temperature decrease in the first 10 min after recanalization is within the target range for a neuroprotective effect in AIS therapy, since the molecular pathways of a reperfusion injury are most prominent in the first 15 min after reperfusion. Furthermore, the results of the imitated recanalization showed that a potentially neuroprotective temperature decrease of $\approx 2\,°C$ can be reached within the time window of MT treatment independent of the considered cerebral vascular anatomy. Although the recanalization led to the highest cooling effect for brain parenchyma, the systemic temperature was with a temperature decrease smaller than 0.2 °C hardly affected.
Since the assessed endovascular blood-cooling catheter was only recently developed, there are no clinical studies or other simulation studies with the new catheter system. As a result, a direct comparison of the model's results with clinical measurements or simulations performed by other groups was not possible. In a recent animal study with nine sheep, the performance of the novel cooling catheter system was analyzed. Compared to these unique in vivo results, the temperature model in this thesis led to a similar course of temperature decrease. However, a direct comparison of the temperature decreases is not meaningful due to the different arterial

and cerebral anatomies in human and sheep.
As human brain temperature cannot be measured directly during endovascular blood cooling, there is additionally a lack of measured values for other cooling methods such as cold saline infusion (CSI). Therefore, only simulated temperature results could be found in the literature. To enable a reliable comparison between the model developed in this work and other simulation models in the literature, the possibility to model the effects of CSI was added to the model. To this end, an additional constant cold saline inflow was added to the right internal carotid artery (ICA) in the hemodynamics model, and a corresponding additional blood temperature mixing was integrated in the temperature model. For the simulation of CSI and the assumption of similar perfusion configurations, the model in this work resulted in a similar course of temperature decrease in the affected area to that obtained by Konstas et al. for 10 ml/min and 50 ml/min of CSI.
To sum up, in this thesis a model for the prediction of cerebral spatio-temporal temperature change due to endovascular blood cooling was generated that is unique in complexity for cerebral spatial blood perfusion rates and blood temperature. The questions presented in the beginning of this chapter could be clarified with the help of the model:

- A potentially neuroprotective temperature decrease of approximately 2 °C was reached within the time window (around. 30 min of cooling) of MT treatment for all anatomical variants considered in this thesis. Therefore, the novel cooling catheter is capable of inducing a cold reperfusion (≈ 2 °C temperature reduction, 10 min after recanalization) in the time window of a MT procedure for penumbral tissue.
- The cerebral perfusion rates showed marked influence on the resulting cooling effect: The cooling effect 30 min after the start of cooling varied between 1 and 2 °C for penumbral and physiological perfusion conditions respectively. However, the model results showed that the arterial temperature overlays the influence of perfusion on the cooling effect. In this context, variations in the CoW showed a distinct influence on the cooling effect.
- A mean temperature decrease of 1.9 °C in penumbral tissue was predicted 30 min after the start of cooling for an ischemic scenario[1] in which all remaining blood flow to the infarction area was consisting of cold blood.
- The selective TTM induced by the novelly developed catheter showed a negligible influence (<0.2 °C) on the systemic temperature.

Although, the model allowed for clarifying some general points of interest, the developed model in this thesis can be further utilized for the challenging identification of possible, additional influencing factors in the therapy of AIS with TTM as this remains a timely and highly relevant topic. The model developed in this thesis represents a significant contribution as comparable data can hardly be obtained by studying stroke cases in clinics.

[1] missing PCA-P1 segment

PART IV

APPENDIX

Appendix A

Appendix Hemodynamics Model

A.1 Parameters of the Avolio Model

Table A.1: Parameters of the segments in the Avolio model [22].

Segment	Artery description	Length (cm)	Radius (cm)	Wall thickness (cm)	E-modulus (10^6 Pa)
1	Aorta	4	1.45	0.163	0.4
2	Aortic arch A	2	1,12	0.132	0.4
3	Subclavian a. A	3.4	0.42	0.067	0.4
4 & 12	Common carotid a. A	8.9	0.37	0.063	0.4
5	Aortic arch B	3.9	1.07	0.127	0.4
6	Brachiocephalic a.	3.4	0.62	0.086	0.4
7 & 15	Internal thoracic a.	15	0.1	0.03	0.8
8 & 14	Subclavian a. B	6.8	0.4	0.066	0.4
9 & 13	Vertebral a	14.8	0.19	0.045	0.8
10 & 22	Common carotid a. B	8.9	0.37	0.063	0.4
11	Des. thoracic aorta A	5.2	1	0.12	0.4
16 & 26	Costocervical trunk	5	0.1	0.12	0.8
17 & 25	Axillary a. A	6.1	0.36	0.062	0.4
18 & 24	Suprascapular a.	10	0.2	0.052	0.8
19 & 23	Thyrocervical trunk	5	0.1	0.03	0.8
20	Common carotid a. C	3.1	0.37	0.63	0.4
21	Des. thoracic aorta B	5.2	0.95	0.116	0.4
27 & 41	Thoracoacromial a.	3	0.15	0.035	1.6
28 & 40	Axillary a. B	5.6	0.31	0.047	0.4
29 & 39	Circumflex scapular a.	5	0.1	0.03	1.6
30 & 38	Subscapular a.	8	0.15	0.035	1.6
31 & 37	External carotid a. A	5.9	0.18	0.045	0.8
32 & 36	Internal carotid a.	11.8	0.15	0.042	0.8
33 & 35	Superior thyroid a	4	0.07	0.02	0.8
34	Des. thoracic aorta C	5.2	0.95	0.0116	0.4
42 & 57	Brachial a. A	6.3	0.28	0.055	0.4
43 & 56	Lingual a.	3	0.1	0.03	0.8

Segment	Artery description	Length (cm)	Radius (cm)	Wall thickness (cm)	E-modulus (10^6 Pa)
44 & 55	External carotid a. B	5.9	0.13	0.039	0.8
45 & 54	Facial a.	4	0.1	0.03	1.6
46 & 53	Middle cerebral artery (MCA)	3	0.06	0.02	1.6
47 & 52	Anterior cerebral artery (ACA) B	5.9	0.08	0.026	1.6
48 & 51	Ophthalmic a.	3	0.07	0.02	1.6
49	Celiac a.	1	0.39	0.064	0.4
50	Aortic abdominalis A	5.3	0.87	0.108	0.4
58 & 70	Deep a. of arm	15	0.15	0.035	0.8
59 & 69	Brachial a. B	6.3	0.26	0.053	0.4
60 & 68	External carotid a. C	5.9	0.08	0.026	1.6
61	Gastric a.	7.1	0.18	0.045	0.4
62	Splenic a.	6.3	0.28	0.054	0.4
63	Hepatic a.	6.6	0.22	0.049	0.4
64 & 67	Renal a.	3.2	0.26	0.053	0.4
65	Aortic abdominalis B	5.3	0.57	0.08	0.4
66	Sup. mesenteric a.	5.9	0.43	0.069	0.4
71 & 79	Brachial a. C	6.3	0.25	0.052	0.4
72 & 78	Sup. ulnar collateral a.	5	0.07	0.02	1.6
73 & 77	Sup. temporal a.	4	0.06	0.02	1.6
74 & 76	Maxillary a.	5	0.07	0.02	1.6
75	Aortic abdominalis C	5.3	0.57	0.08	0.4
80 & 86	Inf. ulnar collateral a.	5	0.06	0.02	1.6
81 & 85	Brachial a. D	4.6	0.24	0.05	0.4
82 & 84	Common iliac a.	5.8	0.52	0.076	0.4
83	Inf. mesenteric a.	5	0.16	0.043	0.4
87 & 94	Ulnar a. A	6.7	0.21	0.049	0.8
88 & 93	Radial a. A	11.7	0.16	0.043	0.8
89 & 92	External iliac a. A	8.3	0.29	0.055	0.4
90 & 91	Internal iliac a.	5	0.2	0.04	1.6
95 & 102	Ulnar a. B	8.5	0.19	0.046	0.8
96 & 101	Interosseous a.	7.9	0.009	0.028	1.6
97 & 100	Radial a. B	11.7	0.16	0.043	1.6
98 & 99	External iliac a. B	6.1	0.27	0.053	0.4
103 & 108	Ulnar a. C	8.5	0.19	0.046	0.8
104 & 107	Femoral a. A	12.7	0.24	0.05	0.8
105 & 106	Deep a. of the thigh	12.6	0.23	0.049	1.6
109 & 110	Femoral a. B	12.7	0.24	0.05	0.8
111 & 112	Popliteal a. A	9.4	0.2	0.047	0.8
113 & 114	Popliteal a. B	9.4	0.2	0.05	0.4
115 & 118	Anterior tibial a. A	2.5	0.13	0.039	1.6
116 & 117	Posterior tibial a. A	16.1	0.18	0.045	1.6
119 & 124	Anterior tibial a. B	15	0.1	0.02	1.6
120 & 123	Peroneal a. A	15.9	0.13	0.039	1.6
121 & 122	Posterior tibial a. B	16.1	0.18	0.045	1.6
125 & 128	Anterior tibial a. C	15	0.1	0.02	1.6
126 & 127	Peroneal a. B	15.9	0.13	0.019	1.6

A.2 Extension of the Avolio Model by Schwarz

Table A.2: Parameters of the CoW segments added by Schwarz [121].

Segment	Artery description	Length (cm)	Radius (cm)	Wall thickness (cm)	E-modulus (10^6 Pa)
129	Basilar artery (BA)	2.9	0.162	0.04	1.6
130 & 131	Posterior cerebral artery (PCA) A	0.5	0.107	0.027	1.6
132 & 133	PCA B	8.6	0.105	0.026	1.6
134 & 135	Posterior communicating artery	1.5	0.04	0.018	1.6
136 & 137	ACA A	1.2	0.117	0.029	1.6
138	Anterior communicating artery	0.3	0.04	0.019	1.6

A.3 Extension of the Main Cerebral Arterial Anatomy

Literature is lacking data for all wall thicknesses d needed. Therefore, the values were calculated using the respective segment's radius r ($d = 0.25 \cdot r$). This factor is the mean value of the relation between the radius and wall thickness for all cerebral segments in the orginal Avolio model [22]. The Young's modulus of the segments was also not found in literature. Instead, we used data from arteries of similar dimensions from Avolio's model. All values for the terminal cortical segments were calculated by averaging over the reconstructed, classified, labeled segments of the Brain Vasculature Database [139] due to lack of literature data.

A.3.1 Added Segments in Anatomy I

Table A.3: Anatomy I: Segments of an ACA branching into a typical CmA.

Segment	Artery description	Length (cm)	Radius (cm)	Wall thickness (cm)	Source
139	A2 segment (right & left)	0.77	0.0897	0.0224	[53]
140	A2 segment (r & l)	1.39	0.0897	0.0224	[53]
141	A2 segment (r & l)	0.78	0.0897	0.0224	[53]
142	A3 segment (r & l)	3.63	0.0819	0.0205	[53]
143	A4 segment (r & l)	2.54	0.0624	0.0156	[53]
144	A5 segment (r & l)	1.1	0.0429	0.0107	[53]
145	Callosomarginal a. (r & l)	1.19	0.0702	0.0176	[53]
146	Callosomarginal a. (r & l)	1.55	0.0702	0.0176	[53]
147	Callosomarginal a. (r & l)	1.35	0.0702	0.0176	[53]
148	Callosomarginal a. (r & l)	1.45	0.0702	0.0176	[53]
T139r	Orbito frontal (r)	8.276	0.0310	0.0078	[139]
T140r	Fronto polar (r)	16.083	0.0372	0.0093	[139]
T143r	Superior parietal (r)	16.427	0.0432	0.0108	[139]
T144r	Pericallosal (r)	13.780	0.0399	0.0100	[139]
T145r	Anterior internal frontal (r)	16.753	0.0381	0.0095	[139]
T146r	Middle internal frontal (r)	18.175	0.0404	0.0101	[139]
T147r	Posterior internal frontal (r)	18.314	0.0455	0.0114	[139]
T148r	Precentral a. (r)	17.260	0.0411	0.0103	[139]
T139l	Orbito frontal (l)	8.276	0.031	0.0078	[139]
T140l	Fronto polar (l)	15.363	0.0403	0.0101	[139]
T143l	Superior parietal (l)	19.320	0.0417	0.0104	[139]
T144l	Pericallosal (l)	6.684	0.0434	0.0109	[139]
T145l	Anterior internal frontal (l)	17.511	0.0442	0.0111	[139]
T146l	Middle internal frontal (l)	18.338	0.0397	0.0099	[139]
T147l	Posterior internal frontal (l)	18.267	0.0403	0.0101	[139]
T148l	Precentral (l)	18.003	0.0381	0.0095	[139]

Table A.4: Anatomy I: Added segments for a bifurcating MCA into superior and inferior M2 trunks.

Segment	Artery description	Length (cm)	Radius (cm)	Wall thickness (cm)	Source
149	M1 segment (right)	0.750	0.1170	0.0293	[58, 59]
150	M1 segment (r)	0.590	0.1170	0.0293	[58, 59]
151	M1 segment (r)	0.160	0.1170	0.0293	[58, 59]
152	M2 superior segment (r)	0.450	0.0819	0.0205	[58, 59]
153	M2 superior segment (r)	0.390	0.0819	0.0205	[58, 59]
154	M2 superior segment (r)	0.390	0.0819	0.0205	[58, 59]
155	M2 superior segment (r)	0.030	0.0819	0.0205	[58, 59]
156	M2 inferior segment (r)	0.840	0.0897	0.0224	[58, 59]
157	M2 inferior segment (r)	0.750	0.0897	0.0224	[58, 59]
158	M2 inferior segment (r)	0.200	0.0897	0.0224	[58, 59]
159	M2 inferior segment (r)	0.060	0.0897	0.0224	[58, 59]
160	M2 inferior segment (r)	0.060	0.0897	0.0224	[58, 59]
161	M2 inferior segment (r)	0.160	0.0897	0.0224	[58, 59]
T149	Temporopolar (r)	14.219	0.0464	0.0116	[139]
T150	Anterior temporal (r)	17.505	0.0357	0.0089	[139]
T152	Orbitofrontal (r)	15.689	0.0419	0.0105	[139]
T153	Prefrontal (r)	18.660	0.0418	0.0105	[139]
T154	Precentral (r)	22.274	0.0416	0.0104	[139]
T155	Central (r)	24.129	0.0429	0.0107	[139]
T156	Middle temporal (r)	16.534	0.0474	0.0119	[139]
T157	Posterior temporal (r)	19.601	0.0434	0.0109	[139]
T158	Anterior parietal (r)	23.842	0.0407	0.0102	[139]
T159	Temporo-occipital (r)	26.488	0.0453	0.0113	[139]
T160	Angular (r)	26.426	0.0433	0.0108	[139]
T161	Posterior parietal (r)	26.453	0.0428	0.0107	[139]
162	M1 segment (left)	0.750	0.1170	0.0293	[58, 59]
163	M1 segment (l)	0.590	0.1170	0.0293	[58, 59]
164	M2 superior segment (l)	0.160	0.1170	0.0293	[58, 59]
165	M2 superior segment (l)	0.450	0.0819	0.0205	[58, 59]
166	M2 superior segment (l)	0.390	0.0819	0.0205	[58, 59]
167	M2 superior segment (l)	0.390	0.0819	0.0205	[58, 59]
168	M2 inferior segment (l)	0.030	0.0819	0.0205	[58, 59]
169	M2 inferior segment (l)	0.840	0.0897	0.0224	[58, 59]
170	M2 inferior segment (l)	0.750	0.0897	0.0224	[58, 59]
171	M2 inferior segment (l)	0.200	0.0897	0.0224	[58, 59]
172	M2 inferior segment (l)	0.060	0.0897	0.0224	[58, 59]
173	M2 inferior segment (l)	0.060	0.0897	0.0224	[58, 59]
T162	Temporopolar (l)	13.615	0.0447	0.0112	[139]
T164	Orbitofrontal (l)	13.802	0.0379	0.0095	[139]
T165	Prefrontal (l)	18.054	0.04330	0.0108	[139]
T166	Precentral (l)	20.995	0.0448	0.0112	[139]
T167	Central (l)	21.082	0.0422	0.0106	[139]
T168	Anterior temporal (l)	15.184	0.0401	0.0100	[139]
T169	Middle temporal (l)	16.862	0.0379	0.0095	[139]
T170	Posterior parietal (l)	25.303	0.0423	0.0106	[139]
T171	Anterior parietal (l)	24.230	0.04012	0.0100	[139]
T172	Angular (l)	25.400	0.0437	0.0109	[139]
T173a	Posterior temporal (l)	20.312	0.0419	0.0105	[139]
T173b	Temporo-occipital (l)	24.294	0.0451	0.0113	[139]

Table A.5: Anatomy I: Added segments for the PCA.

Segment	Artery description	Length (cm)	Radius (cm)	Wall thickness (cm)	Source
174	P2 segment (right & left)	1.44	0.1131	0.0283	[60]
175	P2 segment (r & l)	0.16	0.1131	0.0283	[60]
176	P2 segment (r & l)	0.87	0.1131	0.0283	[60]
177	P2 segment (r & l)	0.37	0.1131	0.0283	[60]
178	P2 segment (r & l)	1.06	0.1131	0.0283	[60]
T174r	Hippocampal (r)	10.004	0.0491	0.0123	[139]
T175r	Anterior temporal (r)	12.887	0.0108	0.0143	[139]
T176r	Parieto-occipital (r)	19.023	0.0105	0.0176	[139]
T177r	Posterior temporal (r)	15.257	0.0102	0.0176	[139]
T178r	Calcarine (r)	14.079	0.0410	0.0103	[139]
T174l	Hippocampal (l)	9.941	0.0410	0.0103	[139]
T175l	Anterior temporal (l)	13.173	0.0411	0,0103	[139]
T176l	Parieto-occipital (l)	18.418	0.0424	0.0106	[139]
T177l	Posterior temporal (l)	15.336	0.0392	0.0098	[139]
T178l	Calcarine (l)	13.261	0.0434	0.0109	[139]

A.3.2 Added Segments in Anatomy II

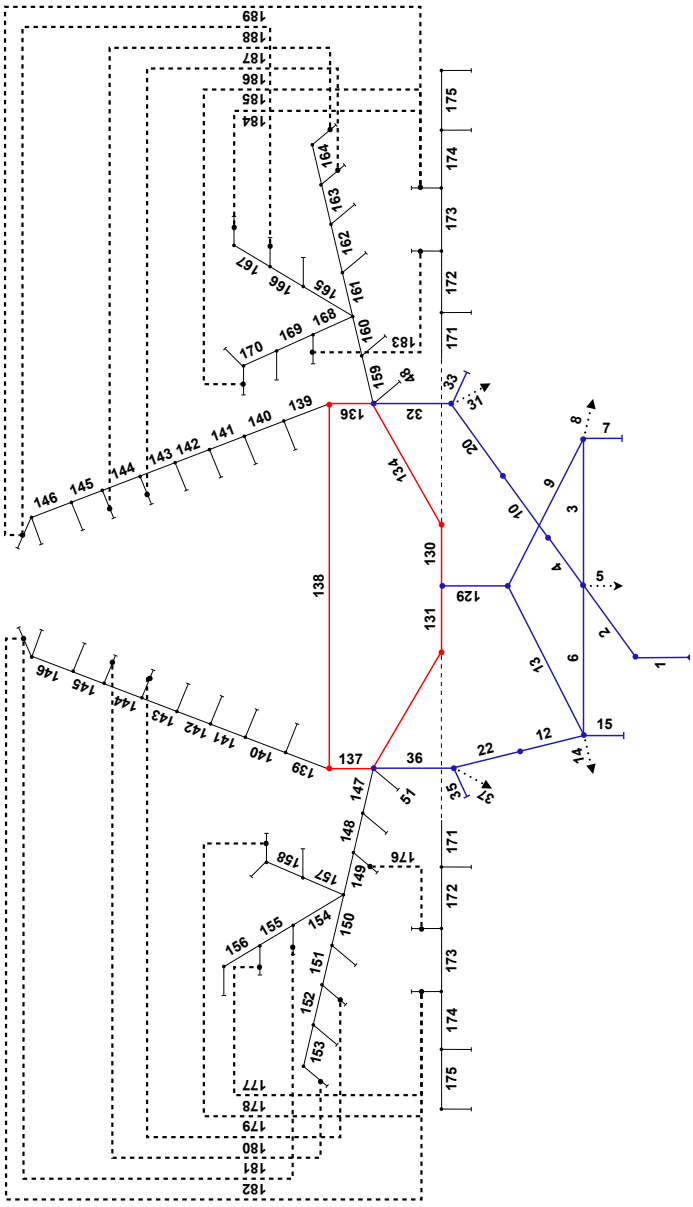

Figure A.1: Schematic cerebral hemodynamics of Anatomy II with a trifurcating MCA into superior, middle and inferior M2 trunks and an ACA consisting of an atypical CmA. ACA segments: 139–146, MCA segments: 147–170, PCA segments: 171–175, SLCs: 176–189. The blue segments were taken from the work of Avolio [22]. The red segments represent the CoW which was added to Avolio's model by Schwarz et al. [120]. The dotted black arrows indicate the branching of further arteries (5: aorta thoracica (torso), 8 and 14: Subclavian arteries (arms), 31 and 37: External carotid arteries). The numbers represent the respective arterial segments (compare Table A.6, A.7, A.8). For the terminal segments of the cortical branches, the numbers have been omitted here for a clearer presentation but can be found in the respective tables.

Table A.6: Anatomy II: Added segments for an ACA branching into an atypical CmA. Values assigned with a * were estimated from values of comparable segments.

Segment	Artery description	Length (cm)	Radius (cm)	Wall thickness (cm)	Source
139	A2 segment (right & left)	7.7	0.115	0.0288	[53]
140	A2 segment (r & l)	13.9	0.115	0.0288	[53]
141	A3 segment (r & l)	19.7	0.105	0.0263	[53]
142	A3 segment (r & l)	15.5	0.105	0.0263	[53]
143	A4 segment (r & l)	13.5	0.08	0.0200	[53]
144	A4 segment (r & l)	14.5	0.08	0.0200	[53]
145	A5 segment (r & l)	16.8	0.08*	0.0200	[53]
146	A5 segment (r & l)	11.0	0.08*	0.0200	[53]
T139r	Orbito frontal (r)	8.262	0.0310	0.0078	[139]
T140r	Fronto polar (r)	16.648	0.0396	0.0099	[139]
T141r	Anterior internal frontal (r)	17.384	0.0409	0.0102	[139]
T142r	Middle internal frontal (r)	18.829	0.0380	0.0095	[139]
T143r	Posterior internal frontal (r)	19.039	0.0435	0.0109	[139]
T144r	Precentral a. (r)	18.239	0.0414	0.0104	[139]
T145r	Superior parietal (r)	17.852	0.0427	0.0107	[139]
T146ra	Inferior parietal (r)	17.504	0.0388	0.0097	[139]
T146rb	Pericallosal (r)	5.030	0.0349	0.0087	[139]
T139l	Orbito frontal (l)	6.752	0.0310	0.0078	[139]
T140l	Fronto polar (l)	16.864	0.0379	0.0095	[139]
T141l	Anterior internal frontal (l)	16.292	0.0414	0.0104	[139]
T142l	Middle internal frontal (l)	18.778	0.0427	0.0107	[139]
T143l	Posterior internal frontal (l)	17.647	0.0404	0.0101	[139]
T144l	Precentral a. (l)	17.155	0.0428	0.0107	[139]
T145l	Superior parietal (l)	17.248	0.0402	0.0101	[139]
T146la	Inferior parietal (l)	17.283	0.0416	0.0104	[139]
T146lb	Pericallosal (l)	7.383	0.0438	0.0110	[139]

Table A.7: Anatomy II: Added segments for a trifurcating MCA into superior, middle and inferior M2 trunks. The segments indicate with a * were evenly split.

Segment	Artery description	Length (cm)	Radius (cm)	Wall thickness (cm)	Source
147	M1 segment (right)	0.750	0.117	0.0293	[58, 59]
148	M1 segment (r)	0.590	0.117	0.0293	[58, 59]
149	M1 segment (r)	0.160	0.117	0.0293	[58, 59]
150	M2 superior segment (r)	0.450	0.0546	0.0137	[58, 59]
151	M2 superior segment* (r)	0.390	0.0546	0.0137	[58, 59]
152	M2 superior segment* (r)	0.390	0.0546	0.0137	[58, 59]
153	M2 superior segment (r)	0.030	0.0546	0.0137	[58, 59]
154	M2 middle segment (r)	1.790	0.0897	0.0224	[58]
155	M2 middle segment (r)	0.120	0.0897	0.0224	[58, 59]
156	M2 middle segment (r)	0.160	0.0897	0.0224	[58, 59]
157	M2 inferior segment (r)	0.840	0.0819	0.0205	[58, 59]
158	M2 inferior segment (r)	0.750	0.0819	0.0205	[58, 59]
T147	Temporopolar (r)	14.558	0.041	0.0103	[139]
T148	Anterior temporal (r)	14.797	0.040	0.0100	[139]
T150	Orbitofrontal (r)	15.961	0.047	0.0118	[139]
T151	Prefrontal (r)	15.816	0.044	0.0110	[139]
T152	Precentral (r)	19.978	0.042	0.0105	[139]
T153	Central (r)	21.647	0.042	0.0105	[139]
T154	Anterior parietal (r)	21.548	0.041	0.0103	[139]
T155	Angular a. (r)	23.477	0.039	0.0098	[139]
T156	Posterior parietal (r)	23.450	0.041	0.0103	[139]
T157	Middle temporal (r)	15.269	0.036	0.0090	[139]
T158a	Posterior temporal (r)	17.779	0.044	0.0110	[139]
T158b	Temporo occipital (r)	25.077	0.040	0.0100	[139]
159	M1 segment (left)	0.740	0.117	0.0293	[58, 59]
160	M1 segment (l)	0.830	0.117	0.0293	[58, 59]
161	M2 superior segment (l)	0.320	0.066	0.0166	[58, 59]
162	M2 superior segment* (l)	0.460	0.066	0.0166	[58, 59]
163	M2 superior segment* (l)	0.460	0.066	0.0166	[58, 59]
164	M2 superior segment (l)	0.270	0.066	0.0166	[58, 59]
165	M2 middle segment (l)	1.550	0.0741	0.0185	[58, 59]
166	M2 middle segment (l)	0.080	0.0741	0.0185	[58, 59]
167	M2 middle segment (l)	0.09	0.0741	0.0185	[58, 59]
168	M2 inferior segment (l)	0.26	0.0819	0.0205	[58, 59]
169	M2 inferior segment (l)	1.000	0.0819	0.0205	[58, 59]
170	M2 inferior segment (l)	0.470	0.0819	0.0205	[58, 59]
T159	Temporopolar (l)	11.113	0.0435	0.0109	[139]
T161	Orbitofrontal (l)	14.065	0.0484	0.0121	[139]
T162	Prefrontal (l)	16.846	0.0432	0.0108	[139]
T163	Precentral (l)	20.174	0.0409	0.0102	[139]
T164	Central (l)	19.903	0.0436	0.0109	[139]
T165	Post. parietal (l)	23.978	0.0416	0.0104	[139]
T166	Ant. parietal (l)	22.615	0.0426	0.0106	[139]
T167	Angular (l)	23.798	0.0435	0.0109	[139]
T168	Ant. temporal (l)	15.425	0.0463	0.0116	[139]
T169	Middle temporal (l)	16.044	0.0361	0.0090	[139]
T170a	Post. temporal (l)	17.289	0.0438	0.0109	[139]
T170b	Temporo-occipital (l)	23.599	0.0428	0.0107	[139]

Table A.8: Anatomy II: Added segments for the PCA.

Segment	Artery description	Length (cm)	Radius (cm)	Wall thickness (cm)	Source
171	P2 segment (r & l)	1.44	0.1131	0.0283	[60]
172	P2 segment (r & l)	0.16	0.1131	0.0283	[60]
173	P2 segment (r & l)	0.87	0.1131	0.0283	[60]
174	P2 segment (r & l)	0.37	0.1131	0.0283	[60]
175	P2 segment (r & l)	1.06	0.1131	0.0283	[60]
T171r	Hippocampal (r)	10.004	0.0491	0.0123	[139]
T172r	Anterior temporal (r) (PCA)	12.887	0.0108	0.0143	[139]
T173r	Parieto-occipital (r)	19.023	0.0105	0.0176	[139]
T174r	Posterior temporal (r) (PCA)	15.257	0.0102	0.0176	[139]
T175r	Calcarine (r)	14.079	0.0410	0.0103	[139]
T171l	Hippocampal (l)	9.941	0.0410	0.0103	[139]
T172l	Anterior temporal (l)	13.173	0.0411	0.0103	[139]
T173l	Parieto-occipital (l)	18.418	0.0424	0.0106	[139]
T174l	Posterior temporal (l)	15.336	0.0392	0.0098	[139]
T175l	Calcarine (l)	13.261	0.0434	0.0109	[139]

Table A.9: Anatomy II: Added ipsilateral SLCs.

Segment	Description	Connected Segments	Length (cm)	Radius (cm)	Source
176	PCA–MCA (r)	T149-T172r	27.684	0.0416	[139, 146, 147]
177	PCA–MCA (r)	T155-T173r	36.802	0.0431	[139, 146, 147]
178	PCA–MCA (r)	T158a-T173r	42.500	0.0406	[139, 146, 147]
179	ACA–MCA (r)	T143r-T151	34.855	0.0438	[139, 146, 147]
180	ACA–MCA (r)	T144r-T153	39.886	0.0417	[139, 146, 147]
181	ACA–MCA (r)	T146rb-T154	26.578	0.0380	[139, 146, 147]
182	PCA–ACA (r)	T146rb-T173r	24.053	0.0390	[139, 146, 147]
183	PCA–MCA (l)	T168-T172l	28.598	0.0437	[139, 146, 147]
184	PCA–MCA (l)	T167-T173l	42.216	0.0428	[139, 146, 147]
185	PCA–MCA (l)	T170a-T173l	35.707	0.0431	[139, 146, 147]
186	ACA–MCA (l)	T143l-T163	37.821	0.0407	[139, 146, 147]
187	ACA–MCA (l)	T144l-T164	37.058	0.0432	[139, 146, 147]
188	ACA–MCA (l)	T146lb-T166	29.998	0.0432	[139, 146, 147]
189	PCA–ACA (l)	T146lb-T173l	25.801	0.0431	[139, 146, 147]

A.4 Segmentation of Cortical Branches

Table A.10: Results of the segmentation (Sec. 4.2.4) of the arterial trees in the Brain Vascular Database [139].

Tree ID	ACA		MCA	
	left	right	left	right
BG0002	atypical CmA	atypical CmA	Trifurcation	Trifurcation
BG0003	atypical CmA	atypical CmA	Trifurcation	Bifurcation
BG001	typical CmA	typical CmA	Trifurcation	Bifurcation
BG0014	typical CmA	atypical CmA	Bifurcation	Trifurcation
BG0019	atypical CmA	atypical CmA	Bifurcation	Bifurcation
BG0020	typical CmA	atypical CmA	Bifurcation	Bifurcation
BG0021	typical CmA	atypical CmA	Bifurcation	Bifurcation
BG0022	atypical CmA	typical CmA	Trifurcation	Bifurcation
BG04	typical CmA	typical CmA	Bifurcation	Bifurcation
BG05	atypical CmA	typical CmA	Bifurcation	Bifurcation
BG06	typical CmA	typical CmA	Bifurcation	Bifurcation
BG07	atypical CmA	typical CmA	Bifurcation	Trifurcation
BG08	atypical CmA	atypical CmA	Bifurcation	Bifurcation
BG09	typical CmA	atypical CmA	Bifurcation	Bifurcation
BG10	atypical CmA	atypical CmA	Trifurcation	Bifurcation
BG11	typical CmA	atypical CmA	Bifurcation	Bifurcation
BG12	atypical CmA	typical CmA	Bifurcation	Bifurcation
BG13	atypical CmA	atypical CmA	Trifurcation	Bifurcation
BG15	atypical CmA	typical CmA	Bifurcation	Bifurcation
BG17	typical CmA	atypical CmA	Bifurcation	Bifurcation
BG18	typical CmA	typical CmA	Bifurcation	Trifurcation
BH0002	typical CmA	atypical CmA	Bifurcation	Bifurcation
BH0003	typical CmA	atypical CmA	Bifurcation	Bifurcation
BH0004	atypical CmA	typical CmA	Bifurcation	Bifurcation
BH0005	atypical CmA	atypical CmA	Trifurcation	Bifurcation
BH0006	atypical CmA	typical CmA	Trifurcation	Bifurcation
BH0008	atypical CmA	atypical CmA	Bifurcation	Trifurcation
BH0009	typical CmA	atypical CmA	Bifurcation	Bifurcation
BH0010	atypical CmA	atypical CmA	Bifurcation	Bifurcation
BH0011	atypical CmA	atypical CmA	Bifurcation	Bifurcation
BH0012	atypical CmA	atypical CmA	Bifurcation	Bifurcation
BH0013	atypical CmA	atypical CmA	Bifurcation	Trifurcation
BH0014	atypical CmA	atypical CmA	Bifurcation	Bifurcation
BH0015	typical CmA	atypical CmA	Trifurcation	Trifurcation
BH0016	atypical CmA	atypical CmA	Bifurcation	Bifurcation
BH0017	typical CmA	atypical CmA	Bifurcation	Bifurcation
BH0018	atypical CmA	atypical CmA	Trifurcation	Bifurcation
BH0019	typical CmA	atypical CmA	Bifurcation	Bifurcation
BH0020	atypical CmA	atypical CmA	Trifurcation	Bifurcation

Tree ID	ACA		MCA	
	left	right	left	right
BH0021	exceptional	atypical CmA	Trifurcation	Bifurcation
BH0022	atypical CmA	atypical CmA	Bifurcation	Bifurcation
BH0023	typical CmA	atypical CmA	Bifurcation	Trifurcation
BH0024	typical CmA	atypical CmA	Bifurcation	Bifurcation
BH0025	typical CmA	typical CmA	Bifurcation	Bifurcation
BH0026	atypical CmA	atypical CmA	Trifurcation	Bifurcation
BH0027	atypical CmA	atypical CmA	Bifurcation	Bifurcation
BH0029	atypical CmA	atypical CmA	Bifurcation	Bifurcation
BH0030	atypical CmA	atypical CmA	Trifurcation	Bifurcation
BH0031	atypical CmA	typical CmA	Trifurcation	Trifurcation
BH0032	atypical CmA	atypical CmA	Bifurcation	Trifurcation
BH0033	typical CmA	atypical CmA	Bifurcation	Bifurcation
BH0034	atypical CmA	bihemispheric	Bifurcation	Trifurcation
BH0035	typical CmA	atypical CmA	Bifurcation	Trifurcation
BH0036	atypical CmA	atypical CmA	Bifurcation	Bifurcation
BH0037	atypical CmA	typical CmA	Bifurcation	Bifurcation
BH0038	atypical CmA	atypical CmA	Bifurcation	Bifurcation
BH0039	atypical CmA	atypical CmA	Bifurcation	Bifurcation
BH0040	atypical CmA	typical CmA	Bifurcation	Trifurcation
BI0001	atypical CmA	typical CmA	Bifurcation	Bifurcation
Set9	atypical CmA	atypical CmA	Bifurcation	Bifurcation

A.5 Variations of the Circle of Willis

To evaluate variations in the forming of the primary collaterals in the circle of Willis (CoW), ten different variations were considered (compare Sec. 4.3.1).

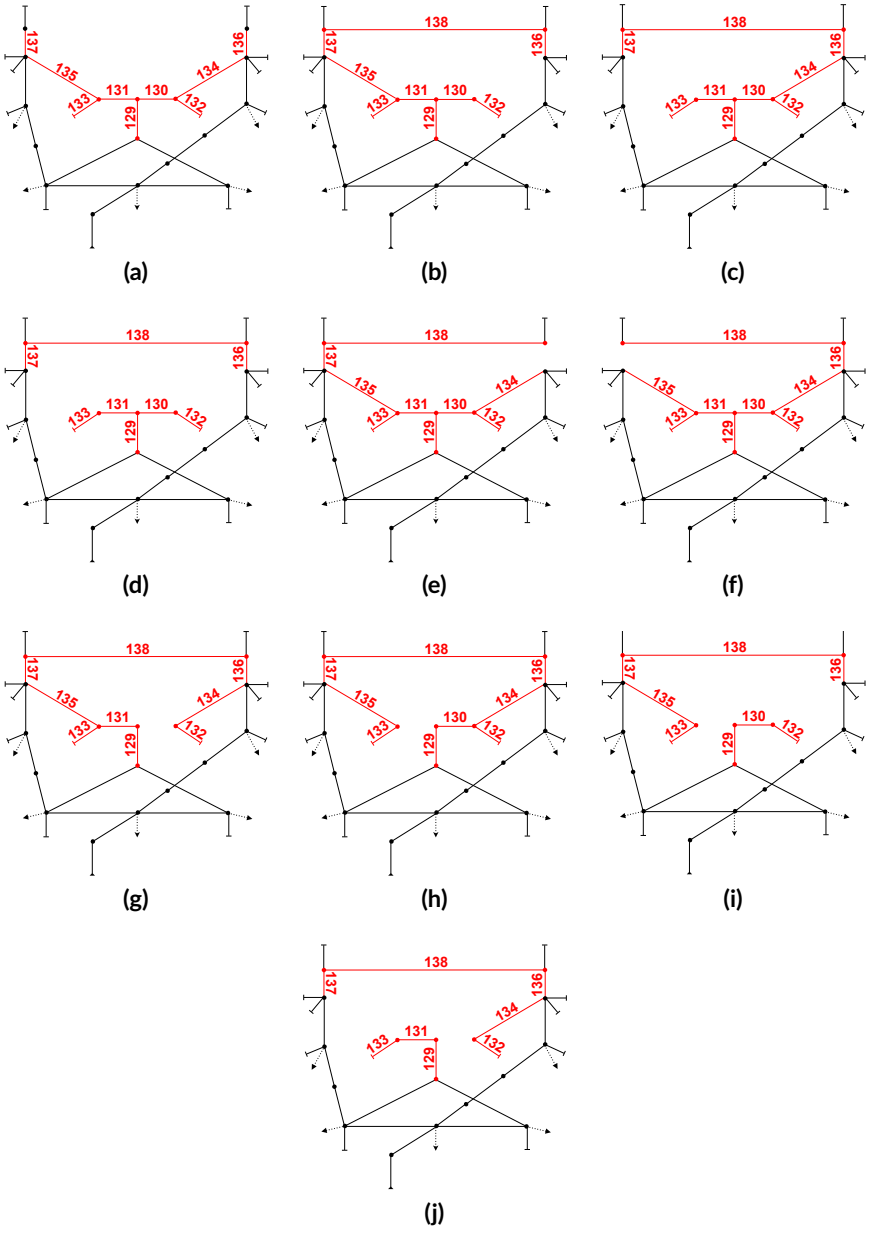

Figure A.2: Topology of the CoW variations modeled. The missing segments for each variation are listed in Table 4.2.

Appendix **B**

Appendix Temperature Model

B.1 Coupling of the Models

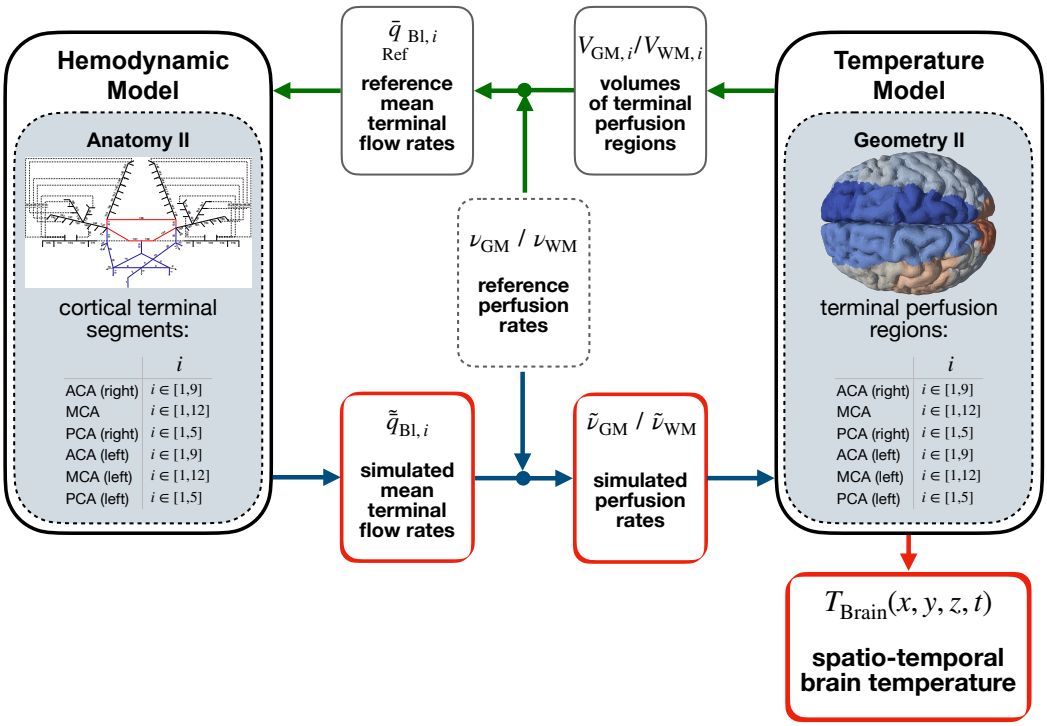

Figure B.1: Coupling of the hemodynamics and temperature model for Anatomy / Geometry II.

B.2 Thermal Tissue Properties

Table B.1: Thermal tissue properties. Values from [119].

Tissue	$\nu\left(\frac{1}{s}\right)$	$P_{Met}\left(\frac{W}{m^3}\right)$	$\lambda\left(\frac{W}{m\cdot K}\right)$	$c\left(\frac{J}{kg\cdot K}\right)$	$\rho\left(\frac{kg}{m^3}\right)$
Air	0	0	0.03	1.00E3	1.16
Blood	0	0	0.52	3.62E3	1.05E3
CSF	0	0	0.57	4.10E3	1.01E3
GM	0.0133	1.62E4	0.55	3.70E3	1.04E3
Skin	1.96E-3	1.83E3	0.37	3.39E3	1.11E3
Skull	4.54E-4	421	0.32	1.79E3	1.54E3
WM	3.63E-3	4.50E3	0.48	3.58E3	1.04E3

B.3 Geometry Generation

B.3.1 Alignment of Shape Models for Brainstem & Cerebellum

For the alignment of the segmented and extracted surfaces of the cerebellum and the brainstem to the refined brain geometry (cf. 5.2.1) (Fig. 5.3b), the characteristic shape of the lateral ventricles in the magnetic resonance (MR) images [195] was used. The segmented surface of the lateral ventricles was used as pivot element to achieve an alignment with the lateral ventricle (Fig: B.2) in the refined brain geometry. The following translation vector (in mm) was found heuristically:

$$t = \begin{bmatrix} 91 \\ 128 \\ 72 \end{bmatrix}.$$

Discussion & Limitation

Since the MR images built the basis for the generation of the refined brain geometry (cf. 5.2.1), the heuristical alignment resulted in almost exact visual conformity of the surfaces and an additional rotation of the shape models was not performed. Nevertheless, an alignment process that takes into account a minimization of the mean distance between the nodes and an additional rotation could lead to an optimal result. However, due to the subsequently nearest neighbor mapping (cf. 5.2.1) this process was considered to be not necessary.

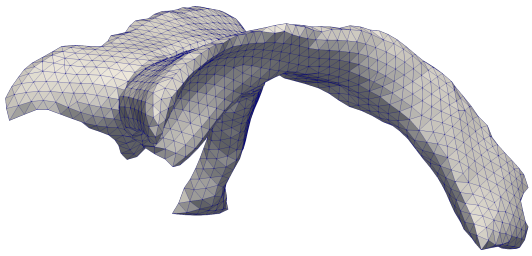

Figure B.2: The ventricles in the refined mesh for temperature calculation were used for alignment of the shape models of the cerebellum and brainstem to the corresponding surfaces in the refined mesh.

B.3.2 Parameters of the Terminal Perfusion Regions

Geometry I

Table B.2: Geometry I: Parameters of the terminal perfusion regions.

Segment	Cortical branch	ID (WM)	ID (GM)	V (GM) (ml)	V (WM) (ml)	V (total) (ml)
T139r	Orbito frontal (r)	65	165	7.3	4.0	11.3
T140r	Fronto polar (r)	66	166	8.6	9.4	18.0
T143r	Superior parietal (r)	71	171	7.3	10.5	17.7
T144r	Pericallosal (r)	64	164	6.2	28.6	34.8
T145r	Anterior internal frontal (r)	67	167	12.6	11.3	23.9
T146r	Medial internal frontal (r)	68	168	21.7	22.2	43.9
T147r	Posterior internal frontal (r)	69	169	11.9	13.1	25.0
T148r	Precentral (r)	70	170	10.0	17.2	27.3
T139l	Orbitofrontal (l)	73	173	5.5	2.2	7.8
T140l	Frontopolar (l)	74	174	9.4	10.8	20.2
T143l	Superior parietal (l)	79	179	7.8	7.9	15.7
T144l	Pericallosal (l)	72	172	11.2	35.1	46.3
T145l	Anterior internal frontal (l)	75	175	11.8	8.6	20.4
T146l	Medial internal frontal (l)	76	176	20.6	23.2	43.8
T147l	Posterior internal frontal (l)	77	177	14.7	19.5	34.2
T148l	Precentral (l)	78	178	10.0	14.6	24.6
T149	Temporopolar (r)	30	130	21.5	12.4	33.9
T150	Anterior temporal (r)	31	131	12.0	12.8	24.8
T152	Orbitofrontal (r)	36	136	13.9	14.3	28.2
T153	Prefrontal (r)	37	137	19.6	25.6	45.2
T154	Precentral (r)	41	141	13.6	29.7	43.2
T155	Central (r)	38	138	14.7	33.7	48.4
T156	Middle tempora (r)l	32	132	21.3	11.7	33.0
T157	Posterior temporal (r)	33	133	17.4	15.0	32.4
T158	Anterior parietal (r)	39	139	13.9	20.6	34.5
T159	Temporo-occipital (r)	34	134	9.3	9.0	18.3
T160	Angular (r)	35	135	8.3	4.9	13.2
T161	Posterior parietal (r)	40	140	13.0	23.0	36.0
T162	Temporopolar (l)	50	150	17.4	11.0	28.4
T164	Orbitofrontal (l)	51	151	11.0	12.2	23.2
T165	Prefrontal (l)	43	143	22.2	32.0	54.2
T166	Precentral (l)	46	146	13.8	21.9	35.7
T167	Central (l)	52	152	16.5	31.4	47.9
T168	Anterior temporal (l)	49	149	13.1	12.6	25.7
T169	Middle temporal (l)	48	148	13.8	6.0	19.8
T170	Posterior parietal (l)	45	145	10.1	10.6	20.7
T171	Anterior parietal (l)	53	153	13.9	29.1	43.0
T172	Angular (l)	42	142	5.2	2.3	7.4
T173a	Posterior temporal (l)	47	147	21.1	24.2	45.3
T173b	Temporo-occipital (l)	44	144	9.5	10.1	19.6

Segment	Cortical branch	ID (WM)	ID (GM)	V (GM) (ml)	V (WM) (ml)	V (total) (ml)
T174r	Hippocampal (r)	54	154	5.6	8.2	13.8
T175r	Anterior temporal (r)	55	155	11.2	15.4	26.6
T176r	Parieto-occipital (r)	57	157	15.4	25.4	40.8
T177r	Posterior temporal (r)	56	156	8.9	13.5	22.5
T178r	Calcarine (r)	58	158	12.2	20.7	32.9
T174l	Hippocampal (l)	59	159	8.9	9.3	18.2
T175l	Anterior temporal (l)	60	160	15.9	18.0	33.9
T176l	Parieto-occipital (l)	63	163	18.5	30.5	49.0
T177l	Posterior temporal (l)	61	161	9.7	13.9	23.6
T178l	Calcarine (l)	62	162	11.7	17.4	29.1

Geometry II

Table B.3: Geometry II: Parameters of the terminal perfusion regions.

Segment	Cortical branch	ID (WM)	ID (GM)	V (GM) (ml)	V (WM) (ml)	V (total) (ml)
T139r	Orbito frontal (r)	12	112	7.9	4.0	12.0
T140r	Fronto polar (r)	13	113	8.5	10.6	19.0
T141r	Anterior internal frontal (r)	14	114	13.5	12.1	25.6
T142r	Medial internal frontal (r)	15	115	15.1	14.9	30.0
T143r	Posterior internal frontal (r)	20	120	16.3	15.9	32.2
T144r	Precentral (r)	16	116	11.0	19.4	30.4
T145r	Superior parietal (r)	17	117	7.1	8.5	15.5
T146ra	Inferior parietal (r)	18	118	5.3	9.1	14.4
T146rb	Pericallosal (r)	19	n.a.	0.0	22.5	22.5
T139l	Orbito frontal (l)	22	122	5.5	2.3	7.8
T140l	Fronto polar (l)	23	123	7.9	7.5	15.4
T141l	Anterior internal frontal (l)	24	124	11.2	9.9	21.1
T142l	Medial internal frontal (l)	25	125	16.0	15.9	31.9
T143l	Posterior internal frontal (l)	26	126	16.9	19.4	36.3
T144l	Precentral (l)	29	129	12.3	18.2	30.5
T145l	Superior parietal (l)	28	128	9.8	14.3	24.1
T146la	Inferior parietal (l)	27	127	4.2	3.5	7.7
T146lb	Pericallosal (l)	21	121	7.6	31.0	38.6

Segment	Cortical branch	ID (WM)	ID (GM)	V (GM) (ml)	V (WM) (ml)	V (total) (ml)
T147	Temporopolar (r)	30	130	21.6	11.9	33.5
T148	Anterior temporal (r)	31	131	12.0	12.9	24.8
T150	Orbitofrontal (r)	36	136	12.7	11.3	24.0
T151	Prefrontal (r)	37	137	21.5	37.1	58.5
T152	Precentral (r)	41	141	13.4	22.2	35.6
T153	Central	38	138	14.6	35.7	50.4
T154	Anterior parietal (r)	39	139	13.9	21.1	35.0
T155	Angular (r)	35	135	8.5	2.5	11.0
T156	Posterior parietal (r)	40	140	13.1	25.0	38.1
T157	Middle temporal (r)	32	132	18.5	8.8	27.3
T158a	Posterior temporal (r)	33	133	19.0	13.9	33.0
T158b	Temporo-occipital (r)	34	134	9.7	10.4	20.0
T159	Temporopolar (l)	50	150	17.6	11.5	29.1
T161	Orbitofrontal (l)	51	151	10.9	11.2	22.1
T162	Prefrontal (l)	43	143	23.4	38.7	62.0
T163	Precentra (l)l	46	146	13.5	18.3	31.9
T164	Central (l)	52	152	16.2	30.4	46.6
T165	Posterior parietal (l)	45	145	9.7	7.3	16.9
T166	Anterior parietal (l)	53	153	14.7	33.5	48.3
T167	Angular (l)	42	142	4.9	3.1	8.0
T168	Anterior temporal (l)	49	149	11.9	11.2	23.1
T169	Middle temporal (l)	48	148	13.8	6.8	20.6
T170a	Posterior temporal (l)	47	147	20.8	18.6	39.4
T170b	Temperor-occipital (l)	44	144	10.6	12.2	22.8
T171r	Hippocampal (r)	54	154	5.6	8.2	13.8
T172r	Anterior temporal (r)	55	155	11.2	15.4	26.6
T173r	Parieto-occipital (r)	57	157	15.4	25.4	40.8
T174r	Posterior temporal (r)	56	156	8.9	13.5	22.5
T175r	Calcarine (r)	58	158	12.2	20.7	32.9
T171l	Hippocampal (l)	59	159	8.9	9.3	18.2
T172l	Anterior temporal (l)	60	160	15.9	18.0	33.9
T173l	Parieto-occipital (l)	63	163	18.5	30.5	49.0
T174l	Posterior temporal (l)	61	161	9.7	13.9	23.6
T175l	Calcarine (l)	62	162	11.7	17.4	29.1

List of Figures

List of Tables

References

[1] E. J. Benjamin, S. S. Virani, C. W. Callaway, et al., "Heart disease and stroke statistics-2018 update: a report from the american heart association," *Circulation*, vol. 137, no. 12, pp. e67–e492, 2018.

[2] R. A. Seupaul and L. G. Wilbur, "Does therapeutic hypothermia benefit survivors of cardiac arrest?" *Annals of Emergency Medicine*, vol. 58, no. 3, pp. 282–283, Sep. 2011.

[3] S. A. Bernard, T. W. Gray, M. D. Buist, et al., "Treatment of comatose survivors of out-of-hospital cardiac arrest with induced hypothermia," *The New England Journal of Medicine*, vol. 346, no. 8, pp. 557–563, Feb. 2002.

[4] M. Holzer, E. Cerchiari, P. Martens, et al., "Mild therapeutic hypothermia to improve the neurologic outcome after cardiac arrest," *The New England Journal of Medicine*, vol. 346, no. 8, pp. 549–556, Feb. 2002.

[5] H. Chen, M. Chopp, Z. G. Zhang, et al., "The effect of hypothermia on transient middle cerebral artery occlusion in the rat," *Journal of Cerebral Blood Flow & Metabolism*, vol. 12, no. 4, pp. 621–628, Jul. 1992.

[6] M. P. Ehrlich, J. N. McCullough, N. Zhang, et al., "Effect of hypothermia on cerebral blood flow and metabolism in the pig," *The Annals of Thoracic Surgery*, vol. 73, no. 1, pp. 191–197, Jan. 2002.

[7] V. D. Worp, H. Bart, E. S. Sena, et al., "Hypothermia in animal models of acute ischaemic stroke: a systematic review and meta-analysis," *Brain*, vol. 130, no. 12, pp. 3063–3074, Dec. 2007.

[8] S. Schwab, D. Georgiadis, J. Berrouschot, et al., "Feasibility and safety of moderate hypothermia after massive hemispheric infarction," *Stroke*, vol. 32, no. 9, pp. 2033–2035, Sep. 2001.

[9] T.-C. Wu and J. C. Grotta, "Hypothermia for acute ischaemic stroke," *The Lancet Neurology*, vol. 12, no. 3, pp. 275–284, Mar. 2013.

[10] H. B. van der Worp, M. R. Macleod, P. M. W. Bath, et al., "EuroHYP-1: European multicenter, randomized, phase III clinical trial of therapeutic hypothermia plus best medical treatment vs. best medical treatment alone for acute ischemic stroke," *International Journal of Stroke: Official Journal of the International Stroke Society*, vol. 9, no. 5, pp. 642–645, Jul. 2014.

[11] Y.-H. Hwang, J.-S. Jeon, Y.-W. Kim, et al., "Impact of immediate post-reperfusion cooling on outcome in patients with acute stroke and substantial ischemic changes," *Journal of NeuroInterventional Surgery*, vol. 9, no. 1, pp. 21–25, Jan. 2017.

[12] T. C. Jackson and P. M. Kochanek, "A new vision for therapeutic hypothermia in the era of targeted temperature management: a speculative synthesis," *Therapeutic Hypothermia and Temperature Management*, vol. 9, no. 1, pp. 13–47, Feb. 2019.

[13] C. Wu, W. Zhao, H. An, et al., "Safety, feasibility, and potential efficacy of intraarterial selective cooling infusion for stroke patients treated with mechanical thrombectomy," *Journal of Cerebral Blood Flow & Metabolism*, vol. 38, no. 12, pp. 2251–2260, Dec. 2018.

[14] G. Cattaneo, M. Schumacher, J. Wolfertz, et al., "Combined selective cerebral hypothermia and mechanical artery recanalization in acute ischemic stroke: in vitro study of cooling performance," *American Journal of Neuroradiology*, vol. 36, no. 11, pp. 2114–2120, Nov. 2015.

[15] J. N. Stankowski and R. Gupta, "Therapeutic targets for neuroprotection in acute ischemic stroke: lost in translation?" *Antioxidants & Redox Signaling*, vol. 14, no. 10, pp. 1841–1851, May 2011.

[16] G. Cattaneo and S. Meckel, "Review of selective brain hypothermia in acute ischemic stroke therapy using an intracarotid, closed-loop cooling catheter," *Brain Circulation*, vol. 5, p. 211, Jan. 2019.

[17] J. Caroff, R. M. King, J. E. Mitchell, et al., "Focal cooling of brain parenchyma in a transient large vessel occlusion model: proof-of-concept," *Journal of NeuroInterventional Surgery*, vol. 12, no. 2, pp. 209–213, Feb. 2020.

[18] S. S. Song and P. D. Lyden, "Overview of therapeutic hypothermia," *Current Treatment Options in Neurology*, vol. 14, no. 6, pp. 541–548, Dec. 2012.

[19] R. F. H. Schmidt, Ed., *Physiologie des Menschen : mit Pathophysiologie; mit 85 Tabellen; mit herausnehmbaren Repetitorium*, 31st ed., Springer-Lehrbuch. Heidelberg: Springer, 2010.

[20] S. Silbernagl, A. Despopoulos, and R. I. Gay, Eds., *Taschenatlas Physiologie*, 8th ed. Stuttgart [u.a.]: Thieme, 2012.

[21] L. M. Jiji, *Heat Conduction*, 3rd ed. Berlin: Springer, 2009.

[22] A. P. Avolio, "Multi-branched model of the human arterial system," *Medical & Biological Engineering & Computing*, vol. 18, no. 6, pp. 709–718, Nov. 1980.

[23] H. H. Pennes, "Analysis of tissue and arterial blood temperatures in the resting human forearm," *Journal of Applied Physiology*, vol. 85, no. 1, pp. 5–34, 1948.

[24] A. C. Guyton and J. E. Hall, *Textbook of Medical Physiology*, 9th ed. Philadelphia, Pa. [u.a.]: Saunders, 1996.

[25] E. P. Widmaier, H. Raff, and K. T. Strang, *Vander's Human Physiology: The Mechanisms of Body Function*. McGraw-Hill Higher Education, 2008.

[26] R. Brandes, F. Lang, and R. F. Schmidt, Eds., *Physiologie des Menschen: mit Pathophysiologie*, 32nd ed., Springer-Lehrbuch. Berlin Heidelberg: Springer-Verlag, 2019.

[27] W. M. Bayliss, "On the local reactions of the arterial wall to changes of internal pressure," *The Journal of Physiology*, vol. 28, no. 3, pp. 220–231, May 1902.

[28] E. M. Renkin and C. Crone, "Microcirculation and Capillary Exchange," in *Comprehensive Human Physiology: From Cellular Mechanisms to Integration*, R. Greger and U. Windhorst, Eds. Berlin, Heidelberg: Springer, 1996, pp. 1965–1979.

[29] T. M. Sundt and A. G. Waltz, "Cerebral ischemia and reactive hyperemia. Studies of cortical blood flow and microcirculation before, during, and after temporary occlusion of middle cerebral artery of squirrel monkeys," *Circulation Research*, vol. 28, no. 4, pp. 426–433, Apr. 1971.

[30] R. C. Gur, B. I. Turetsky, M. Matsui, et al., "Sex differences in brain gray and white matter in healthy young adults: correlations with cognitive performance," *Journal of Neuroscience*, vol. 19, no. 10, pp. 4065–4072, May 1999, publisher: Society for Neuroscience Section: ARTICLE.

[31] H. Blumenfeld, *Neuroanatomy Through Clinical Cases*. Second edition. Sunderland, Mass. : Sinauer Associates, 2010.

[32] D. J. A. Heylings, S. W. Carmichael, S. J. Leinster, et al., *McMinn's Concise Human Anatomy.*, vol. Second edition. CRC Press, 2018.

[33] F. Paulsen and J. Waschke, *Sobotta Atlas of Human Anatomy: Head, Neck and Neuroanatomy*. Elsevier,Urban & Fischer Verlag, Apr. 2013.

[34] M. B. Carpenter, *Core Text of Neuroanatomy*. Williams & Wilkins, 1985.

[35] E. Luders, P. M. Thompson, and A. W. Toga, "The development of the corpus callosum in the healthy human brain," *The Journal of Neuroscience*, vol. 30, no. 33, pp. 10 985–10 990, Aug. 2010.

[36] M. Shoykhet and R. S. B. Clark, "Structure, Function, and Development of the Nervous System," in *pediatric critical care*, fourth edition ed., B. P. Fuhrman and J. J. Zimmerman, Eds. Saint Louis: Mosby, Jan. 2011.

[37] U. Wolf, M. J. Rapoport, and T. A. Schweizer, "Evaluating the affective component of the cerebellar cognitive affective syndrome," *The Journal of Neuropsychiatry and Clinical Neurosciences*, vol. 21, no. 3, pp. 245–253, 2009.

[38] "Anatomy," Mar. 2020, library Catalog: www.brainfacts.org.

[39] K. DeVault, P. A. Gremaud, V. Novak, et al., "Blood flow in the circle of Willis: modeling and calibration," *Multiscale Modeling & Simulation*, vol. 7, no. 2, pp. 888–909, Jan. 2008, publisher: Society for Industrial and Applied Mathematics.

[40] E. Schulte, U. Schumacher, and M. Schünke, *PROMETHEUS Kopf, Hals und Neuroanatomie: LernAtlas Anatomie*. Georg Thieme Verlag, Sep. 2018.

[41] M. Trepel, *Neuroanatomie: Struktur und Funktion*, 5th ed. München: Elsevier, Urban & Fischer, 2012.

[42] F. H. Martini, M. J. Timmons, and R. B. Tallitsch, *Anatomie-Kompaktlehrbuch*, 6th ed., Pearson, no. 4198. München [u.a.]: Pearson, 2013.

[43] B. N. Tillmann, "Kopf," in *atlas der anatomie des menschen*, Springer-Lehrbuch, B. N. Tillmann, Ed. Berlin, Heidelberg: Springer, 2010, pp. 19–145.

[44] "Circle of Willis anatomy: overview, gross anatomy, natural variants," Nov. 2019, publication: Medscape - eMedicine.

[45] D. S. Liebeskind, "Collateral circulation," *Stroke*, vol. 34, no. 9, pp. 2279–2284, Sep. 2003.

[46] M. J. de Boorder, J. van der Grond, A. J. van Dongen, et al., "Spect measurements of regional cerebral perfusion and carbondioxide reactivity: correlation with cerebral collaterals in internal carotid artery occlusive disease," *Journal of Neurology*, vol. 253, no. 10, pp. 1285–1291, Oct. 2006.

[47] A. van der Zwan, B. Hillen, C. A. Tulleken, et al., "A quantitative investigation of the variability of the major cerebral arterial territories," *Stroke*, vol. 24, no. 12, pp. 1951–1959, Dec. 1993.

[48] J. Alastruey, K. H. Parker, J. Peiró, et al., "Modelling the circle of willis to assess the effects of anatomical variations and occlusions on cerebral flows," *Journal of Biomechanics*, vol. 40, no. 8, pp. 1794–1805, 2007.

[49] R. A. Bergman and A. K. Afifi, *Anatomy: An Encyclopedic Reference to the Language of Anatomy and Neuroanatomy*. Outskirts Press, Jul. 2016.

[50] K. A. Hafez, N. M. Afifi, and F. Z. Saudi, "Anatomical variations of the circle of Willis in males and females on 3D MR angiograms," *The Egyptian Journal of Hospital Medicine*, vol. 26,

no. 1, pp. 106–121, Jan. 2007, publisher: Ain Shams University, Faculty of Medicine, Pan Arab League of Continuous Medical Education.

[51] H. Lippert and R. Pabst, *Arterial Variations in Man: Classification and Frequency*. J.F. Bergmann-Verlag München, 1985.

[52] F. Mut, S. Wright, G. A. Ascoli, et al., "Morphometric, geographic and territorial characterization of brain arterial trees," *International journal for numerical methods in biomedical engineering*, vol. 30, no. 7, pp. 755–766, Jul. 2014.

[53] M. A. Stefani, F. L. Schneider, A. C. Marrone, et al., "Anatomic variations of anterior cerebral artery cortical branches," *Clinical Anatomy (New York, N.Y.)*, vol. 13, no. 4, pp. 231–236, 2000.

[54] H. Krayenbühl, P. Huber, and M. G. Yaşargil, *Cerebral Angiography*. Thieme, 1982.

[55] A. G. Osborn, *Diagnostic Cerebral Angiography*. Lippincott Williams & Wilkins, 1999.

[56] D. Perlmutter and A. L. Rhoton, "Microsurgical anatomy of the distal anterior cerebral artery," *Journal of Neurosurgery*, vol. 49, no. 2, pp. 204–228, Aug. 1978.

[57] L. Zarrinkoob, K. Ambarki, A. Wåhlin, et al., "Blood flow distribution in cerebral arteries," *Journal of Cerebral Blood Flow & Metabolism*, vol. 35, no. 4, pp. 648–654, Apr. 2015.

[58] F. Umansky, S. M. Juarez, M. Dujovny, et al., "Microsurgical anatomy of the proximal segments of the middle cerebral artery," *Journal of Neurosurgery*, vol. 61, no. 3, pp. 458–467, Sep. 1984.

[59] K. Cilliers and B. J. Page, "Anatomy of the middle cerebral artery; cortical branches, branching pattern and anomalies," *Turkish Neurosurgery*, 2016.

[60] A. A. Zeal and A. L. Rhoton, "Microsurgical anatomy of the posterior cerebral artery," *Journal of Neurosurgery*, vol. 48, no. 4, pp. 534–559, 1978.

[61] I. R. Winship, "Cerebral collaterals and collateral therapeutics for acute ischemic stroke," *Microcirculation*, vol. 22, no. 3, pp. 228–236, Apr. 2015.

[62] N. Tariq and R. Khatri, "Leptomeningeal collaterals in acute ischemic stroke," *Journal of Vascular and Interventional Neurology*, vol. 1, no. 4, pp. 91–95, Oct. 2008.

[63] A. Shuaib, K. Butcher, A. A. Mohammad, et al., "Collateral blood vessels in acute ischaemic stroke: a potential therapeutic target," *The Lancet Neurology*, vol. 10, no. 10, pp. 909–921, Oct. 2011.

[64] M. Pham and M. Bendszus, "Facing time in ischemic stroke: an alternative hypothesis for collateral failure," *Clinical Neuroradiology*, vol. 26, no. 2, pp. 141–151, Jun. 2016.

[65] J. T. V. Hansen, *Netter's Clinical Anatomy*, 4th ed., Netter basic science, F. H. Netter, Ed. Philadelphia, PA: Elsevier, 2019.

[66] G. A. Donnan, M. Fisher, M. Macleod, et al., "Stroke," *The Lancet*, vol. 371, no. 9624, pp. 1612–1623, May 2008.

[67] F. Guercini, M. Acciarresi, G. Agnelli, et al., "Cryptogenic stroke: time to determine aetiology," *Journal of thrombosis and haemostasis*, vol. 6, no. 4, pp. 549–554, Apr. 2008.

[68] A. K. Tripathi, "Cerebral Stroke: An Introduction," in *Advancement in the Pathophysiology of Cerebral Stroke*, R. Patnaik, A. K. Tripathi, and A. Dwivedi, Eds. Singapore: Springer Singapore, 2019, pp. 1–9.

[69] Virani Salim S., Alonso Alvaro, Benjamin Emelia J., et al., "Heart disease and stroke statistics—2020 update," *Circulation*, vol. 0, no. 0, publisher: American Heart Association.

[70] S. Bundesamt, "Statistisches Bundesamt Deutschland - GENESIS-Online," Mar. 2020.

[71] "Stroke: hope through research: national institute of neurological disorders and stroke (ninds)," Oct. 2015.

[72] L. Singleton, K. A. K. A. Johnson, and L. Villarosa, *The Black Health Library Guide to Stroke*. New York : Henry Holt and Co., 1993.

[73] C. R. Gomez, "Time is brain!" *Journal of Stroke and Cerebrovascular Diseases*, vol. 3, no. 1, pp. 1–2, 1993.

[74] Saver Jeffrey L., "Time is brain-quantified," *Stroke*, vol. 37, no. 1, pp. 263–266, Jan. 2006, publisher: American Heart Association.

[75] C. R. Gomez, "Time is brain: the stroke theory of relativity," *Journal of Stroke and Cerebrovascular Diseases*, vol. 27, no. 8, pp. 2214–2227, Aug. 2018, publisher: Elsevier.

[76] M. Goyal, B. K. Menon, W. H. van Zwam, et al., "Endovascular thrombectomy after large-vessel ischaemic stroke: a meta-analysis of individual patient data from five randomised trials," *The Lancet*, vol. 387, no. 10029, pp. 1723–1731, Apr. 2016.

[77] A. M. Kuczynski, A. M. Demchuk, and M. A. Almekhlafi, "Therapeutic hypothermia: applications in adults with acute ischemic stroke," *Brain Circulation*, vol. 5, no. 2, pp. 43–54, 2019.

[78] J. M. Simard, J. Sahuquillo, K. N. Sheth, et al., "Managing malignant cerebral infarction," *Current treatment options in neurology*, vol. 13, no. 2, pp. 217–229, Apr. 2011.

[79] R. T. Higashida, A. J. Furlan, H. Roberts, et al., "Trial design and reporting standards for intra-arterial cerebral thrombolysis for acute ischemic stroke," *Stroke*, vol. 34, no. 8, pp. e109–137, Aug. 2003.

[80] J. E. Fugate, A. M. Klunder, and D. F. Kallmes, "What is meant by "TICI"?" *AJNR. American journal of neuroradiology*, vol. 34, no. 9, pp. 1792–1797, Sep. 2013.

[81] O. O. Zaidat, A. J. Yoo, P. Khatri, et al., "Recommendations on angiographic revascularization grading standards for acute ischemic stroke," *Stroke*, vol. 44, no. 9, pp. 2650–2663, Sep. 2013.

[82] *Rosen's Emergency Medicine: Concepts and Clinical Practice*. Philadelphia : Mosby/Elsevier, 2006.

[83] D. A. Cooley, D. A. Ott, O. H. Frazier, et al., "Surgical treatment of aneurysms of the transverse aortic arch: experience with 25 patients using hypothermic techniques," *The Annals of Thoracic Surgery*, vol. 32, no. 3, pp. 260–272, Sep. 1981.

[84] D. J. A. Brown, H. Brugger, J. Boyd, et al., "Accidental hypothermia." *The New England Journal of Medicine*, vol. 367, no. 20, pp. 1930–1938, 2012.

[85] D. W. Benson, G. R. Williams, F. C. Spencer, et al., "The use of hypothermia after cardiac arrest," *Anesthesia & Analgesia*, vol. 38, no. 6, pp. 423–428, Dec. 1959.

[86] S. Shankaran, A. R. Laptook, R. A. Ehrenkranz, et al., "Whole-body hypothermia for neonates with hypoxic-ischemic encephalopathy," *The New England Journal of Medicine*, vol. 353, no. 15, pp. 1574–1584, Oct. 2005.

[87] C. Metz, M. Holzschuh, T. Bein, et al., "Moderate hypothermia in patients with severe head injury: cerebral and extracerebral effects," *Journal of Neurosurgery*, vol. 85, no. 4, pp. 533–541, Oct. 1996.

[88] E. A. Bering, "Effect of body temperature change on cerebral oxygen consumption of the intact monkey," *American Journal of Physiology-Legacy Content*, vol. 200, no. 3, pp. 417–419, Mar. 1961, publisher: American Physiological Society.

[89] P. A. Steen, L. Newberg, J. H. Milde, et al., "Hypothermia and barbiturates: individual and combined effects on canine cerebral oxygen consumption," *Anesthesiology*, vol. 58, no. 6, pp. 527–532, Jun. 1983.

[90] S. L. Mehta, N. Manhas, and R. Raghubir, "Molecular targets in cerebral ischemia for developing novel therapeutics," *Brain Research Reviews*, vol. 54, no. 1, pp. 34–66, Apr. 2007.

[91] P. G. Lysko, C. L. Webb, T. L. Yue, et al., "Neuroprotective effects of tetrodotoxin as a Na+ channel modulator and glutamate release inhibitor in cultured rat cerebellar neurons and in gerbil global brain ischemia," *Stroke*, vol. 25, no. 12, pp. 2476–2482, Dec. 1994.

[92] H. Karibe, G. J. Zarow, S. H. Graham, et al., "Mild intraischemic hypothermia reduces postischemic hyperperfusion, delayed postischemic hypoperfusion, blood-brain barrier disruption, brain edema, and neuronal damage volume after temporary focal cerebral ischemia in rats," *Journal of Cerebral Blood Flow & Metabolism*, vol. 14, no. 4, pp. 620–627, Jul. 1994.

[93] C. M. Maier, G. H. Sun, D. Cheng, et al., "Effects of mild hypothermia on superoxide anion production, superoxide dismutase expression, and activity following transient focal cerebral ischemia," *Neurobiology of Disease*, vol. 11, no. 1, pp. 28–42, Oct. 2002.

[94] N. Kawai, M. Kawanishi, M. Okauchi, et al., "Effects of hypothermia on thrombin-induced brain edema formation," *Brain Research*, vol. 895, no. 1-2, pp. 50–58, Mar. 2001.

[95] Hemmen Thomas M., Raman Rema, Guluma Kama Z., et al., "Intravenous thrombolysis plus hypothermia for acute treatment of ischemic stroke (ictus-l)," *Stroke*, vol. 41, no. 10, pp. 2265–2270, Oct. 2010, publisher: American Heart Association.

[96] M. A. Peberdy, C. W. Callaway, R. W. Neumar, et al., "Part 9: post-cardiac arrest care: 2010 American heart association guidelines for cardiopulmonary resuscitation and emergency cardiovascular care," *Circulation*, vol. 122, no. 18 Suppl 3, pp. S768–786, Nov. 2010.

[97] K. H. Polderman, S. M. Peerdeman, and A. R. Girbes, "Hypophosphatemia and hypomagnesemia induced by cooling in patients with severe head injury," *Journal of Neurosurgery*, vol. 94, no. 5, pp. 697–705, May 2001.

[98] D. Sessler, *Therapeutic Hypothermia*. New York: CRC Press, 2005.

[99] H. A. Choi, S.-B. Ko, M. Presciutti, et al., "Prevention of shivering during therapeutic temperature modulation: the Columbia anti-shivering protocol," *Neurocritical Care*, vol. 14, no. 3, pp. 389–394, Jun. 2011.

[100] M. A. Lazzaro and S. Prabhakaran, "Induced hypothermia in acute ischemic stroke," *Expert Opinion on Investigational Drugs*, vol. 17, no. 8, pp. 1161–1174, Aug. 2008.

[101] W. Qiu, H. Shen, Y. Zhang, et al., "Noninvasive selective brain cooling by head and neck cooling is protective in severe traumatic brain injury," *Journal of Clinical Neuroscience: Official Journal of the Neurosurgical Society of Australasia*, vol. 13, no. 10, pp. 995–1000, Dec. 2006.

[102] H. Wang, W. Olivero, G. Lanzino, et al., "Rapid and selective cerebral hypothermia achieved using a cooling helmet," *Journal of Neurosurgery*, vol. 100, no. 2, pp. 272–277, Feb. 2004.

[103] E. Keller, H.-G. Imhof, S. Gasser, et al., "Endovascular cooling with heat exchange catheters: a new method to induce and maintain hypothermia," *Intensive Care Medicine*, vol. 29, no. 6, pp. 939–943, Jun. 2003.

[104] M. Holzer, M. Müllner, F. Sterz, et al., "Efficacy and safety of endovascular cooling after cardiac arrest: cohort study and Bayesian approach," *Stroke*, vol. 37, no. 7, pp. 1792–1797, Jul. 2006.

[105] E. Esposito, M. Ebner, U. Ziemann, et al., "In cold blood: intraarteral cold infusions for selective brain cooling in stroke," *Journal of Cerebral Blood Flow & Metabolism*, vol. 34, no. 5, pp. 743–752, May 2014.

[106] G. Cattaneo, M. Schumacher, C. Maurer, et al., "Endovascular cooling catheter for selective brain hypothermia: an animal feasibility study of cooling performance," *American Journal of Neuroradiology*, vol. 37, no. 5, pp. 885–891, May 2016.

[107] O. Dössel, *Bildgebende Verfahren in der Medizin: Von der Technik zur medizinischen Anwendung*, 2nd ed., SpringerLink. Berlin, Heidelberg: Springer Vieweg, 2016.

[108] R. G. Gordon, R. B. Roemer, and S. M. Horvath, "A mathematical model of the human temperature regulatory system - transient cold exposure response," *IEEE Transactions on Biomedical Engineering*, vol. BME-23, no. 6, pp. 434–444, Nov. 1976, conference Name: IEEE Transactions on Biomedical Engineering.

[109] B. Bindu, A. Bindra, and G. Rath, "Temperature management under general anesthesia: Compulsion or option," *Journal of Anaesthesiology, Clinical Pharmacology*, vol. 33, no. 3, pp. 306–316, 2017.

[110] M. Lopez, D. I. Sessler, K. Walter, et al., "Rate and gender dependence of the sweating, vasoconstriction, and shivering thresholds in humans," *Anesthesiology*, vol. 80, no. 4, pp. 780–788, Apr. 1994.

[111] A. Taguchi and A. Kurz, "Thermal management of the patient: where does the patient lose and/or gain temperature?" *Current Opinion in Anaesthesiology*, vol. 18, no. 6, pp. 632–639, Dec. 2005.

[112] A. Kurz, D. I. Sessler, F. Birnbauer, et al., "Thermoregulatory vasoconstriction impairs active core cooling," *Anesthesiology*, vol. 82, no. 4, pp. 870–876, Apr. 1995.

[113] G. Meyrowitz, "Automatisierung der Herz-Lungen-Maschine," PhD Thesis, Mensch & Buch Verlag, Berlin, 2005.

[114] H. Oertel, Ed., *Führer durch die Strömungslehre: Grundlagen und Phänomene*, 13th ed. Springer Vieweg, 2012.

[115] J. Wittenburg and E. Pestel, *Festigkeitslehre: ein Lehr- und Arbeitsbuch*. Wiley & Son, 2001.

[116] A. Schmidt, *Technical Thermodynamics for Engineers: Basics and Applications*, 1st ed., Springer eBooks. Cham: Springer, 2019.

[117] H. Windisch, *Thermodynamik: Ein Lehrbuch für Ingenieure*, 5th ed., De Gruyter Ingenieurswissenschaften. München: De Gruyter, 2014.

[118] R. Eberhart and A. Shitzer, *Heat Transfer in Medicine and Biology: Analysis and Applications*, no. Bd. 2. Springer US, 2012.

[119] P. Hasgall, F. Di Gennaro, C. Baumgartner, et al., "IT'IS Database for thermal and electromagnetic parameters of biological tissues," May 2018.

[120] M. Schwarz, M. W. Krueger, H. Busch, et al., "Model-based assessment of tissue perfusion and temperature in deep hypothermic patients," *IEEE Transactions on Biomedical Engineering*, vol. 57, no. 7, pp. 1577–1586, Jul. 2010.

[121] M. Schwarz, "Modellbasierte Operationsplanung und Überwachung hypothermer Patienten," PhD thesis, Universität Karlsruhe (TH), Karlsruhe, 2009.

[122] S. Sindeev, J. S. Kirschke, S. Prothmann, et al., "Evaluation of flow changes after telescopic stenting of a giant fusiform aneurysm of the vertebrobasilar junction," *BioMedical Engineering OnLine*, vol. 18, no. 1, p. 82, Jul. 2019.

[123] S. Moore, T. David, J. G. Chase, et al., "3D models of blood flow in the cerebral vasculature," *Journal of Biomechanics*, vol. 39, no. 8, pp. 1454–1463, Jan. 2006.

[124] C. Zhang, L. Wang, X. Li, et al., "Modeling the circle of Willis to assess the effect of anatomical variations on the development of unilateral internal carotid artery stenosis," *Bio-Medical Materials and Engineering*, vol. 24, no. 1, pp. 491–499, 2014.

[125] L. R. John, "Forward electrical transmission line model of the human arterial system," *Medical & Biological Engineering & Computing*, vol. 42, no. 3, pp. 312–321, May 2004.

[126] H. P. Boll, "Mobile Überwachung der Funktionalität des kardiovaskulären Systems - Konzepte und Simulationen," PhD thesis, Universität Karlsruhe, Karlsruhe, 2008.

[127] T. E. Hodrus, M. Schwarz, and V. Krebs, "A time discretization method for a class of hybrid systems," *IFAC Proceedings Volumes*, vol. 37, no. 13, pp. 1365–1370, Sep. 2004.

[128] A. Noordergraaf, P. D. Verdouw, and H. B. K. Boom, "The use of an analog computer in a circulation model," *Progress in Cardiovascular Diseases*, vol. 5, no. 5, pp. 419–439, Mar. 1963.

[129] S. Schulz, "Modellierung der Hämodynamik des kardiovaskulären Systems," PhD thesis, Universität Karlsruhe (TH), Karlsruhe, 2000.

[130] K. Cieslicki and D. Ciesla, "Investigations of flow and pressure distributions in physical model of the circle of Willis," *Journal of Biomechanics*, vol. 38, no. 11, pp. 2302–2310, Nov. 2005.

[131] F. Cassot, V. Vergeur, P. Bossuet, et al., "Effects of anterior communicating artery diameter on cerebral hemodynamics in internal carotid artery disease. A model study," *Circulation*, vol. 92, no. 10, pp. 3122–3131, Nov. 1995.

[132] M. A. Helal, "Derivation of closed-form expression for the cerebral circulation models," *Computers in Biology and Medicine*, vol. 24, no. 2, pp. 103–118, Mar. 1994.

[133] S. M. Moore, K. T. Moorhead, J. G. Chase, et al., "One-dimensional and three-dimensional models of cerebrovascular flow," *Journal of Biomechanical Engineering*, vol. 127, no. 3, pp. 440–449, Sep. 2004.

[134] L. Krames, "Modelling of the human cerebral collateral circulation evaluation of the impact on the cerebral pathophysiology in case of ischaemic stroke," Bachelor's Thesis, Institute of Biomedical Engineering, Karlsruhe Institute of Technology (KIT), Karlsruhe, 2018.

[135] R. Daschner, "Generation of a simplified brain geometry for the calculation of local cerebral temperature using a 1D-hemodynamics model," Bachelor's Thesis, Institut für Strömungsmechanik, Karlsruhe Institute of Technology (KIT), 2018.

[136] T. Meissner, "Adaption and partitioning of a brain geometry for spatially detailed calculation of local cerebral temperatures," Master's thesis, Institute of Biomedical Engineering, Karlsruhe Institute of Technology (KIT), 2019.

[137] H. Gibo, C. C. Carver, A. L. Rhoton, et al., "Microsurgical anatomy of the middle cerebral artery," *Journal of Neurosurgery*, vol. 54, no. 2, pp. 151–169, Feb. 1981.

[138] H. C. Ugur, G. Kahilogullari, A. F. Esmer, et al., "A neurosurgical view of anatomical variations of the distal anterior cerebral artery: an anatomical study," *Journal of Neurosurgery*, vol. 104, no. 2, pp. 278–284, Feb. 2006.

[139] S. N. Wright, P. Kochunov, F. Mut, et al., "Digital reconstruction and morphometric analysis of human brain arterial vasculature from magnetic resonance angiography," *NeuroImage*, vol. 82, pp. 170–181, Nov. 2013.

[140] G. A. Ascoli, J. L. Krichmar, S. J. Nasuto, et al., "Generation, description and storage of dendritic morphology data." *Philosophical Transactions of the Royal Society of London. Series B*, vol. 356, no. 1412, pp. 1131–1145, Aug. 2001.

[141] W. Schroeder, B. Lorensen, and K. Martin, "The visualization toolkit: an object-oriented approach to 3D graphics," 2004.

[142] D. L. Collins, A. P. Zijdenbos, V. Kollokian, et al., "Design and construction of a realistic digital brain phantom," *IEEE Transactions on Medical Imaging*, vol. 17, no. 3, pp. 463–468, Jun. 1998.

[143] B. Foundation, "Home of the blender project - free and open 3D creation software," www.blender.org.

[144] F. McVerry, D. Liebeskind, and K. Muir, "Systematic review of methods for assessing leptomeningeal collateral flow," *American Journal of Neuroradiology*, vol. 33, no. 3, pp. 576–582, 2012.

[145] X. Leng, H. Fang, T. W. H. Leung, et al., "Impact of collaterals on the efficacy and safety of endovascular treatment in acute ischaemic stroke: a systematic review and meta-analysis," *J Neurol Neurosurg Psychiatry*, vol. 87, no. 5, pp. 537–544, May 2016.

[146] H. M. Vander Eecken and R. D. Adams, "The anatomy and functional significance of the meningeal arterial anastomoses of the human brain," *Journal of Neuropathology & Experimental Neurology*, vol. 12, no. 2, pp. 132–157, Apr. 1953.

[147] H. vander Eecken, *The Anastomoses Between the Leptomeningeal Arteries of the Brain: Their Morphological, Pathological, and Clinical Significance*. C.C. Thomas, 1959.

[148] Y. Lutz, T. Meißner, L. Krames, et al., "Selective brain hypothermia for ischemic MCA-M1 stroke: influence of cerebral arterial circulation in a 3D brain temperature model," *IEEE Transactions on Biomedical Engineering (submitted: Minor Revisions))*, 2020.

[149] Y. Lutz, R. Daschner, L. Krames, et al., "Modeling selective therapeutic hypothermia in case of acute ischemic stroke using a 1D hemodynamics model and a simplified brain geometry," *Mathematical Biosciences and Engineering*, vol. 17, no. 2, p. 1147, 2020.

[150] Y. Lutz, R. Daschner, L. Krames, et al., "Estimating local therapeutic hypothermia in case of ischemic stroke using a 1d hemodynamics model and an energetic temperature model," in *2019 41st Annual International Conference of the IEEE Engineering in Medicine and Biology Society (EMBC)*, Jul. 2019, pp. 3983–3986, iSSN: 1557-170X.

[151] R. Daschner, L. Krames, Y. Lutz, et al., "Generation of a simplified brain geometry for the calculation of local cerebral temperature using a 1D hemodynamic model," in *Current Directions in Biomedical Engineering*, vol. 5. De Gruyter, 2019, pp. 529–532, issue: 1.

[152] L. Krames, R. Daschner, Y. Lutz, et al., "Modeling of the human cerebral collateral circulation: evaluation of the impact on the cerebral perfusion in case of ischemic stroke," in *Current Directions in Biomedical Engineering*, vol. 5. De Gruyter, 2019, pp. 533–536, issue: 1.

[153] M. Anliker, R. L. Rockwell, and E. Ogden, "Nonlinear analysis of flow pulses and shock waves in arteries," *Zeitschrift für angewandte Mathematik und Physik ZAMP*, vol. 22, no. 2, pp. 217–246, Mar. 1971.

[154] L. M. Parkes, W. Rashid, D. T. Chard, et al., "Normal cerebral perfusion measurements using arterial spin labeling: reproducibility, stability, and age and gender effects," *Magnetic Resonance in Medicine*, 2004.

[155] M. Schwarz, C. Heilmann, M. W. Krueger, et al., "Model based monitoring of hypothermic patients," *Metrology and Measurement Systems*, no. Vol. 16, nr 3, pp. 443–455, 2009.

[156] D. W. Newell, R. Aaslid, A. Lam, et al., "Comparison of flow and velocity during dynamic autoregulation testing in humans," *Stroke*, vol. 25, no. 4, pp. 793–797, Apr. 1994.

[157] K. T. Moorhead, J. G. Chase, T. David, et al., "Metabolic model of autoregulation in the Circle of Willis," *Journal of Biomechanical Engineering*, vol. 128, no. 3, pp. 462–466, Jun. 2006.

[158] MATLAB, *version 7.10.0 (R2019b)*. Natick, Massachusetts: The MathWorks Inc., 2019.

[159] J. Zhong, X.-Y. Chen, T. W. H. Leung, et al., "Significance of raised flow velocity in basilar artery in patients with acute ischemic stroke: focal stenosis, coexistent stenosis, and collateral flow," *Journal of Neuroimaging: Official Journal of the American Society of Neuroimaging*, vol. 25, no. 6, pp. 922–926, Dec. 2015.

[160] R. Fahrig, H. Nikolov, A. J. Fox, et al., "A three-dimensional cerebrovascular flow phantom," *Medical Physics*, vol. 26, no. 8, pp. 1589–1599, Aug. 1999.

[161] D. Navarro-Orozco and J. C. Sánchez-Manso, "Neuroanatomy, middle cerebral artery," in *StatPearls*. Treasure Island (FL): StatPearls Publishing, 2020.

[162] Spencer M P and Reid J M, "Quantitation of carotid stenosis with continuous-wave (C-W) Doppler ultrasound." *Stroke*, vol. 10, no. 3, pp. 326–330, May 1979.

[163] S. K. Piechnik, M. Czosnyka, K. Cieślicki, et al., "Problems in application of purely linear models in cerebral circulation," *Journal of Biomechanics*, vol. 35, no. 4, pp. 553–554, Apr. 2002.

[164] A. Aracri, "Simulation study: parameterization of a hemodynamics model and conception of a multidimensional sensitivity analysis," Bachelor's Thesis, Institute for Anthropomatics and Robotics; Karlsruhe Institute of Technology (KIT), 2019.

[165] T. Lillicrap, M. Tahtal, A. Neely, et al., "A model based on the Pennes bioheat transfer equation is valid in normal brain tissue but not brain tissue suffering focal ischaemia," *Australasian Physical & Engineering Sciences in Medicine*, vol. 40, no. 4, pp. 841–850, Dec. 2017.

[166] J. C. Chato, "Heat transfer to blood vessels," *Journal of Biomechanical Engineering*, vol. 102, no. 2, pp. 110–118, May 1980, publisher: American Society of Mechanical Engineers Digital Collection.

[167] Q. He, L. Zhu, D. E. Lemons, et al., "Experimental measurements of the temperature variation along artery-vein pairs from 200 to 1000 microns diameter in rat hind limb," *Journal of Biomechanical Engineering*, vol. 124, no. 6, pp. 656–661, Dec. 2002.

[168] W. Wulff, "The energy conservation equation for living tissue," *IEEE Transactions on Biomedical Engineering*, vol. BME-21, no. 6, pp. 494–495, Nov. 1974, conference Name: IEEE Transactions on Biomedical Engineering.

[169] H. G. Klinger, "Heat transfer in perfused biological tissue. I. General theory," *Bulletin of Mathematical Biology*, vol. 36, no. 4, pp. 403–415, Aug. 1974.

[170] S. Weinbaum and L. M. Jiji, "A two phase theory for the influence of circulation on the heat transfer in surface tissue," *Advances in Bioengineering*, pp. 179–182, 1979.

[171] M. M. Chen and K. R. Holmes, "Microvascular contributions in tissue heat transfer," *Annals of the New York Academy of Sciences*, vol. 335, no. 1, pp. 137–150, 1980.

[172] S. Weinbaum, L. M. Jiji, and D. E. Lemons, "Theory and experiment for the effect of vascular microstructure on surface tissue heat transfer–Part I: Anatomical foundation and model conceptualization," *Journal of Biomechanical Engineering*, vol. 106, no. 4, pp. 321–330, Nov. 1984.

[173] S. Weinbaum and L. M. Jiji, "A new simplified bioheat equation for the effect of blood flow on local average tissue temperature," *Journal of Biomechanical Engineering*, vol. 107, no. 2, pp. 131–139, May 1985.

[174] W. J. Song, S. Weinbaum, and L. M. Jiji, "A theoretical model for peripheral tissue heat transfer using the bioheat equation of Weinbaum and Jiji," *Journal of Biomechanical Engineering*, vol. 109, no. 1, pp. 72–78, Feb. 1987.

[175] H. Arkin, L. X. Xu, and K. R. Holmes, "Recent developments in modeling heat transfer in blood perfused tissues," *IEEE Transactions on Biomedical Engineering*, vol. 41, no. 2, pp. 97–107, Feb. 1994.

[176] S. Weinbaum, L. X. Xu, L. Zhu, et al., "A new fundamental bioheat equation for muscle tissue: Part I–Blood perfusion term," *Journal of Biomechanical Engineering*, vol. 119, no. 3, pp. 278–288, Aug. 1997.

[177] A. Lakhssassi, E. Kengne, and H. Semmaoui, "Modifed Pennes' equation modelling bioheat transfer in living tissues: analytical and numerical analysis," *Natural Science*, vol. 2, no. 12, pp. 1375–1385, Dec. 2010.

[178] Z.-Z. He and J. Liu, "A coupled continuum-discrete bioheat transfer model for vascularized tissue," *International Journal of Heat and Mass Transfer*, vol. 107, pp. 544–556, Apr. 2017.

[179] L. Zhu and J. Bischof, "A new simplified bioheat equation for the effect of blood flow on local average tissue temperature," Feb. 2019.

[180] J. Hartnett, T. Irvine, and Y. Cho, *Advances in Heat Transfer: Bioengineering Heat Transfer*, ISSN. Elsevier Science, 1992.

[181] F. A. Shah and M. I. Awana, "A computational wavelet method for solving dual-phase-lag model of bioheat transfer during hyperthermia treatment," *Computational and Mathematical Methods*, p. e1095, Apr. 2020.

[182] C. Cattaneo, "A form of heat conduction equation which eliminates the paradox of instantaneous propagation," *Comptes rendus de l'Académie des sciences*, no. 247, pp. 431–433, 1958.

[183] P. Vernotte, "Les paradoxes de la theorie continue de I equation de l a chleur," *Comptes rendus de l'Académie des sciences*, no. 247, p. 3154-3155, 1958.

[184] D. Tzou and Y. D, *Macro- to Micro-Scale Heat Transfer: The Lagging Behavior*, Chemical and Mechanical Engineering Series. Taylor & Francis, 1996.

[185] S. Devarakonda, P. Bulusu, M. Al-rjoub, et al., "Influence of external head cooling on the head, core body and blood temperatures using 3D whole-body model," *International Journal of Numerical Methods for Heat & Fluid Flow*, vol. 28, Oct. 2018.

[186] H. Li, R. K. Chen, Y. Tang, et al., "An experimental study and finite element modeling of head and neck cooling for brain hypothermia," *Journal of Thermal Biology*, vol. 71, pp. 99–111, Jan. 2018.

[187] B. H. Dennis, R. C. Eberhart, G. S. Dulikravich, et al., "Finite-element simulation of cooling of realistic 3-D human head and neck," *Journal of Biomechanical Engineering*, vol. 125, no. 6, pp. 832–840, Dec. 2003.

[188] C. Collins, M. Smith, and R. Turner, "Model of local temperature changes in brain upon fuctional activation," *Journal of applied physiology (Bethesda, Md. : 1985)*, vol. 97, pp. 2051–5, Dec. 2004.

[189] C. M. Collins, W. Liu, J. Wang, et al., "Temperature and SAR calculations for a human head within volume and surface coils at 64 and 300 MHz," *Journal of Magnetic Resonance Imaging*, vol. 19, no. 5, pp. 650–656, May 2004.

[190] E. Keller, R. Mudra, C. Gugl, et al., "Theoretical evaluations of therapeutic systemic and local cerebral hypothermia," *Journal of Neuroscience Methods*, vol. 178, no. 2, pp. 345–349, Apr. 2009.

[191] R. Oostenveld, P. Fries, E. Maris, et al., "FieldTrip: Open source software for advanced analysis of MEG, EEG, and invasive electrophysiological data," *Computational Intelligence and Neuroscience*, vol. 2011, p. 156869, 2011.

[192] F. Tadel, S. Baillet, J. C. Mosher, et al., "Brainstorm: a user-friendly application for meg/eeg analysis," 2011.

[193] G. E. Strangman, Z. Li, and Q. Zhang, "Depth sensitivity and source-detector separations for near infrared spectroscopy based on the Colin27 brain template," *PloS One*, vol. 8, no. 8, p. e66319, 2013.

[194] J. D. López, V. Litvak, J. J. Espinosa, et al., "Algorithmic procedures for Bayesian MEG/EEG source reconstruction in SPM," *NeuroImage*, vol. 84, pp. 476–487, Jan. 2014.

[195] C. J. Holmes, R. Hoge, L. Collins, et al., "Enhancement of MR images using registration for signal averaging," *Journal of Computer Assisted Tomography*, vol. 22, no. 2, p. 324, Apr. 1998.

[196] Q. Fang and D. A. Boas, "Monte Carlo simulation of photon migration in 3D turbid media accelerated by graphics processing units," *Optics Express*, vol. 17, no. 22, pp. 20 178–20 190, Oct. 2009.

[197] Q. Fang and D. Boas, "Tetrahedral mesh generation from volumetric binary and gray-scale images," 2009, pp. 1142–1145.

[198] Q. Fang, "Mesh-based monte carlo method using fast ray-tracing in Plücker coordinates," *Biomedical Optics Express*, vol. 1, no. 1, pp. 165–175, Jul. 2010.

[199] "Monte Carlo eXtreme: GPU-based Monte Carlo Simulations: MMC/Colin27AtlasMesh."

[200] "igl | Interactive Geometry Lab | ETH Zurich | Instant Field-Aligned Meshes."

[201] W. Jakob, D. Panozzo, and O. Sorkine-Hornung, "Instant field-aligned meshes," *ACM Transactions on Graphics*, vol. 34, pp. 1–15, Oct. 2015.

[202] C. Geuzaine and J.-F. Remacle, "Gmsh: A 3-D finite element mesh generator with built-in pre- and post-processing facilities," *International Journal for Numerical Methods in Engineering*, vol. 79, no. 11, pp. 1309–1331, 2009.

[203] Algiane, "Mmg Platform – Upgrade your meshes," library Catalog: www.mmgtools.org.

[204] C. Dobrzynski and P. Frey, "Anisotropic delaunay mesh adaptation for unsteady simulations," in *proceedings of the 17th international meshing roundtable*, R. V. Garimella, Ed. Berlin, Heidelberg: Springer Berlin Heidelberg, 2008, pp. 177–194.

[205] C. Dapogny, C. Dobrzynski, and P. Frey, "Three-dimensional adaptive domain remeshing, implicit domain meshing, and applications to free and moving boundary problems," *Journal of Computational Physics*, Apr. 2014.

[206] D. A. Nelson and S. A. Nunneley, "Brain temperature and limits on transcranial cooling in humans: quantitative modeling results," *European Journal of Applied Physiology and Occupational Physiology*, 1998.

[207] C. Diao, L. Zhu, and H. Wang, "Cooling and rewarming for brain ischemia or injury: theoretical analysis," *Annals of Biomedical Engineering*, vol. 31, no. 3, pp. 346–353, Mar. 2003.

[208] A.-A. Konstas, M. A. Neimark, A. F. Laine, et al., "A theoretical model of selective cooling using intracarotid cold saline infusion in the human brain," *Journal of Applied Physiology (Bethesda, Md.: 1985)*, vol. 102, no. 4, pp. 1329–1340, Apr. 2007.

[209] P. A. Yushkevich, J. Piven, H. C. Hazlett, et al., "User-guided 3D active contour segmentation of anatomical structures: significantly improved efficiency and reliability," *NeuroImage*, vol. 31, no. 3, pp. 1116–1128, Jul. 2006.

[210] "ITK-SNAP Home," www.itksnap.org.

[211] N. R. Pal and S. K. Pal, "A review on image segmentation techniques," *Pattern Recognition*, vol. 26, no. 9, pp. 1277–1294, Sep. 1993.

[212] J. Beyerer, F. P. León, and C. Frese, *Machine Vision: Automated Visual Inspection: Theory, Practice and Applications*. Berlin Heidelberg: Springer-Verlag, 2016.

[213] J. Bloomenthal, *Skeletal Design of Natural Forms*. University of Calgary, 1995, accepted: 2005-07-29T22:07:06Z.

[214] S. Abbott, "Introduction to topological manifolds," *The Mathematical Gazette*, vol. 85, no. 502, pp. 183–184, Mar. 2001, publisher: Cambridge University Press.

[215] T. Rashid, S. Sultana, and M. A. Audette, "Watertight and 2-manifold surface meshes using dual contouring with tetrahedral decomposition of grid cubes," *Procedia Engineering*, vol. 163, pp. 136–148, 2016.

[216] Y. Ge, R. I. Grossman, J. S. Babb, et al., "Age-related total gray matter and white matter changes in normal adult brain. part ii: quantitative magnetization transfer ratio histogram analysis," *American Journal of Neuroradiology*, vol. 23, no. 8, pp. 1334–1341, Sep. 2002, publisher: American Journal of Neuroradiology Section: BRAIN.

[217] J. S. Allen, H. Damasio, and T. J. Grabowski, "Normal neuroanatomical variation in the human brain: an MRI-volumetric study," *American Journal of Physical Anthropology*, vol. 118, no. 4, pp. 341–358, Aug. 2002.

[218] E. G. Lee, W. Duffy, R. L. Hadimani, et al., "Investigational effect of brain-scalp distance on the efficacy of transcranial magnetic stimulation treatment in depression," *IEEE Transactions on Magnetics*, vol. 52, no. 7, pp. 1–4, Jul. 2016, conference Name: IEEE Transactions on Magnetics.

[219] E. G. Lee, P. Rastogi, R. L. Hadimani, et al., "Impact of non-brain anatomy and coil orientation on inter- and intra-subject variability in TMS at midline," *Clinical Neurophysiology*, vol. 129, no. 9, pp. 1873–1883, Sep. 2018.

[220] Y. Lutz, A. Loewe, S. Meckel, et al., "Combined local hypothermia and recanalization therapy for acute ischemic stroke: estimation of brain and systemic temperature using an energetic numerical model." *Journal of Thermal Biology*, vol. 84, pp. 316–322, 2019, publisher: Pergamon.

[221] M. Baldry, V. Timchenko, and C. Menictas, "Thermal modelling of controlled scalp hypothermia using a thermoelectric cooling cap," *Journal of Thermal Biology*, 2018.

[222] J. Slotboom, C. Kiefer, C. Brekenfeld, et al., "Locally induced hypothermia for treatment of acute ischaemic stroke: a physical feasibility study," *Neuroradiology*, vol. 46, no. 11, pp. 923–934, Nov. 2004.

[223] S. Mustafa and O. Thulesius, "Cooling-induced carotid artery dilatation: an experimental study in isolated vessels," *Stroke*, vol. 33, no. 1, pp. 256–260, Jan. 2002.

[224] M. Zhu, J. J. H. Ackerman, A. L. Sukstanskii, et al., "How the body controls brain temperature: the temperature shielding effect of cerebral blood flow," *Journal of Applied Physiology (Bethesda, Md.: 1985)*, vol. 101, no. 5, pp. 1481–1488, Nov. 2006.

[225] A. L. Sukstanskii and D. A. Yablonskiy, "Theoretical model of temperature regulation in the brain during changes in functional activity," *Proceedings of the National Academy of Sciences of the United States of America*, vol. 103, no. 32, pp. 12 144–12 149, Aug. 2006.

[226] A. L. Sukstanskii and D. A. Yablonskiy, "Theoretical limits on brain cooling by external head cooling devices," *European journal of applied physiology*, vol. 101, no. 1, pp. 41–49, Sep. 2007.

[227] H. D. V. Baehr, *Wärme- und Stoffübertragung*, 10th ed., Springer eBooks, K. V. Stephan, Ed. Berlin: Springer Vieweg, 2019.

[228] J. D. Hardy and C. Muschenheim, "The radiation of heat from the human body. iv. the emission, reflection, and transmission of infra-red radiation by the human skin," *Journal of Clinical Investigation*, vol. 13, no. 5, pp. 817–831, Sep. 1934.

[229] F. J. Sanchez-Marin, S. Calixto-Carrera, and C. Villaseñor-Mora, "Novel approach to assess the emissivity of the human skin," *Journal of Biomedical Optics*, vol. 14, no. 2, p. 024006, Mar. 2009.

[230] A. Seim, "Detaillierte Berechnung zerebraler Temperaturverläufe durch Implementierung und Kopplung eines Temperaturmodells des systemischen Körpers," Master's thesis, Institut für Strömungsmechanik, Karlsruhe Institute of Technology (KIT), 2019.

[231] J. Werner and M. Buse, "Temperature profiles with respect to inhomogeneity and geometry of the human body," *Journal of Applied Physiology (Bethesda, Md.: 1985)*, vol. 65, no. 3, pp. 1110–1118, Sep. 1988.

[232] D. Fiala, K. J. Lomas, and M. Stohrer, "A computer model of human thermoregulation for a wide range of environmental conditions: the passive system," *Journal of Applied Physiology*, vol. 87, no. 5, pp. 1957–1972, Nov. 1999.

[233] A. Schwarzhaupt, "Regelung der extrakorporalen Zirkulation auf der Basis eines Modells des menschlichen Kreislaufes," PhD Thesis, Cuvillier, Göttingen, 1999, iSBN: 3897125137.

[234] J.-C. Baron, "Perfusion thresholds in human cerebral ischemia: historical perspective and therapeutic implications," *Cerebrovascular Diseases*, vol. 11, no. Suppl. 1, pp. 2–8, 2001.

[235] I. Harukuni and A. Bhardwaj, "Mechanisms of brain injury after global cerebral ischemia," *Neurologic Clinics*, vol. 24, no. 1, pp. 1–21, Feb. 2006.

[236] I. Marshall, B. Karaszewski, J. M. Wardlaw, et al., "Measurement of regional brain temperature using proton spectroscopic imaging: validation and application to acute ischemic stroke," *Magnetic Resonance Imaging*, vol. 24, no. 6, pp. 699–706, Jul. 2006.

[237] B. Karaszewski, J. M. Wardlaw, I. Marshall, et al., "Measurement of brain temperature with magnetic resonance spectroscopy in acute ischemic stroke," *Annals of Neurology*, vol. 60, no. 4, pp. 438–446, Oct. 2006.

[238] J. Wolfertz, S. Meckel, A. Guber, et al., "Mathematical, numerical and in-vitro investigation of cooling performance of an intra-carotid catheter for selective brain hypothermia," *Current Directions in Biomedical Engineering*, vol. 1, no. 1, pp. 390–394, 2015.

[239] J. Müller, V. Schreiter, E. Böhl, et al., "Application of thermography for cerebral perfusion imaging during aneurysm surgery," *Current Directions in Biomedical Engineering*, vol. 4, no. 1, pp. 29–32, Sep. 2018.

List of Publications and Supervised Theses

Journal Articles

- **Y. Lutz**, A. Loewe, S. Meckel, O. Dössel, and G. Cattaneo, *Combined local hypothermia and recanalization therapy for acute ischemic stroke: Estimation of brain and systemic temperature using an energetic numerical model*, Journal of Thermal Biology, vol. 84, pp. 316-322, 2019
- **Y. Lutz**, R. Daschner, L. Krames, A. Loewe, G. Cattaneo, S. Meckel, and O. Dössel, *Modeling selective therapeutic hypothermia in case of acute ischemic stroke using a 1D hemodynamics model and a simplified brain geometry*, Mathematical Biosciences and Engineering, vol. 17(2) , pp. 1147-1167, 2019
- **Y. Lutz**, T. Meißner, L. Krames, G. Cattaneo, S. Meckel, O. Dössel and A. Loewe *Selective Brain Hypothermia for Ischemic MCA-M1 Stroke: Influence of Cerebral Arterial Circulation in a 3D Brain Temperature Model*, IEEE Transactions on Biomedical Engineering, (submitted), 2020
- A. Loewe, **Y. Lutz**, M. Wilhelms, D. Sinnecker, P. Barthel, E. P. Scholz, O. Dössel, G. Schmidt, and G. Seemann, *In-silico assessment of the dynamic effects of amiodarone and dronedarone on human atrial patho-electrophysiology*, Europace : European pacing, arrhythmias, and cardiac electrophysiology : journal of the working groups on cardiac pacing, arrhythmias, and cardiac cellular electrophysiology of the European Society of Cardiology, vol. 16(S4) , pp. iv30-iv38, 2014
- A. Loewe, **Y. Lutz**, D. Nairn, A. Fabbri, N. Nagy, N. Toth, X. Ye, D. H. Fuertinger, S. Genovesi, P. Kotanko, J. G. Raimann, and S. Severi, *Hypocalcemia-Induced Slowing of Human Sinus Node Pacemaking*, In Biophysical Journal, 2019
- A. Loewe, **Y. Lutz**, N. Nagy, A. Fabbri, C. Schweda, A. Varró, and S. Severi, *Inter-Species Differences in the Response of Sinus Node Cellular Pacemaking to Changes of Extracellular Calcium*, In bioRxiv - the preprint server for biology, 2019

Refereed Conference Articles

- **Y. Lutz**, A. Loewe, O. Dössel, and G. Seemann, *Specific antiarrhythmic therapy for familial atrial fibrillation in a numerical model of human atrial electrophysiology*, In Biomedizinische Technik / Biomedical Engineering, vol. 59(s1) , pp. s933-s936, 2014
- G. Lenis, **Y. Lutz**, G. Seeman, A. García-Alberola, J. L. Rojo-Álvarez, O. Barquero-Peréz, E. Gil, and O. Dössel, *Post Extrasystolic T Wave Change in Subjects With Structural Healthy Ventricles Measurement and Simulation*, In Computing in Cardiology, vol. 41, pp. 1069-1072, 2014
- A. Loewe, **Y. Lutz**, M. Wilhelms, E. P. Scholz, O. Dössel, and G. Seemann, *Optimization of pharmacotherapy for familial atrial fibrillation in a numerical model of human atrial electrophysiology*, In Computing in Cardiology, vol. 41, pp. 745-748, 2014
- **Y. Lutz**, R. Daschner, L. Krames, A. Loewe, O. Dössel, and G. Cattaneo, *Estimating Local Therapeutic Hypothermia in Case of Ischemic Stroke Using a 1D Hemodynamics Model and an Energetic Temperature Model*, In 41st Annual International Conference of the IEEE Engineering in Medicine and Biology Society (EMBC), pp. 3983-3986, 2019
- R. Daschner, L. Krames, **Y. Lutz**, A. Loewe, O. Dössel, and G. Cattaneo, *Generation of a Simplified Brain Geometry for the Calculation of Local Cerebral Temperature using a 1D Hemodynamic Model*, In Current Directions in Biomedical Engineering, vol. 5(1) , pp. 529-532, 2019
- L. Krames, R. Daschner, **Y. Lutz**, A. Loewe, O. Dössel, and G. Cattaneo, *Modeling of the Human Cerebral Collateral Circulation: Evaluation of the Impact on the Cerebral Perfusion in Case of Ischemic Stroke*, In Current Directions in Biomedical Engineering, vol. 5(1) , pp. 533-536, 2019
- A. Loewe, **Y. Lutz**, N. Nagy, A. Fabbri, C. Schweda, A. Varro, and S. Severi, *Inter-Species Differences in the Response of Sinus Node Cellular Pacemaking to Changes of Extracellular Calcium*, In 41st Annual International Conference of the IEEE Engineering in Medicine and Biology Society (EMBC), pp. 1875-1878, 2019

Conference Presentations

- G. Seemann, A. Loewe, **Y. Lutz**, M. Wilhelms, and O. Dössel, *Simulating the Effects of Drugs and Genetic Defects on Atrial Electrophysiology*, In TRM Forum, 2013
- A. Loewe, M. Wilhelms, **Y. Lutz**, O. Dössel, and G. Seemann, *Modeling human atrial patho-electrophysiology: genetic defects and pharmacological agents*, In Simula Cardiac Modeling Workshop, 2014
- **Y. Lutz**, A. Fabbri, S. Severi, O. Dössel, and A. Loewe, *Plasma electrolyte concentrations in patients with chronic kidney disease influence cardiac pacemaking in a computational model*, In BMTMedPhys 2017, vol. 62(s1 - V71) , pp. 67, 2017

- **Y. Lutz**, L. Krames, A. Loewe, G. Cattaneo, O. Dössel, *A Model of Cerebral Collateral Circulation for Evaluation of Blood Flow in Case of M1-Stenosis*, In 52th DGBMT annual conference, 2018
- A. Loewe, **Y. Lutz**, A. Fabbri, S. Severi, G. Seemann, and D. Dössel, *Influence of Electrolyte Concentration Changes on Sinus Node Function - A new Player Regarding Sudden Cardiac Death in Patients with Chronic Kidney Disease?*, In Gordon Research Conference on Cardiac Arrhythmia Mechanisms, 2017
- **Y. Lutz**, A. Loewe, O. Dössel, G. Cattaneo, *Numerical Model of Brain and Systemic Temperature during local Hypothermia for Ischemic Stroke Treatment*, In Interdisciplinary Cerebrovascular Symposium (ICS), Magdeburg, Germany, 2018
- A. Loewe, **Y. Lutz**, A. Fabbri, and S. Severi, *Severe sinus bradycardia due to electrolyte changes as a pathomechanism of sudden cardiac death in chronic kidney disease patients undergoing hemodialysis*, In Heart Rhythm, vol. 15(5S) , pp. S354-S355, 2018
- S. Severi, A. Fabbri, M. Paci, R. Wilders, **Y. Lutz**, and A. Loewe, *Computational Modeling of the Cardiac Pacemaking in Humans*, In INdAM Workshop on Mathematical and Numerical Modeling of the Cardiovascular System, 2018
- **Y. Lutz**, A. Loewe, G. Cattaneo, O. Dössel, *Adaption of Avolio's 1D Hemodynamics Model for Use in Cerebral Tempera-ture Calculation*, In 53th DGBMT annual conference, 2019
- S. Voß, **Y. Lutz**, A. Boese, F. Klink, A. Ding, G. Janiga, O Beuing *Experimentelle Untersuchung der Perfusion im Kontext der milden therapeutischen Hypothermie*, In 4th Conference on Image-Guided Interventions, Digitalisierung in der Medizin, 2019
- A. Loewe, **Y. Lutz**, A. Fabbri, and S. Severi, *Sinus Bradycardia Due to Electrolyte Changes as a Potential Pathomechanism of Sudden Cardiac Death in Hemodialysis Patients*, In Biophysical Journal, vol. 116, pp. 231A, 2019

Reports and Theses

- **Y. Lutz**, *Specific Antiarrhythmic Therapy for Familial Atrial Fibrillation in a Numerical Model of Human Atrial Electrophysiology*, Bachelor Thesis, Institute of Biomedical Engineering, Karlsruhe Institute of Technology (KIT), 2013
- **Y. Lutz**, *Influence of Electrolyte Concentration Changes on Sinus Node Function - A new player regarding sudden cardiac death in patients with chronic kidney disease?*, Master Thesis, Institute of Biomedical Engineering, Karlsruhe Institute of Technology (KIT), 2016

Supervised Student Theses

- Lorena Krames, *Modeling of the Human Cerebral Collateral Circulation -Evaluation of the Impact on the Cerebral Pathophysiology in Case of Ischemic Stroke*, Bachelor Thesis, Institute of Biomedical Engineering, Karlsruhe Institute of Technology (KIT), 2018
- Angelo Aracri, *Modeling of the Human Cerebral Circulation -Evaluation of the Influence of Gender and Age on Average Dimensions of the Circle of Willis*, Bachelor Thesis, Institute of Anthropomatics and Robotics, Karlsruhe Institute of Technology (KIT), 2019
- Ole Pauer, *Modeling of the Human Cerebral Circulation -Adaption of a Hemodynamics Model Based on Avolio for Temperature Calculation*, Bachelor Thesis, Institute of Biomedical Engineering, Karlsruhe Institute of Technology (KIT), 2019
- Rosa Daschner, *Generierung einer vereinfachten Gehirngeometrie zur Berechnung der lokalen zerebralen Temperatur mit einem 1D-Hämodynamik-Modell*, Bachelor Thesis, Institut für Strömungsmechanik, Karlsruhe Institute of Technology (KIT), 2019
- Tobias Meißner, *Adaptation and Partition of a Brain Geometry for a Spatially Detailed Calculation of Local Cerebral Temperatures*, Master Thesis, Institute of Biomedical Engineering, Karlsruhe Institute of Technology (KIT), 2019
- Alice Seim, *Detaillierte Berechnung zerebraler Temperaturverläufe durch Implementierung und Kopplung eines Temperaturmodells des systemischen Körpers*, Master Thesis, Institut für Strömungsmechanik, Karlsruhe Institute of Technology (KIT), 2019
- Alexander Seer, *Parameterization of a Spatial Cerebral Temperature Model Using Thermal Image Information*, Master Thesis, Institute of Biomedical Engineering, Karlsruhe Institute of Technology (KIT), 2019

Awards & Grants

- 1st place in student competition, 48th DGBMT annual conference, 2014, **Y. Lutz**, A. Loewe, M. Wilhelms, O. Dössel, G. Seemann, *Specific antiarrhythmic therapy for familial atrial fibrillation in a numerical model of human atrial electrophysiology*.